Antarctic Meteorites XXX

Papers presented to the Thirtieth Symposium on Antarctic Meteorites

June 6-8, 2006

NATIONAL INSTITUTE OF POLAR RESEARCH
TOKYO

国立極地研究所
南極隕石センター

Tuesday, June 6, 2006

0900–1200 **Registration** **Auditorium (6th Floor)**

Oral sessions will be held in the auditorium, 6th floor of the Main Building
* *denotes speaker*

0925–0930 **Fujii Y.** (Director-General, NIPR)
Opening Address

Chairs: Fagan T. and Arai T.

Chairs: Kimura M. and Uesugi M.

—Special Talk (I)—

Chair: Yamaguchi A.

1715–1915 **Welcome Party (6th Floor)**

Wednesday, June 7, 2006

Chairs: Kaiden H. and Nagao K.

Chairs: Mikouchi T. and Noguchi T.

—Special Talk (II)—

Chair: Misawa K.

Thursday, June 8, 2006

Chairs: Hiroi T. and Tachibana S.

1200–1300 —Lunch—

Chairs: Hoffmann V. and Bérczi Sz.

ABSTRACTS

The difference of apparent strain of olivine crystals between clastic and nonclastic parts of Naryilco LL6 chondrite. T. Aoki[1] and Y. Nakamuta[2], [1]Department of Earth and Planetary Sciences, Graduate School of Sciences, Kyushu University, [2]Kyushu University Museum, Kyushu University.

Introduction

Most meteorites are subjected to shock metamorphism in some degree. It is important to estimate the degree of shock in order to know the evolution processes on a planet and also of the solar system. Stöffler *et al.* [1] classified the chondrites into 6 classes based on shock textures on olivine and plagioclase. After that, Uchizono *et al.* [2] found that the apparent strain of olivine has a proportional relation to shock pressure loaded on it based on shock experiments using an olivine single crystal.

Naryilco LL6 chondrite shows clastic and nonclastic textures in parts. In this study, we examined the differences of shock effects on olivine between clastic and nonclastic parts of Naryilco chondrite.

Sample and Experiments

The specimen of Naryilco chondrite examined in this study is 5.5×2×0.5 cm in size. The chondrite shows clastic and nonclastic textures in parts. The specimen was cut into three chips of nearly equal area for the investigation. We prepared polished thin sections of each chip, and they were observed under an optical microscope with polarizing plates.

Fifty-eight olivine grains in the sections were analyzed by an electron probe micro analyzer (EPMA). The accelerating voltage and specimen current are 15 kV and 1.0×10^{-8} A, respectively.

Eighteen olivine grains, having homogeneous chemical compositions and being less than 100 μm in size, were taken from three polished thin sections under a binocular microscope for the X-ray analysis using a Gandolfi camera. Precise peak positions and breadths of each diffraction line were determined by using a profile-fitting technique [3]. The apparent strains of each olivine crystal were determined by plotting $\tan\theta$ vs. β, based on the equation, $\beta=4e\tan\theta$, where β, e and θ are integral breadth of each diffraction line, apparent strain of the crystal and a half of diffraction angle of each diffraction line, respectively [4].

Results and Discussions

The photograph of the specimen and microphotographs of each polished thin section are shown in Fig.1. As shown in Fig.1, the clastic part of Naryilco chondrite is composed of an intimate mixture of variable sized clasts and shock melt. Olivine grains in both clastic and nonclastic parts show undulatory extinction, planar fracture and mosaicism formed by shock. These results suggest that Naryilco chondrite can be assigned to S4 or S5 shock stage of Stöffler *et al.* [1], which means that the meteorite was suffered to moderate shock.

Modal abundances of Fa components of olivine for clastic and nonclastic parts are shown in Fig.2. As can be seen in Fig.2, olivine in the clastic part of Naryilco has compositions in the range of $Fa_{27\text{-}35}$ in contrast to $Fa_{25\text{-}30}$ of olivine in the nonclastic part. It is noticeable that olivine in the clastic part are richer in Fe-contents than that in the nonclastic part.

Apparent strains of each olivine crystal are summarized in Fig.3. Apparent strains of olivine in the clastic part are in the range from 0.075 to 0.205 %, and that in the nonclastic part are in the range from 0.155 to 0.278 %. The variation of apparent strains is by about 0.12 % both in the clastic and the nonclastic parts, but maximum and minimum strains of olivine crystals in the nonclastic part are larger than that in the clastic part about 0.7 %. Yamada *et al.* [5] proposed a diagram which relates apparent strains of olivine and shock pressures experienced by it. Using their diagram, shock pressure for olivine in the clastic part is estimated to be 20.3 ± 4.1 GPa and that for nonclastic part is 28.3 ± 5.6 GPa. It is noticeable that shock pressures recorded on olivine in the clastic and the nonclastic parts differ to each other.

The results of this study suggest that chemical compositions and apparent strains of olivine crystals differ between the clastic and the nonclastic parts. The olivines in the clastic part show low apparent strains in comparison to those in the nonclastic part. We interpret the difference of apparent strains of olivine as the results of the reduction of an effective shock pressure at the clastic part by breaking into pieces.

References

[1] Stöffler D. *et al.* (1991) *Geochumica et Cosmochimica Acta, 55*, 3845-3867. [2] Yamada S. *et al.* (2000) *25th Symposium on Antarctic Meteorites, National Institute of Polar Research,* 187-189. [3] Nakamuta Y. (1994) *Zeolite, 11(4),* 171-179. [4] Willson A. J. C. (1962) *X-Ray Optics.* [5] Uchizono A. *et al.* (1999) *Mineralogical J. 21(1)*, 15-23.

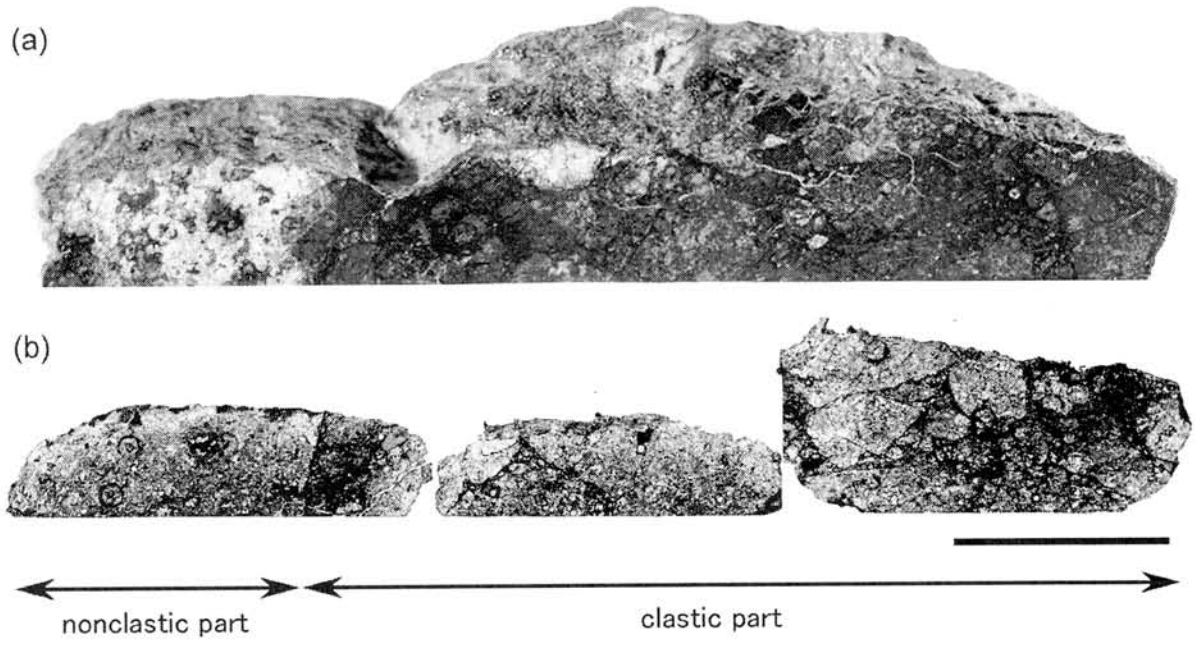

Fig.1. The photograph of a polished surface of the specimen (a) and microphotographs of three polished thin sections (b). The bar under the photographs shows 1 cm.

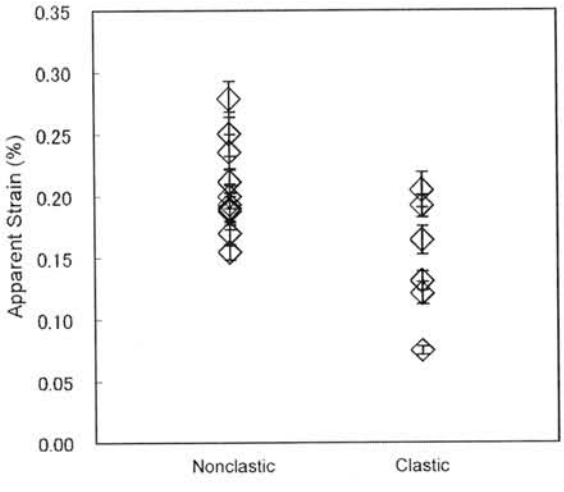

Fig.2. The apparent strains of olivine crystals obtained by the X-ray analysis both in nonclastic and clastic parts. Apparent strains of olivine in the clastic part are in the range from 0.075 to 0.205 %, and that in the nonclastic part are in the range from 0.155 to 0.278 %.

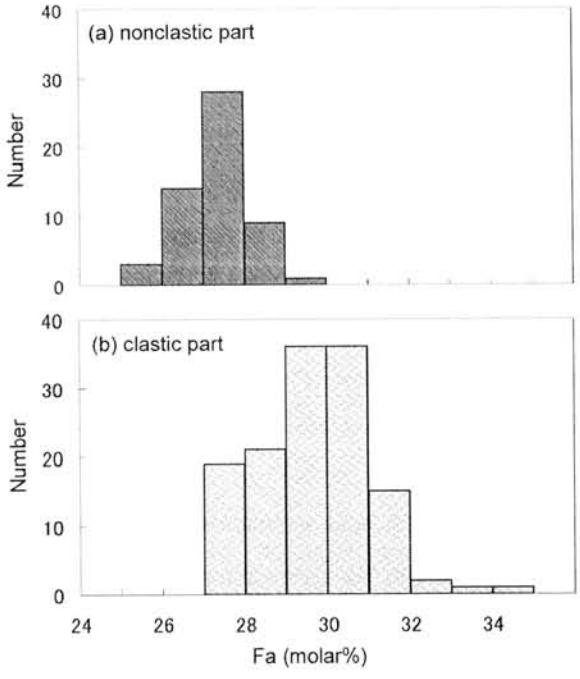

Fig.3. Histograms of fayalite components of olivine in nonclastic part (a) and clastic part (b). The averaged Fa modal abundances in the nonclastic and the clastic parts are 26.3 (σ=0.8) and 28.7 (σ=1.4) %, respectively, where σ is a standard deviation.

Ion microprobe study of Apollo 14 oldest basalt. T. Arai, H. Kaiden, K. Misawa, and H. Kojima. Antarctic Meteorite Research Center, National Institute of Polar Research, Kaga, Itabashi, Tokyo 173-8515, Japan (tomoko@nipr.ac.jp).

Introduction: Apollo 14 site yields the relative abundance and diversity of lithologies from ancient, pre-Imbrium magmatism, such as Mg-rich rocks, alkali-rich rocks, high-aluminum, low-titanium basalts, high-potassium basalts, and KREEP basalts. Besides these rocks, the oldest (4.23 Ga) olivine-rich basalt cumulate clast 14305, 92 has been also reported, implying that mare-type volcanism commenced as early as 4.23 Ga in the Fra Mauro region [1]. There are two annoying features for this clast to deduce its petrogenesis. Firstly, it shows a systematic compositional variation from "primitive" to "evolved" across the 1-cm clast, reflecting either primitive cryptic layering or secondary re-equilibration by evolved inter-cumulus liquid. Secondly, *mg* [=100×Mg/(Mg+Fe)] of the bulk clast (63.5) [1] is too Mg-rich to crystallize the most magnesian olivine (Fo_{73}). Even after all the cumulus olivines are subtracted, the *mg* is sill too magnesian, indicating that the whole clast is not a simple mixture of the cumulus phases and trapped liquid. This excessive *mg* parallels with the textural evidence that some of the olivines were re-absorbed while pyroxene crystallized. Hence, the major-element composition of the parent melt for the basalt is difficult to be properly estimated, and the subtraction of the cumulus phases seems to represent a liquid composition with a minimum enrichment in the incompatible elements. In this study, rare earth element (REE) compositions of olivine, pyroxene, and plagioclase to further elucidate the petrogenesis of this enigmatic ancient basalt cumulate in light of the trace element characteristics. In addition, a petrogenetic connection with mare basalt as suggested by [1] and other lithologies occurring in Apollo 14 site are evaluated, since a recent study has suggested a possible link with VHK basalts [2].

Sample and method: A polished thin section 14305, 92 provided by NASA JSC, was studied. Ion microprobe analyses were done with the SHRIMP II at National Institute of Polar Research (NIPR). A modified energy filtering technique [3] was used to discriminate against complex molecular interferences. Major-element mineral compositions were analyzed by a JEOL 8200 electron microprobe at NIPR.

REE compositions of minerals: Analyzed points in the basalt clast are shown in the backscattered electron image (Fig. 1). The major-element mineral compositions are: the olivines range from Fo_{73} to Fo_{61}, the plagioclase from An_{92} to An_{67}, and the pyroxenes are co-existing pigeonite ($Wo_8Fs_{25}En_{67}$ to $Wo_{12}Fs_{24}En_{64}$) and augites ($Wo_{32}Fs_{17}En_{57}$ to $Wo_{37}Fs_{15}En_{48}$). The REE abundances of olivines, pyroxenes and plagioclases relative to CI chondrite [4] are shown in Fig. 2. The LREE concentrations of olivines are extremely low with large error bars. The REE abundance increases as the Fo value decreases, with nearly the same patterns. The most Fe-rich olivines 4 and 5 are a factor of 7-8 enriched in HREE than the Mg-rich olivines 1 and 3. Augites are enriched in LREE (100-200×) and in HREE (23-90×) compared to pigeonites. The three plagioclases analyzed show analogous REE abundances and patterns to each other.

Petrogenesis: The melt in equilibrium with each mineral with the most primitive composition was calculated by dividing measured REE concentrations with appropriate distribution coefficients ([5] for olivine, [6] and [7] for pyroxenes, and [8] for plagioclase) (Fig. 3). Note that a melt for the most primitive cumulus olivine might likely represent the primary melt composition, whereas those for the pyroxene and plagioclase tend to indicate compositions of the inter-cumulus melt. The REE abundance and pattern of the melt for the pyroxene is remarkably similar to that of the bulk clast composition [1], especially in HREE. The similarity in the REE abundance between the melt for the pyroxene and the bulk clast seems coincidental. The melt for plagioclase is slightly enriched in LREE (a factor of 2.5 in La, and 1.8 in Sm) and similar HREE abundance with a distinct HREE-depleted pattern, compared to the bulk clast composition [1]. The abundances of only Gd and Yb are calculated for the melt for the olivine, due to the limited availability of the distribution coefficients [5] and the extremely low concentration of LREE. The melt for the olivine is enriched in HREE than the bulk clast composition and the melt for the pyroxene by a factor of 4-5, which is nearly identical (0.8 - 0.9 times) to the REE abundance of high-K KREEP [9], though the LREE and Eu signatures are not currently constrained.

The melt in equilibrium with the most Mg-rich olivine (Fo_{73}) is *mg* = 47 assuming $K_D^{ol\text{-}liq}$= 0.33 [10]. Provided that the bulk clast composition represents olivine cumulates + isolated primary melt + re-absorbed olivines, a simple mass balance calculation shows the olivines are to be initially 64 vol% or more in the whole clast to attain the bulk clast *mg* = 63.5, despite the apparent modal abundance of olivine is ~40 vol%. The estimated ratios of the cumulus olivine (64 vol%) and the interstitial melt (36 vol%) coupled with the REE abundances of the olivine 1 and the melt for the olivine 1 successfully reproduced the REE abundance similar (1.7 times higher) to that of the bulk clast, with higher olivine mode (i.e. 70 vol%) leading to further proximity to the bulk clast REE composition. This implies that the bulk clast originally consists of cumulus olivines of modal ~70 vol%, resulting in the composition extensively depleted (a factor of 4-5) in REE content, compared with that of the primary melt. The estimated melt composition for the olivine, equivalent of the high-K KREEP (at least in HREE) suggests that the basalt clast probably crystallized from a KREEP basaltic magma as well as Mg-rich rocks [11, 12] and alkali-rich rocks [13], and not originated from a typical mare basalt magma.

References: [1] Taylor L. A. et al. (1983) *EPSL*, **66**, 33-47. [2] Arai T. et al. (2006) *PLPSC*, **31**, 877-892. [3] Ireland T. R. et al. (1994) *EPSL*, **128**, 199-213. [4] Anders E. and Grevesse N.(1989) *GCA*, **53**, 197-214. [5] McKay G. A. (1986) *GCA*, **50**, 69-79. [6] McKay G. A. et al. (1986) *GCA*, **50**, 927-937. [7] McKay G. A. et al. (1991) LPS XXII, 883-884. [8] Phinney W. C. and Morrison D. A. (1990) *GCA*, **54**, 1639-1654. [9] Warren P. H. (1989) Workshop on Moon in Transition, LPI Tec. Rep. 89-03,149-153. [10] Grove T. H. and Vaniman D. H. (1978) *Mare Crisum: The view from Luna 24*, 445-471. [11] Papike J. J. et al. (1996) *GCA*, **60**, 3967-3978. [12] Shervais J. W. and McGee J. J. (1998) *GCA*, **62**, 3009-3023. [13] Shervais J. W. and McGee J. J. (1999) *Am.Mineral.* **84**, 805-820.

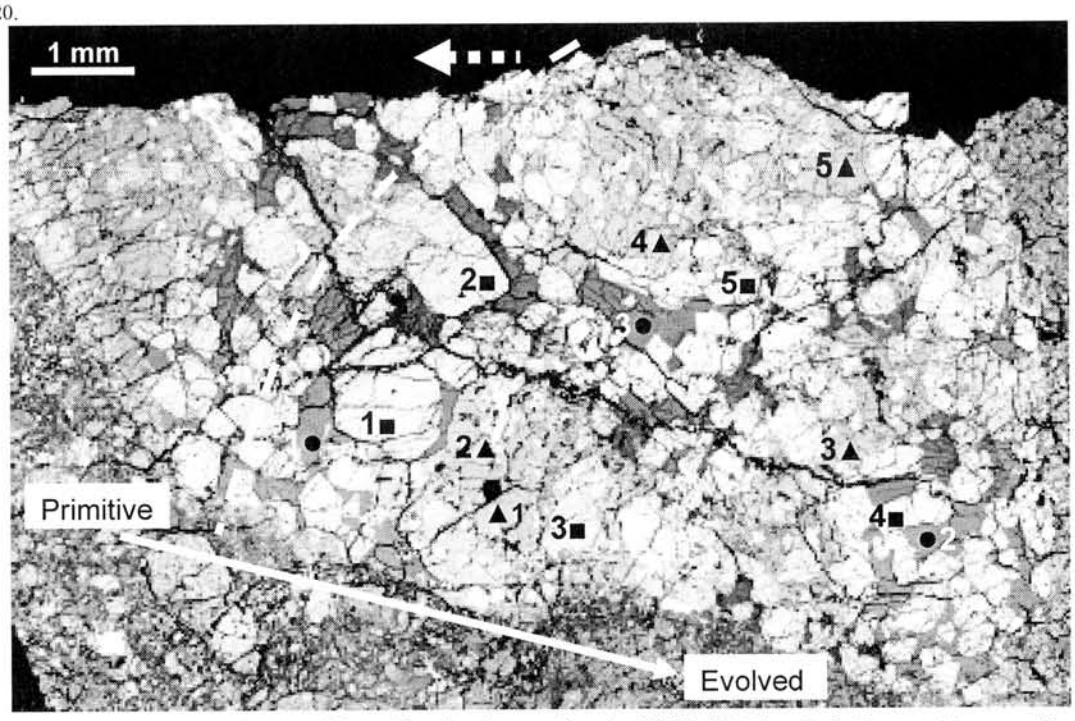

Fig.1 Back-scattered electron image of the oldest basalt cumulate in 14305, 92. Mineralogical compositions vary from "primitive" to "evolved" across the 1-cm clast. Analyzed points by ion probe are shown with solid squares (olivine), solid triangles (pyroxene), and solid circles (plagioclase). A dotted curved line and a dotted arrow indicate the area that could not be analyzed by ion probe because the clast is located to the edge of the thin section, a part of which is physically interfered with a sample holder.

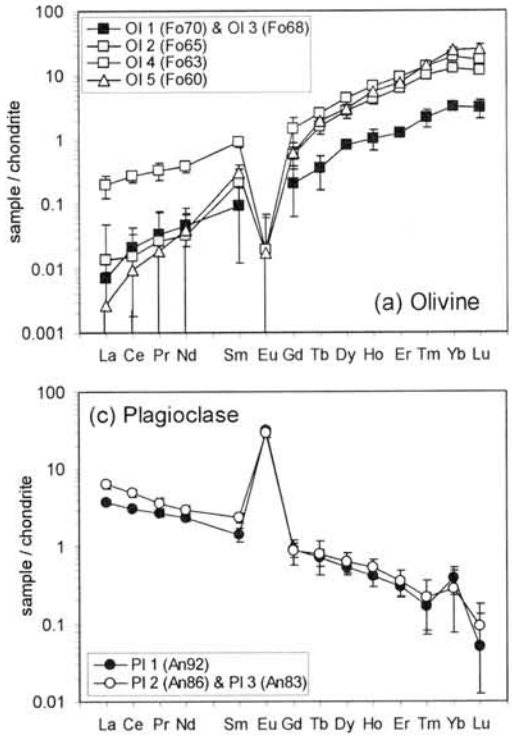

Fig. 2 REE abundances of minerals.

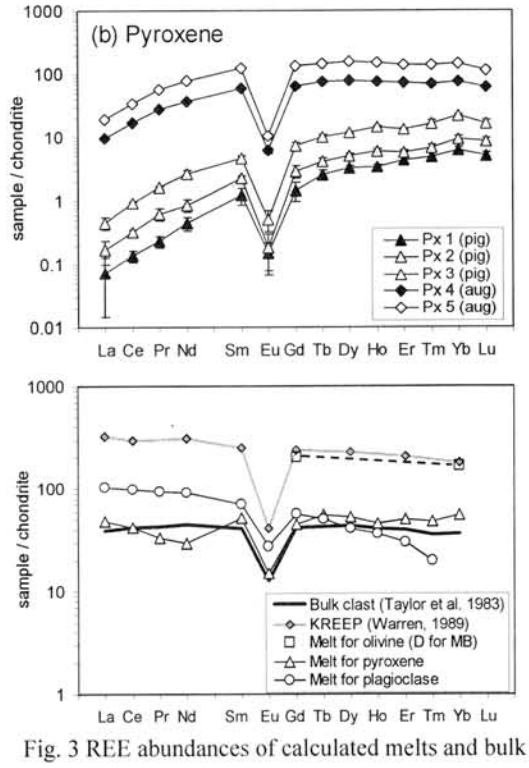

Fig. 3 REE abundances of calculated melts and bulk clast.

HOW WE USED NIPR ANTARCTIC EDUCATIONAL THIN SECTION SET IN PLANETARY AND MATERIAL SCIENCE STUDIES: 10 YEARS OF STUDIES IN EÖTVÖS UNIVERSITY, HUNGARY. ***Bérczi Sz.[1,2], Gál-Sólymos, K.[2], Gucsik A.[3], Hegyi S.[4], Hudoba, Gy.[5], Józsa S.[2], Kókány A.[4], Kubovics I.[2], Lukács B.[6], Puskás Z.[2], Szakmány Gy.[2], Varga T.[7],*** [1]Eötvös University, Institute of Physics, Dept. Materials Physics, Cosmic Materials Space Res. Group, H-1117 Budapest, Pázmány Péter sétány 1/a. Hungary, [2]Eötvös University, Dept. Petrology and Geochemistry, H-1117 Budapest, Pázmány P. s. 1/c. Hungary, [3]University of West Hungary, Bajcsy-Zs. u. 4., Sopron, H-9400, Hungary, [4]Pécs University, Faculty of Science, Dept. Informatics and G. Technology, H-7624 Pécs, Ifjúság u. 6. Hungary, [5]BMF Kandó Kálmán College, Inst. of Computer Technology, H-8000 Székesfehérvár, Budai út 45., Hungary, [6]Central Research Inst. for Physics, KFKI-RMKI, Hungarian Academy of Science, H-1525 Budapest 114, P.O.Box. 49, Hungary, [7]VT-Patent Office Kft. H-1111 Budapest, Bertalan Lajos u. 20. Hungary,. (bercziszani@ludens.elte.hu)

Introduction: We began to study NIPR Antarctic meteorite sample educational set from 1994 and we could loan it year by year (with interruptions) for almost 10 years on Eötvös University, Budapest. Various programs on the set were reported on the NIPR, LPSC and Meteoritical Society annual conferences. Here we summarize the highlights of the programs. ***Petrographic studies***: overview of the thermal history stages of a chondritic parent body. ***Comparative petrographic studies and Parallel sets developed:*** samples with counterparts from a) Hungarian meteorites, b) NASA lunar samples, c) terrestrial rocks, d) industrial materials. ***Educational materials preparations***: a) films, b) CD on lectures and reports, c) concise planetary atlases. ***Complex studies triggered by NIPR set***: a) space robotics (Hunveyor-Husar models), b) works with them on testfields, c) theoretical studies, and d) spherules [1-4].

Samples: A) Samples of first chondritic evolution period (metamorphism) in the set:

Carbonaceous Chondrites: - C1 - NIPR 27, CM2 - NIPR 28, CO3 - NIPR 29, CV3 - NIPR 30.

Unequilibrated Chondrites: EH3 - NIPR 14, H3 - NIPR 15, L3 - NIPR 19, LL3 - NIPR 23.

Equilibrated Chondrites: H4 - NIPR 16, H5 - NIPR 17, H6 - NIPR 18, L4 - NIPR 20, H5 - NIPR 21, H6 - NIPR 22, LL4 - NIPR 24, LL5 - NIPR 25, LL6 - NIPR 26.

Primitive Achondrite: PA - NIPR 13.

B) Samples of second chondritic evolution period (differentiation) in the set:

Basalts - Achondritic: Aubrite - NIPR 3, Diogenite A - NIPR 5, Diogenite B - NIPR 6, Howardite - NIPR 7, Eucrite A - NIPR 8, Eucrite B - NIPR 9.

Ultramafic Mantle type rock: Ureilite - NIPR 4.

Stony-irons: Palasite - NIPR 1, Mesosiderite - NIPR 2

C) Other planetary samples of in the set:

Lunar samples: breccia: - NIPR 11, *basalt:* - NIPR 12.

Basaltic Martian sample: - NIPR 10.

Parallel sets developed: Analog rock thin sections were collected and prepared to use them as counterparts to various meteorite, lunar and martian samples in comparisons (i.e. Szarvaskõ, gabbro with high Ti content, basalt, picrite and komatiite, basalt of Disco-Island with reduced iron grains, boninite for high Mg counterpart), impact breccias (i.e. Ries, Mien, Siljan impact breccias), industrial analog materials (i.e. various ceramics with breccia-like textures).

Petrographic studies and **Comparative petrographic studies:** The thermal history of the chondritic parent body, transformational sequence of samples were studied in various forms. Main steps observed: Ostwald rippening and diffusion processes phenomena at thermal metamorphism sequence, global onion-shell body model (with higher temperature types in the core, lower temperature types at the margin of the body, uppermost layers are regolith type carbonaceous chondrites.) For the H, L and LL groups of chondrites the NIPR SET allows comparisons of the H, L and LL vSW sequences.

Special effects studied: A) Diffusion: well observable on ureilites, where diffusion of carbon give dark margins to the large grains of the granular ultramafic texture and as a result of reduction of FeO in silicates by carbon at the dark carbonaceous margins tiny metal grains of iron appears. B) Iindication of gravity: a) impact shock triggers diaplectic glass (NIPR 10 (Shergottite) and NIPR 12 (Norite) exhibits maskelynite), b) more frequent impacts cause frequent fragmentation on a larger body. Comparison of fragmented texture of asteroidal braccias (brecciated achondritres of NIPR 6, NIPR 7 and NIPR 9) with lunar surface breccias (14305, 65015 and 72275 of the NASA set) and with regolith breccias (15229 of the NASA set and NIPR 11) we can observe that more generation of impact fragmentation resulted in wider range of grain size distribution on the larger body, c) by comparison of samples of chondrites in a sequence of increasing petrologic type, from petrologic type 4 through 6 and 7 types iron grain size distribution changes as a consequence of percolation, well observable to fit mesosiderites to this sequence, d) the final effect of gravitation in chondritic body evolution is the separation of phases: iron-and sulfide melt and basaltic melt [7-8].

Educational materials preparations: A) Lecture Note Series: After 5 years of use we began to publish a lecture note series booklet on Antarctic Meteorites and Lunar samples [6] and other related lunar, meteoritic and planetary studies.

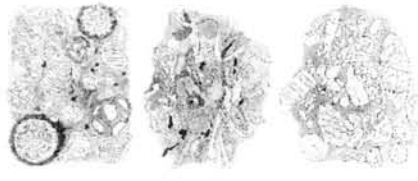

Fig. 1. The lecture note on meteorites and lunar samples.

B) Films: We also recorded videofilm on the NIPR and NASA thin sections, and later on lectures of studying these sets and other planetary materials [9]. Units of the film, (video, CD) were selected to correspond to the units of the booklet for students to observe textures in petrologic microscopy and work them in the booklet pages. Our film on technologies and materials helped to compare processes in indus-

try and in planetary geology, explaining that industrial material science has various relations parallel with lunar textures. This way materials structures in planetary science and technology products in factories can be learned parallel. C) Planetary maps: Further extension of our studies was the planetary map preparation: Moon, Venus, Mars, Mercury. Lunar textures were involved in the lunar map, which was prepared in 6 languages [10-11].

Complex studies triggered by using NIPR set: A) Robotics Hunveyor and Husar: The branching of our NIPR Anarctic meteorite Set studies were a special extension of the planetary science education by robotics. A Surveyor like planetary lander space-probe construction began and together with the construction of the lander we studied details of the field works and scientific goals during the joint activity [12-13]. B: Lunar, planetary and Antarctic analog test field for Hunveyor: Further extension of the analog studies was a test field as if Hunveyor were landed on a planetary or Antarctic surface.

Fig. 2. Informastics Minister visits Hunveyor-4 probe model.

The most important rock types from the Solar System rocky bodies were arranged around it. On the sandy surface Husar rover moved between the rock samples imaging their surface textures [14-15]. C) Theoretical studies: After the publication of the compositional data of the NIPR Antarctic meteorites in 1995 (Yanai, Kojima, Haramura, [16]) we could calculate various evolutionary compositional processes for the VSW types in the Urey-Craig Field (Fe compound data projections) [17]. D) Spherules: New perspective of the NIPR an NASA cosmic material collections that their samples can be used to studies of cosmic spherules. Their types are: lunar spherules (both volcanic – 74220, and impact – NIPR 11 and 15229), the chondrules themselves and from parallel terrestrial sets the spherules from the Earth [18-19].

Summary: The first impression of the value and possibilities of the NIPR collection was shown by the Photographic Catalog of Antarctic Meteorites [20]. Ten years use of the 30 polished thin sections of the NIPR Antarctic meteorite set proved and overwritten our hopes. Comparisons of the textures in this set with other cosmic material sets (NASA lunar sample set) were useful tools not only for education but for the synthetic view of the chondritic parent body thermal evolution phenomena, which can be connected to the great number of ordered sample in the NIPR Set. At the same time not only students but wider audience could observe meteoritic, lunar and one Martian thin sections in microscopes in more than 25 towns in Hungary. The concise atlas booklet series were distributed in more than 200 schools in the Carpathian basin. Hunveyor is constructed in 7 colleges and universities. When summarize the effect of NIPR Anarctic meteorite Set studies in Hungary we may tell that it was a fruitful present from NIPR and we hope that other new programs will begin in the next 10 years, giving the possibility to further space and planetary science education in Hungary and in Central Europe.

Acknowledgments: Thanks to NIPR Meteorite Research Center and personally for curators Keizo Yanai and Hideyasu Kojima, for loan of the NIPR Antarctic meteorite thin section set. This work has been supported by the MUI-TP-190/2005 and 154/2005 funds.

References: [1] Bérczi Sz., Holba Á., Lukács B. (1995): Thermal Transformations in the Meteorites' Parent Bodies. *20th NIPR Symp. Antarctic Meteorites*, Tokyo, Japan, p. 26; [2] Bérczi Sz., Lukács B. (1995): A Comparison Among Chondrite Compositions. *20th NIPR Symp. Antarctic Meteorites*, Tokyo, Japan, p. 30; [3] Kubovics I., Bérczi Sz., Lukács B., Szakmány Gy. (1995): The Meteorites in the Light of the NIPR Japanese Antarctic Meteorite Collection. *20th NIPR Symp. Antarctic Meteorites*, Tokyo, Japan, p. 125; [4] Bérczi Sz., Holba Á. & Lukács B. (1996): On discriminating chondrites on the basis of statistical analysis of iron-bearing compounds: NIPR Antarctic samples. *21th NIPR Symp. Antarctic Meteorites,* Tokyo,. p. 17-19; [5] Bérczi Sz., Kiss A. & Lukács B. (1996): Comparison of the reduction processes in native-iron bearing basalts from Disko Island, and in chondrites. *21th NIPR Symp. Antarctic Meteorites*, Tokyo, p. 14-16; [6] Bérczi Sz. (2001): *Holdkőzetekről, meteoritekről. (Planatary and Material Maps of Lunar Samples and Meteorites.)* (In Hungarian) UNICONSTANT. Püspökladány; [7] Lukács B., Bérczi Sz. (1996): Competition of C and H_2O for Fe in E, H, and C chondrites. *21th Symp. Antarctic Meteorites*, Tokyo, p. 90-92; [8] Bérczi Sz., Holba Á., Lukács B. (1996): On the Thermodynamics of Meteorites and Parent Bodies. KFKI-1996-15/C. p. 38. Budapest; [9] Bérczi Sz., Maros G. Szabó Soki L., Varga T., (2001): *Lecture on Solar System Materials.* 60 min. (videofilm) *XXXIII. LPSC*, LPI, Houston, Texas, 2002, March 4-8. [10] Multilingual map of Moon, Mars. Editors; language sections: Hungarian: H. Hargitai, Czech: A. Rükl, Croatian: D. Roša, Polish: T. Kundera [11] Map of Mars. Cartographers: L. S. Oreshina, L. Yu. Baeva. Editors: B. V. Krasnopevtseva, K. B. Shingareva, Moscow State University for Geodesy and Cartography (MIIGAiK); [12] Sz. Bérczi, V. Cech, S. Hegyi, B. Drommer, T. Borbola, T. Diósy, Z. Köllõ, Sz. Tóth (1998): Construction of a planetary lander, Hunveyor, to emphasize the role of connections between planetary science and technology (robotics) education. The use of Hunveyor in Antarctic research. *23rd NIPR Symposium Antarctic Meteorites*, Tokyo,. p. 8-10; [14] Sz. Bérczi, B. Drommer, V. Cech, S. Hegyi, J. Herbert, Sz. Tóth, T. Diósy, F. Roskó, T. Borbola. (1999): New Programs with the Hunveyor Experimental Lander in the Universities and High Schools in Hungary. *LPSC XXX*, #1332, LPI, Houston; [15] Balogh, Zs., Bordás, F., Bérczi, Sz., Diósy, T., Hegyi, S., Imrek, Gy., Kabai, S., Keresztesi, M. (2002):Manipulator Arms and Measurements with them on Hunveyor College Lander: Soil Hardness Measurements in the Test Terrain Surrounding the Lander. In *LPSC XXXIII*, #1085, LPI, Houston; [16] Yanai K., Kojima H., Haramura H., (1995): Catalog of Antarctic Meteorites. NIPR, Tokyo [17] Sz. Bérczi, Á. Holba, B. Lukács, (1999): Splitting of the two Wiik lines in the Urey-Craig field: C-s are related to H-s like as LL-s are related to L-s. (Statistical Analyses of the NIPR dataset: VII). *24th NIPR Symposium Antarctic Meteorites*, Tokyo, p.9-11; [18] Bérczi Sz., Detre Cs., Don Gy. (1998). *Spherules.* 10 min. videofilm made for the *23rd Antarctic Meteorites Symposium,* NIPR, Tokió, 1998, June 10-12; [19] Sz. Bérczi, Cs. Detre, Gy. Don, L. Dosztály, V. Cech, B. Drommer, A. Gucsik, S. Józsa, B. Lukács, G. Marosi, P. Solt, L. Szabó Soki, Gy. Szakmány, I. Vécsey (1998): Spherules in a Solar System wide stratigraphy. *23rd NIPR Symposium Antarctic Meteorites*, Tokyo,. 11-13; [20] Yanai K., Kojima H., (1987): Photographic Catalog of Antarctic Meteorites, NIPR, Tokyo.

ENGINEERING AND THERMAL BALANCE STUDIES FOR LUNAR BASE CONSTRUCTION WITH ON SITE MATERIAL UTILIZATION AND WITH ANTARCTIC ARCHITECTURAL APPLICATIONS. ***B. Boldoghy[1], J. Kummert[1], I. Szilágyi[2], T. Varga[2], Sz. Bérczi[3]***, [1] Ferroelektric Engineering Pan Konceptum Ltd., H-1116 Budapest, Vasvirág sor 72., Hungary, (konceptum@vipmail.hu), [2] VTPatent Agency, H-1111 Budapest, Bertalan L. u. 20., Hungary (info@vtpatent.hu), [3]Eötvös Loránd University, Institute of Physics, H-1117 Budapest, Pázmány P. s. 1/a., Hungary (bercziszani@ludens.elte.hu).

Abstract: Extremal lunar physical conditions need studies of the strategies, technologies, designs of the Lunar Base architectural construction from the viewpoint of physical constraints (i.e. energy balance, strength and insulating properties of the lunar materials), engineering constraints (i.e. building technology, transports, insulating layers) and geological environment (allocation of the buildings). The output of this study may have benefits in Antarctic architectural constructions, too. Our results contain proposals on the general strategy, on the local production technology, on arrangement and insulation solutions and the emplacement of the lunar base. Aspects of Antarctic applications are also summarized.

Introduction: First data of the physical properties of the lunar environment were measured by Surveyors [1,2] and Apollo Missions, i. e. [3,4,5]. Surveyor mechanical and soil data were measured by their robotic arm and camera systems [6-11]. Further details were given by the Apollo Missions, on a wider range of the lunar surface environment characteristics - of lunar soil (Gast, PLSE Team) [12], of heat flow (Langseth et al) [13], of soil mechanics (Mitchell et al) [14]. Development of lunar soil simulants, like JSC-1 [15], a glass-rich basaltic ash sample, a chemical and mineralogical analog material was available for engineering experiments, and even its electrostatic characteristics and charging properties were measured [16] and were compared to those of Apollo-17 lunar dust [17]. On the basis of these data we made both calculations and modeling of the engineering of a permanent lunar base construction. The aim of our studies is to give a **complex project** plan for construction a lunar architectural environment, using local resources [18].

Strategy for lunar architectural environment: In our complex planning first we made a strategy study. The first architectural lunar base constructions of hability modul and structural materials are to be transported to the site. Structural materials are stress holding frames and insulating foliating materials.

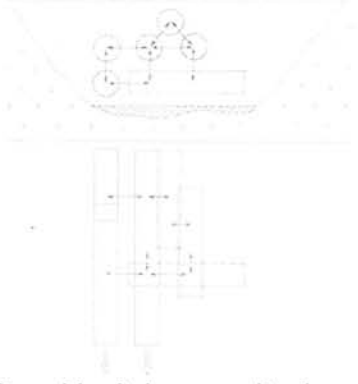

Fig. 1. Hability module cylinders arranged in a lunar valley.

For the hability modul the cylindrical geometry, size and arrangement of the International Space Station units are the best first approach. They serve as economic preliminary lunar station unit candidates in our lunar architectural system. During the on site construction a spatial skeletal structure is built on the site first. This holds the stresses and load of the weight of both the cylindrical modules and the other insulating layers.

For insulating material there is a free access for local regolith material. This should be used in two kinds of layers. The first layer is surrounding the ISS-like hability moduls by quilted-coat like insulating wall units. These units are on site prepared from the foliated stress holding material transported to the site and from the lunar soil. The modular insulating units are attached to the outer wall of the ISS cylinder.

The second layer is a free large masses of regolith used to surround the ISS cylinders so that they became embedded and buried into the local regolith material. This outer insulating layer, which forms a thick regolith mass surrounding the living space bubble architecture has not only role of insulating, but radiation and impact bombardment shielding, too.

Fig. 2. Burial of the cylinder lunar base hability units.

Thermal aspects of our proposal: The heat received by radiation is stored by heat-storing crystals, from which the heat can be gradually regained in the shadowy period. This technology involves 3 tasks: 1) Receipt and intake of solar energy of two-week insolation periods, 1) Storing, 2) Continuous and regulated output meanwhile and during shadowy period. **Heat intake:** Continuously with a mirror system by automatic following the Sun (energy concentration) focuses it into a channel which reflects it into a heat-storing material, in given case to salt (changing its aggregate or phase, or melts it.) **Heat-storing:** Placing the heated, (or melted) heat-storing material in an insulated material. **Heat retrieving:** The heat-storing material egresses the heat during a heat-exchanging process, while it sets, e.g. changed in the aggregate.

Theoretical concepts: The possible methods of heat-storing: 1) heating of heat-storing material, 2) change of aggregate, 3) change of crystal-structure.

1) By heating the heat-storing material: The quantity of the heat depends on the specific heat, the mass as well as the change of temperature of the heat-storing material. $Q=c\ m\ \Delta t$. This storing method is less effective.

2 and 3) By utilization of the change of phase or aggregate: In this case the material can take in a big quantity of heat with minor change of temperature. The quantity of heat depends only on the heat and bulk of the change of phase (melting, freezing) of the heat-storing material. $Q = c_o\ m$. This is a more efficient method.

Heat-storing by change of phase or aggregate under Moon conditions has adventages on the Moon compared to the case on Earth): 1) it can be a change of aggregate of higher temperature, 2) radiating period is considerably longer (14 days) 3) metals, salts, material-compozites, whose chemical composition does not change due to this melting, can be considered as heat-storing materials (low melting point materials are suitable for this procedure in a comparatively low temperature range).

Experimental type description: It would be important, that material used for storing heat: e.g. some variant of a salt, could be produced from lunar rocks, (in terrestrial conditions salts of sulfur content are applied).

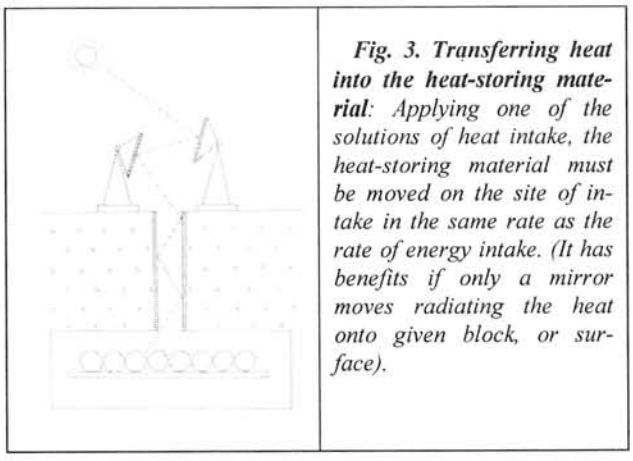

***Fig. 3. Transferring heat into the heat-storing material**: Applying one of the solutions of heat intake, the heat-storing material must be moved on the site of intake in the same rate as the rate of energy intake. (It has benefits if only a mirror moves radiating the heat onto given block, or surface).*

Practical solutions: 1) heat-storing material is moved in a mechanical conveyor to the place of heating, respectively removed from there the same way, 2) a bigger block of heat-storing material is formed, which is rotated in a carousel below the place of radiation, 3) the heat-storing material melts, it can be flown from the place of heating. (It has benefits if only a mirror moves radiating the heat onto given block, or surface) The first collecting mirrors can be foil-mirrors fixed to a simple frame structure. The additional projecting and focusing mirrors are mechanically stable metal or glass mirrors of small loss, which project the compiled great energy-stream to the heat-storing material. It is important that the heat-utilizing unit must be part of the human habitable residence, preferably in the centre of it.

Materials to be delivered to the Moon: 1) mirrors and manipulating structures, 2) units for holding and moving the heat-storing material, 3) heat-exchangers, 4) structural frame of heat-utilizing unit, 5) either with assembly on the Earth or transporting it as a whole unit, or partial local assembly and local completion, 6) heat-storing material in special case.

Technology: Using the insulating and strength data of the lunar soil the following main technology phases of construction of the lunar base architecture was proposed. After transport of the primary container ISS type unit blocks from Earth to the lunar surface: 1) grading and basis forming in the bedrock for the frame, 2) assembly of the architectural constructions of the frame, 3) fixing the thermal balancing salt units on the cover of the ISS type hability modules, 4) parallel filling the insulating quilted-coat like units with lunar fine soil, 5) fixing the quilted-coat like second insulating units to the surface of ISS type unit blocks, 6) final emplacement of the container blocks on the frame, 7) burial of the living bubble units by the lunar regolith from the plains surrounding the valley of lunar base locality. For this a lunar rover type buldoser is used (Fig. 1.).

Geological environment and the allocation of the base: It is economic to place the first long term used buildings below the surface. This way large mass of lunar soil can be used as insulator. Lunar soil can be moved by a lunar rover buldoser to cover the deposited container with regolith. The best geological site is at the mouth of a smaller valley which have about 10 meters width. We propose the locality of the Aristarchus crater, where several rilles can be found (Fig. 4. Lunar Orbiter 4, 151H, detail), where many larger valleys contain smaller central valleys on their floor.

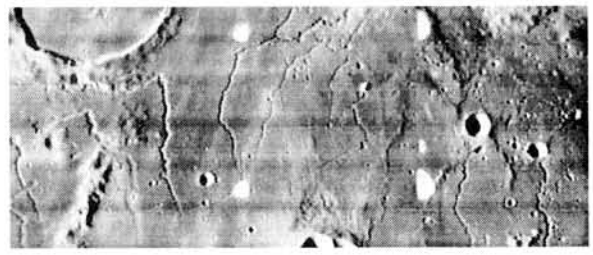

Fig. 4. A proposed locality for the permanent lunar base emplacement with several rilles, north of the Aristarchus crater. Lunar Orbiter 4, 151H image. LPI-web.South is up.

Summary: We proposed a complex architectural design for the lunar environment: strategy, on site technologies, design, arrangements of the Lunar Base construction. Our concepts were studied from functional aspects and from thermal equilibrium, local material technologies and surface soil insulating aspects. We proposed a double insulating layer system both using lunar soil as thermal insulator and an additional third one with phase changing salt as energy storage material. We also proposed a geological setting of the implementation of the architectural units in a groove or small valley mouth where not only the deposition of soil is economic but the enlargement of the station is possible in valley direction.

References: [1] The Surveyor Investigator Teams (1967) JPL, CIT. Techn. Report 32-1177. Pasadena; [2] The Surveyor Investigator Teams (1968) JPL, CIT. Techn. Report 32-1264, Part II. Pasadena; [3,4,5] Apollo 15,-16,-17 Preliminary Science Reports, (1971, 1972, 1973), NASA JSC, Houston; [6] Christensen E.M. et al. (1967) NASA-JPL Techn. Report 32-1177, p.111-153. [7] Choate R. et al. (1968) NASA-JPL Techn. Report 32-1264, p.77-134, [8] Scott R. F., Roberson F. I. (1967) NASA-JPL Techn. Report 32-1177, p.69-110. [9] Scott R. F., Roberson F. I. (1968) NASA-JPL Techn. Report 32-1264, p.135-187. [10] Shoemaker E. M. et al. (1967) NASA-JPL Techn. Report 32-1177, p.9-67. [11] Shoemaker E. M. et al. (1968) NASA-JPL Techn. Report 32-1264, Part II. p.9-76. [12] Gast, P.W. et al. (1973): Preliminary Examination of the Lunar Samples. NASA SP-330, JSC; [13] Langseth, M.G. et al. (1973): Heat Flow Experiment. NASA SP-330, JSC; [14] Mitchell, J.K. et al, (1973): Soil mechanics. NASA SP-330, JSC; [15] McKay, D.S.; Carter,J.L.; Boles,W.W.; Allen,C.C.; Allton, J.H. (1993): JSC-1: A new lunar regolith stimulant. *24th LPSC*, Part 2. G-M p 963-964.; [16] Horányi, M., Robertson, S., Walch, B., (1995): Electrostatic charging properties of simulated lunar dust. *Geophys. Res. Lett.* **22**, 2079-2082; [17] Horányi, M., Walch, B., Robertson, S., Alexander, D. (1998): Electrostatic charging properties of Apollo 17 lunar dust. *JGR*, **103**, Issue E4, p. 8575-8580; [18] Haskin, L. A.; Colson, R. O. (1992): Resource availability at Taurus-Littrow. In: *Lunar Science Inst., Workshop on Geology of the Apollo 17 Landing Site* p 9-14;

A record of extreme FeO/(MgO+FeO) enrichment during igneous crystallization on the Moon preserved in lunar meteorite Northwest Africa 773. T. J. Fagan, [1]Department of Earth Sciences, Waseda University, 1-6-1 Nishiwaseda, Shinjuku, Tokyo, 169-8050, Japan (fagan@waseda.jp)

Introduction:

The evolution of major element compositions in typical igneous suites on Earth involve progressive enrichment in SiO_2 and increase in FeO/(FeO+MgO). In the tholeiitic trend, FeO/(FeO+MgO) increases to high values prior to significant SiO_2-enrichment, whereas SiO_2-enrichment dominates in the calc-alkaline trend. Oxygen fugacity, among other variables, has been postulated as a control on whether a given magmatic system follows a tholeiitic or a calc-alkaline trend (e.g., [1]). These trends lead to distinct types of rocks in later stages of differentiation, even though initial compositions might have been similar.

In this study, a tholeiitic-type trend is inferred from the breccia of lunar meteorite Northwest Africa 773 (NWA 773). Lithic fragments in the breccia show a textural similarities and a progressive increase in FeO/(FeO+MgO), suggesting that they formed as part of a single evolving magmatic system on the Moon [2,3]. Free silica occurs in rocks which have attained high FeO/(FeO+MgO). This trend is roughly analogous to the terrestrial tholeiitic trend. In contrast, granitic rocks (with free silica, K-feldspar and relatively albitic plagioclase) in Apollo 15 sample 15405 are characterized by pyroxene with moderate FeO/(FeO+MgO) [4,5]. The contrast between granitic clasts in NWA 773 and those in 15405 suggest that lunar magmatic systems evolved by different extents of SiO_2- and FeO/(FeO+MgO)-enrichment.

In a general sense, these trends are comparable to terrestrial calc-alkaline and tholeiitic trends. However, oxygen fugacity may be associated with the opposite trend on the Moon. Namely, systems with relatively high $f(O_2)$ on the Moon might evolve along a tholeiitic path.

Analytical Methods:

Two polished thin sections of NWA 773 were studied using standard petrographic techniques. Major element compositions of minerals were determined by electron microprobe analysis (EPMA) using a Cameca SX-50 instrument at the University of Hawaii at Manoa [2]. The Cameca SX-50 was also used to collect X-ray elemental maps and back-scattered electron images at a variety of scales.

Igneous differentiation of NWA 773 breccia:

Petrologic, geochemical, noble gas and oxygen isotopic data were used to document NWA 773 as a lunar meteorite in 2003 [2]. The meteorite is composed of a gabbroic lithology with olivine cumulate texture and a fragmental breccia (Fig. 1). Sm-Nd data from the olivine cumulate yield the youngest igneous age (~2.87 Ga) of any analyzed rock from the Moon [6]. A petrologic connection with very-low-Ti basalts [3] and pairings with more recently found meteorites [7] have been proposed.

A variety of clasts occur in the NWA 773 breccia, including: gabbro; zoned two-pyroxene clasts, ferroan gabbroic to granitic rocks (Fig. 2); silica-hedenbergite-fayalite symplectite; and rocks with transitional symplectic textures. Gabbroic lithic clasts have mineral textures and olivine-hosted melt inclusions similar to those in the gabbro lithology. Pyroxene and olivine compositions range from identical to those of the gabbro lithology ($Wo_{11}En_{65}$, $Wo_{35}En_{50}$, Fo_{68}) to somewhat more ferroan values (Fig. 3). Pigeonitic pyroxene shows a continuous spread in major element composition to near Fe-endmember compositions (Fig. 3). In contrast, olivine with intermediate compositions is not observed, but ferroan olivine coexisting with silica ±K,Ba-feldspar occurs in symplectite and coarse-grained clasts (Figs. 2,3). K,Ba-feldspar is also present in inter-cumulus domains enriched in incompatible elements in the gabbro [2].

From the textural similarities and trends in mineral composition and assemblages, these types of breccia clasts are interpreted as products of progressive differentiation in a magmatic system that formed the gabbro at early stages [2,3]. Differentiation resulted in silica-bearing rocks, but only after extensive FeO/(FeO+MgO)-enrichment in pyroxene (Fe# > 65 in symplectite, Fe# > 85 in coarser-grained clasts; see Fig. 3).

In contrast, silica-bearing clasts from Apollo 15 coexist with more magnesian pyroxene (Fig. 3), suggesting different proportions of increase in SiO_2-content and FeO/(FeO+MgO) in different magmatic systems on the Moon. As has been suggested for terrestrial systems [1], oxygen fugacity may be a significant variable determining between these two trends. On Earth, relatively high $f(O_2)$ results in formation of Fe-oxides, removing Fe from the silicate system, leading to SiO_2-enrichment. On the Moon, relatively high $f(O_2)$ may diminish the role of metal and sulfides, increasing the Fe available to silicate minerals, leading to tholeiitic-like FeO/(FeO+MgO) enrichment (also see [8]).

References:

[1] Yagi K. and Takeshita H. (1987) in Magmatic processes: Physicochemical principles (Mysen B.O., ed.) p. 183-190. [2] Fagan T.J. et al. (2003) MaPS 38, 529-554. [3] Jolliff B. et al. (2003)

GCA 67, 4857-4879. [4] Ryder G. (1976) *EPSL 29*, 255-268. [5] Meyer C. et al. (1996) MaPS 31, 370-387. [6] Borg L.E. et al. (2004) Nature 432, 209-211. [7] Bunch T.E. et al. (2003) LPSC XXXVII, #1375. [8] Snyder G.A. et al. (1999) LPSC XXX, #1499.

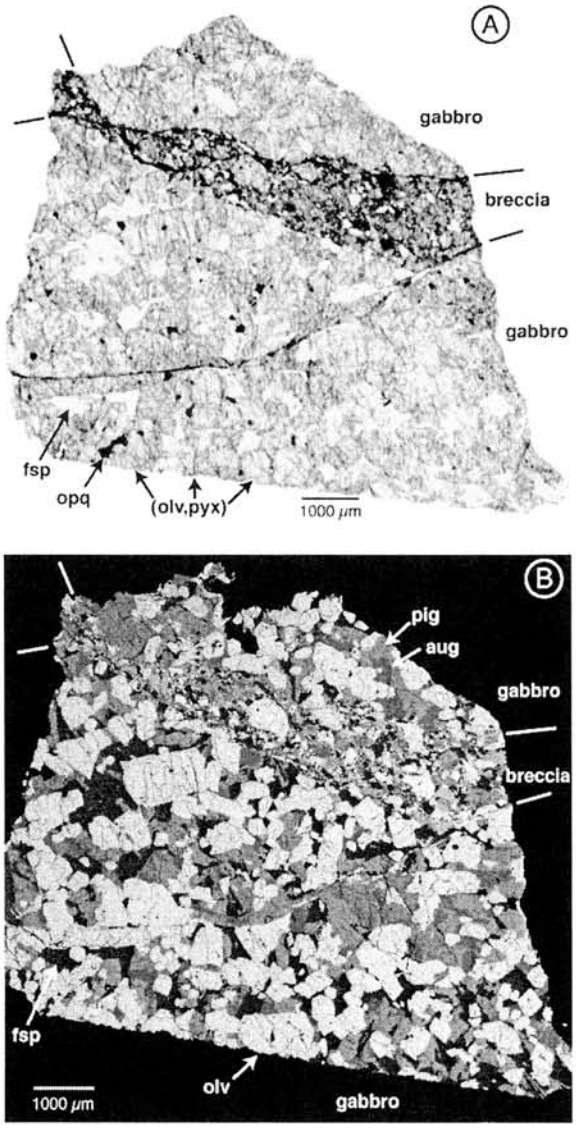

Figure 1. Olivine cumulate gabbro and breccia textures in one thin section of NWA 773. (A) Transmitted light (not plane-polarized). Olivine and pyroxenes appear similar, with higher relief than feldspar. (B) False-color elemental map (R=Mg, G=Fe, B=Ca Kα), reduced to gray-scale. Abbreviations: aug = augite; fsp = feldspar; olv = olivine; opq = opaque minerals; pig = pigeonite.

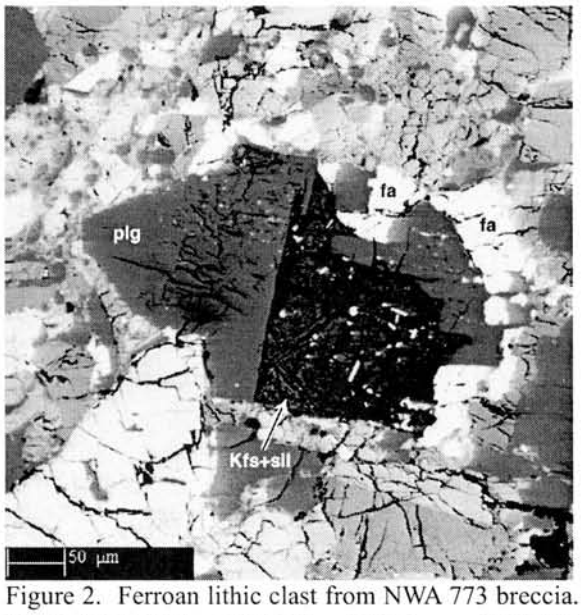

Figure 2. Ferroan lithic clast from NWA 773 breccia. Back-scattered electron image. Mineral abbreviations: fa = fayalite (Fa_{97}); Kfs+sil = K-feldspar intergrown with silica; plg = plagioclase feldspar (An_{72}).

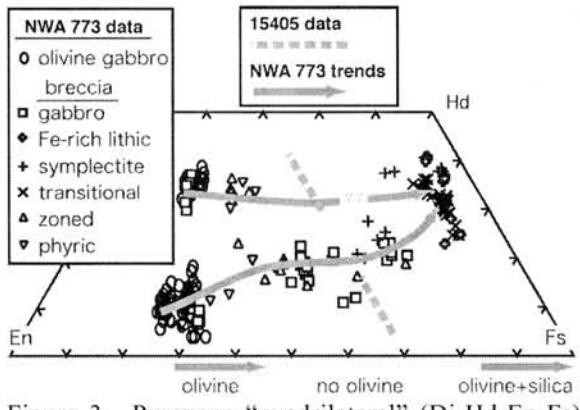

Figure 3. Pyroxene "quadrilateral" (Di-Hd-En-Fs) showing compositional variations in pyroxene from NWA 773 olivine gabbro and breccia, and from Apollo sample 15405 (thin sections 57 and 145, data from [3,4]). Pyroxene from a variety of clast types in NWA 773 breccia were analyzed, including gabbro, FeO-rich lithic fragments, symplectite, transitional symplectite, a zoned pyroxene mineral clast, and a pyroxene-phyric basalt. Individual analyses for 15405 are not plotted. Compositional ranges for olivine and olivine coexisting with silica in NWA 773 are also shown. Compositional trends for NWA 773 are shown.

Analyses of stable chlorine isotopes in chondritic meteorites (1): Preliminary results for ordinary chondrites. T. Fujitani[1,2] and N. Nakamura[1,3], [1]Graduate School of Sci. and Technol., Kobe University, Nada, Kobe 657-8105, Japan, [2]Marine Technical College, Ashiya 659-0026, Japan, [3]Dept. of Earth and Planet. Sci., Faculty of Sci., Kobe University, Kobe 657-8501, Japan.

Introduction:

Chlorine is one of mobile elements and highly diffusive among vapor, fluids and solid during geochemical processes. There exist two stable isotopes, ^{35}Cl (75.8%) and ^{37}Cl (25.2%), and thus a large relative mass difference among them. Therefore, natural variations in $^{37}Cl/^{35}Cl$ ratio are expected for planetary processes as well as nebular environments, which might provides useful natural tracers to investigate evolution processes of planetary materials. Due to analytical difficulties, however, the isotopic studies on stable chlorine isotopes in planetary materials are limited, particularly for rare cosmic materials with low Cl concentrations, like meteorites.

In order to examine variations of chlorine isotope compositions in chlorinated organic and inorganic compounds related to environmental problems, we have developed an analytical technique by thermal ionization mass spectrometry (TIMS) using Cs_2Cl^+ ion mode [1,2,3]. Extending our environmental works, we have newly established precision techniques of isotope dilution and isotopic analysis of chlorine, which is applicable to small silicate materials, as demonstrated for standard rocks [8,9].

Except a few cases [4,5,6], analyses of chlorine isotopes for meteorites have rarely been reported and thus general isotopic features of chlorine in the early solar system have not been well understood. In order to identify possible characteristic variations of chlorine isotopes, we have initiated systematic isotopic analysis of chlorine for different kinds of chondrites. Here we report an analytical technique and preliminary results for ordinary chondrites.

Analytical technique:

In view of possible contamination of seawater derived chlorine, we analyzed mostly non-Antarctic meteorites but a few Antarctic meteorites such as Y-74191 (L3) and ALHA 77304 (LL3) with weathering category A were also selected for detailed examination. In order to obtain more representative bulk chondrites, we tried to use larger samples as much as possible available for us. The chondrite samples weighing about 0.7~1.5 grams were carefully cleaned and pulverized, and splitted into three parts: the first one for concentration analyses by isotope dilution of negative thermal ionization mass spectrometry (N-TIMS ID), and second one for isotopic analyses by positive TIMS, the third one for later use. Samples of about 20 mg were spiked and decomposed with hydrofluoric acid, and chlorine was isolated by precipitation of silver chloride after neutralization with $Ca(OH)_2$ [7,8]. The ammonical solution of AgCl was then subjected to N-TIMS. For isotopic analyses, samples weighing 0.2~1.3 grams containing about 50 μ g Cl were treated by hydrofluoric acid leaching method in the similar way of ID-MS. Chlorine was recovered as AgCl (recovery 70~90%) and converted to CsCl with Cs-form ion exchange resin. The sample was loaded as CsCl form containing 2 μ g Cl on a Ta filament together with graphite powder. The TIMS measurement of isotopic ratio was carried out as Cs_2Cl^+ ion [1,2]. Laboratory standard (CsCl reagent) and seawater were repeatedly analyzed during the course of this study.

Results and Discussion:

An internal error (2 σ m) of $^{37}Cl/^{35}Cl$ ratio of N-TIMS was better than 0.1%. Including procedural blanks, uncertainties of chlorine concentrations are $\pm$~1 %. Results for nine standard rocks obtained in the early part of the works are partly in agreement but not necessarily with recommended values, if they are available [8]. The concentrations in chondrites ranges for H: from 44ppm (Allegan H5) to 251ppm (Brownfield H3); for L: from 147ppm (Homestead L5) to 278ppm (Y-74191 L3); for LL: from 64ppm (Dhurumsala LL4) to 72-79 ppm (ALHA 77304 LL3 and Parnallee LL4). It seems likely that Cl concentration decreases from low metamorphic grade to higher grade.

As shown in Table 1, the internal standard error (2 σ m) of the mean ($^{37}Cl/^{35}Cl$) ratio of each isotopic measurement (400 ratios) was ~0.2 ‰ and the external errors (1 σ) of replicate analyses (n=5~12) were 0.2~0.3‰ for most samples

Table 1. Results for CsCl standard

Run No	$\delta\ ^{37}Cl_{SMOC}$* $\pm$2 σ m (‰)
1	-2.53 $\pm$0.23
2	-2.22 $\pm$0.22
3	-2.36 $\pm$0.21
4	-2.59 $\pm$0.22
5	-2.14 $\pm$0.26
6	-2.03 $\pm$0.20
7	-2.68 $\pm$0.25
8	-2.65 $\pm$0.21
9	-2.54 $\pm$0.19
10	-2.57 $\pm$0.23
11	-2.58 $\pm$0.19
12	-2.70 $\pm$0.20
Average	-2.47 $\pm$0.22 (1 σ)
Numata et al., 2001[2]	-2.49 $\pm$0.22 (1 σ)

*relative to seawater: see definition in text.

The Cl isotopic composition is defined as $\delta^{37}Cl_{SMOC}$ (‰), permil deviation from Standard Mean Ocean Chloride (SMOC);

$$\delta^{37}Cl_{SMOC}\,(‰) = \{[^{37}Cl/^{35}Cl]_{Sample}/[^{37}Cl/^{35}Cl]_{SMOC} - 1\}\times 1000$$

So far, we analyzed 12 ordinary chondrites (4H, 4L, 4LL) for concentration and isotopic composition of chlorine. The ranges of $\delta^{37}Cl$ (‰) for each group is; for H: -0.6 (Tahara H5) ~+5.0 (Allegan H5); for L: -4.6 (Y-74191 L3) ~-0.7 (Homestead L5); for LL: -3.2 (Parnallee LL4) ~+2.2 (ALHA77304 LL3). The typical examples are shown in Figs. 1-3. It is interesting to note that ordinary chondrites appear to show isotopic variations characteristic of chondrite group. In general, H-group shows the highest $\delta^{37}Cl_{SMOC}$ and L-group the lowest and the LL-group show middle. Among 12 ordinary chondrites, the Y-74191 (L3) indicate the lowest $^{37}Cl/^{35}Cl$ ratio ($\delta^{37}Cl_{SMOC}$ = -4.6‰) of and Allegan (H5) the highest ($\delta^{37}Cl_{SMOC}$ =+5.0‰). It is worth noting that bulk ordinary chondrites indicate wide variations (up to 10‰) in chlorine isotopic composition, which is much larger than those previously reported for halite and/or water soluble components in Zag (H4) [6] and sodalite in Allende (CV3) [10]. Our bulk data suggest that there exist components in ordinary chondrites carrying even lighter and/or heavier chlorine. We therefore suggest that chlorine isotopes may be more important as a tracer to study of the early solar system processes.

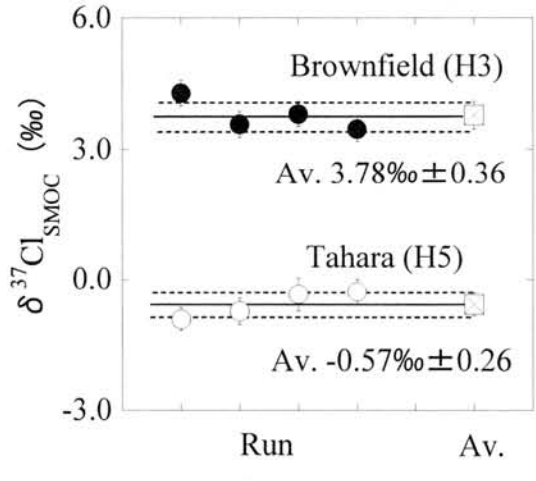

Fig. 1 Results of replicate analyses for H-chondrites.

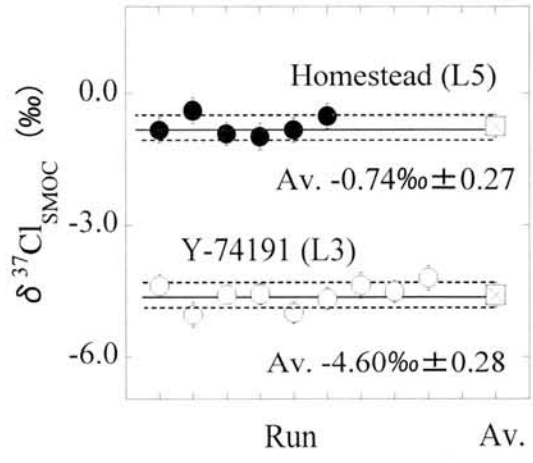

Fig. 2. Results of replicate analyses for L-chondrites.

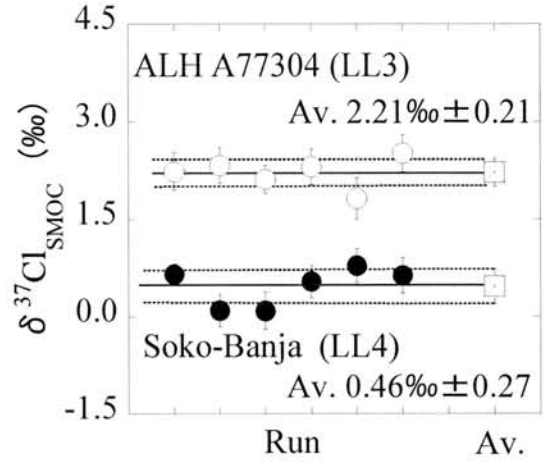

Fig. 3. Results of replicate analyses for LL-chondrites

References:

[1] Xiao Y. K. and Zhang C. G. (1992) *Int. J. Mass Spectrom. Ion Proc.* 116, 183-192. [2] Numata M. et al. (2001) *Geochem. J.*, 35, 89-100. [3] Numata M. et al. (2002) *Environ. Sci. Technol.* 36, 4389-4394. [4] Magenheim A. J. et al. (1994) *GCA* 58, 3117 -3121. [5] Magenheim A.J. et al., (1995) *Earth planet Sci. Lett.* 131, 427-432. [6] Bridges J. C. et al. (2004) *Meteor Planet Sci.* 39, 657-666. [7] Musashi M. et al. (1998) *Analyt. Chim. Acta* 362, 261-269. [8] Fujitani T. and Nakamura N. (2006) *Geostandard Geoanal Res.* (in press). [9] Fujitani T. et al (2005) *6th Int. Natl. Sympos. Appl. Isotope Geochem.* 79-80. [10] Barnes J. D. et al. (2005) *Goldschmidt Conf. Abstracts 2005*, A393.

Final answer for the origin of glassy spherules collected from water tank of the dome Fuji station. T. Fukuoka[1], N. Hoshi[1], Y. Tazawa[2], Y. Saito[3] and K. Azuma[4], [1]Department of Environmental Systems, Faculty of Geo-Environmental Science, Rissho University, Kumagaya, Saitama 360-0194, Japan (tfukuoka@ris.ac.jp). [2]Department of Physics and Astrophysics, Graduate School of Science, Kyoto University, Kyoto 606-8502, Japan. [3]Radio Isotope Laboratory, College of Science and Engineering, Aoyama Gakuin University, Sagamihara 229-8551, Japan. [4]National Institute of Polar Research, Kaga, Itabashi, Tokyo 173-8515, Japan.

Introduction

Glassy spherules had been separated form deposit in the water tanks of the dome Fuji station, Antarctica which was collected by the 37th Japanese Antarctic Research Expedition team. 400 liters of water were prepared every day from accumulated snow around the station. Shapes of glassy spherules are sphere, droplets, and sometimes dumb-bells. They are mainly yellow, rarely brown. They contain a lot of babbles.

Chemical composition of five glassy spherules had been analyzed by instrumental neutron activation analysis (INAA). Chemical composition of 12 glassy spherules had also been analyzed by EPMA and SHRIMP. These results showed that high Ca and Al contents with low Si, Fe, Mg, and Na contents. The CI chondrites normalized REE patterns showed fractionated patterns with higher La values. Siderophiles such as Ir and Au which are typical extraterrestrial elements could not detected (1). Dosztaly and Don (1977) found glassy spherules in a number of stratigraphic levels from Upper Permian formations to recent fluvial sediments in Hungary. Their shapes, color etc were similar to the dome Fuji glassy spherules. The chemical compositions of those were surprisingly similar to the dome Fuji spherules. How to explain similar physical and chemical features and different locality and age was big problem (1).

There are both possibilities for terrestrial and extraterrestrial origin for the dome Fuji spherules. In this study, as a possible candidate for terrestrial origin of the dome Fuji spherules, glassy spherules collected form rock wool insulator of the dome Fuji station have been analyzed by INAA.

Samples and Experimental

Glassy spherules have been collected from rock wool insulator around the water tank of the dome Fuji station. Their shapes, color etc are similar to glassy spherules from water tank. Chemical compositions (26 elemental compositions) of four glassy spherules have been analyzed by INAA. Analytical procedures are shown in (2 and 3).

Results and Discussion

The results of INAA are shown in Table 1. Abundance patterns normalized to CI condrite for minor and trace lithophile elements are shown in Fig. 1 with it of spherules from water tank. The most chemical compositions of glassy spherules from insulator show extremely good agreement with those of glassy spherules from water tank within the errors except for Na contents. Na contents of glassy spherules from insulator are higher compared to those of glassy spherules from water tank. This difference are possible to explain that Na of glassy spherules from water tank were dissolved to water, during stay on the bottom of water tank.

Conclusion

The origin of glassy spherules from water tank of the dome Fuji station is glassy spherules from insulator of the station. This is final answer based on the chemical

compositions.

References

(1) Fukuoka *et al.* (1999) Antarctic Meteorites XXIV, 24-25.

(2) Fukuoka and Tazawa (1996) Antarctic Meteorites XXI, 33-34.

(3) Tazawa *et al.* (2006) Antarctic Meteorites XXX (in this volume).

Tabel 1. INAA results of glassy spherules collected from insulator of the dome Fuji station.

Sample		1	2	3	4	JB-1	JB-1 (std)	Error*
Wt	μg	6.0	7.3	6.5	7.0	17.3	32.7	%
(SiO_2)	%	(49.14)	(41.54)	(39.86)	(37.21)	(53.19)		
Al_2O_3	%	11.9	13.3	13.5	16.1	14.7	=14.53	0.6
FeO[1)]	%	0.19	0.21	0.27	0.37	7.11	= 8.11	10-15
MgO	%	6.8	6.5	4.8	6.1	9.3	= 7.71	25
CaO	%	29.9	36.3	39.2	37.5	9.9	= 9.25	8
Na_2O	%	0.61	0.67	0.66	0.71	2.67	= 2.77	0.1
K_2O	%	0.37	0.43	0.51	0.50	1.68	= 1.43	5
TiO_2	%	0.88	0.86	1.0	1.3	1.31	= 1.32	15
MnO	%	0.21	0.18	0.20	0.21	0.149	= 0.153	7
Cr	ppm	127	80	102	282	500	=425	2
V	ppm	14	9.4	33	27	207	=211	20
Rb	ppm	19	22	15	10	68	= 41.3	20-40
Sr	ppm	528	686	760	696	411	=444	15
Ba	ppm	775	835	586	706	452	=493	50
Sc	ppm	17	19	25	24	28.5	= 27.5	0.5
La	ppm	44	49	56	57	38.3	= 38.6	2
Ce	ppm	86	94	107	102	83	= 67.8	1
Sm	ppm	11	11	13	13	5.42	= 5.13	0.3
Eu	ppm	3.0	3.2	3.4	3.4	1.4	= 1.49	4
Yb	ppm	6.2	6.8	7.9	8.0	2.5	= 2.13	2
Lu	ppm	1.1	1.2	1.3	1.2	0.34	= 0.31	5
Zr	ppm	200	196	349	416	158	=141	35
Hf	ppm	5.6	5.9	6.5	6.4	4.1	= 3.31	8
Th	ppm	12	13	16	16	10	= 9.3	2
U	ppm	10	10	11	12	2.6	= 1.67	20
Ta	ppm	0.82	0.96	0.60	0.85	2.9	= 2.93	45
Co	ppm	3.2	1.5	3.2	2	38.4	= 38.2	1-5

* Errors for INAA are due to counting statistics.
1) Total iron as FeO

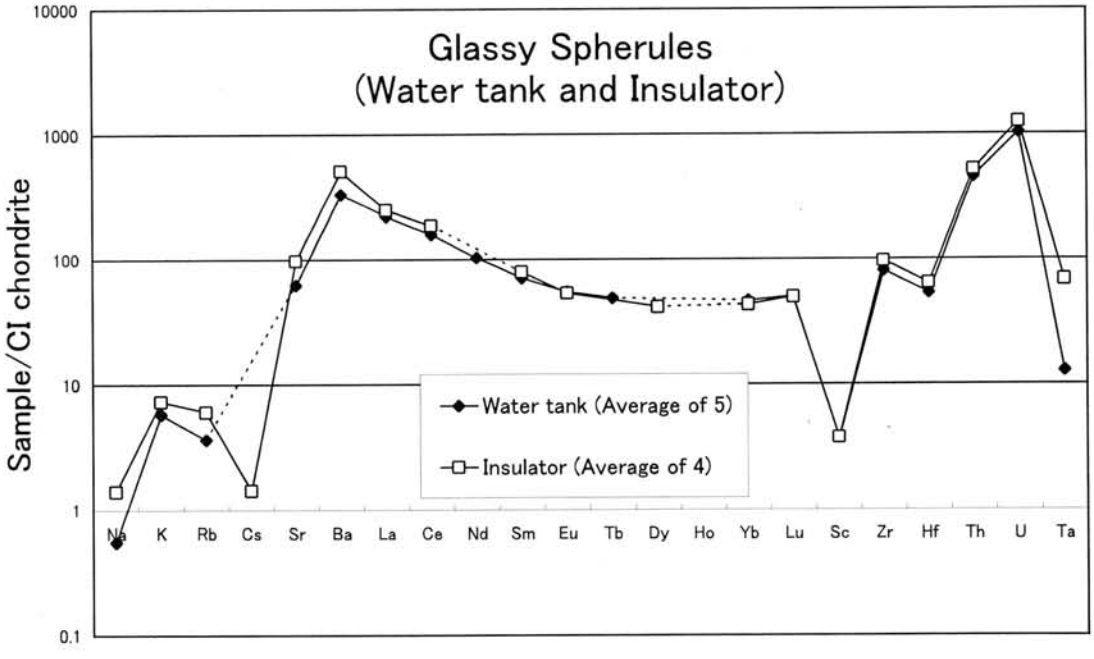

Fig. 1 Abundance patterns normalized to CI chondrite for minor and trace lithophile elements of glassy spherules from water tank and insulator.

Field testing of Hunveyor and Husar educational robot in planetary analog sites.

S. Hegyi[1], B. Drommer[1], A. Hegyi[1], T. Biró[1], A. Kókány[1], Gy. Hudoba[2], Sz. Bérczi[3], H. Hargitai[3] 1) Pécs University, Dept. Informatics and G. Technology, H-7624 Pécs, Ifjúság u. 6. Hungary, (hegyis@ttk.pte.hu) 2) Budapest Polytechnik, Kandó Kálmán College of Engineering, H-6000, Székesfehérvár, Budai út, Hungary, 3) Eötvös University, Department of General Physics, Cosmic Materials Space Research Group, H-1117, Budapest, Pázmány P. s. 1/a, Hungary (berczi szani@ludens.elte.hu)

Introduction: In our planetary educational robotics program we developed a rover working together with the human explorer in the field.Husar-2b was first tested in Szentbékálla, Hungary (October 2005) and in Utah Mars Analog field workstation of the Mars Desert Research Station (January 2006) by Hargitai.

Szentbékkálla: North of Szentbékálla village the basaltic tuff and rocks were erupted from the Sátormahill and Boncostetõ 3 Myears ago. The tuff contains various inclusions from the strata penetrated by the eruption. Of the inclusions the peridotite xenolithic series with several types is the most important for planetary analog studies because they are far counterparts of Martian shergottites. Mot peridotite inclusions can easily be recognized by their green color given by the olivines. Hunveyor and Husar models were used to carry out filed investigations of the rocks, they recognized and distinguished the various inclusions.

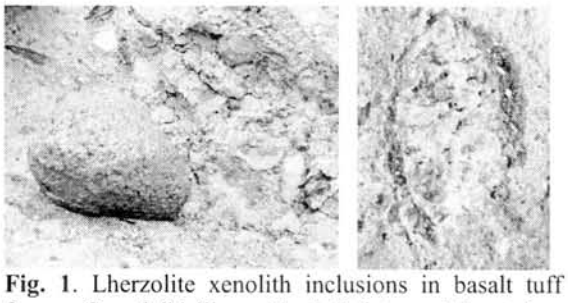

Fig. 1. Lherzolite xenolith inclusions in basalt tuff from Szentbékkálla, North-Balaton Mountains, Hungary.

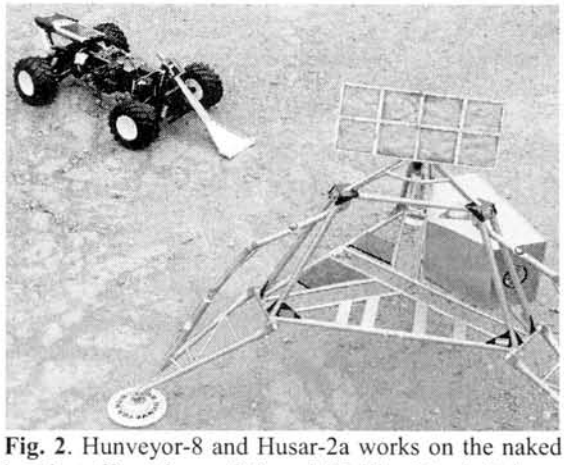

Fig. 2. Hunveyor-8 and Husar-2a works on the naked basalt tuff surface of Szentbékkálla, North-Balaton Mountains, Hungary.

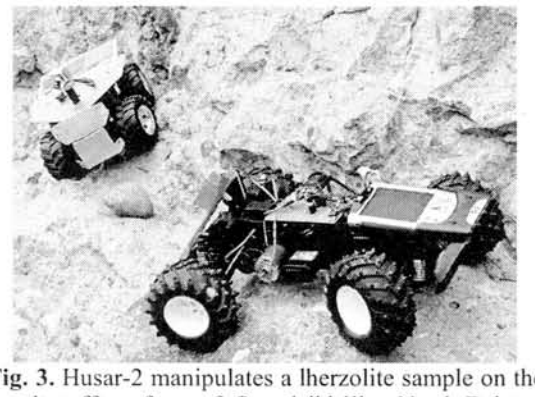

Fig. 3. Husar-2 manipulates a lherzolite sample on the basalt tuff surface of Szentbékkálla, North-Balaton Mountains, Hungary.

Hegyestű: Not far from Szentbékálla a beautiful basalt peak with left query can be visited as Mining Museum. There the basalt flow formed hexagonal columns and a landscape where broken hexagon prisms can be seen is very similar to sites where Spirit studied Gusev crater plain in the first quarter year.

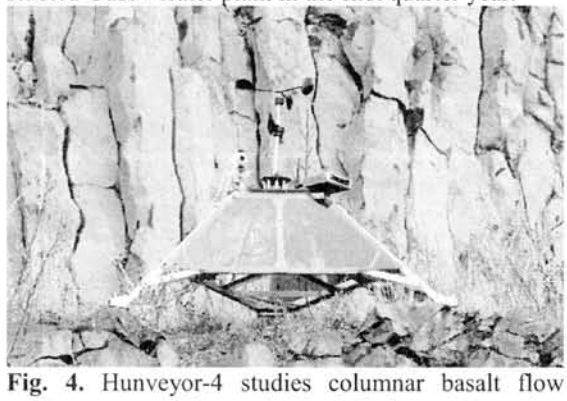

Fig. 4. Hunveyor-4 studies columnar basalt flow environment at Hegyestû, North-Balaton Mountains, Hungary.

Testing in Utah US:.

Fig. 5. Rover is studying the surface with its camera and collects data of its environment

Husar-2b for 12K students: The development of the Husar-2b focus on the basic planetary surfaceactivities. This rover contains a camera and a solarpanel on its board placed on a model-car chassis. Thedrive is on the back wheels by electric engines, movements are controlled by the camera view through a wireless connection to the computer. Husar-2b was used by 12K age students for roving between rocks and observing their surfaces. The camera transmits images with 30 frame/sec, and it has wireless connection with
the computer (1200 MHz). Onto the impact-defense plate surface chemical molecule sensors are planned made by students (Husar-2b on Fig.2.)
Husar-2a for university students: The development of this larger rover focus on programcontrolled direction of the rover. On a larger chassis Husar-2a has independent driving on all the four wheels. This fact allows a special movement direction. The rover can turn in a very narrow arc which is important to move to side direction objects. The wheels in one axis are connected by differential. The structural framework, the driving and the direction all have a left- and right-hand side symmetric structure (Husar-2a on Fig.3.)

The movements are directed through servo engines, which were originally designed for analogous direction, however, even 8 of these servos can be computer directed by a microcontroller. This microcontroller gets the position of the servo motors through RS 232 port of the computer.

The brain of the rover is a HP-PDA computer which contains a WIFI card and which is in contact with the terrestrial control computer through internet. The computing capacity of the PDA is enough for the autonomous tasks. During rover motion the coordinates of the target is given and the rover choose the track to it.

If the rover moves on a free test field then its position can be determined by a differential GPS. The receiver of the differential GPS is placed in the territory of the Pécs University. This position is given through the server of the geologists of the University. If the rover moves in the working room, or can not see the satellite, a transformed optical mouse can give increments to the DPA according to the rover motion.

Instruments: On the board of the rover the most important instrument is the robotic arm which has three degrees of freedom. The maximal length of extension is 30 cm, and the arm can lift up 500 g load at the most extended state. The arm has commutable tools. It will carry out a) measurements of soil strength, b) measuring the distance of the target rocks, and c) dust collecting package for Martian studies.

There are 2 cameras on board of the Husar-2 rover with VGA resolution. They were placed on the two sides of the rover. Both can be rotated separately toward discrete target objects but if they are moved simultaneously, panoramic stereo images can be made with them, too. Such operation of eyes occurs in nature at cameleon.s eyes.

Husar-4 for college students in Székesfehérvár: The development of this rover focus on the Ice-Hunveyor program, planned to the winter Balaton Lake. The rover has different sized front and back wheel pairs. Smaller back wheels are pulled only, the larger front wheels has drive by stepping motors. The rover will have T measuring sensor and ultrasound distance measurement. When move farther from Hunveyor-4 on the ice to observe micro-fissures it will contact with it by radio waves. (Hunveyor-4 is on Fig.4.)

Summary: Various Hunveyor and Husar rover constructions were tested on field trips at the North-Balaton Mountains, at the Mecsek Mountains in Hungary and in Utah, US as on Mars analog sites. We suggest continuing this work on the Antarctic. It may help meteorite colleting on the ice field area. Rover can recognize with its camera the tiny grains of meteorites along its pathway.

Acknowledgment: The MÜI-TP-190/2003 and MÜI-TP-190/2004 funds are highly acknowledged.

References: [1] Sz. Bérczi, V. Cech, S. Hegyi, T. Borbola, T. Diósy, Z. Köllõ, Sz. Tóth (1998): In LPSC XXIX, #1267, LPI, Houston [2] Sz. Bérczi, B. Drommer, V. Cech, S. Hegyi, J. Herbert, Sz. Tóth, T. Diósy, F. Roskó, T. Borbola. (1999): LPSC XXX, #1332, LPI, Houston; [3] T. Diósy, F. Roskó, K. Gránicz, B. Drommer, S. Hegyi, J. Herbert, M. Keresztesi, B. Kovács, A. Fabriczy, Sz. Bérczi (2000): LPSC XXXI, #1153, LPI, Houston; [4] F. Roskó, T. Diósy, Sz. Bérczi, A. Fabriczy, V. Cech, S. Hegyi (2000):Spectrometry of the NASA Lunar Sample Educational Set. LPSC XXXI, #1572, LPI, Houston; [5] Sz. Bérczi, S. Hegyi, Zs. Kovács, E. Hudoba, A. Horváth, S. Kabai, A. Fabriczy, T. Földi (2003): LPSC XXXIV, #1166, LPI, Houston; [6] S. Hegyi, Sz. Bérczi, Zs. Kovács, T. Földi, S. Kabai, V. Sándor, V. Cech, F. Roskó (2001): MAPS, 36, Supplement, p. A77 [7] T. Földi, H. Hargitai, S. Hegyi, Gy. Hudoba, Zs. Kovács, F. Roskó, Sz. Tóth, A. Pintér, Sz. Bérczi (2005): LPSC XXXVI, #1147, LPI, Houston.

Removal and replacement of primary metal in ferroan lodranite MAC 88177.

J. S. Herrin[1], D. W. Mittlefehldt[1], M. Humayun[2], [1]NASA/Johnson Space Center, Houston, TX, USA (jason.s.herrin1@jsc.nasa.gov), [2]National High Magnetic Field Laboratory and Dept. of Geological Sciences, Florida State University, Tallahassee, FL 32310, USA.

Introduction: Collectively, acapulcoites and lodranites form a clan of primitive achondrites generally thought to have originated from the same parent body on the basis of similarities in petrology, mineral compositions, bulk compositions, cosmic ray exposure ages and oxygen isotope compositions [1-6], although considerable variation in some of these parameters has shown that the parent body was not entirely uniform [7]. The presence of relict chondrules in several acapulcoites indicates that all were likely derived from chondrite-like precursor materials. The transition from acapulcoite to lodranite is gradual and corresponds to increasing metamorphic grade. Lodranites are generally coarser grained, but petrographic distinction between the two groups can also be made by modal abundances of troilite and plagioclase. Depletion of both these phases and incompatible lithophile trace elements in lodranites is consistent with their restitic origin formed by >10% extraction of basaltic melt [8,9]. Magnesian lodranites (e.g. Gibson, GRA 95209, Y-75274, Y-8002), some of which might also be considered transitional acapulcoites [9], have mineral and chemical compositions consistent with derivation by thermal metamorphism and partial melt extraction from acapulcoites, as would seem logical if samples represented different grades of metamorphism along a linear evolution trend. Ferromagnesian silicates in these lodranites tend to be displaced toward lower fe# (opx fe# 4-6) than the distribution observed in acapulcoites (opx fe# 6-11) (Figure 1). A subset of lodranites, termed "ferroan lodranites" [7] (e.g. FRO 90011, LEW 88280, Lodran, MAC 88177, Y-74357, Y-791491/Y-791493), have ferromagnesian silicate minerals that are too Fe-rich (fe#>10) to have formed as simple restites from any known acapulcoite. Like silicates, metal-sulfide systematics of the ferroan lodranites are also inconsistent with a simple restitic origin. Logically, restitic lodranites should have been depleted in FeS during extraction of partial melts, since melting of the metal-sulfide system initiates at lower temperatures than melting of silicates. Yet, puzzlingly, ferroan lodranites contain significant quantities (1.9-5.3 modal%) of troilite [2,8,10], indicating either (1) metal-sulfide partial melts were retained during basaltic melt extraction or (2) later infusion of metal-sulfide melts has occurred [7]. In this study, we use trace siderophile elements in metals to assess the relative importance of each in creating the observed troilite enrichment.

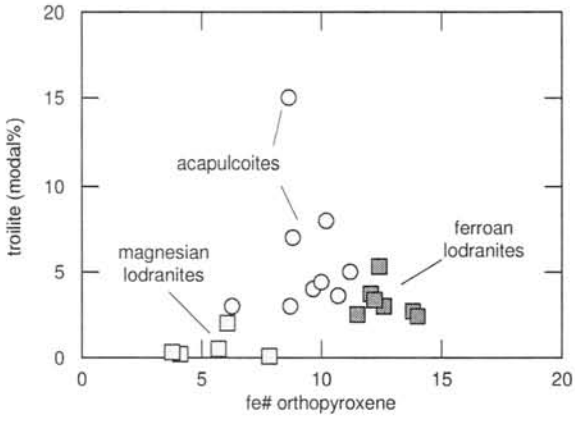

Figure 1. Ferroan lodranites have distinctly higher average fe# of orthopyroxene and modal abundance of troilite. Data compiled from numerous sources.

Methods: We compared the trace siderophile element composition of metals in ferroan lodranite MAC 88177 with seven other acapulcoites and lodranites from the U.S. Antarctic Meteorite Collection spanning a range of metamorphic grades. Antarctic samples are preferred since metals and sulfides are readily altered by terrestrial weathering. Analyses were performed *in situ* on polished thin sections by LA-ICP-MS at the ICP-MS facility of the National High Magnetic Field Laboratory/Florida State University using the methodology of [11] and obtaining similar analytical precision. With proper instrumentation and adequate care, LA-ICP-MS can be a nearly non-destructive technique, with a typical working range of 20-150 μm spot sizes. Due to the scarcity and high scientific value of these specimens, care was taken to

produce only minimal damage at specific points of interest. Metal, sulfide, and silicate phases in these samples were characterized by EPMA at NASA Johnson Space Center prior to LA-ICP-MS analysis.

Results: Fe,Ni-metal comprises <1 modal% of MAC 88177 and contains a range of Ni contents (6-32 wt%). The average composition of metal is more Ni-rich (14.5 wt%) than in any other sample analyzed, and the modal sulfide/metal ratio (4:1) is also higher. Metal is strongly depleted in highly compatible siderophiles (Re,Os,Ir,Pt) relative to other samples, yet contains comparable concentrations of less compatible siderophile elements (As,Pd,Au).

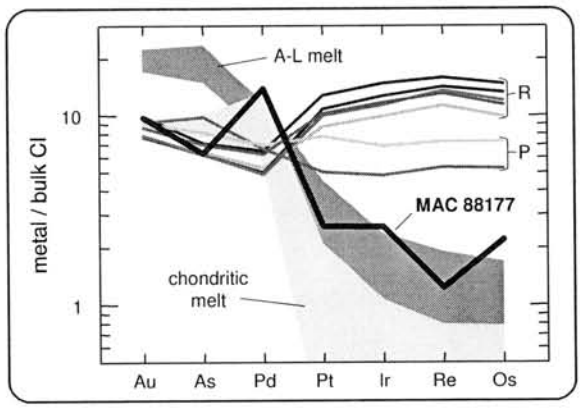

Figure 2. Average metallic siderophile element abundances in MAC 88177 metals compared to metals of primitive (P) and restitic (R) clan members normalized to bulk CI chondrite in order of increasing solid metal/liquid metal partitioning at a melt composition of 25 mol% S. Also shown are fields for calculated compositions of low-degree partial melts derived from metals of other clan members (A-L) and chondritic metals.

Discussion: Metal composition in MAC 88177 strongly resembles low degree metallic partial melts (Figure 2). Considering also the low metal and relatively high troilite content, it seems apparent that all or nearly all of the original metal in this sample has been lost and replaced by metallic melts from elsewhere. Presumably this occurred sometime after MAC 88177 underwent extensive partial melting (>20% [8]), when temperatures fell closer to the Fe-Ni-S cotectic (~980°C) low-degree metallic melts from elsewhere in the parent body infused in. It is unclear whether the last stages of removal of refractory metal occurred simultaneous with the extraction of silicate partial melts or resulted from through-fluxing by fertile S-rich melts, which could potentially have had a dissolution effect. Samples with comparably high 2-pyroxene temperatures (~1200°C [method of 12]) but more typical fe# of ferromagnesian silicates, such as ALHA 81187 and GRA 95209, contain matrix metals of refractory composition and, thus, appear to have retained much of their original metal content. Future research on metal compositions in other ferroan lodranites yielding lower 2-pyroxene temperatures, such as Y-74357 and Y-791491/Y-791493, will hopefully provide a more detailed history of the metallic system in ferroan lodranites and perhaps yield clues to their genesis.

References: [1] McCoy *et al.* (1997a) *GCA* 61(3):623-637. [2] Nagahara & Ozawa (1986) *NIPR Spec. Issue* 41:181-205. [3] Mayeda *et al.* (1987) *NIPR Spec Issue* 46:144-150. [4] Clayton & Mayeda (1996) *GCA* 60:1999-2017. [5] McCoy *et al.* (1996) *GCA* 60:2681-2708. [6] Mittlefehldt *et al.* (1996) *GCA* 60(5):867-882. [7] Mittlefehldt (2003) *M&PS* 38(*Supp.*1):A95 [8] McCoy *et al.* (1997b) *GCA* 61(3):639-650. [9] Patzer *et al.* (2004) *M&PS* 39(1):61-85. [10] Miyamoto & Takeda (1994) *JGR* 99(E3):5669-5677. [11] Campbell *et al.* (2002) *GCA* 66:647-660. [12] Brey & Köhler (1990) *JOP* 31(6):1353-1378.

The black boulder on the asteroid Itokawa. N. Hirata[1,2], M. Ishiguro[3], D. Tholen[4], T. Hiroi[5], T. Noguchi[6], S. Sasaki[7], R. Nakamura[8] and J. Saito[9], [1]Dept. Computer Software, Univ. of Aizu, Ikki-machi, Aizu-Wakamatsu, Fukushima 965-8580, JAPAN (naru@u-aizu.ac.jp), [2]Kobe University, [3]Seoul National University, [4]University of Hawaii, [5]Brown University, [6]Ibaraki University, [7]National Astronomical Observatory of Japan, [8]National Institute of Advanced Industrial Science and Technology, [9]Japan Aerospace Exploration Agency.

We report the first result from brightness and color analysis on a unique, remarkably dark boulder on the asteroid Itokawa by using images taken by the asteroid multi-band imaging camera (AMICA) onboard to the HAYABUSA spacecraft. We also discuss on possible origins of the boulder, and on their implications of geologic processes on the asteroid and its parent body.

Asteroid explorations and meteorites:

The HAYABUSA asteroid explorer arrived at a S-type near earth asteroid 25143 Itokawa on September 12, 2005 after over 2 years cruising with ion thrusters. The spacecraft continuously stayed a rendezvous position close to the asteroid for three months, and remote sensing observations with onboard instruments were carried out [1-6]. At the end of the rendezvous phase, touchdown operations were carried out to land on the asteroid surface and correct samples of the surface materials [7]. Even though the spacecraft was originally designed as an engineering demonstrator, great scientific products were also expected of this mission. One of the most important scientific goals is to link asteroids and meteorites together with both remote sensing data and analysis of samples of the asteroid surface, which will be returned to the Earth in 2010.

Direct observation data of asteroids are valuable to discuss on various geologic processes on asteroids and their parent bodies, such as formation of planetesimals, thermal evolution, impact cratering, collisional disruption and subsequent re-accumulation, and space weathering. Although some of these processes partly left several evidences in meteorite samples, direct observation of asteroid would provide more detailed information on such processes. Most meteorite samples and features in the specimens are very small, so there is a difficulty in discussions on the extent of the geologic processes that made the features remained in the samples. Because the direct observations cover from large global features to small-scale surface textures near the resolution limit, they would give geological contexts of the evidences in small meteorite samples. On the other hand, detailed laboratory investigation of meteorites gives comprehensive knowledge of physical condition at the geologic processes.

From this point of view, material variation of the asteroid is one of the most interesting features to be investigated. The results from the near infrared spectrometer and the X-ray spectrometer show that LL5-6 ordinary chondrites are the most possible representatives of the asteroid, although other possibilities are not excluded. The near infrared spectra show certain diversity, which is probably a result of space weathering and/or different physical condition of the surface material [3]. Except for those diversities, any detectable material differences are not reported from near infrared spectroscopy at present.

The spatial resolutions of the spectrometers are limited, so we also use AMICA images to investigate variations in surface brightness and color. The brightness difference is approximately 10-20 % on distant images and as 30 % on close-up images. The pattern of dark/bright regions correlates well to the distribution of surface topography and slope [8]. This feature can be explained as a result of surface processes on the asteroid: space weathering by micrometeorite impacts and/or exposure to solar wind and gravitational movement of the surface material.

The black boulder on the head of Itokawa:

AMICA observations also revealed that there is another kind of the brightness and color variation than the dark/bright regions. At the top of the "head" part of the asteroid [1], a boulder with unusually low brightness was found (Figure 1). The darkness of this boulder form a striking contrast with surroundings, so the HAYABUSA project adopts it as the marker of the prime meridian of the asteroid coordination [9].

This boulder, referred as "the black boulder" hereafter, has a pyramid or a cone shape of 6 x 6 m in the basement size and 5 m in height. No apparent fracture system or surface texture was observed within the resolution limit. The black boulder is the only boulder with such low brightness among boulders of comparable size range on the surface of the asteroid, whereas there are more than 500 boulders in this size range [2]. Because space weathering should be a universal process on the asteroid surface, it is inappropriate to the origin of the black boulder. For further discussion, a new data calibration procedure including a correction of scattered light is developed. A visible-near infrared spectrum of the black boulder is constructed from calibrated color images with selected filters, and will be compared with reflectance spectra of various kinds of meteorites.

References:

[1] Fujiwara A. et al. (2006) Science, in press. [2] Saito J. et al. (2006) Science, in press. [3] Abe M.

et al. (2006) Science in press. [4] Okada T. et al. (2006) Science, in press. [5] Abe S. et al. (2006) Science, in press. [6] Barnouin-Jha O. et al. (2006) LPS XXXVII, #1773. [7] Yano H. et al. (2006) Science, submitted. [8] Sasaki S. et al. (2006) LPS XXXVII, #1671. [9] Demura H. et al. (2006) Science, submitted.

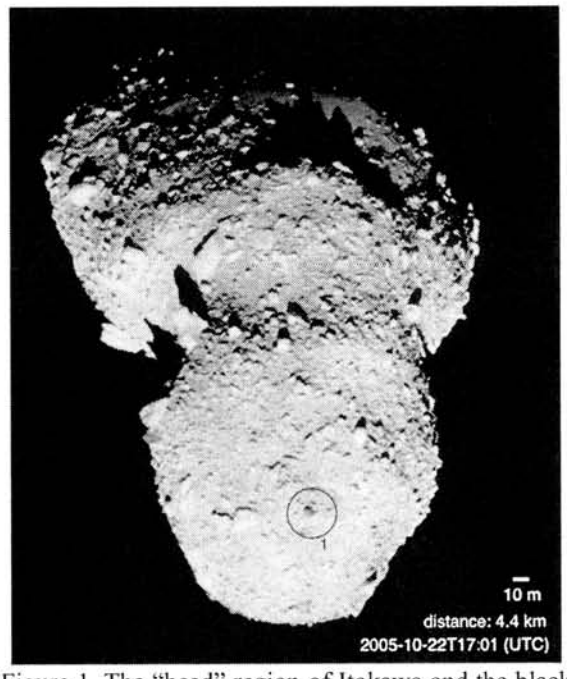

Figure 1. The "head" region of Itokawa and the black boulder (marked as a blue circle #1). AMICA image number: ST_2482160259.

The S-type asteroid – ordinary chondrite controversy and discoveries by the Hayabusa mission to asteroid 25143 Itokawa. T. Hiroi[1], M. Abe[2], K. Kitazato[2,3], S. Abe[4], B. E. Clark[5], S. Sasaki[6], and M. Ishiguro[7], [1]Department of Geological Sciences, Brown University, Providence, RI 02912, USA (takahiro_hiroi@brown.edu), [2]Inst. of Space and Astronautical Science, Japan Aerospace Exploration Agency, Sagamihara, Kanagawa 229-8510, [3]Department of Earth and Planetary Science, University of Tokyo, Tokyo 113-0033, [4]Graduate School of Science and Technology, Kobe University, Kobe 657-8501, [5]Ithaca College, 267 Center for Natural Sciences, Ithaca, New York 14850-7288, USA, [6]Mizusawa Astrogeodynamics Observatory, National Astronomical Observatory of Japan, Mizusawa 023-0861, [7]School of Earth Environmental Sciences, College of Natural Sciences, Seoul National University, Seoul 151-742, Korea.

Introduction:

There has been a long-standing controversy concerning the parent bodies of ordinary chondrites and the identity of the S-type asteroids. Although their visible and near-infrared reflectance spectra show similar absorption bands of olivine and pyroxene minerals, their spectral matches were poor due to the red continua and subdued absorption bands of the S asteroid spectra. While the recent ground-based spectral observations of small, near-earth asteroids have been revealing the link between the S asteroids and ordinary chondrites [1]. the successful rendez-vous and observations of asteroid 25143 Itokawa by the Japanese Hayabusa spacecraft have given us some decisive discoveries relevant to the issue.

S asteroid – ordinary chondrite controversy:

The name of "S" was meant to be "stony" or "silicaceous", and in that sense it is still valid. However, the speculation that the S asteroids are ordinary chonrites has been altered greatly over history. Seven subclasses of S asteroids were proposed, where only one of them, S(IV), was characterized as having olivine and pyroxene mineral assemblages consistent with those of ordinary chondrites [2]. Many researchers used to think that the red spectral profile of the S asteroids was due to metallic iron and the silicate composition of the S asteroids such as olivine/pyroxene modal abundance can be estimated from their reflectance spectra by simply removing and disregarding the continuum.

However, through some experimental and modeling studies, it has become clear that the red profile is due to space weathering [3, 4], and later studies further showed that the definition of the S(IV) class would significantly change by grain size and space weathering [5, 6]. Yet, high degrees of space weathering of the S asteroids suggest that they have high abundances of metallic iron because metallic iron in their regolith can probably promote space weathering by enriching nanophase reduced iron (npFe0) inside vapor coating on the regolith grains produced by micrometeorite impacts.

Discoveries by Hayabusa mission to Itokawa:

Hayabusa spacecraft rendezvoused with asteroid Itokawa from September to December 2005, during which period it performed two-dimensional color imaging with the Asteroid Multiband Imaging Camera (AMICA) [7] and point-target near-infrared spectroscopic observations with the Near Infrared Spectrometer (NIRS) [8] as well as several sampling attempts [9]. The mission outline and the global properties of Itokawa are summarized in [10]. Itokawa has revealed its detailed appearance which is unlike any other asteroids visited by a spacecraft in the past. The surface is full of boulders and pebbles of varying sizes [9], and there are clear brightness and color differences among its geologic units [7]. The length is about 550 m and the density is estimated to be 2 ± 0.2 g/cm^3 [10].

So far, the compositional information detected by NIRS is consistent with LL5 or 6 chondrites and there is no significant compositional heterogeneity detected [8]. Combined with the above bulk density estimate, this implies a macroporosity of about 40 %. On the other hand, brightness and color differences due to differences in grain size and degree of space weathering are found to be significant [7, 8]. Possibly most weathered surfaces are found in depressed areas where gravitational stability could have sustained the surface materials longer than other areas. Further calibrations and analyses of AMICA color and NIRS data as well as supporting laboratory data are being undertaken to reveal more quantitative descriptions of the surface materials, which we hope to present at the meeting.

References:

[1] Binzel R. P. et al. (2004) *Icarus, 170*, 259-294. [2] Gaffey M. J. et al. (1993) *Icarus*, *106*, 573-602. [3] Cassidy W. and Hapke B. (1975) *Icarus*, *25*, 371-383. [4] Yamada M. et al. (1999) *EPS*, *51*, 1255-1265. [5] Ueda Y. et al. (2002) *LPS XXXIII*, Abst. #2023). [6] Burbine T. H. et al. (2002) *LPS XXXIII*, Abst. #1359. [7] Ishiguro M. et al. (2006) *LPS XXXVII*, Abst. #1533. [8] Abe M. et al. (2006) *Science* (in press). [9] Yano H. et al. (2006) *LPS XXXVII*, Abst. #2463. [10] Fujiwara A. et al. (2006) *Science* (in press).

Comparative magnetic signature of Martian meteorites Yamato 000593, Yamato 000749, Yamato 000802, Yamato 980459, Yamato 793605 and ALH 77005

V. Hoffmann[1], M. Funaki[2]

[1] Institute for Geosciences, University of Tübingen, Sigwartstrasse 10, 72076 Tübingen, and Department of Geo- and Environmental Sciences, University of München.

[2] National Institute of Polar Research, Tokyo, Japan, 9-10 Kaga 1 Itabashi, Tokyo 173-8515.

Introduction:

Strong magnetic anomalies due to crustal magnetisation/remanence have been a major unexpected discovery of the Mars Global Surveyor (MGS) mission. It is generally believed that these anomalies are due to magnetite-bearing rocks which cooled in an Earth-like strong magnetic dipole-field (10-100ÌT), in analogy to the magnetization of the Earth oceanic crust. There is some speculation about plate-tectonic-like processes on Mars which could have produced these magnetic lineament"-like anomalies. A strong magnetic dipole-field is believed to have existed for about 1Gyr on Mars being the cause for the strong magnetisation as well as representing a major precondition for the possible development and existence of life (or at least prebiotic structures) on Mars.

Meteorites from Mars are the only rock samples which we have from this planet. Magnetic measurements of meteorites are non destructive techniques allowing to investigate in the case of SNC's:
-the type of magnetic minerals (accessories),
-the possible in situ remanence in order to interpret the observed crustal magnetization,
-the intensity of the magnetic field in which the natural remanent magnetization (NRM) is acquired,
-the petrofabric through the anisotropy of magnetic susceptibility.

A systematic investigation of the Martian meteorites by paleo-, rock- and mineral magnetic means will help to unreveal and understand the record about the Martian magnetic field and the crustal anomalies. Iron sulfides may also play an important role in the prebiotic phase of the origin of life. The different SNC meteorites offer magnetic material of different ages beginning with the 4.5 Gyr-old SNC meteorite ALH84001. Shock metamorphism features on the magnetic phases have to be taken into account as a result of the ejection of the SNC from Mars due to large impacts. Potential alteration effects due to processes on Mars as well as on Earth during the residence time are studied in detail. The SNC magnetic signature is used to develop a well constrained magneto-mineralogical model.

Samples and experiments

We have started to investigate the magnetic signature of all NIPR Martian Meteorite specimens. First data about Yamato 000593, a nakhlite, were published by [1], or [2][3] Here we report data of new magnetic experiments on the following NIPR specimen: Yamato 000593, Yamato 000749 and Yamato 000802, all classified as nakhlites, Yamato 793605 and ALH 77005, both lherzolitic shergottites, and Yamato 980459, an olivine-phyric shergottite.

For the nakhlites Yamato 000593, Yamato 000802 and Yamato 000749 mass specific magnetic susceptibility (measured with AGICO KLY3) was found to be slightly higher than for most of the other nakhlites. Much lower values were found for the lherzolitic shergottite Yamato 793605, in the range of other lherzolites. ALH 77055, however, showed the highest values which also differ significantly from other lherzolites and Yamato 793605. Anisotropy of magnetic susceptibility (AGICO KLY3), here the P factor, is in the range of 1,01-1,05 which is typical for volcanic or shallow subsurface intrusive rocks.

This is confirmed by the values of the intensity of NRM (Natural Remanent Magnetization, 2G Cryogenic) and its alternating field demagnetization (AF-Demag). In addition, IRM (Isothermal Remanent Magnetization) and ARM (Anhysteretic Remanent Magnetization) experiments were performed on the same samples.

Optical microscopy, magnetic microstructure analysis, thermomagnetic analysis and Raman Spectroscopy revealed the presence of a low-titanium magnetite phase, a ferrimagnetic pyrrhotite phase and ilmenite (exolution lamellae and individual grains) in the Yamato 000593 nakhlite. For the first time, graphite as a carbon phase was detected by Raman Spectroscopy in SNC meteorites.

[1] Funaki M., Hoffmann V., Fukuma K.: The meaning of unstable remanent magnetization of Y000593 (nakhlite). Ant. Meteor., **27** (2002), 23-24. [2] Rochette P., Gattacceca J., Chevrier V., Hoffmann V., Lorand J.P., Funaki M., Hochleitner R.: Matching Martian crustal magnetization and meteorite magnetic properties. Meteorite Planet. Sci., 2005, in press. [3] Rochette P., Gattacceca J., Chevrier V., Hoffmann V., Lorand J.P., Funaki M., Hochleitner R.: A synthesis on the magnetic properties of martian meteorites. LPSC 2005.

Are the local/regional geophysical anomalies and material findings (FeSi components and diamond/fullerene containg carbon spherules) in SE Bavaria related to an impact?

V. Hoffmann[1], W. Rösler[1], A. Patzelt[2], B. Raeymaekers[3]

[1]Institute for Geosciences, University of Tübingen, Sigwartstr. 10, D-72076 Tübingen, Germany. [2]Terrana Geophysik, Zeppelinstr. 15 D-72116 Mössingen, Germany. [3]Infraserv Gendorf, D-84504 Burgkirchen, Germany.

As part of the EU-funded MAGPROX project potential hot spots of top soil magnetic susceptibility in SE Bavaria were investigated in more detail in order to trace environmental pollution effects of the nearby chemical and metallurgical industries [1]. After the initial 10 km by 10 km grid mapping campaign, the area within the so-called „chemical triangle" near the German/Austrian border was indicated by a few slightly increased values of top soil magnetic susceptibility (MS). The area was revisited whereby top soil as well as shallow soil core MS were recorded for 120 sampling locations in undisturbed forest areas. The grid density was about 1km by 1 km within larger forests. Fierte almost all the cores the resulting vertical MS profiles revealed a substantial increase with depth within the first 10-20 cm until reaching the underlying fluvial/glacial till beds. The signature of the MS profiles can be neither interpreted as typically "industrial" with peak values on top, nor as typically "geogenic". Also, pedogenic processes cannot account for the observed regional magnetic susceptibility anomalies. The existence of a high concentration of spherical, highly magnetic particles can provide an explanation for some of the investigated spots in deeper soil horizons (B/C). The magneto-mineralogy is dominated by magnetite-rich spinels which do not show the typical geogenic chemistry. In addition, Fe-silicide phases could be detected in the magnetic extract which are shown to be common in this area in deeper soil layers but are otherwise extremely rare on earth (e. g. known from fulgurites).

In the same region in SE Bavaria, many small scale (5 m to ca. 100 m diameter) circular, bowl shaped structures are known and have been previously interpreted as archaeological objects or geologic structures [2] [3]. Some of these structures posses a well-developed crater rim; in a few of them fractured boulders or even melt rocks can be found. We have selected one specific and extraordinary bowl shaped, crater-like structure of 11 m diameters formed in Holocene till beds for a detailed geophysical characterization. The well pronounced crater wall which is of ca. 0.5 m in height consists of mechanically and thermo-plastically deformed bed rocks indicating temperatures exceeding 1500° C throughout the whole crater wall of ca. 20 m diameter. The GPR survey (Ground Penetrating Radar) shows that the

morphology of the crater walls continues into depths of several meters with strong reflections from the crater floor. Both magnetic surveys (MS and magnetic mapping) reveal strong magnetic anomalies associated with the thermally altered crater wall material. In the surrounding forest soil and within melt crusts of the thermally altered bed rocks, spherules and inclusions of iron silicon phases [4] and diamond/fullerene containg carbon [5] materials could be found. In conclusion, the thermal effects and internal structure of the investigated crater-like structure cannot be explained by glacial geology, archaeology, bombing, or primitive industrial processes such as Iron-ore production. The occurrence of FeSi and Carbon materials indicates a high-energy, reducing environment [6]. However, presently there is no accepted proof for an impact related origin of these phenomena.

References: [1] Hoffmann V., Rösler W.. 2004, Anomalous magnetic signature of soils in Burghausen area, SE Bavaria. Geophys. Res. Abstr. 6/2004, 05041.[2] F. Weber 1909. Die vorgeschichtlichen Denkmale des Königreiches Bayern, 1. Munich. [3] G. Doppler 1980. PhD thesis Univ. Munich. [4] D. Schryvers, B. Raeymaekers, 2004, Abstract #MS16.P13 13th European Microscopy Congress, Antwerp, Belgium. [5] Rösler W., Hoffmann V., Raeymaekers B., Schryvers, Popp J.: Diamonds in carbon spherules - evidence for a cosmic impact? International Meteoritical Society Conference, 2005. [6] A. A. Sheffer et al. 2003. Abstract #1467 Lunar and Planetary Science Conference.

Chemical composition of eleven Antarctic HED meteorites. T. Houzumi, Y. Oura and M. Ebihara, Department of Chemistry, Tokyo Metropolitan University, Minami-Ohsawa, Hachiouji, Tokyo, 192-0397, Japan.

Introdution

Howardite, eucrite, and diogenite (HED) meteorites are igneous rocks and are considered to have originated on the same asteroid, presumably 4 Vesta. It is well acknowledged that HED meteorites give us basic information in considering the early stage evolution of our solar system.

Abundance of trace elements, especially incompatible elements like rare earth elements (REEs), are largely affected by such igneous processes as partial melting and fractional crystallization. Based on their mineralogical and chemical compositions, eucrites are classified into cumulate eucrites and non-cumulate eucrites. Non-cumulate eucrites are further divided into two distinct groups, unequilibrated and equilibrated (ordinary) eucrites. Equilibrated eucrites consists of three sub-groups, main group, Stannern type and Nuevo Laredo type.

These classifications were mostly initiated by mineralogical observations. As these mineralogical varieties were generated by igneous activities on the HED parent body(ies), related chemical characteristics must have been accompanied at the same time. In this study, we analyzed 11 Antarctic HED meteorites for major, minor and trace elements. Based on elemental data obtained, we firstly evaluate our analytical data and then discuss the relation between mineralogical characterization and chemical features based on our elemental data.

Samples and analytical methods

In this study, six eucrites (Yamato-790260, Y-790266, Y-792510, Y-793547, Y-82082, Y-981651), three diogenites (Asuka-87146, A-87147, Y-791000), and two howardites (Y-790727, Y-791208) were analyzed. These Antarctic meteorites were loaned by the National Institute of Polar Research (NIPR). Among them, six meteorites (A-87146, A-87147, Y-792510, Y-793547, Y-82082, Y-981651) were supplied in powder and the remaining meteorites were in chips. For the determination of chemical compositions, three nuclear analytical techniques (prompt gamma-ray analysis (PGA), instrumental neutron activation analysis (INAA) and instrumental photon activation analysis (IPAA)) and inductively coupled plasma mass spectrometry (ICP-MS) were used. Samples were first analyzed by PGA. After PGA, chip samples were crushed and ground into powder in an agate mortar. For INAA, IPAA and ICP-MS, portions of each powder sample were used.

Results and discussion

(1) PGA data vs. wet chemistry data

Most major elements are able to be determined by PGA. By comparing our PGA data with wet chemistry data for comparable elements, it was confirmed that both data sets are consistent with each other with exceptions of Ti and Mn abundance in Y-82082, for which PGA data are systematically higher than wet chemistry data. Such difference may be partly due to the heterogeneity of these elements in the meteorite. Considering that PGA is non-destructive and induces no significant residual-radioactivity, it could be routinely applied for the bulk chemical analysis along with (or in place of) the wet chemistry procedure.

(2) Classification of eucrites based on elemental compositions

Figure 1 shows a plot of TiO_2 vs. FeO/MgO for 11 Antarctic meteorites analyzed in this study. On this plot, main-group eucrites characterized by low incompatible trace element contents and high mg# in non-cumulate eucrites are localized at the point starting two arrows, which correspond to Nuevo Laredo- and Stannern- trends.

Among six eucrites analyzed in this study, only Y-981651 can be recognized to be cumulate in origin. The remaining five eucrites are located in the non-cumulate eucrite region in Fig. 1. Among them, Y-793547 and Y-792510 appear to be plotted on the line of Stannern-trend and Nuevo Laredo-trend, respectively and Y-790266 is located in-between. Both Y-82082 and Y-790260 are considered as main-group eucrites in Fig. 1.

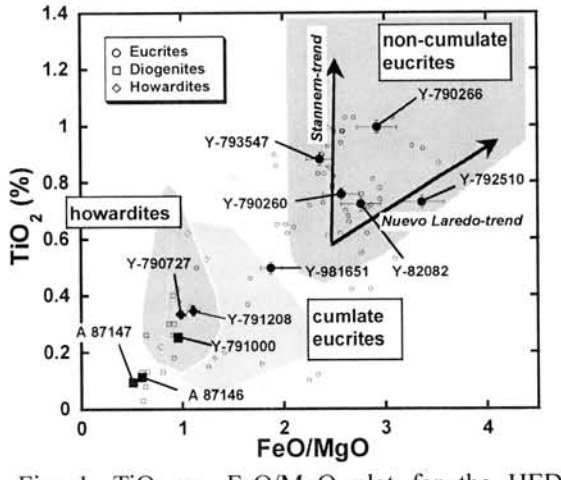

Fig. 1. TiO_2 vs. FeO/MgO plot for the HED meteorites analyzed in this study. The area is from [1]. Open symbols are literature data from [2] and [3].

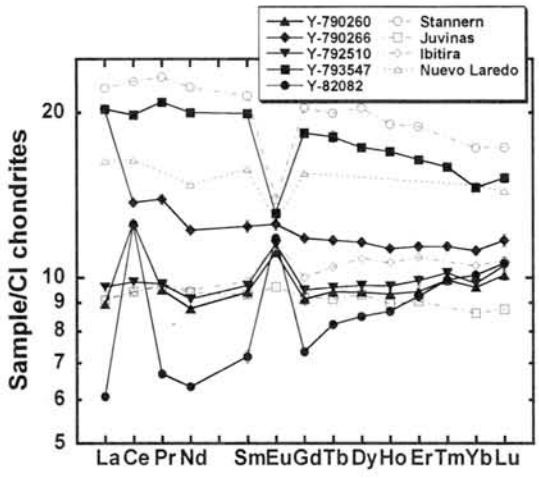

Fig. 2. CI chondrite-normalized REE abundance patterns for non-cumulate eucrites. Open symbols are literature data from [2] and [4].

Figure 2 shows CI chondrite-normalized REE abundance patterns for the five non-cumulate eucrites analyzed in this study. For comparison, REE abundance patterns for four representative non-cumulative, non-Antarctic eucrites also are shown in Fig. 2. REE abundance patterns of Y-790260 and Y-792510 are essentially identical except for Ce and are very similar to that for main group eucrite Juvinas. Although Y-792510 is located along the Nuevo Laredo-trend in Fig. 1, its REE abundances along with Ti content are in the range of main group eucrites. On the plot of Fig. 1, Y-793547 is located on the Stennern-trend, which is consistent with its Stannern like REE abundance pattern shown in Fig. 2. REE abundance pattern of Y-790266 seems to be somewhat puzzling; middle to heavy REE abundances of Y-790266 are similar to those for main group eucrites while its light REE abundances are apparently higher than those for main group eucrites.

Although Y-82082 seems to belong to main group eucrites, its REE abundance pattern is not similar to those of such group of meteorites; light REEs are considerably depleted with a large positive anomaly of Ce. Presumably, such features of REE abundance were produced by terrestrial weathering on Antarctica.

REE abundance pattern of Y-981651 (not shown) is similar to that of cumulate eucrite Moore County, suggesting that Y-981651 is a cumulate eucrite, which is consistent with the grouping shown in Fig. 1.

(3) Chemical characteristics of diogenites and howardites

Two diogenites, A-87146 and A-87147 have essentially the same REE abundances, suggesting that these meteorites are pairs. REE abundance patterns of these two diogenites are also similar to that of Johnstown, which is typical diogenite. In contrast, Y-791000 has a different REE abundance pattern from those for such typical diogenites. Its REE pattern is almost flat with a CI-normalized value of 4 except for Eu, which shows a slight negative anomaly. From these characteristics of REE abundances along with Ti contents, A-87146 and A-87147 are common diogenites while Y-791000 is a Type B diogenite [5].

Two howardites, Y-790727 and Y-791208 show similar chemical compositions, suggesting a possibility of pairs. Their REE abundances are characterized by a relative depletion of light REE and a positive Eu anomaly. Such features of REE abundances can be explained by mixing of cumulate eucrites and diogenites.

References:

[1] Barrat J. A. et al. (2003) *Geochem. Cosmochem. Acta 67*, 3959-3970. [2] Barrat J. A. et. al. (2000) *Meteorit. Planet. Sci. 35*, 1087-1100. [3] Yanai K. and Kojima H. (1995) *Catalog of the Antarct. Meteorites.43-76.* [4] Kitts K. and Lodders K. (1998) *Meteorit. Planet. Sci. 33*, A197. [5] Mittlefehldt D. W. and Lindstrom M. M. (1993) *Proc. NIPR Symp. Antact. Meteorites,* 6, 268-292.

Petrology of unusual ureilite NWA 1241

Yukio Ikeda. Department of Material and Biological Sciences, Ibaraki Univ., Mito 310, JAPAN. y-ikeda@mx.ibaraki.ac.jp

Petrography: NWA 1241 was recovered from the Libyan desert in 2001, and was classified as a ureilite [1]. It is a non-brecciated monomict ureilite, consisting mainly of pyroxene, olivine, suessite, and graphite. The modal abundances are pyroxene 68 vol.%, olivine 13 %, suessite 7 %, graphite 4 %, and others (mainly weathering products such as calcite) 8 %.

Pyroxenes are mainly pigeonite and minor magnesian orthopyroxene with a negligible amount of diopside. The main pigeonite is $En_{76}Fs_{14\text{-}16}Wo_{8\text{-}10}$ with mg# = 0.82-0.84. The magnesian orthopyroxene (Wo = 0-6%) and magnesian pigeonite (Wo = 6-11%) occur as small patches at rims of the main pigeonite or along fractures in the main pigeonite, ranging in mg# from 0.85 to 0.99. Olivine cores are 0.82 to 0.85 in mg#, and olivine shows reverse zoning to magnesian rims up to 0.99. The reduced magnesian olivine rims include many tiny (<1 μ m) metallic grains in addition to rare diopside grains (several μ m across). Metallic phases are mainly suessite (Fe_3Si) ranging in Si from 12 to 15 wt%. Small (mostly <1 μ m) grains of kamacite and schreibersite are very rarely included in pigeonite or olivine grains. Glass occurs in a negligible amount at silicate grain boundaries. The major-element composition of the glass corresponds to a mixture of sodic plagioclase ($An_{9\text{-}17}Ab_{81\text{-}87}Or_{3\text{-}5}$) and silica components. Graphite occurs patches of fine-grained aggregates, a few hundreds of μ m across.

Unusual Characteristics: NWA 1241 has two unusual characteristics; (A) Pyroxene overwhelms olivine in amounts for NWA 1241, although the situation is reverse for normal ureilites, and (B) metallic phases are almost suessite in NWA 1241, although most normal ureilites contain kamacite predominantly. The pyroxene-rich nature of NWA 1241 could be explained by a sampling problem, because NWA 1241 is coarse-grained and it might be heterogeneous in the scale of petrologic thin sections. Otherwise, the source materials for NWA 1241 should be enriched in pyroxene components. Recently, an anomalous ureilite MET 01085 is reported to consist mainly of pyroxene without olivine [2] & [3], although the origin is not yet clarified. NWA 1241 contains a small amount of olivine, unlike both normal ureilites and the anomalous MET 01085. The pyroxene-rich nature of NWA 1241 remains unsolved.

Suessite occurs at silicate grain boundaries and seems to be in equilibrium with the reduced olivine rims (mg#=0.99). The suessite (Sue) may be produced by reduction of olivine (Ol) with kamacite (Ka) and graphite (Gr.), and a plausible candidate for reduction equations is;

$$Fe_2SiO_4 + Fe + 4C \rightarrow Fe_3Si + 4CO\ .$$
$$\text{Ol} \quad \text{Ka} \quad \text{Gr.} \quad \text{Sue}$$

Probably the oxygen fugacity for NWA 1241 was lower than those for normal monomict ureilites. Diopside occurs as small grains in the reduced olivine, and magnesian orthopyroxene grains occur near the diopside. Thus, application of a two-pyroxene geothermometer [4], using the diopside, gives equilibrium temperatures of about 1100℃, which may be near the solidus temperatures. A ureilite parent body which was still at high temperatures was broken, and some ejected blocks of ureilites may have suffered reduction at about 1100℃ to produce suessite and the reduced olivine rims in NWA 1241.

References: [1] Russell et al. (2002) MAPS 37, Meteoritical Bull., A164. [2] McCoy et al. (2002), Antarc. Meteor. Newsletter 25, No.2, p15. [3] Kallemeyn and Warren (2005) LPS XXXVI, #2165. [4] Lindsley and Andersen (1983) Proc. 14 LPS Conf., JGR 88, Suppl., A887-A906.

A HYPOTHESIS PAPER ON THE CRUST THICKNESS OF ENCELADUS

E. Illés-Almár, Konkoly Observatory of the Hungarian Academy of Sciences, H-1525 Budapest Box 67, Hungary, e-mail: illes@konkoly.hu

Abstract

On the basis of the high-resolution Cassini images we suggest that the crust thickness of Enceladus might be different on the Northern and the Southern hemispheres. In a homogeneous layered body the cause of such a hemispheric thickness difference can only be the circulation of a mantle. If this suggestion proves to be right it means that Enceladus has to possess a water or slushy ocean beneath the ice crust.

Already on Voyager images [1] (Fig.1) old cratered terrain, as well as long lineaments were visible on the surface of Enceladus. The Cassini images [2] not only strengthened this observational fact, but demonstrated that the distribution of the impact craters is peculiar (Fig.2): the crust is full with impact craters around the North Pole (here the surface is very old), contrary to the vicinity of the South Pole, where there are no impact craters at all (that is, the surface is very young). Moreover, beyond the tidal cracks on Enceladus there are a number of fissures in the vicinity of the South Pole (Fig.3). Along this „tiger stripes" the temperature is not only higher by 10 K but new water-rich material was extruded to the surface (this is demonstrated by the different structure of the ice crystals on the Cassini image Fig.4). What is more, active geysers have been observed here (Fig.5). It means that under the South Pole a warm plume of the mantle should exist.

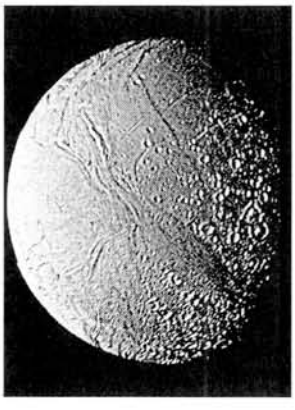

Fig. 1
Voyager image of Enceladus

Where the energy supplying this activity could come from? One can not suppose that such a small icy moon of 500 km, accumulated at the distance of Saturn, could have enough radioactive material to supply the energy. This supposition would be contradicted by the lack of activity on Mimas, which is about the same size as Enceladus. It is rather probable that orbiting in a satellite system in 2:1 resonance with Dione the tidal heating is supplying the energy. But if Enceladus gets tidal heating, why Mimas does not? It orbits also in 2:1 resonance (with Tethys) and is even nearer to Saturn than Enceladus.

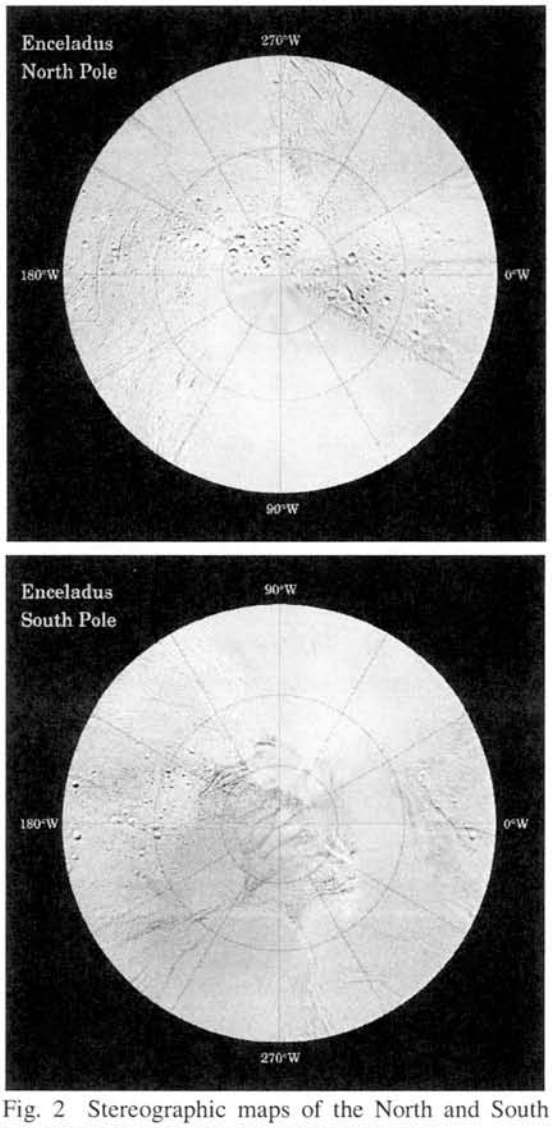

Fig. 2 Stereographic maps of the North and South hemispheres on the basis of Cassini images.

But Mimas shows up no trace of any tidal cracking or of any geologic activity. The explanation of Mimas' passivity might be that Mimas is already solid for a long time (demonstrated by the huge Hershel crater that shows up no trace of relaxation) and the tidal heating is much weaker in a solid body.

The tidal heating, however, is supposed to heat a body of uniform composition symmetrically. Consequently, it is not understandable why the activity takes place on the one side of Enceladus only.

Such an asymmetric activity center can evolve only if the mantle circulation helps in the redistribution of the heat. If Enceladus has a water (or slushy) mantle, and a one-cell circulation is working inside the moon, the observations could be somehow qualitatively explained. The descending branch of the

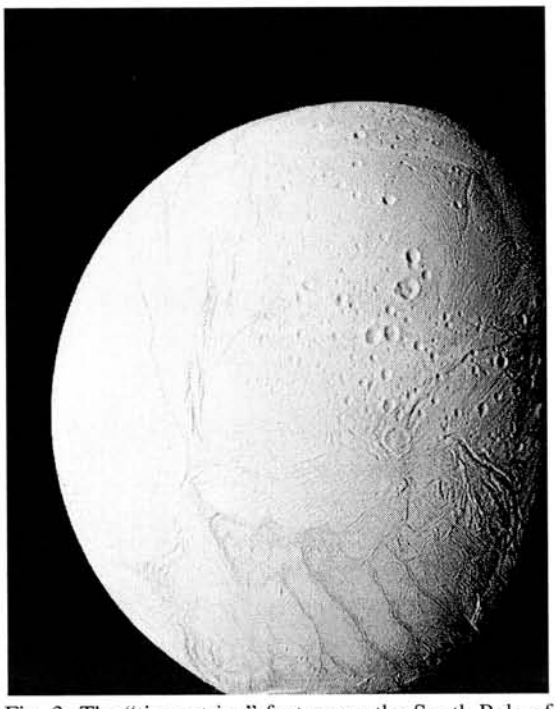

Fig. 3 The "tiger stripe" feature on the South Pole of Enceladus (Cassini image).

water-mantle circulation might be on the North Pole, the ascending plume on the South Pole. Here the warm material of the plume makes the ice crust thin from below by thermal erosion. Moreover new material can be extruded along the fissures.

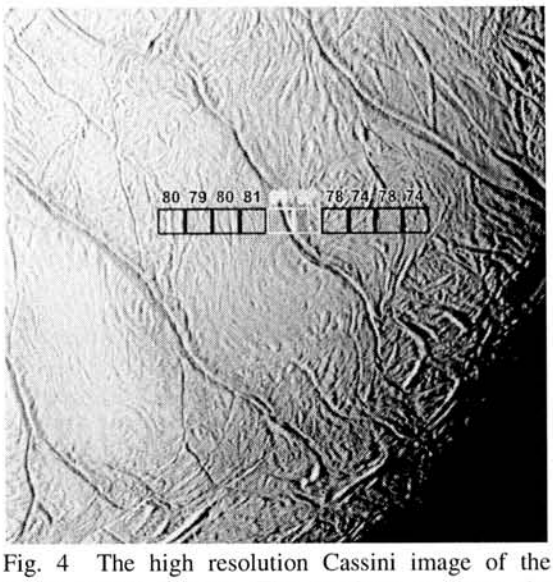

Fig. 4 The high resolution Cassini image of the "tiger stripe" fissures. The numbers represent the temperature in the boxes. The lower albedo along the "stripes" means a different crystal structure from the surroundings.

The fact that Enceladus has any activity center – to the contrary to Mimas – is also in favor of its liquid ocean because strong tidal heating can arise in fluid state.

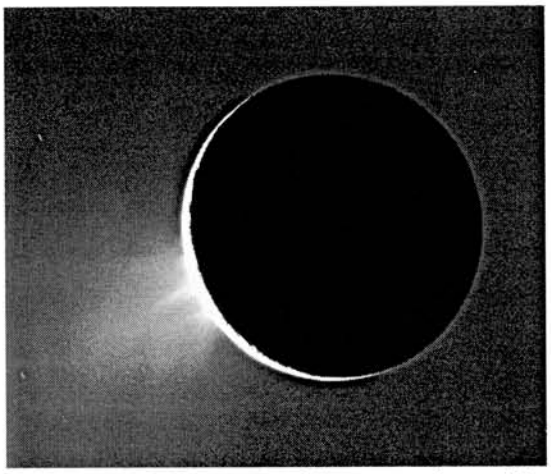

Fig. 5 Fountain-like source of fine spray of material on the South Pole (Cassini image).

What can be the cause that Mimas is solid and Enceladus is not? Let us suppose that at the time of the heavy bombardment Enceladus has got more or larger impacts than Mimas, then Enceladus started its thermal history with larger heat-reserve. Consequently, the tidal heating could keep its interior fluid even up to now if it moved continuously in resonance.

Acknowledgement
The author is indebted to Mr. P. Decsy for the preparation of the paper.

References

[1] Smith, B.A., Soderblom, L., Batson, R., Bridges, P., Inge, J., Masursky, H., Shoemaker, E., Beebe, R., Boyce, J., Briggs, G., Bunker, A., Collins, S.A., Hansen, C., Johnson, T.V., Mitchell, J.L., Terrile, R.J., Cook II., A.F., Cuzzi, J., Pollack, J.B., Danielson, G.E., Ingersoll, A.P., Davies, M.E., Hunt, G.E., Morrison, D., Owen, T., Sagan, C., Veverka, J., Strom, R., Suomi, V.E.: A new look at the Saturn system: the Voyager 2 images. 1982, Science, 215, 504-537

[2] http://saturn.jpl.nasa.gov/home/index.cfm

On the Origin of the Two Saturnian Ring Systems.

E. Illés-Almár, Konkoly Observatory, H-1525 Budapest P.O.B. 67, Hungary, e-mail: illes@konkoly.hu

Abstract

On the basis of Cassini measurements it is supposed that Saturn has *two* ring systems of different origin. The low albedo dust rings come into existence similarly to those of other giant planets. The ice ring system (the B+A ring) takes its origin by the fragmentation of an icy body. Very probable, a single model cannot describe the Saturnian ring systems, neither in composition nor in layer type.

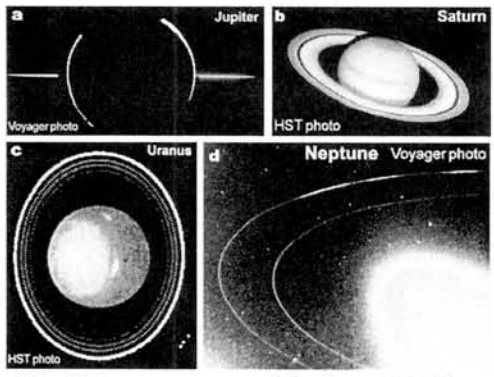

Fig. 1 The appearances of the rings of the four giant planets. The Saturnian ring is peculiar.

Introduction

Comparing the rings of the four giant planets (Fig.1) it is evident that the ring-system of Saturn is peculiar with its broad and bright stripe. The other three giant planets have dark, thin ring-systems. Saturn's ring-system is not only brighter but a thousand times more massive than the most massive dust ring – the Uranian ring system [1]. Saturn's ring has an integrated mass comparable to those of significant satellites like Mimas or Enceladus [2].

It has been proven only recently by the Galileo results [3] at Jupiter, that the dark dust rings are created by micrometeoroid bombardment onto the small, dark, inner moons of the giant planets. Because of the focusing effect of the giant planets of large masses, the flux of the impacting bodies onto these near moons is higher and the impact velocity is enhanced by such a rate, that an impacting body can excavate several hundred times more dust from the moons than its own mass. The excavated dark dust particles then revolve around the planet forming the dark dust rings. The dusting of the different satellites gives rise to the different components of the dust rings. The outer edges of the rings are rather sharp, but the inner edges are diffuse because of the Poynting Robertson effect. So the components of the rings overlap each other. In the case of Jupiter, however, the distances between the inner moons are large enough, therefore the four ring-components could be separated.

Dark dust rings at Saturn as well

It was discovered on Pioneer, later on Voyager (the F ring, the faint dust ring in the Encke division) and now on Cassini (new ones along the orbit of Atlas and Pan) images that Saturn has thin, dark dust rings as well. The newly discovered tenuous rings demonstrate that the low albedo dust rings come into being in the Saturnian system also in the same way as they come into existence in the case of other giant planets. In the divisions, namely, the particles are driven out quickly by the gravitational disturbing effect of one or other moon. So, for example, on the orbit of Atlas we can see only the pristine low albedo dust particles that just left their parent moons. In the Saturnian ring-systems in places, other than the divisions, we can not follow the birth of a low albedo dust ring because around Saturn revolve numerous dust-ejecting moons, and so the rings are overcrowded: we can not separate the different components of the rings.

Bright, icy ring-system at Saturn

The composition of Saturnian ring is mostly water ice, as it was stated already in the 1970s on the basis of measurements from the Earth [4,5,6,7] as well as of the Voyager measurements [8]. The recent high spatial resolution Cassini-measurements demonstrated more precisely, that there are places where almost pure low albedo dust and there are places where almost pure ice is present [9]. In the divisions and in the F and C ring there is mainly low albedo dust, while in the B ring there is mainly pure water ice, at the same time in the A ring there is dirty water ice (Fig.2).

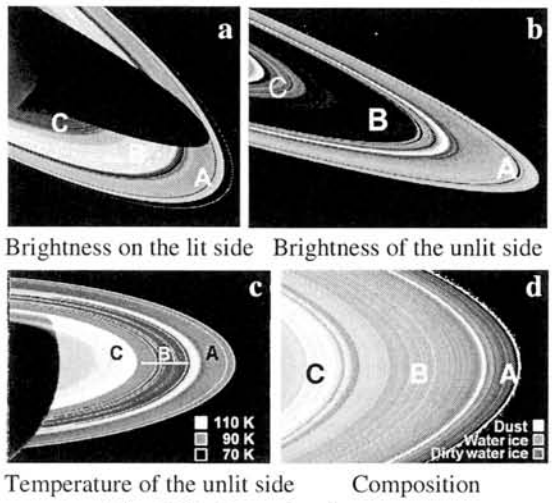

Brightness on the lit side Brightness of the unlit side

Temperature of the unlit side Composition

Fig. 2 The Saturnian ring system.

Discussion

How could it have happened that at Saturn in some places the dark dust and the ice are separated, but in some places they are mixed together? And how could it have happened that there are ices in the ring-system of Saturn and there are no ices in the ring systems of the other three giant planets? If the process of the icy ring's origin would be a common one, then all the other giant planets should have to possess bright rings as well. As it is not the case, some peculiar, single event had to have happened with Saturn.

The origin of the icy ring system

Dones [1] has suggested that a Chiron-like giant cometary nucleus was captured by Saturn that disintegrated inside the Roche-limit, supplying the material of the icy ring. He estimated that the occurrence frequency of such encounters is one in the lifetime of the Solar System. Accepting Dones' hypothesis we conclude that on the same place Saturn has two ring systems of independent origin and evolution, but interacting with each other [10,11].

One kind of the Saturnian rings is the low albedo dust-ring system that is stationary by dynamical equilibrium. The dust particles themselves disappear always in a timescale of 10^8 years from the ring, because of the Poynting Robertson effect, but it is supplied and maintained continuously by the newly knocked out dust particles from the inner moons. The low albedo dust rings are stationary as long as their parent moons exist. The other kind of the Saturnian rings is the ice-ring system that is temporary in that sense, that if the material of the icy body is exhausted, there will be no supply.

The two ring systems occupy the same place and both of them suffer from the moons. The influence of gravitational action of the moons, namely, forms divisions in both ring systems at the same distances from Saturn, and restrict the spreading in some places, e.g. at the outer edge of A ring. Their small dust particles move inward because of the Poynting Robertson effect, only the ice particles move more slowly than the low albedo dust particles because of their higher albedo. Interaction occurs, however, between the two kinds of rings-systems: for example the low albedo dust particles make the ice pieces dirty if they collide, especially often near the birth-place of the low albedo dust particles. Since near the A ring there are many dust-ejecting moons the A ring is more dirty than the B ring.

The disintegration of a fragment of the giant comet might occur at that distance from the planet, where the B ring is the brightest on the lit side, and the darkest and the coldest on the unlit side (Fig.2). Another fragment of the disrupted cometary nucleus can be the spongy Hyperion that is so different from the other icy moons (Fig.3). That is why I consider a cometary nucleus is more reliable suggestion for the source of the icy ring than a middle size icy moon.

When the icy moon or the giant cometary nucleus started to break up, its material started to disperse into the B+A icy ring. The moons with their gravitational disturbances immediately started to create the gaps, for example dividing the B+A ring into B and A.

The disintegration is probably continuing even now. This is demonstrated 1.) by the non-uniform brightness of the B+A ring, 2.) by the non-uniform opacity of the B+A ring (that is, the particles still can be too near to each other in the middle of the B ring: here the ring can be "many-particles thick" and here the sunlight can not pass through the ring; that can be the reason why the B ring is so cold there), 3.) by the non-uniform dirtiness (that is, the B+A ring is not uniformly dirty: the low albedo dust particles had still not enough time to penetrate everywhere), and 4.) by the fact that the C ring contains mostly low albedo dust particles (either the micrometeoroid bombardment had still not enough time to pulverize the ice chunks and/or the icy dust had still not enough time to reach the C ring spiraling inward more slowly because of its higher albedo).

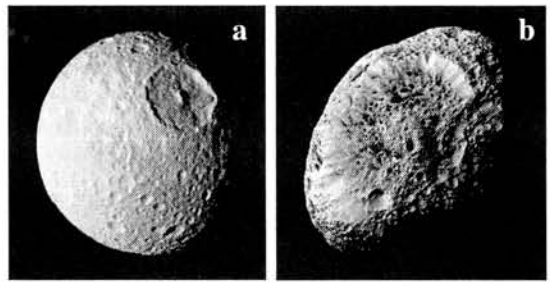

Fig. 3 A "normal" icy moon (**a:** Mimas) and a spongy icy body (**b:** Hyperion)

Summary

It is suggest that Saturn has two ring-systems of different origin. The dust ring system originates from the dust-loss of the low albedo inner moons and is stationary by dynamic equilibrium like all the other planetary rings. The temporary icy ring-system, according to Dones' suggestion [1], could have come into existence as a consequence of a rare peculiar event: by the tidal disruption of a giant cometary nucleus.

We suggest that the B+A icy ring started to break up at the very distance from Saturn, where the B ring is the brightest on the lit side, darkest and coldest on the unlit side. Here the disintegration and the spreading can continue even now, that is demonstrated by the non-uniform brightness of the B+A ring, by the non-uniform opacity, by the non-uniform dirtiness, and by the fact that the C ring contains mostly low albedo dust particles.

There where the disruption continues even now the ring can be many-particles-thick in contrast with the edges, where it can be a monolayer type. It may be possible that a single model can not describe the whole ring, neither in composition nor in layer type.

References

[1] Dones, L. (1991) *Icarus, 92*, 194-203. **[2]** Sicardy, B. (2005) *Space Sci. Rev., 116*, 457-470. **[3]** http://galileo.jpl.nasa.gov **[4]** Pilcher, C.B., Chapman, C.R., Lebofsky L.A., Kieffer, H.H. (1970): *Science, 167*, 1372-1373. **[5]** Goldstein, R.M., Morris, G.A. (1973) *Icarus, 20*, 260-262. **[6]** Goldstein, R.M., Green, R.R. (1977) *Icarus, 30*, 104-110. **[7]** Cuzzi, J.N., Pollack, J.B. (1978) *Icarus, 33*, 233-262. **[8]** Esposito, L.W., Cuzzi, J.N., Holberg, J.B., Marouf, E.A., Tyler, G.L., Porco, C.C. (1984) In: Saturn. pp. 463-589. Eds.: Gehrels, T., Matthews, M.S., Univ. of Arizona Press, Tucson, Arizona. **[9]** http://saturn.jpl.nasa.gov/home/index.cfm **[10]** Illés, E. (2005) *World of Nature* (*Természet Világa* in Hungarian) *136*, No.3. and 4. (March and April 2005), pp. 106-109. and 178-180. **[11]** Illés-Almár, E. (2005) Geophysical Research Abstracts, Vol.7, 05076, SRef-ID: 1607-7962/gra/EGU05-A-0507

On the Origin of the Dark Material on Iapetus

E. Illés-Almár Konkoly Observatory H-1525 Budapest P.O.B. 67, Hungary, e-mail: illes@konkoly.hu

Abstract

In this hypothesis paper it is suggested on the basis of the earlier Voyager and the recent Cassini images that the emplacement of the dark material to the surface of Iapetus happened by geyser-like activity. The thin coating was dark or darkened later by the ultraviolet light of the Sun.

Introduction

Iapetus is one of the most interesting and enigmatic bodies in the Solar System with its large quasi-hemispheric differences, as regards its surface albedo. As the density of Iapetus and the albedo of its bright trailing hemisphere is about the same as that of the other icy satellites of Saturn, and because there are dark-floored craters in the brighter area but no light-floored craters within the dark area [1], it was supposed that the dark leading hemisphere is the one where something has to have happened: dark material is superimposed on the bright terrain.

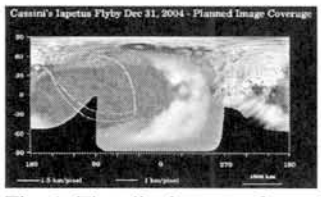

Fig. 1 The albedo map of Iapetus constructed on the basis of Voyager images.

Fig. 2 Dark side of Iapetus. Cassini photo.

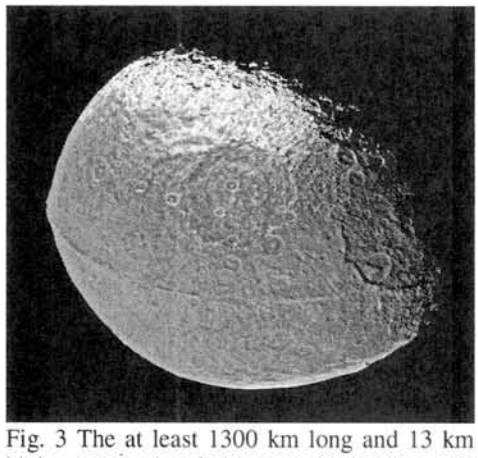

Fig. 3 The at least 1300 km long and 13 km high compressional ridge on the leading side of Iapetus. Cassini photo.

Two main types of mechanisms have been suggested so far to explain the presence of the dark material. 1.) It has been suggested, as external source, that impacting icy meteoroids stuck to the trailing hemisphere [2] or the dust left behind by Phoebe [3,4,5] or by Titan [6] impacted onto the leading hemisphere. The dark dust would have been swept up by the locked Iapetus. 2.) As an endogenous source, dark volcanic material would have been extruded [7].

On the basis of the Voyager images it was stated that the albedo contours of the dark material are roughly elliptical in shape (Fig.1), centred at the apex of orbital motion, flattened at the poles and elongated along the equator. The albedo is the smallest (0.04) in the interior parts of the leading hemisphere. The transition between the dark and bright material is rather gradual than sharp [8]. So some kind of volcanic activity seemed to be a more reliable mechanism. Wilson and Sagan [9], however, ruled out this possibility as improbable on the basis of the position of the elliptical albedo-contours of the dark material that would rather match impact flux contours [10].

Recent Earth-based radar and Cassini measurements

Recent Earth-based radar observations by Black et al. [11] from Arecibo demonstrated that at 13 cm radar wavelength the albedoes of the two sides of Iapetus do not differ from each other. This observational evidence hints at a very fine, thin surface layer upon the material underneath. So a thick volcanic flooding can be ruled out on the basis of this observation. This conclusion should not be changed on the basis of the Cassini radar measurements at 2,2 cm wavelength [12], in spite of the fact that the "albedo is dramatically higher on the trailing side than the leading side" as it requires only that "up to depth of at least several decimeters the water ice is significantly 'dirtier' on the leading side", as some decimeter is, however, a fine surface layer.

The Cassini images with their high resolution, taken on the Eve of 2004 (Fig.2, 3; [13]) on the leading hemisphere of Iapetus, show in detail that the boundary of the dark material is not only diffuse, but somewhere ceases in a "tongue"-like form (Fig.3). It really rules out the thick volcanic flooding explanation. On the basis of Fig.2 it is evident that the dark material is not filling up exactly the cross section that is, a total hemisphere, what would be expected if it would originate from outside (this was clear otherwise already on the basis of the Voyager 2 images), so we can rule out the external source as well.

Discussion

On the Cassini image PIA06166 (Fig.3) one can see an at least 1300 km long and 13 km high compressional ridge on the leading side of Iapetus. This ridge seems to be the consequence of a one-cell circulation of the mantle (the upwelling plume was/is on the bright side of the moon, and the downwelling sheet along the equator on the dark leading hemisphere where, because of the compression, the crust piles up into the ridge). I suppose that in the not too distant past, in connection with the compression a series of geysers (or volcanic plumes of low viscosity lava) could be active along the compressional ridge and could spray out a material that was dark or became dark later on the surface [14].

On the basis of the images taken by Cassini at the first close encounter of Iapetus it is not clear yet how long the compressional ridge really is. I suppose that the ridge is not encircling the moon and the compressional ridge and the dark material have about the same extent in longitude.

It is interesting that on Iapetus on the dark region of the northern hemisphere the poleward facing walls of the impact craters are bright in contrast with the equatorward facing walls. This observational fact favours the geyser like model and contradicts to the external source.

The brightness or darkness of the crater-walls, namely, could be explained by the incident angle of the trajectory of the fallen material. In the geyser like model in the case of the poleward facing walls this angle is flat, to the contrary to the equatorward facing walls, where the fallen dust particles arrive quasi perpendicularly in the midlatitudes.

There is another argument in favour of our suggestion supposing that Iapetus was/is a geologically active body. Among the circular features, there is one that with its triple "mottle" (Fig.4a) cannot be impact crater. It is more similar to the ones on Europa (for example Fig.4b, [15]).

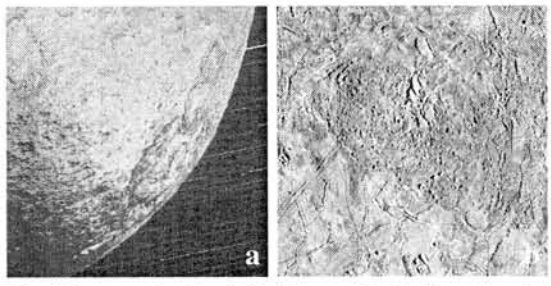

Fig. 4 Iapetus (**a**, Cassini), Europa (**b**, Galileo photo)

Observational analogies from outer Solar System

The above-mentioned suggestion, that geyser like activity or volcanic plume of low viscosity lava could have caused the creation of the dark material on Iapetus, is based on several observational facts from the outer Solar System (Fig.5, 6, 7).

Fig. 5 Triton with its geysers demonstrates how a surface darkens (there methane finds its way to the surface). Voyager 2 photo.

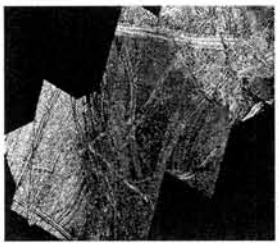

Fig. 6 With this image Europa demonstrates in detail how a thin surface layer appears. Galileo photo.

Fig. 7 An umbrella shape volcanic plume of low viscosity lava on Io. Voyager 1 photo.

As it was mentioned, on Iapetus the transition from the dark to the bright surface on the northern boundary is diffuse and tongue-like ([13], Fig.3). Very probably the "tongues" are showing the traces of the outbursts of separate, independent geysers, as they are clearly visible separately on Triton's polar cap (Fig.5). On Triton, namely, there are not too many geysers, therefore one can see separately all traces. Nevertheless, in the case of Iapetus numerous independent geysers might be in action – simultaneously or consecutively – so now their traces overlap each other. Therefore, they cannot be distinguished, except in some places at the edge of the dark-bright boundary.

Summary

As regards the earlier models of the strong quasi-hemispheric differences on Iapetus all external-source models can be ruled out on the basis that the dark material does not fill up the cross section, that is the total hemisphere (Fig.2). The thick volcanic flooding model can be ruled out on the basis of the radar observations and the diffuse boundary between the bright and dark material (Fig.3).

We suggest that the dark material on Iapetus' leading side is a young or revived thin coating that was placed by geyser like activity. A large number of geysers (or volcanic plumes of low viscosity lava) were/are working in connection with the compressional ridge along the equator on the leading side. If the compressional ridge along the equator really has about the same extent in longitude than the dark territory on Iapetus this observation will strengthen our hypothesis.

Acknowledgement The author is indebted to Mr. P. Decsy for the preparation of the paper.

References

[1] Morrison, D., Johnson, T.V., Shoemaker, E.M., Soderblom, .A., Thomas, P., Veverka, J., Smith, B.A. (1984) In: Saturn. Pp 609-116, 631-639. Eds.: Gehrels, T., Matthews, M.S. The Univ. Arizona Press, Tucson, Arizona. **[2]** Peterson, C. (1975) Icarus 24, 499-503. **[3]** Soter, S. (1974) Space Sci. Rev. 21. **[4]** Cruikshank, D.P., Bell, J.F., Gaffey, M.J., Brown, R.H., Howell, R., Beerman, C. Rognstad, M. (1983) Icarus 53, 90-104. **[5]** Bell, J.F., Cruikshank, D.P., Gaffey, M.J. (1985) Icarus 61, 192-207. **[6]** Owen, T.C., Cruikshank, D.P., Dalle Ore, C.M., Geballe, T.R., Roush, T.L., de Berdh, C., Meier, R., Pendleton, Y.J., Khare, B.N. (2001) Icarus 149, 160-172. **[7]** Smith B.A., Soderblom, L.A., Batson, R. et al. (1982) Science 215, 504-537. **[8]** Squyres, S.W., Buratti, B., Veverka, J., Sagan, C. (1984) Icarus 59, 426-435. **[9]** Wilson, P.D., Sagan, C. (1996) Icarus 122, 92-106. **[10]** Squyres, S.W., Sagan, C. (1983) Nature 303, 782-785. **[11]** Black, G.J., Campbell, D.B., Carter, L.M., Ostro, S.J. (2004) Science 304, 553. **[12]** Ostro, S.J., West, R.D., Janssen M.A., et al. (2005) AGU 2005 P22A-01. **[13]** http://saturn.jpl.nasa.gov/home/index.cfm. **[14]** Illés-Almár, E. (12005) Geophysical Research Abstracts, Vol.7, 05055, SRef-ID: 1607-7962/gra/EGU05-A-05055. **[15]** http://galileo.jpl.nasa.gov/

Crystallization of nakhlite melts in comparison with synthetic experiments. N. Imae[1] and Y. Ikeda[2], [1]Antarctic Meteorite Research Center, National Institute of Polar Research, 9-10, Kaga 1-chome, Itabashi-ku, Tokyo 173-8515, Japan (imae@nipr.ac.jp), [2]Department of Material and Biological Sciences, Ibaraki University, Mito 310-8512, Japan.

Introduction:

Nakhlite is an unmetamorphosed igneous meteorite, classified into cumulated clinopyroxenites. So far, seven nakhlites have been recovered in the world. We have been petrologically studying two Antarctic nakhlites, the Yamato nakhlites and the MIL 03346 nakhlite, and have estimated each parental melt composition based on the mass balance calculation [1,2]. In the study, we examine these nakhlites in view of the crystallization from intercumulus melts toward mesostasis, and we compare synthetic experimental results with these crystallization sequences.

Crystallization of intercumulus melts for the Yamato nakhlites and the MIL 03346 nakhlite:

The Yamato nakhlites (Fig. 1a): The modal volume fractions of the intercumulus melt and cumulus phases are 0.3 and 0.7, respectively. $Fa_{\sim 80}$ (0.03 in mode), inner rim augite (0.15), and outer rim Ca-poorer pyroxenes (0.01) grew from the intercumulus melt. Mesostasis mostly consists of plagioclase (0.11). The mesostasis composition was estimated from the interstitial melt and is consistent with averaged composition of mesostasis analyzed by EPMA (Fig. 1a).

The MIL 03346 nakhlite (Fig. 1b): The modal volume fractions of the intercumulus melt and cumulus core augites are 0.435 and 0.565, respectively. The modal fractions of phases in a polished thin section did not produce the mesostasis by the mass balance calculation of the intercumulus melt. Instead, the calculation suggests that Fa_{55} (0.035 in mode), inner rim augite (0.112), skeletal Fa_{93} (0.022), titanomagnetite (0.013), and outer hedenburgitic rim (0.087) grew from the intercumulus melt to produce the glassy mesostasis (0.166) (Fig. 1b).

Synthetic experiments:

We prepared two kinds of glasses (gl-1 and gl-5) as starting experimental materials (Table 1). The gl-1 and gl-5 are similar to the intercumulus melt for Nakhla [3] and for the Yamato nakhlites [2], respectively.

Isothermal experiments: Liquidus temperatures for nakhlite melts of gl-1 and gl-5 are 1140-1150 °C, at which augites co-crystallize with titanomagnetites (gl-1) or chromian magnetite (gl-5). Augite in gl-1 has the composition of $En_{44.1}Fs_{17.7}Wo_{38.2}$, which is more magnesian than that of core augites ($En_{36-39}Fs_{21-25}Wo_{39-40}$) in nakhlites. Augite in gl-5 has the composition of $En_{37.2}Fs_{24.4}Wo_{38.4}$ (Table 1), which is nearly identical with that of core augites in nakhlites.

Cooling experiments: The cooling condition was 4.2 °C/h from 1240 to 890 °C under the ~QFM buffer at 1 bar using gl-1 and gl-5. Core augite compositions obtained from the runs using gl-1 is $En_{40}Fs_{20}Wo_{40}$ which is nearly similar to those of core augites in nakhlites. On the other hand, the composition of core augites obtained by a cooling experiment of 4.2 °C/h from 1250 °C to 1000 °C under the ~QFM, at 1 bar for gl-5 is $En_{38.4}Fs_{28.6}Wo_{33.0}$, whose composition is somewhat more ferroan than those of core augites in nakhlites.

The composition of core augites by the cooling experiment is inconsistent with core composition of augites obtained by isothermal experiments. The delay of the nucleation during the supercooling of melt seems to result in more ferroan compositions of core augites by the cooling experiments than the most magnesian augites by isothermal experiments. Rim augites in a run (IMC-8) with gl-1 are divided into two: ferroan inner rim and hedenburgitic outer rim, which are also similar to MIL 03346 (Fig. 2). Dendritic fayalitic olivines ($Fa_{\sim 83}$) and dendritic titanomagnetites in mesostasis crystallize in the run, and they are similar to those in MIL 03346. Plagioclases crystallize in mesostasis of this run, although no plagioclase occurs in MIL 03346. The run product is very similar to the MIL 03346 nakhlite in texture except plagioclase crystallization (Fig. 3). However, the grain size of the run (~100 μm) is smaller than that of MIL 03346 (≥~400 μm) (Fig. 3).

Slow cooling experiments of 1 °C/h from 1250 °C to 1000 °C under the ~ QFM at 1 bar for gl-1 form the outer rim of low Ca pyroxenes on ferroan inner rim, and plagioclase crystallizes in mesostasis of this run. This texture obtained under this condition is similar to that of the Yamato nakhlites.

Discussions:

The textural similarity between a run (IMC-8) and MIL 03346 may suggest their similar physico-chemical conditions. The series of experiments suggest that (A) the inner rim and the hedenburgitic outer rim observed in MIL 03346 would have formed by the crystallization under a rapid cooling condition, and (B) the crystallization of plagioclase precedes the formation of the outer rim of Ca-poor pyroxene at the slower cooling, which is observed in the Yamato nakhlites.

Different crystallization trends for the two nakhlites were therefore derived by experiments using the different cooling rates. The experiments may suggest that the MIL 03346 crystallized at ~4

°C/h and the Yamato nakhlites cooled at ~1 °C/h.

References:

[1] Imae N. et al. 2005. MAPS 40, 1581-1598. [2] Imae N. and Ikeda Y. 2005. MAPS 40, A72. [3] Harvey R. P and McSween H. Y. J. 1992. EPSL 111, 467-482.

Table 1. Compositions of two starting glasses of gl-1 and gl-5 and the intercumulus melt for the Yamato nakhlites (YIM), respectively. Chemical composition of augites crystallized from the isothermal run in gl-5, core augite of the Yamato nakhlites, and core augite of MIL 03346, respectively.

	gl-1	gl-5	YIM	Aug (gl-5)	Core augite (Y)	Core augite (MIL)
SiO_2	46.90	47.02	47.93	51.40	51.40	52.05
TiO_2	2.07	0.15	0.16	0.05	0.25	0.27
Al_2O_3	8.15	4.67	5.05	1.20	0.85	0.96
FeO	22.09	28.53	26.44	15.00	15.03	14.04
MgO	6.03	5.22	4.95	12.80	12.39	12.66
CaO	10.57	11.71	11.42	18.40	18.63	19.13
Na_2O	1.70	1.84	1.82	0.29	0.23	0.28
K_2O	1.31	0.49	0.58	0.01	0.01	0.01
P_2O_5	-	0.26	0.65	0.04	0.04	0.02
Cr_2O_3	-	0.10	0.19	0.33	0.33	0.22
Total	98.82	99.99	99.19	99.52	99.16	99.64

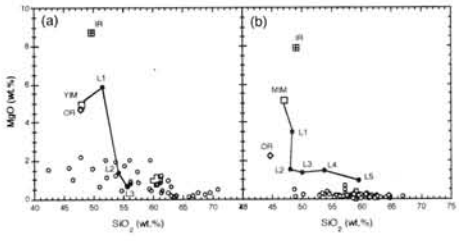

Fig. 1 (a) A SiO_2-MgO diagram for the Yamato nakhlites. Small open circle: mesostasis. Open cross: averaged mesostasis. (b) A SiO_2-MgO diagram for MIL 03346. IR: inner rim. OR: outer rim. MIM: the intercumulus melt for MIL 03346. Small open circle: glassy mesostasis. Open cross: averaged glassy mesostasis.

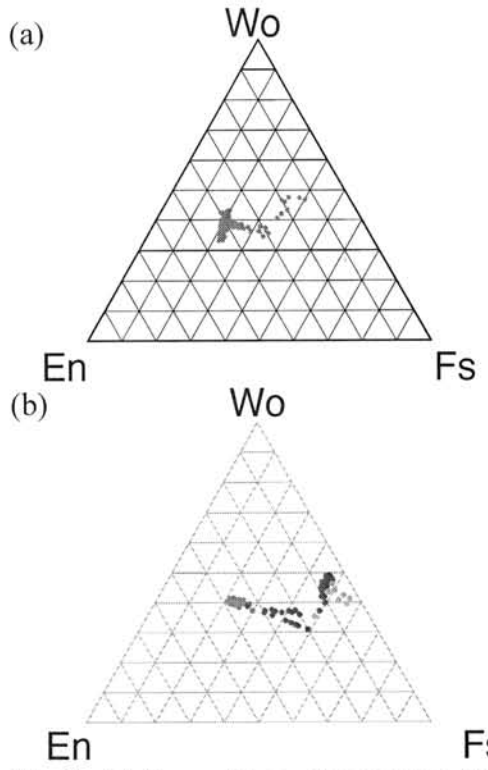

Fig. 2. (a) Compositions of pyroxenes for the run product (IMC-8) from the cooling experiment (4.2 °C/h) using gl-1. (b) Pyroxenes for MIL 03346. Red: Core augites. Black: Inner rim. Blue: Outer rim. Green: Mesostasis.

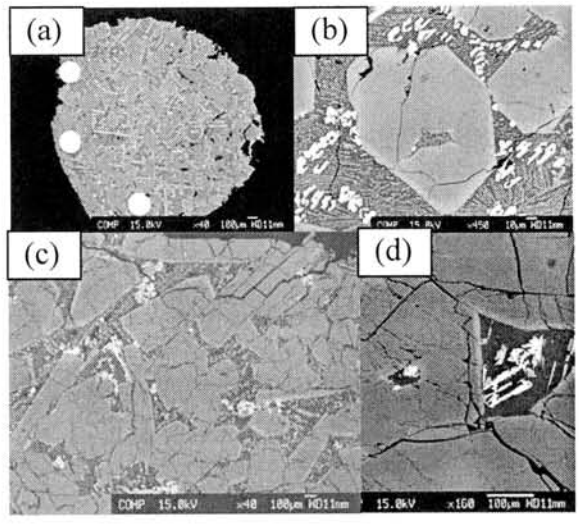

Fig. 3(a) Run product (Run number: IMC-8). (b) A close up view of IMC-8. (c) and (d) MIL 03346.

A Possible AD552 Comet Sighting In Japan And Its Parallels With Phenomena Associated With The Sarasvati River Of Ancient India. Robert A. Juhl[1], RN Iyengar[2], [1]Independent researcher, Penang, Malaysia, [2]Department of Civil Engineering, Indian Institute of Science.

Introduction:

The *Enoshima Engi* (江嶋縁起: EE) was written in AD1047 by the Japanese monk Kokei. The narrative mentions spectacular phenomena that took place in the early summer of AD552, including dark clouds covering the sea, earthquakes, the appearance of a bright goddess (Benzaiten/Sarasvati) above the clouds, boulders falling from the sky, lightning-bolts, rocks and sand spurting up from the sea, flames on the water, the emergence of an island, and the descent of the goddess onto the island. Juhl translated and studied parts of the EE in 2003 [1].

The Prabhasa-ksetra-mahatmya book (PK) of the Skanda-purana, which was compiled earlier than the 9th century AD, contains scattered references to similar phenomena associated with the Sarasvati River. In 2004 Iyengar published an article on comet-related phenomena in the PK [2].

Discussion:

Following is a list of possible comet-related parallels scattered through the PK. All parallels with the EE are from Juhl's translation [1].

The PK mentions objects making holes in the ground in association with a smoky demon [3]. The EE parallel is the "dark clouds covering the sea" and "great boulders descending from above the clouds".

In one episode, the Sarasvati River, carrying fire, enters the ocean. Iyengar translates: "With fire in his hand, the ocean lit up... Due to the gases emanating from the sea, the waters overflowed..." [4] The EE parallel is the description "flames flickered amidst the white-tipped waves".

The level of the sea apparently rose and dropped. Iyengar writes: "... after the fire started burning, initially the sea exceeded in its boundaries but later the coast started receding... In the 346th chapter, there is reference to large-scale loss of life associated most probably with a ... tsunami" [5]. The EE parallel is the loss of life as the dragon (the floodwaters) invaded the villages.

The PK has a chapter entitled Sarasvati-avatara-mahima-varnanam, meaning "description of the purpose of the avatara (descent) of Sarasvati" [6]. The EE parallel is the descent of Benzaiten from the sky.

Iyengar comments on a related story: "The further verses indicate that a metallic object eventually landed on earth, leading to earthquakes..." [7]. The EE parallel is the earthquakes before the descent of the goddess.

In a separate paper, Iyengar translates a reference to a comet adorned with an ornament: "Broomstick mega-comet with hibiscus flowers as his ear ornament .... " [8] The EE parallel is the description of the goddess descending "adorned with a long jade pendant."

Conclusions:

Most of the phenomena described in the EE are similar to phenomena scattered through the PK. However, they are not copies, only similar. Kokei most likely used ancient Japanese documents as his sources for the EE. The Indian parallels merely confirmed to him that the goddess who descended at Enoshima was Benzaiten (the Japanese counterpart of Sarasvati). A fuller account of the parallels is on the Internet [9]. The presence of such close parallels between phenomena described in unrelated Indian and Japanese documents suggests that the phenomena actually did take place substantially as described. The phenomena may be comet/meteor related and deserve further investigation.

References:

[1] Juhl, 2003. http://www2.gol.com/users/terukoj/TranslationSeg-2.html and http://www2.gol.com/users/bartraj/goddessindex-1.html. [2] RN Iyengar. Profile of a Natural Disaster in Ancient Sanskrit Literature, *Indian Journal of History of Science*, 39, 1, 11-49, 2004, available as pdf at http://civil.iisc.ernet.in/~rni/ancientdisaster.pdf. [3] Iyengar. 2004, pg 7. [4] Iyengar. 2004, pg 11. [5] Iyengar. 2004, pgs 11 and 16. [6] Iyengar. 2004, pg 22. [7] Iyengar. 2004, pg 22. [8] RN Iyengar. Some Celestial Observations Associated With Krishna-Lore, pg. 6 (accepted for publication in *Indian J of History of Science), INSA, N. Delhi*, available as pdf at http://civil.iisc.ernet.in/~rni/krishnalore.pdf. [9] Juhl. *Parallels between the Celestial and Terrestrial Phenomena at Enoshima and Similar Phenomena Associated with the Sarasvati River of Ancient India*, http://www2.gol.com/users/bartraj/ParallelsWSarasvatiR.html

Heterogeneous distribution of high-pressure minerals in the Gujba CB chondrite. M. Kimura[1], M. K. Weisberg[2,3], A. Suzuki[4], E. Ohtani[4] and N. Sugiura[5] [1]Faculty of Science, Ibaraki University, Mito 310-8512, Japan, makotoki@mx.ibaraki.ac.jp, [2]Department of Physical Sciences, Kingsborough College And Graduate Center of the City University of New York, Brooklyn, NY 11235, [3]Department of Earth and Planetary Sciences, American Museum of Natural History, New York, NY10024, USA, [4]Institute of Mineralogy, Petrology and Economic Geology, Tohoku University, Sendai 980-8578, Japan, [5]Department of Earth and Planetary Science, Univ. of Tokyo, Japan.

Introduction:

The CB chondrites are unusual carbonaceous chondrites. Their characteristic features have been summarized [1] and include: (1) high metal abundances (60-80 vol.% metal), (2) most chondrules have cryptocrystalline or barred textures, (3) moderately volatile lithophile elements are highly depleted, and (4) nitrogen is enriched in the heavy isotope. The CB chondrites have been interpreted to be primitive nebular materials containing metal that condensed directly from the nebular gas [1-4]. Others have contended that they formed in a vapor cloud produced during a shock event [5, 6]. Recent ^{207}Pb-^{206}Pb dating of chondrules in the Gujba CB chondrite show formation ages younger than those in other chondrites [7]. Although it seems to be consistent with shock models for formation of the chondrules [7], the CB parent body experienced an extensive post accretion shock history that has obscured some of its primary character.

Using a combination of petrology and Raman spectroscopy, we have been studying high-pressure minerals in the Gujba chondrite. We preliminarily reported our finding of some high-pressure minerals, such as majorite and wadsleyite in Gujba [8, 9]. Here we report results of our discovery of two more high-pressure minerals in Gujba. Our goal is to explore the thermal - shock history of the CB chondrites and their parent body.

Results:

The Gujba chondrite consists of large round and irregular-shaped metal, chondrules and chondrule fragments, surrounded by finer-grained brecciated areas interspersed with melt. Its petrographic characteristics are fairly typical of CBa chondrites [1], with the exception of containing some chondrules that are complete spheres. Most silicate chondrules and fragments are barred olivine in texture and some are cryptocrystalline. Barred chondrules consist of olivine bars with low-Ca pyroxene and/or Ca-pyroxene, in some cases MgAl spinel, and an interstitial phase with a feldspathic composition.

We studied areas that are interstitial to the large metal and silicate chondrules in Gujba. The areas consist of small (10μm to 1mm) barred olivine fragments, surrounded by a fine (sub-micrometer) matrix. The matrix is dominated by silicate phases and dotted with tiny (2-30μm-size) blebs of FeNi metal.

Raman Spectra were collected from points in fragments and matrix in the areas described above. The Raman spectra show that the barred fragments and matrix in these regions have various combinations of majorite-pyrope garnet and wadsleyite, as well as olivine and low-Ca pyroxene. In addition, some grains of SiO_2 are present in the matrix (Fig. 1a), and they are coesite or coesite-quartz associations (Fig. 1b). These silica phases are surrounded by fine-grained olivine and low-Ca pyroxene. We also discovered Ca-rich garnet in a barred olivine fragment (Fig. 2a), in association with olivine and small amount of spinel. This garnet is present among olivine bars. Raman spectrum indicates that this is not majorite, but grossular-pyrope garnet (Fig. 2b). Our preliminary microprobe data are consistent with this identification. Such garnet is also encountered as a fine fragment in the matrix.

Discussion:

We previously reported majorite-pyrope garnet and wadsleyite in the matrix and in barred olivine fragments in Gujba [8, 9]. These minerals have been already reported in ordinary chondrites [e.g., 10-12]. However, our discovery was the first report of high-pressure minerals in a carbonaceous chondrite. The occurrence of grossular-pyrope garnet indicates that it was formed from Ca-rich mesostasis among olivine laths in the barred fragment under high pressure and temperature conditions. Coesite has been found in tektites and terrestrial craters [e.g., 13, 14]. We now report coesite in the matrix of Gujba. This is the first discovery of coesite in a meteorite. Coesite and quartz are present with Mg-rich olivine ($\sim Fo_{77}$) in the matrix, which suggests that such disequilibrated assemblages survived shock metamorphism. Although silica minerals have not yet been discovered in Gujba chondrules, it was reported in a chondrule from the Isheyevo CB/CH chondrite [15]. Coesite or quartz grains discovered here may be fragments from such silica-bearing chondrules.

The assemblage of coesite and quartz might have resulted from the back-transformation of higher-pressure silica polymorphs. In ordinary chondrites, such back-transformation was observed [15]. However, the transformation from coesite to quartz should take a much longer time than that from silicate spinel to olivine [16, 17]. If quartz formed

from coesite, we would not expect the occurrence of wadsleyite in Gujba, inconsistent with our observation. Therefore, it is probable that quartz is a relic phase, which survived shock metamorphism.

The high-pressure phases observed in Gujba record a wide range of pressure conditions; Wadsleyite and majorite should have formed under higher pressure conditions than coesite [18]. Additionally, within Gujba, the occurrence of high-pressure phases is variable from one area to another, on the scale of millimeters or less. These observations suggest heterogeneous distribution of pressures due to the shock event.

Heavy shock event(s) suggest that resetting of chondrule ages due to loss of Pb is a possibility and formation ages of the CB chondrules may be difficult to obtain. All CB chondrites contain shock melt areas throughout, suggesting a planetesimal wide collision. Based on the presence of similar shock melt textures in all of the CB chondrites, we predict that high-pressure minerals are present in all of them.

References: [1] Weisberg M. K. et al. (2001) MAPS, 36, 401-418. [2] Weisberg M. K. et al. (1990) Meteoritics, 25, 269-279. [4] Krot A. E. et al. (2002) MAPS, 37, 1451-1490. [5] Kallemeyn G. W. et al. (1978) GCA, 42, 507-515. [6] Campbell A. J. et al. (2002) GCA, 66, 647-660. [7] Krot A. E. et al. (2005) Nature 436, 989-992. [8] Weisberg M. K. and Kimura M. (2004) LPSC XXXV, #1599. [9] Weisberg M.K. et al. (2006) LPSC XXXVII, #1788. [10] Smith J. V. and Mason B. (1970) Science, 168, 832-833. [11] Chen M. et al. (1996) Science, 271, 1570-1573. [12] Kimura M. et al. (2003) EPSL, 217, 141-150. [13] Stöffler D. (1971) JGR, 76, 5474-5488. [14] Stöffler D. and Langenhorst F. (1994) Meteoritics 29, 155-181. [15] Krot A.E. et al. (2006) LPSC XXXVII, #1224. [16] Perrillat J. P. et al. (2003) J. Petrol., 44, 773-788. [17] Ming L. C. et al. (1991) Pys. Chem. Minerals., 18, 171-179. [18] Presnall D. C. (1995) in Mineral Physics & Crystallography.

Figure 1. (a) BEI of fine-grained matrix in Gujba including an assemblage of silica minerals. (b) Raman spectrum of the assemblage showing the intimate association of coesite and quartz.

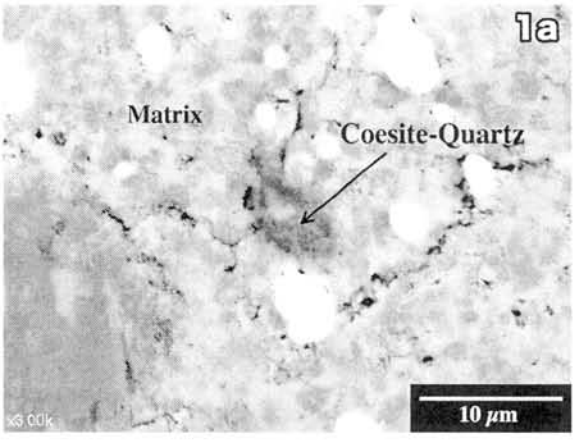

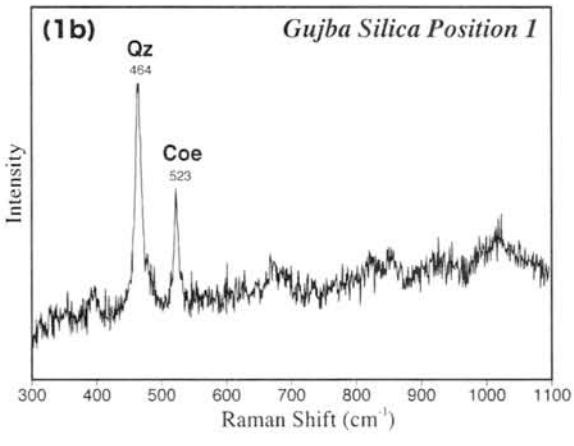

Figure 2. (a) A part of a barred olivine fragment in Gujba consisting of olivine bars and interstitial garnet with spinel. (b) Raman spectrum of the garnet, showing a solid solution mainly of grossular and pyrope.

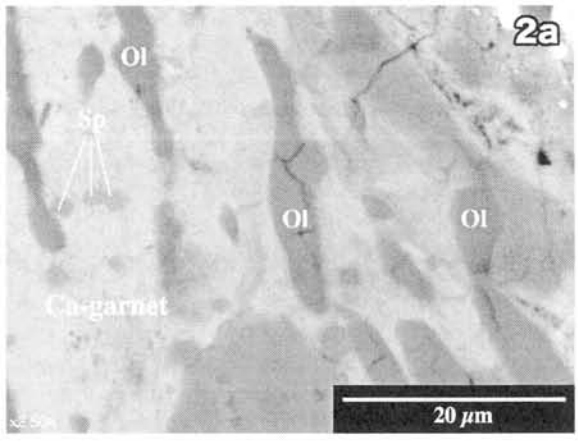

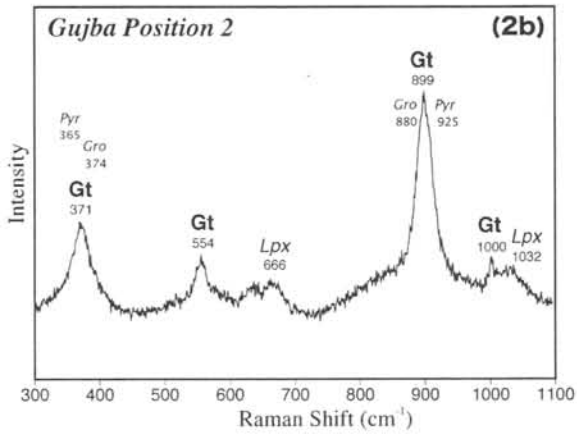

Possible terrestrial weathering effects on platinum group element abundances in Antarctic carbonaceous chondrites. Y. Koiwa* and M. Ebihara, Department of Chemistry, Tokyo Metropolitan University, Hachioji, Tokyo 192-0397 (koiwa-yositaka@ed.tmu.ac.jp).

Introduction:

Among elements, platinum group elements (PGEs) play an important role in studying geochemical and cosmochemical processes because of their refractory and siderophile natures. Recently, it was recognized that PGE abundances in carbonaceous chondrites showed systematic variations among CI, CM, CO, CV and CK [1, 2, 3].

In considering bulk chemical compositions of Antarctic and non-Antarctic finds, it is essential to evaluate the effect of terrestrial weathering on their elemental abundances. A typical effect of the terrestrial weathering on chemical compositions of Antarctic meteorites is an overabundance of halogens (e.g. Cl and I), which are suggested to be caused by airborne sea mist [4, 5]. It is also well acknowledged that both Antarctic and non-Antarctic finds have a large variation of Na concentrations mostly with Na depletion, which must be caused by selective leaching of alkaline elements in chondrites. The effect of terrestrial weathering on PGE abundances, however, isn't well understood yet.

Two classification schemes for specify the degree of terrestrial weathering are applied to meteorite finds [e.g. 6, 7]. These weathering classifications mainly depend on degrees of oxidization of metal and/or sulfide and alteration of silicates. But it isn't clear whether these classifications correlate with bulk chemical compositions.

In case of PGEs, it is unlikely that the terrestrial weathering increases PGE abundances because the earth crust has extremely low PGE concentrations. In addition, PGEs are thought to be the least mobile elements in the environments on the earth. Therefore, it seems to be highly probable that PGEs in meteorite hold their indigenous PGE abundances even for finds.

In this study, we aimed to make clear whether there is any effect of the terrestrial weathering on PGE abundances in carbonaceous chondrite finds. As there appeared some such effects, we considered how such effects are characterized and further whether weather-induced variations of PGE abundances correlate with those of other elemental abundances.

Samples and Analytical technique:

We have analyzed 14 Antarctic carbonaceous chondrites (CM, CO, CV and CK). In addition, 3 finds and 15 falls of non-Antarctic carbonaceous chondrites were analyzed. Some of PGE data have been already presented by [3]. Sample names and their classifications (with weathering categories) are shown below.

·*Antarctic finds*

CM2: LEW90500 (B), PCA91008 (B), Y791198 and Y793321; CO3: Y791717, Y81020 and Y82094; CV3: Y86751; CK4-6: ALHA85002 (A), EET87507 (B), EET87860 (A/B), EET99430 (C), LEW86258 (B) and LEW87009 (Ae).

·*non-Antarctic finds*

CO3: Colony; CV3: Leoville; CK4-an: Maralinga.

·*falls*

CM2: Boriskino, Cold bokkeveld, Erakot, Murchison, Murray and Nogoya; CO3: Lancé, Ornans and Warrenton; CV3: Allende, Grosnaja, Mokoia and Vigarano; CK4: Karoonda and Kobe.

For PGE analyses, each sample in chunk was ground to powder in a clean agate mortar, and about 10mg of each powdered sample was used. All PGEs were simultaneously determined by ICP-MS after NiS fire-assay pre-concentration. Isotope dilution was applied to PGE except Rh, which was determined by calibration method with yield correction [8].

Bulk chemical composition of each sample was determined by using neutron-induced prompt gamma ray analysis (PGA).

Results and discussion:

PGE data of CM, CO, CV and CK groups are shown in Fig. 1a~d, respectively, where PGE/Ir ratios are normalized to individual average values of falls. Obviously, finds show notable depletions of Os, Pt and Pd, and various combinations of depleted elements appear among finds. In the comparisons with data for falls, Antarctic CM and CO seem to hold indigenous PGE abundances while Antarctic CK seems to have low PGE abundances.

On weathering of PGEs host phases, it is likely for PGEs to be eluviated with host phase components. In ordinary chondrites, PGEs are mostly concentrated in metal phases (e.g. taenite, martensite and kamacite), with PGEs and other siderophiles being distributed differently among these metal phases [9]. If such metal phases were weathered by different degrees, bulk PGEs abundance patterns would be modified. Carbonaceous chondrites (except CR, CB and CH) have either little or no metal contents, and PGEs host phases in such carbonaceous chondrites aren't well known. Elementally specific PGEs depletions shown in Fig. 1 imply that PGEs are distributed differently among PGEs host phases.

Colony is one of the most extensively studied carbonaceous chondrite finds, possibly because it is the least metamorphosed and badly weathered CO chondrite [10]. In this work, it was observed that

PGE abundances in Colony have distinct depletions of Os, Pt, Rh and Pd (Fig. 1b). It was reported for Colony that lithophiles (Mg and Mn), siderophiles (Ni and Co) and chalcophiles (Se and Zn) are all depleted by factors of 10-40% [11]. Although large depletions of PGEs must be explained by weathering of their host phases, there seems to clear correlation in abundance variations between PGE and other elements.

References:

[1] Jochum K. P. (1996) *GCA, 60*, 3353-3357. [2] Horan M. F. et al. (2003) *Chem. Geol., 196*, 5-20. [3] Koiwa Y. et al. (2006) *LPS XXXVII*, abstract #1928. [4] Langenauer M., Krähenbühl U. (1993) *Earth Planet. Sci. Lett., 120*, 431-442. [5] Oura Y. et al. (2004) *Antarct. Meteorite Res., 17*, 172-184. [6] Grossman J. N. (1994) *Meteoritics, 29*, 100-143. [7] Wlotzka F. (1993) *Meteoritics, 28*, 460. [8] Shirai N. et al. (2003) *Geochem. J., 37*, 531-536. [9] Kong P. et al. (1995) *Earth Planet. Sci. Lett., 136*, 407-419. [10] Noguchi T. et al. (1999) *Antarct. Meteorite Res., 12*, 36-56. [11] Rubin A. E. et al. (1985) *Meteoritics, 20*, 175-196.

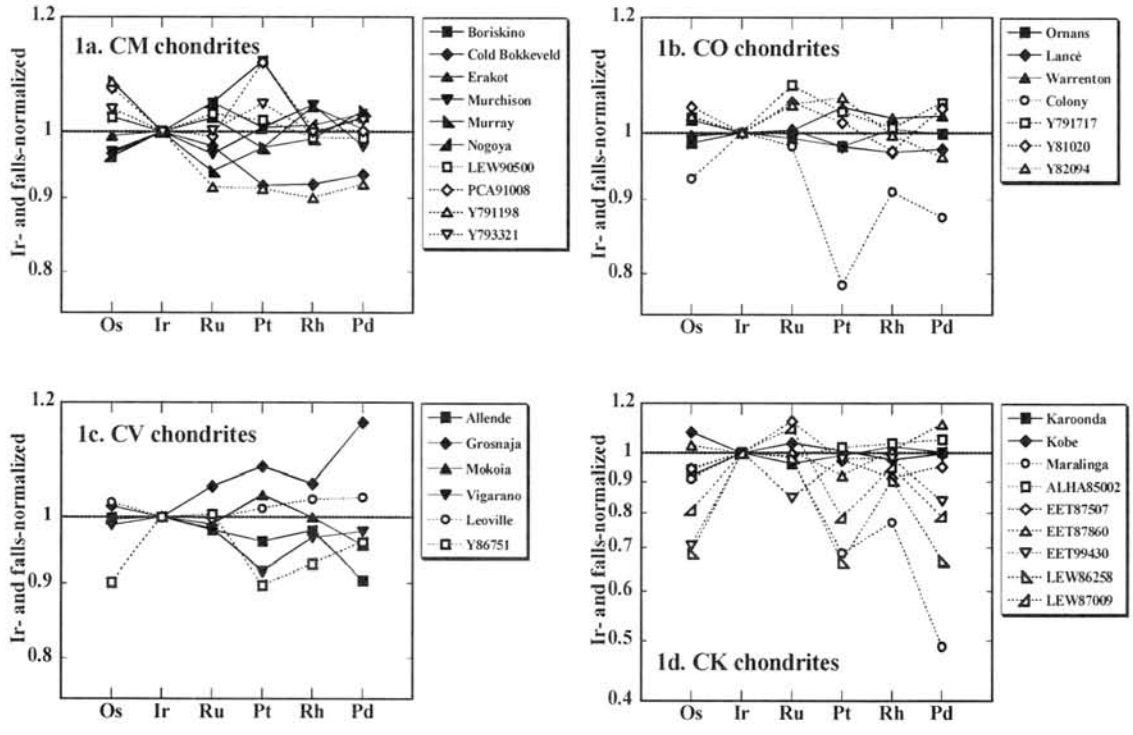

Fig. 1a~d Ir- and falls-normalized PGEs abundance patterns
Antarctic finds: open polygons; non-Antarctic finds: open circles; falls: closed polygons.

Mineralogy and petrography of the oxidized CV chondrite Yamato 86009. M. Komatsu[1], A. N. Krot[2], T. Fagan[3], M. Miyamoto[1], T. Mikouchi[1], and K. Keil[2], [1]Department of Earth & Planetary Science, University of Tokyo, Japan (mutsumi@um.u-tokyo.ac.jp), [2]Hawaii Institute of Geophysics and Planetology, University of Hawaii at Manoa, USA, [3]Department of Earth Sciences, School of Education, Waseda University, 1-6-1 Nishiwaseda Shinjuku-ku Tokyo, Japan.

Introduction: The CV chondrites are subdivided into the oxidized Allende-like (CV_{oxA}), oxidized Bali-like (CV_{oxB}), and reduced (CV_{red}) subgroups [1]. In both oxidized subgroups, common secondary minerals in chondrules, CAIs, and matrices include magnetite, Ni-rich metal, Fe,Ni-sulfides, Ca,Fe-rich pyroxenes, and andradite. Phyllosilicates and fayalite ($Fa_{>90}$) are common in the CV_{oxB} (e.g., Bali, Kaba, Mokoia), whereas secondary fayalitic olivine (Fa_{30-50}), nepheline, and sodalite are observed largely in the CV_{oxA} (e.g., Allende, ALH84028) [2,3]. Secondary minerals in the CV_{red} chondrites Efremovka and Leoville are similar to those in the CV_{oxA}, but much less abundant.

It has been previously suggested that the major chemical and mineralogical differences between the CV subgroups largely reflect their complex alteration [4]. In order to understand the alteration history of the CV chondrites, we performed mineralogical studies of the Yamato 86009 CV3 carbonaceous chondrite.

Analytical methods: Two polished thin sections of Yamato-86009, 51-1 and 51-2 were studied by optical microscopy and in the BSE mode with Hitachi S-4500 and JEOL 5900LV scanning electron microscopes. Chemical analyses and X-ray maps were obtained using JEOL JCM-733, JX-8900, and Cameca-SX50 electron microprobes.

Results: Y-86009 consists of chondrules (53 vol%), AOAs (2 vol%), Ca-Al-rich inclusions (1 vol%) and fine-grained matrix (43 vol%) with isolated mineral fragments (1 vol%).

Chondrules: Chondrules in Y-86009 cover various textural types (porphyritic, barred and cryptocrystalline), size ranges (50 μm–1.1 mm), and shapes (spherical and fragmental). Type I chondrules in Y-86009 consist of magnesian olivine ($Fo_{>90}$) and low-Ca pyroxene phenocrysts, opaque nodules and glassy mesostasis with or without high-Ca pyroxene. Most of anorthite-normative mesostasis is partly replaced by Al-bearing phyllosilicates, nepheline and sodalite. The opaque nodules consist of Fe-Ni-sulfides and magnetite extensively replaced by ferrous ($Fa_{>70}$) olivine and, occasionally, Ca-Fe-rich pyroxenes. Fayalite grains in the outer portion of chondrules show inverse compositional zoning zoning (Fig. 1a). Occasionally, fine-grained rims around Type I chondrules are crosscut by fayalite-magnetite-sulfide veins, which typically start at the opque nodules and extend into the Y-86009 matrix (Fig. 1b).

AOAs: AOAs are irregularly-shaped objects, 50-750 μm in size, composed of anhedral, fine-grained (1-20 μm) olivines and refractory, Ca-Al-rich nodules. The degree of alteration varies between individual AOAs. Lightly-altered AOAs (Fig. 2) consist of nearly pure forsterite ($Fo_{>98}$), high-Ca pyroxene, anorthite ± spinel (FeO < 1 wt.%). Anorthite is partly replaced by phyllosilicates (Fig. 2), but it is much less common than in heavily-altered AOAs. In some cases, enstatite (Wo_5En_{94}) is present around the metal-magnetite nodules. Lightly-altered AOAs are texturally similar to AOAs in Y-81020 (CO3.0), except having phyllosilicates and magnetite. Representative analyses of primary minerals of AOAs from Y-86009 are listed in Table 1.

Heavily-altered AOAs have porous textures, and are mainly composed of fine-grained forsteritic olivine (Fo_{96-99}) and Al-diopside (Fig. 4). They typically show enrichment in FeO along the cracks and grain boundaries. Anorthite is rare and largely replaced by fine-grained Mg-Al-silicates, which although are too small to be analyzed by EPMA, appear to be similar in BSE images to phyllosilicates described in CAIs from Mokoia [5], Bali and Kaba [6]. The anhderal grains of Ca-Fe-rich pyroxene (hedenbergite?) occur along grain boundaries. Euhedral fayalitic olivine grains (Fa_{63-71}) overgrow forsterite. Hedenbergite and fayalite are occasionally observed in direct contact with phyllosilicates. Occasionally, fayalite grains are rather coarse and show inverse compositional zoning (Fig. 3b). Some forsterite grains are overgrown by euhedral pyroxene ($Wo_{41}En_{56}Fs_3$, <10 μm in size) along the rim of AOAs. This type of pyroxene has higher content of MnO and Cr_2O_3 (~1.9 wt%) than Al-diopside associated with spinel in the interior of the AOA.

CAIs: Most CAIs are porous and consist of spinel (FeO < 1 wt%) and Al-diopside. Melilite and anorthite are probably replaced by Al-phyllosilicates.

Matrices: Matrix is dominated by platy, lath-shaped and irregular-shaped fayalitic olivine crystals (1-5 μm, Fa_{30-50}). The grain sizes of matrix olivine are larger than those in CV_{oxB}, but much smaller than those in CV_{oxA}. Some irregularly-shaped fayalitic olivines in the matrix show normal Mg-Fe zoning (Mg-rich core and Fe-rich rim) which is also observed in the Allende matrix. Texturally, the matrix appears to be intermediate between CV_{red}, CV_{oxA} and CV_{oxB} [7].

Discussion: Based on our observations, we infer that Y-86009 experienced hydrous alteration that resulted in formation of secondary phyllosilicates, magnetite, Fe-Ni-sulfides, fayalite, Ca-Fe-rich pyroxenes, and andradite These alteration features are similar to those in the CV_{oxB} chondrites Bali and Mokoia [9]. However, there are some important mineralogical differences as well. The common presence of anorthite in AOAs and rarity of Fa_{100} implies that the degree of aqueous alteration is lower than other CV_{oxB} chondrites. In addition, secondary fayalite in Kaba is rarely shows inverse compositionally zoning and approaches nearly pure fayalite. The presence of nepheline, sodalite and lath-shaped fayalitic olivine in matrix implies that Y-86009 also experienced higher temperature, and possibly more prolonged aqueous alteration than Kaba. We infer that Y-86009, like MET00430 [7], is intermediate between CV_{oxA} and CV_{oxB}. Indeed, inverse chemical zoning of the individual ferrous olivines are similar to those in MET00430 [7], suggesting the dissolution of ferrous olivine and precipitation of more forsteritic olivine from a fluid phase during the late-stage thermal

metamorphism, and probably reflect fluctuations of fluid compositions on a local scale [9].

References: [1] Weisberg M. K. et al. (1997) *Meteorit. Planet. Sci., 32,* A138. [2] Kojima H. and Tomeoka K. (1996) *Geochim. Cosmochim. Acta, 60,* 2651-2666. [3] Krot A. N. et al. (1998) *Meteorit. Planet. Sci., 33,* 623-645. [4] Krot A. N. et al. (1995) *Meteoritics, 30,* 745-775. [5] Krot A. N. et al. (1998) *Meteorit. Planet. Sci., 33,* 1065-1085 [6] Cohen R. E. et al. (1983) *Geochim. Cosmochim. Acta, 41,* 1739-1757. [7] Krot A. N. et al. (2003) *International Symp. Evolution of Solar System Materials,* 61-62. [8] Kimura M. and Ikeda Y. (1998) *Meteorit. Planet. Sci., 33,* 1139-1146. [9] Krot A. N. et al. (2004) *Antarct. Meteorit. Res., 17,* 153-171.

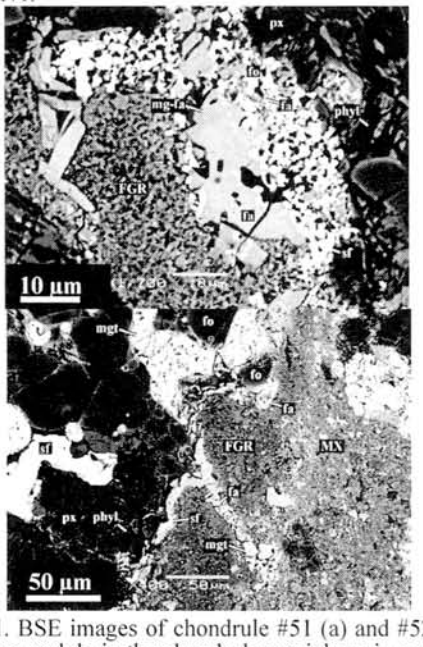

Fig. 1. BSE images of chondrule #51 (a) and #52 (b). (a) Opaque nodule in the chondrule preriphery is replaced by sulfide (sf) and magnetite (mgt); the latter is replaced by fayalite (fa), which in turn is replaced by a more magnesian olivine. (b) Fayalite-magnetite-sulfide veins starting at the opaque nodules and crosscutting the fine-grained rims around the chondrule. px=pyroxene, FGR=fine-grained rim, MX-matrix.

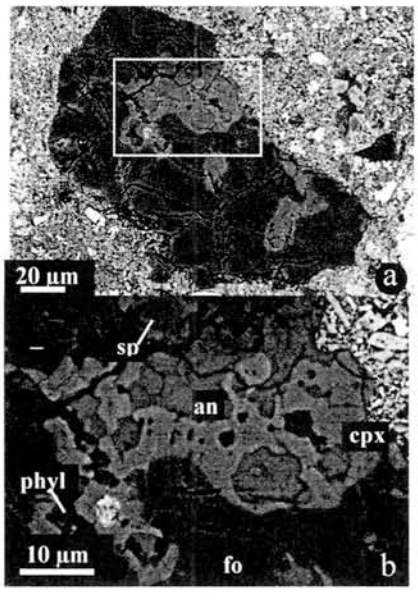

Fig. 2. BSE images of unaltered AOA #214. It consists of nearly pure forsterite (fo), high-Ca pyroxene (cpx), anorthite (an), and spinel (sp). Anorthite is partly replaced by phyllosilicates (phyl).

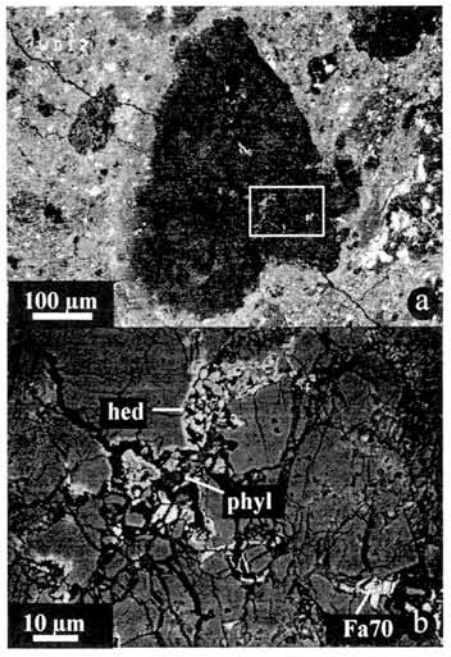

Fig. 3. BSE image of altered AOA #5. Anorthite is completely replaced by phyllosilicates (phyl). Hedenbergite (hed) and fayalite are observed in direct contact with phyllosilicates. Occasionally, fayalite grains are rather coarse and show inverse compositional zoning.

Table 1. Representative analysis of minerals in AOAs.

mineral	Fo	cpx	an	en	cpx
AOA #	15	2	214	202	15
SiO_2	43.6	49.0	42.8	58.8	52.0
Al_2O_3	0.91	5.4	37.2	0.20	5.4
TiO_2	0.30	2.4	0.03	n.a.	0.63
FeO	1.3	1.3	0.93	0.60	0.53
MnO	0.12	0.06	0.01	0.10	2.0
MgO	51.5	22.3	0.7	37.2	18.1
CaO	2.0	20.3	18.4	2.6	18.3
Na_2O	0.05	n.a.	0.15	n.a.	0.11
K_2O	0.04	n.a.	0.02	n.a.	0.02
Cr_2O_3	0.22	0.07	0.04	0.10	1.9
V_2O_3	0.03	n.a.	n.a.	n.a.	n.a
NiO	0.12	n.a.	0.03	0.10	0.03
P_2O_5	n.a.	0.24	0.25	n.a.	0.15
Total	100.2	101.0	100.5	99.9	99.0
Fa	1.4	-	-	-	-
Wo	-	38.8	-	4.8	41.7
En	-	59.3	-	94.3	57.4

fo = forsteritic olivine, cpx = Al-diopside, an = anorthite, en = enstatite, rim cpx = euhedral high-Ca pyroxene in the rim of AOA.

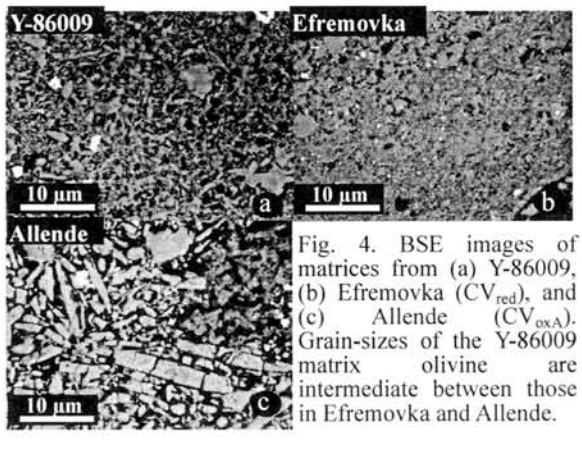

Fig. 4. BSE images of matrices from (a) Y-86009, (b) Efremovka (CV_{red}), and (c) Allende (CV_{oxA}). Grain-sizes of the Y-86009 matrix olivine are intermediate between those in Efremovka and Allende.

Reading the growth process of iron meteorite by a photoelectron emission microscope (PEEM) with synchrotron radiation. M. Kotsugi[1], T. Wakita[2], F. Guo[2], T. Taniuchi[3], K. Ono[4], M. Taniguchi[5], H. Maruyama[6],. [1]Hiroshima Synchrotron Radiation Center, Hiroshima University (HiSOR), 2-313 Kagamiyama, Higashi-Hiroshima, Hiroshima 739-0046, Japan, [2]Japan Synchrotron Radiation Research Institute (JASRI), 1-1-1 Kouto, Sayo, Hyogo 679-5198, Japan, [3]Graduate School of Engineering, The University of Tokyo, 7-3-1 Hongo, Bunkyo-ku, Tokyo 113-8656, Japan, [4]High Energy Acceleration Research Organization (KEK), 1-1 Oho, Tsukuba, Ibaragi 305-0801, Japan, [5]Graduate School of Science, Hiroshima University, 1-3-1 Kagamiyama, Higashi-Hiroshima, Hiroshima 739-8526, Japan

Electron probe microprobe analyzer (EPMA) has been of an useful technique to visualize the local chemical composition using the intensity of emitted x-ray excited by the scanning electron beam with sub-micrometer resolution. Because of its brief visualization capability, it has been widely used not only in planetary science but also materials science. On the other hand, photoelectron emission microscope (PEEM) recently attracts much attention in the research of materials science or nanoscience (Fig. 1) [1, 2].

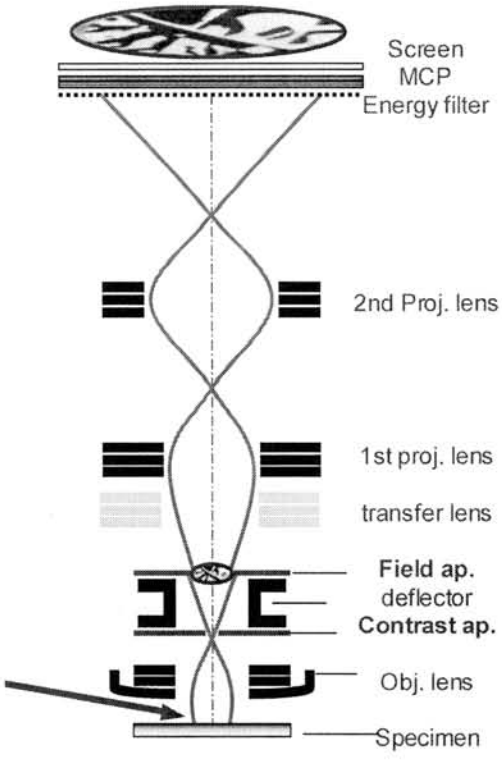

Fig. 1: The schematic drawing of photoelectron emission microscope (PEEM). The spatial distribution of photoelectron emitted by synchrotron radiation (SR) is projected on the screen with the resolution power of several ten nanometers.

It can project the spatial distribution of photoelectron excited by an incident synchrotron radiation (SR) with the resolution power of several ten nanometers. The information of photoelectron directly leads not only the chemical composition but also crystallographic structure, electronic structure and magnetic moments. The information of crystallographic structure or electronic structure can be obtained by the scanning of the photon energy over the x-ray absorption edge. And the magnetic domain structure can be obtained by using a magnetic optical Kerr effect so called as magnetic circular dichroism or linear dichroism (MCD, MLD). Such sophisticated solid-state properties have brought us the key information to understand the fundamental properties of nano-particles or nano-films. However its powerful visualization capability has never been applied on extraterrestrial materials. Here, we will report the first experimental result applying a PEEM on the Gibeon iron meteorite, and argue the growth process of the Widmanstätten structure using various solid-state properties: the chemical composition, crystallographic structure and magnetic structure.

Meteoritic iron has been thought that the long-range thermal diffusion of Fe and Ni in the thermally isolated core constructed an extraterrestrial pattern termed as Widmanstätten structure over the 4 billion years. Thereby, it can be considered as a ferromagnetic material characterized by a segregated microstructure composed of bcc and fcc-FeNi [3]. The local chemical composition and crystallographic structure and magnetic domain structure is observed on the kamacite lamella in Gibeon iron meteorite. It shows spatially homogeneous composition and a body-centered-cubic (bcc) structure [4]. In the observation of magnetic domain structure, the easy-axis rotation from <100>bcc to <110> bcc direction in a striped magnetic domain is found in the middle of kamacite lamella, and it is unfavorable

feature in any synthetic Fe-Ni system (Fig. 2) [5, 6]. The easy-axis of magnetization in bcc-FeNi usually orients to <100> bcc direction due to the minimized direction of total magneto-anisotropy energy, which is expressed as the sum of crystallographic, induced, shape and exchange term [5]. It is reported that the initial growth of bcc-Fe in duplex steel develops along <110> bcc direction [7], and Widmanstätten pattern is formed through extremely slow cooling rate [3]. Such uniaxial and slow growth process generally increases induced magnetic anisotropy, therefore the easy-axis rotation can attribute to the induced-magnetic anisotropy associated with the Widmanstätten structure growth. The detailed investigation on the extraterrestrial materials in the context of solid-state physics could offer a new innovative line of research for the history of solar system.

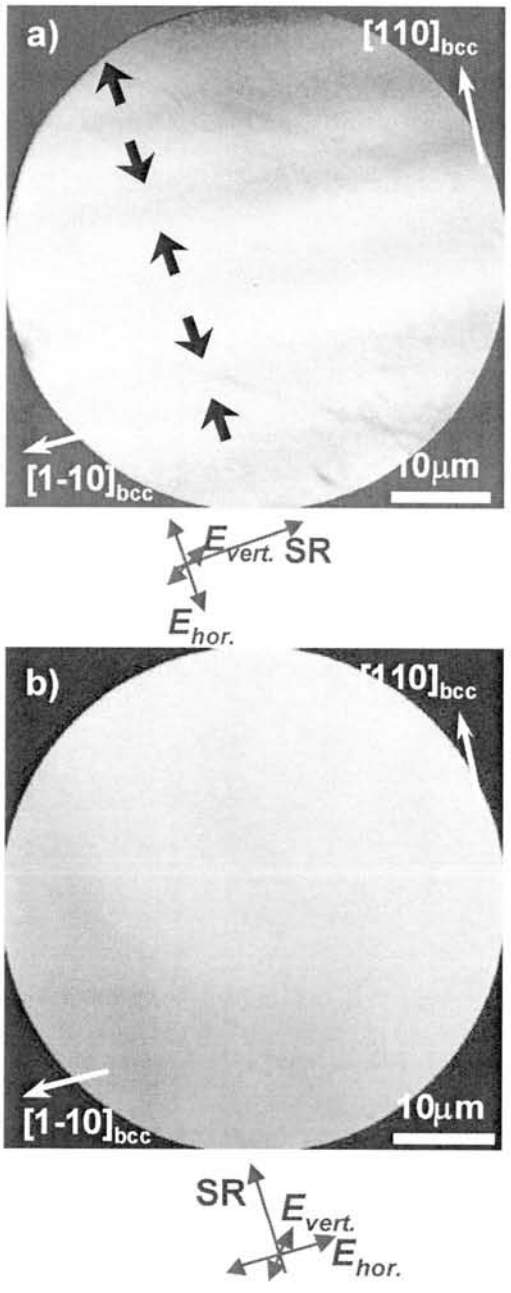

Fig. 2: Magnetic domain structure on the kamacite lamellae of Gibeon iron meteorite observed by a PEEM using MLD technique. The striped magnetic domain structure is clearly appears along [1-10] direction (a), and it is completely vanished in (b)

Reference

[1] J. Stöhr, H. A. Padmore, S. Anders, T. Stammler, M. R. Scheinfein, Surf. Rev. Lett. **5**, 1297 (1998).

[2] W. Kuch, M. Kotsugi et al., Nature Mater., **5**, 128 (2006).

[3] V. F.Buckwald, Handbook of Iron Meteorites (University of California, Berkeley, 1975).

[4] M. Kotsugi et al., e-J. Surf. Sci. Nanotechnol. **4** 490 (2006)

[5] S. Chikazumi, S. Physics of Magnetism (R. E. Krieger, New York, 1964).

[6] A. Hubert, R. Schafer, Magnetic Domains (Springer-Verlag, Berlin, 2000)

[7] C. H. Shek, C. Dong, J. K. L. Lai, K. W. Wong, Metall. Mater. Trans. A **31**, 15 (2000).

Static amorphization of plagioclase: Comparison to the formation pressure of diaplectic glass in laboratory shock experiments. A. Kunikata[1], N. Tomioka[1], T. Nagai[2], T. Narita[3], T. Yamanaka[3], [1]Department of Earth and Planetary Sciences, Kobe University, Kobe 657-8501, Japan, [2]Department of Earth Sciences, Hokkaido University, Sapporo 060-0810, Japan, [3]Department of Earth and Space Science, Osaka University, Toyonaka 560-0043, Japan. E-mail address: nao@kobe-u.ac.jp

Introduction:

In heavily shocked stony meteorites, plagioclase in host rock has transformed into glass, called maskelynite, in a solid-state reaction. The shock-induced plagioclase glass is regarded to be one of the important indicators of the shock stages of chondrites by Stöffler et al. (1991) [1]. The formation pressure of maskelynite has been estimated based on dynamic high-pressure (shock) experiments. However, duration of pressure in laboratory shock experiments is significantly smaller (10^{-6}sec) than that in meteorite parent bodies (10^{0}sec) estimated by the mineralogy of shock-induced melt vein [2,3]. Therefore, there is a possibility that shock pressures of heavily shocked meteorites could be overestimated due to kinetic effect of amorphization. In this study, amorphization pressures of plagioclase were investigated based on static high-pressure experiments using a diamond anvil cell that can produce longer duration of pressures.

Experimental Methods:

Natural plagioclase single crystals with Ab_{99} and Ab_{89} compositions were crushed in an agate mortar. Fine-grained powder (~5-30μm) of Ab_{99} and Ab_{89} plagioclases were compressed at 20, 27, 33, 37, 49 GPa and 31, 34, 45 GPa, respectively at room temperature by a diamond anvil cell, and were kept at elevated pressures for 30 minutes. The powdered sample was directly enclosed in a Re gasket without a pressure medium. Therefore, a large differential stress would have been applied to the samples in the present study as well as shock experiments. Recovered specimens were examined by laser Raman spectroscopy (JASCO NRS2100-F) and transmission electron microscopy (TEM: JEOL JEM-2010).

Results:

In the samples of Ab_{99} plagioclase compressed up to 33 GPa, characteristic Raman peaks (~290, 480, 510 cm^{-1}) of plagioclase were observed, but these peaks were not observed in the samples compressed at 37 and 49 GPa. Among the samples of Ab_{89} plagioclase, Raman peaks of plagioclase were observed only in the sample compressed at 31 GPa. Broad Raman peaks of plagioclase glass could not be observed due to high background counts.

The Ab_{99} plagioclase compressed at 33 GPa shows very weak Raman peaks of plagioclase. In TEM observation of the sample, most of grains show diffuse ring patterns in electron diffraction indicating an amorphous nature. However, a part of the grains shows powder diffraction rings (Fig. 1A). That suggests that original plagioclase grains became extremely fine grained (smaller than 100 nm in size) before amorphization. The pressure of 33 GPa is nearly the critical pressure, at which Ab_{99} plagioclase completely becomes amorphous. The samples (Ab_{99}, 37 GPa; Ab_{89}, 35 GPa) do not show Raman peaks of plagioclase. All of the grains in these samples show diffuse ring patterns from amorphous material in electron diffraction (Fig. 1B).

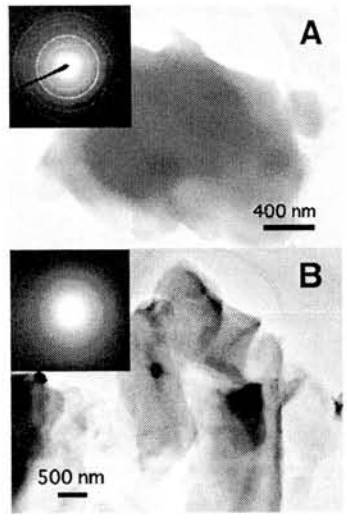

Figure 1. Transmission electron micrographs of recovered samples, (A) Ab_{99} plagioclase compressed at 33 GPa and (B) Ab_{89} plagioclase compressed at 35 GPa. Selected area diffraction patterns are in the inset.

Discussion:

Present Raman spectra and electron diffraction patterns of statically compressed plagioclases revealed that amorphizations of Ab_{89} and Ab_{99} plagioclases are completed at pressure around 33 and 35 GPa, respectively. Previously, Williams and Jeanloz (1989) reported that anorthitic plagioclase (Ab_5) is completely amorphised at ~28 GPa by diamond anvil cell experiments [4]. Hence, the amorphization pressure of plagioclase increases with increasing albite component. It is consistent with the amorphization pressure of experimentally shocked plagioclase that increases with increasing albite component [5,6].

Plagioclase with $Ab_{80\text{-}90}$ composition that

corresponds to that in ordinary chondrites is completely amorphized at ~34-36 GPa according to shock experiments [5,6]. These pressures are slightly higher (~3 GPa) than those in the present static high-pressure experiments (~31-33 GPa), but the pressure differences are not significant.

In a shock compression process, target temperature is also elevated with increasing shock pressure. Shocked chondrites that contain maskelynite would have experienced post-shock temperature of higher than 300 °C [1]. The high temperature possibly activates amorphization process of plagioclase. Therefore, the amorphization pressure could decrease with increasing temperature. In this study, there is no large time dependence of amorphization pressures of plagioclase between dynamic and static high-pressure experiments. However, static compression experiments under high temperature are further required to estimate exact amorphization pressures of plagioclase in natural impact on the parent bodies of meteorites.

References:

[1] Stöffler D. et al. (1991) *Geochim. Cosmoshim. Acta*, **55**, 3845-3867.
[2] Xie et al. (2001) *Eur. J. Mineral.*, **13**, 1177-1190.
[3] Ohtani et al. (2004) *Earth Planetary Sci. Lett.*, **227**, 505-515.
[4] Williams Q. and Jeanloz R. (1989) *Nature*, **338**, 413-415.
[5] Ostertag R. (1983) *J. Geophys. Res.* **88**, 364-376.
[6] Stöffler D. et al. (1986) *Geochim. Cosmoshim. Acta*, **50**, 889-903.

Determination of ^{26}Al contents in Antarctic meteorites using extremely low background γ-ray counting system of ICRR, University of Tokyo, for dating of terrestrial age. H. Kusuno[1], M. Kobayashi[1], T. Fukuoka[1] and H. Kojima[2], [1]Department of Environmental Systems, Faculty of Geo-Environmental Science, Rissho University, Kumagaya, Saitama 360-0194, Japan (tfukuoka@ris.ac.jp). [2]Antarctic Meteorites Research Center, National Institute of Polar Research, Itabashi-ku, Tokyo 173-8515, Japan.

Introduction

Determination of terrestrial ages of Antarctic meteorites supplies useful informations for the frequency of meteorite fall, mechanism of accumulation of meteorites and the age of ice. ^{26}Al ($T_{1/2}$ = 7.17 x 10^5y) is a useful tool for the dating of terrestrial age of meteorite.

There are two types of determination methods for ^{26}Al contents in small amount of meteorites. One is μ-ray counting by extremely low background γ-ray counting system, another is accelerator mass spectrometry (AMS) analysis. In this study, to check consistency of the data obtained from these two methods, ^{26}Al contents in 4 meteorites have been determined by extremely low background γ-ray counting system as basic study.

Samples and Experimental

^{26}Al contents in Yamato-791199, -791192, -791962 and Allende meteorites have been determined non-destructively by extremely low background γ-ray counting system of Institute for Cosmic Ray Research (ICRR), University of Tokyo. The counting system consists of a well type of large volume high pure Ge detector. Absolute counting efficiency of the detector was 1.76% at 1809keV γ-ray of ^{26}Al. 1.73 to 2.34g of crushed samples were packed in plastic vials prior to put into the well of detector.

Results and Discussion

The determination results are shown in Table 1 with the sample weight for determination and the count length. The results are generally consistent with those of previous work (1-3).

Usually, determinations of ^{26}Al contents for more than 100g of samples are performed by γ-ray count non-destructively. However, those for small samples such as less than 20g are very difficult. Recently, AMS analysis has been applied to determination of ^{26}Al in meteorites. Although the sample amount of AMS analysis is small, this analysis is destructive.

For small size of meteorites which original weights are less than 2g, non-destructive determination of ^{26}Al content using extremely low background γ-ray counting system has a great advantage, because we can get other informations such as chemical, petrological and mineralogical informations from the same samples after ^{26}Al determination.

The ^{26}Al content in Allende meteorite is low compared to the other meteorites. Because Allende meteorite fell in Mexico at 1969, ^{26}Al content in Allende should be high. However the ^{26}Al contents in Allende meteorite in this study is low compared to the ^{26}Al contents of the 3 Antarctic meteorites (Table 1). This suggests Allende sample used in this study was located in the deep inside of the original meteorite mass.

References

(1) Fuse and Anders (1969) Geochim. Cosmochim. Acta **33**, 653.

(2) Komura *et al.* (1982) Mem. Natl. Inst.Polar Res., Spec. Issue, **25**, 178.

(3) Fukuoka *et al.* (1993) The 18th Symposium Antarctic Meteorites, 152.

Table 1. ^{26}Al contents in Antarctic meteorites and Allende.

sample	weight (g)	count length (days)	^{26}Al content (dpm/kg)
Y-791199(Anorthosite)	1.78	180	55± 4
Y-791192(Eucrite, polymict texture)	1.73	124	94± 5
Y-791962(Eucrite)	1.73	181	89± 4
Allende (CV3)	2.34	173	41± 4

Tungsten and molybdenum isotopes in achondrites. D-C. Lee, Institute of Earth Sciences, Academia Sinica, Taipei 115, Taiwan, ROC.

Achondrites originated from the silicate portions of differentiated planetary bodies, and can provide valuable information about the time scales of planetary accretion and differentiation, as well as how effectively materials homogenized in the accretion disk. Short-lived ^{182}Hf-^{182}W ($t_{1/2}$ = 8.9 myrs) and Mo isotope systems are selected to study a variety of achondrites originated from different parent bodies in order to better constrain the earliest history of planetary accretion and differentiation.

An acapulcoite, NWA725, and the metal portion of lodranite, GRA95209, are first selected in this study since neither lodranite nor acapulcoite has been studied with W or Mo isotope system. Lodranites and acapulcoites have similar oxygen isotopic compositions, and are generally regarded to have come from the same parent body, but with different petrogenetic history [1]. Preliminary bulk rock analysis indicates that both meteorites exhibit deficits in ^{182}W, with ε_w of -2.6 and -3.3 for NWA725 and GRA95209, respectively. This suggests that the metal-silicate segregation occurred very early in the parent body of lodranites and acapulcoites. The sub-chondritic ε_w are consistent with the observed sub-chondritic ^{180}Hf/^{184}W of 0.59 and 0.007 for NWA725 and GRA95209, respectively. Despite that these two samples along with the CHUR show a general positive correlation in an isochron plot, other evidence, e.g., petrology and oxygen isotopes, seems to suggest that they may not have formed in a single event [1]. Although the ε_w of the metal portion of GRA95209 alone indicates that the formation of lodranites should be no later than 5 myrs since the start of the solar system, an internal isochron study is needed to better constrain the formation age of NWA725.

In addition to W, Mo isotopic compositions for these two primitive achondrites are also measured in order to further constrain the possibility of a heterogeneous distribution of Mo isotopes in the accretion disk of the solar system [2-4]. Within the analytical errors, the preliminary results for both samples exhibit identical Mo isotopic compositions to the terrestrial Mo standard, with the exception of a slight deficit in ^{96}Mo and an excess in ^{100}Mo for the acapulcoite NWA725, although both anomalies are less than 1ε. The preliminary Mo data of these two primitive achondrites are consistent with the Mo data of the other type of primitive achondrites, namely the ureilites. If these preliminary results are correct, they seem to suggest a smaller scale of Mo isotopic heterogeneity than previously proposed [2-3] might be present in the parent body of lodranites and acapulcoites. However, more Mo data from other types of achondrites, e.g., samples from the HED parent body and Mars are needed to better constrain the early distribution of Mo isotopes in the accretion disk.

References

[1] McCoy T.J., Keil K., Clayton R.N., Mayeda T.K., Bogard D.D., Garrison D.H., and Wieler R. (1997) *GCA* **61**, 623-637. [2] Dauphas N., Marty B., and Reisberg L. (2001) *Ap. J.* **565**, 640–644. [3] Yin Q., Jacobsen S.B., and Yamashita K. (2002) *Nature* **415**, 881–883. [4] Becker H., and Walker R.J. (2003) *Nature* **425**, 152–155.

SOURCES OF EXCESS NITROGEN IN LUNAR SOILS: CLUES FROM N AND ARGON IN LUNAR METEORITE Y983885

R. R. Mahajan and S. V. S. Murty, Physical Research Laboratory,
Ahmedabad 380009 India

Introduction: Moon is depleted in volatiles. The large amounts of trapped noble gases and nitrogen in lunar soils are of solar wind origin. However, the enigmatic findings since the availability of returned lunar samples for laboratory studies are the over abundance of N in the lunar soils by about a factor of ten, as compared to solar abundances, and over 30% variation in the $\delta^{15}N$ which still await a proper understanding [1]. Several explanations proposed in the past for the excess N range from indigenous lunar N, contribution from Earth's magnetosphere, and presence of higher proportion of solar flare N-component [2]. Ozima et al [3] have modeled the excess nitrogen and shown that the volatiles in lunar soil could be due to implantation of gases escaping from the Earth's atmosphere. But they all fail to simultaneously account for the observed N content, $^{14}N/^{36}Ar$ ratio and the $\delta^{15}N$ of lunar soils. Recent efforts to analyse individual mineral grains from lunar soils for N and Ar by laser heating have further confirmed the existence of excess N and have also indicated its $\delta^{15}N$ value to be about +50‰ [4,5]. These studies have not been able to establish the release characteristics of the excess N component.

Results of Y983885: We have analysed two samples of the Antarctic lunar meteorite Y983885 (from different locations) for N and noble gases by stepwise pyrolysis by standard procedures [6]. Y983885 has the largest amount of solar wind noble gases among the lunar meteorites investigated so far [7] and also revealed that $^{14}N/^{36}Ar$ ratio is about 10 times more than expected for solar wind, similar to observations in lunar soils [1]. Stepwise temperature pyrolysis data for the two samples of Y983885 shows a $\delta^{15}N$ profile typical of lunar soils [8], with high $\delta^{15}N$ at low temperatures, lower values at intermediate temperatures and higher values at melting temperatures (Fig. 1). Release profile of the elemental ratio $^{14}N/^{36}Ar$ also shows similar pattern (Fig. 2), with higher values of $^{14}N/^{36}Ar$ (upto ~80000) at low temperature, a plateau value of ~ 360, similar to lunar soils, at the intermediate temperatures and again higher values at melting temperatures. The release pattern of $^{14}N/^{36}Ar$ can be interpreted in the following way. Excess (non-solar) N is being added as a surface component of almost pure N (devoid of noble gases) continuously. During the continuous gardening of the lunar surface by micro-meteorite impacts, this excess N gets thoroughly mixed with the SW component, and behaves similar to SW in thermal release. A part of this excess N can also become a volume component in the agglutinates and retain its identity. But the most recently added excess N remains only weakly bound on surface and gets released at a lower temperature (than SW) during pyrolysis. The $\delta^{15}N$ of the low temperature

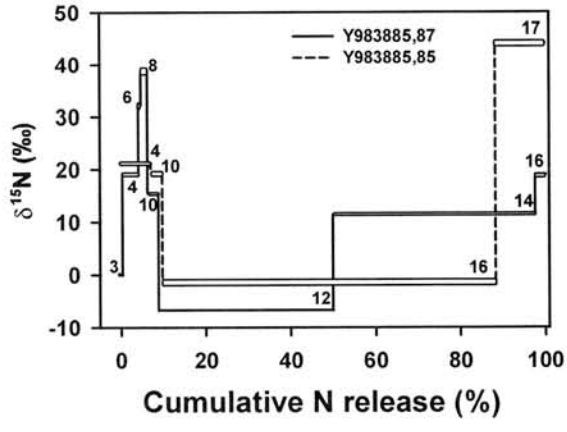

Fig. 1. Release pattern of nitrogen in Y983885 samples

release, with its characteristic high $^{14}N/^{36}Ar$, thus could be closure to the isotopic

signature of excess N and should help in the identification of the source.

Source of excess N: Moon is continuously bombarded by IDPs, which are rich in organics, having positive $\delta^{15}N$. On impact, the volatalised N gets deposited on the surface grains, similar to the parentless ^{40}Ar [9]. This surfacial N component becomes more firmly integrated into the grain in subsequent regolith gardening processes and behaves similar to SW component in thermal release, thus explaining the uniform $^{14}N/^{36}Ar$ in the intermediate temperatures. The high value of the low temperature release for $^{14}N/^{36}Ar$ with positive $\delta^{15}N$ should be characteristic of the source of excess N. Table 1 lists the $^{14}N/^{36}Ar$ and $\delta^{15}N$ for various plausible sources. Only comets and IDPs will be matching the excess lunar N characteristics. It is most plausible that the excess lunar N is due to IDPs and it may provide a means of assessing the IDP flux on Moon in the past, provided the latest surface exposure of the sample can be dated by suitable means.

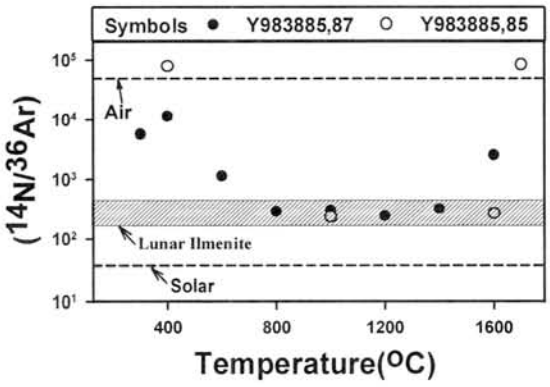

Fig 2. Release pattern of $^{14}N/^{36}Ar$ ratio in two samples of lunar meteorite Y983885. $^{14}N/^{36}Ar$ value of Air, solar component as well as the range observed for lunar soils are also shown in the plot.

Acknowledgements: We thank NIPR, Japan for generously providing the samples of Y983885 for this study.

TABLE 1. N and Ar in Meteorites, comets and IDPs

Source	N (ppm)	$\delta^{15}N$ (‰)	$^{14}N/^{36}Ar$	Reference
Solar		-238	37	10
Earth's Atmosphere		$\equiv 0$	$53x10^3$	
O-Chondrites	1 - 25	-20 to +100	$\sim 6x10^5$	11,12
E-Chondrites	~100	-35	$\sim 3x10^6$	11
C-Chondrites	500 - 2000	+20 to +50	$\sim 2.4x10^6$	11
Comets	Upto 10000	-175 to +1092	$\sim 9x10^4$	13
IDPs	4 to 165	-240 to +220	$\sim 10^5$	14,15
Excess lunar N	10 to 100	~ +50	$\geq 8x10^4$	5,This work

References : [1] Kerridge J.F. (1989) *Science* **245**, 480-486; [2] Marty B. et. al. (2003) *Space Science Rev.* **106**, 175-196; [3] Ozima M. et. al, (2005) Nature **436**, 655-659; [4] Wieler R. et al. (1999) *EPSL* **167**, 47-60; [5] Hashizume K. et al, (2002) EPSL **202**, 201-216; [6] Murty et al, (1997) MAPS **31**, 857-868; [7] Murty et al. (2003) *Evolution of solar system: A new perspective from Antarctic meteorites*; [8] Becker R.H. and Clayton R.N. (1975) *PLSC* **6**, 2131-2149; [9] Manka R.H. and Michel F.C. (1971) *PLSC* **2**, 1717; [10] Hashizume et al (2000) *Science* **290**, 1142-1145; [11] Grady M. M. et al., *Space Science Rev.* **106**, 231-248; [12] Hashizume K. et al. (1995) GCA 59, 4057-4069; [13] Hutsemekers et al (2005) A & A **440** L21-L24; [14] Floss et al (2004) Science 303, 1355-1358; [15] Marty B, et al (2005) *MAPS* **40**, 881-894.

ALUMINUM EFFECT ON THE CALIBRATION OF THE EU OXYBAROMETER FOR NAKHLITES. J. Makishima[1], G. McKay[2], L. Le[3], M. Miyamoto[1] and T. Mikouchi[1]. [1]Department of Earth and Planetary Science, Graduate school of Science, University of Tokyo, 7-3-1 Hongo, Bunkyo-ku, Tokyo, 113-0033, Japan, makki@eps.s.u-tokyo.ac.jp, [2]Mail Code KR, NASA Johnson Space Center, Houston, TX 77058, USA, [3]ESC Group, Jacobs Sverdrup, Houston, TX 77058, USA.

Introduction: Recent studies of Martian meteorites have shown that Martian magma had wide range of oxygen fugacity. In order to estimate the redox state of the Martian crust and mantle, the partitioning coefficient of Eu in the shergottite pyroxene has been extensively studied [1-3]. Nakhlite, a cumulate clinopyroxenite, is another important group of Martian meteorites. We have studied synthetic compositions (NT, NL, NJ, NJ2 and NJ4) in order to estimate the Nakhla parent melt composition [4,5]. In our previous work [6], we calibrated the Eu oxybarometer for nakhlite using the NJ4 composition which we believe is the closest to the Nakhla parent melt. Consequently, we concluded that Nakhla may have crystallized under fairly reducing condition (Table1, Fig.1). However, we also found that the partition coefficient is strongly affected by Al contents in melt and in pyroxene [7]. In this abstract we report the correlation between the D values and Al contents in melt and in pyroxene from our Nakhla experimental studies. Also we check the reliability of our previous calibration of Eu oxybarometer, because REEs are easily affected by Al content in melt and in pyroxene and Nakhla pyroxene shows unusual patchy Al zoning.

Table. 1		Pyroxene D(Eu)/D(Gd)	
Expt	fO2	D(experiment)	D(Nakhla)
817	IW	0.64±.002	0.7±0.1
818	IW+1.5	0.76±0.02	
819	QFM	0.86±0.04	
Oe [8]	QFM	0.86±0.03	

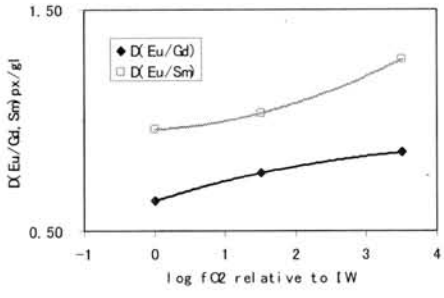

Fig. 1 Calibration of D(Eu/Gd)(pyroxene/glass) and D(Eu/Sm) (pyroxene/glass) versus oxygen fugacities (in log units relative to the IW buffer).

Experimental method: We doped the NJ4 composition with ~1 wt% Sr and REEs, which is a starting material. Then, we put it in the furnace at 1300 °C for 48 hours to homogenize it, quenched and put back below the liquidus under the three oxygen fugacities, IW, IW+1.5 and QFM (IW+3.5), growing pyroxene. Table 2 summarizes thermal histories of these runs. We analyzed samples with the Cameca SX-100 Electron Microprobe at JSC and calculated the D(Eu/Gd).

Table 2. Cooling histories for experiments				
Expt.	Oxygen fugacity	Start cooling	Quench temperature	Cooling rate
817	IW	1155°C	1150°C	0.5°C/h
818	IW+1.5	1155°C	1150°C	0.5°C/h
819	QFM	1159°C	1152°C	0.5°C/h

Results and Discussion: The effects which Al has on D values of REEs are complex. D values are affected not only by Al contents in melt but also by Al contents in pyroxene. Oe et. al. [7,8] grew pyroxene from the various synthetic compositions similar to Nakhla and studied the correlation between D(Ce), one of the trivalent REEs, and Al_2O_3 content in melt for each composition. As is clearly shown in Fig. 2, there is a positive correlation between D(Ce) and Al_2O_3 in melt.

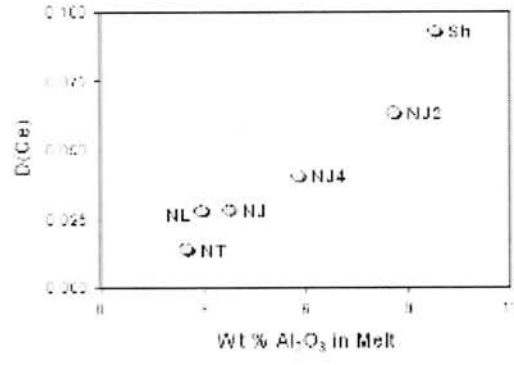

Fig. 2 D(Ce, pyroxene/melt) vs. Al_2O_3 content in pyroxene for experimental pyroxene compositions. NJ4, NL, NT, NJ and NJ2 are synthetic compositions similar to Nakhla and Sh is similar to Shergotty [7].

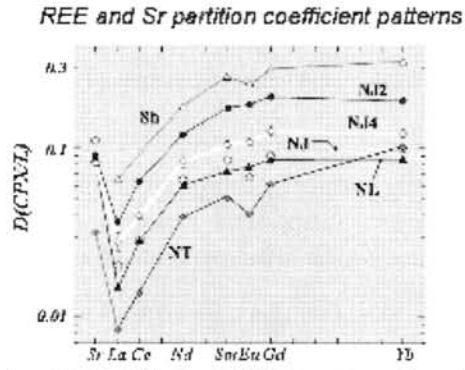

Fig. 3 The partition coefficient patterns for REEs of synthetic compositions [7].

D values of other REE also have similar correlation with Al content in melt (Fig. 3). There is almost an order of magnitude variation in partition coefficients over a range of synthetic Nakhla compositions.

Moreover, Fig. 4 shows that Al contents in our NJ4 synthetic pyroxene at the IW buffer also have strong effects on D values of REEs. Similarly we found Al contents in pyroxene and D values have positive correlation at the IW+1.5 and QFM.

As is shown in the Figs. 5 and 6, D(Sr) and the square root of D(Sm)*D(Gd) are almost the same both at the IW and QFM. This means that our Eu oxybarometer for nakhlite in the previous study may not work for the NJ4 composition. The reason for this is as follows. Under mantle-like condition only Eu among REEs exists in bivalent state and trivalent state, respectively under more reducing condition and more oxidizing condition. Eu behaves differently from the other REEs and we expect a deeper Eu anomaly in the more reducing condition. Eu^{2+} behaves similarly to Sr and Eu^{3+} behaves like intermediate element between Sm and Gd. Therefore, when D(Sr) and the square root of D(Sm)*D(Gd) are almost the same, the there is little difference between $D(Eu^{2+})$ and $D(Eu^{3+})$. In this case the Eu anomaly will be very small for the NJ4 composition. Because Sr is difficult to analyze with the electron microprobe, we need more accurate analyses of D(Sr) with the ion microprobe to confirm this observation.

Consequently, it is difficult to know the accurate D values of REEs in nakhlite because they are affected in a complex way by Al contents both in melt and in pyroxene. Thus, we must be careful to use the appropriate partition coefficient values when we perform SIMS analyses of nakhlite pyroxene and estimate the melt composition with partition coefficients.

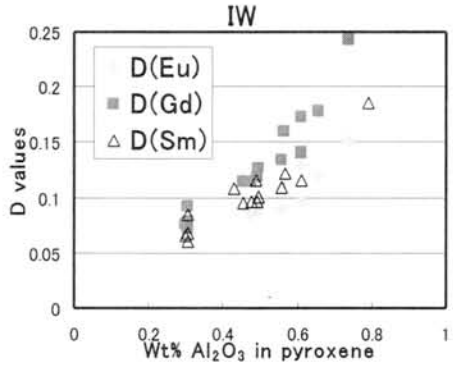

Fig. 4 D values vs. Al_2O_3 in pyroxene at the IW buffer.

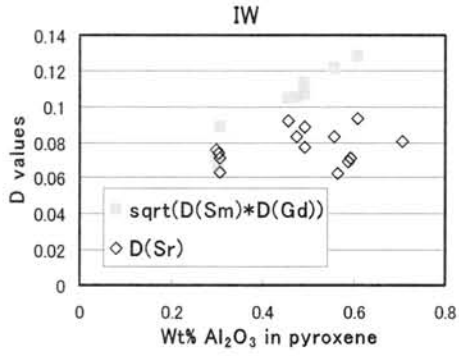

Fig.5 D values vs. Wt% Al_2O_3 in pyroxene at the IW

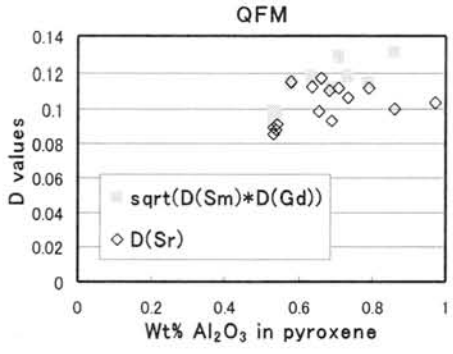

Fig. 6 D values vs. Wt% Al_2O_3 in pyroxene at the QFM

References: [1] Wadhwa M. (2001) *Science*, *291*, 1527-1530. [2] McCanta M. et al. (2004) *GCA*, *68*, 1943-1952. [3] Wadhwa M. et al. (1994) *GCA*, *58*, 4213-4229. [4] McKay G. et al. (1994) *LPSXXV*, 883-884. [5] Kaneda K. et al. (1998) *LPSXXIX*, 1620-1621. [6] Makishima J. et.al. (2006) *LPSXXXVII*, #1589. [7] Oe K. et al. (2001) *LPS XXXII*, #2174. [8] Oe K. et al. (2002) *LPS XXXIII*, #2065.

Triangular chemographic diagram for the mineral assemblages of chondrites and its genetic interpretation. A. A. Marakushev, N .G. Zinovieva, and L. B. Granovsky, Department of Petrology, Geological Faculty, Moscow State University, Leninskie Gory, Moscow 119992, Russia (zinov@geol.msu.ru)

Antarctic meteorites are representative of all types of meteorites, including chondrites. Table 1 reports the average compositions of chondrites The average compositions of chondrites and the compositions of the minerals typical of their major types (carbonaceous C, forsterite-enstatite E, and ordinary LL-L-H-HH) are summarized in a chemographic diagram for mineral assemblages (Fig. 1), which also shows the average Earth's composition, which is the closest to the chemical groups of chondrites rich in iron. Along with many other characteristics [2], the similarities between these compositions provide the basis for the so-called chondritic model of the origin of the Earth.

Table 1
Average compositions (wt % oxides) of chondrites (data from [1])

	LL	L	H	C	E
SiO2	39,30	38,67	35,16	30,22	33,66
TiO2	0,11	0,10	0,08	0,15	0,10
Al2O3	2,63	2,45	2,29	2,84	2,48
Fe2O3	1,02	0,75	3,25	6,08	1,33
FeO	18,31	14,75	10,67	16,49	6,86
MnO	0,32	0,32	0,28	0,23	0,27
MgO	25,62	25,31	23,61	22,15	18,20
CaO	1,82	1,79	1,62	2,04	1,15
Na2O	0,92	0,87	0,74	0,37	0,69
K2O	0,11	0,09	0,08	0,05	0,06
H2O(-)	0,18	0,09	0,22	2,04	0,96
H2O(+)	0,53	0,30	0,87	6,88	4,13
P205	0,26	0,26	0,23	0,26	0,31
Cr2O3	0,49	0,49	0,42	0,47	0,38
FeS	5,96	6,47	5,92	7,44	13,93
Fe	1,88	6,33	13,40	3,01	13,86

The mineral assemblages portrayed in the diagram comprise two types: (i) pyroxene + olivine and (ii) plagioclase + quartz. The former is the predominant and corresponds to the bulk composition of chondrites, which are, however, somewhat shifted toward the latter (clinopyroxene) assemblage in compliance with its low contents in chondrites.

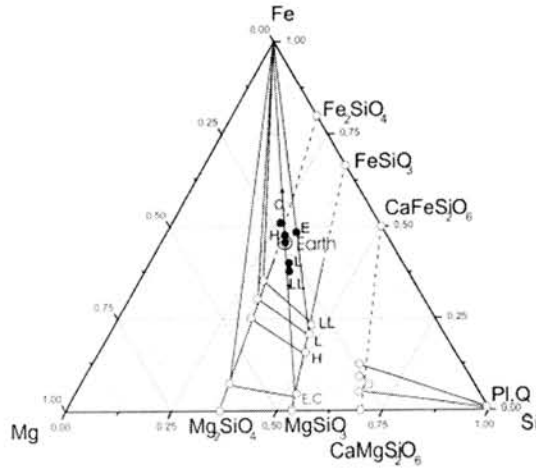

Fig. 1. Chemografic relations between the composition (wt % elemetnts) and mineral assemblages of chondrites in comparison with the average composition of the Earth. Solid and open circles denote the compositions of chondrites and minerals, respectively.

The main, orthopyroxene, assemblage reflects the variations in the orthopyroxene and olivine chemistries in chondrites, with the iron mole fractions of these minerals notably and systematically increasing in the main chondrite types in the succession E-C-HH-H-L-LL, according to the simultaneous decrease in the contents of metallic iron in these chondrite types. These relations, known as Prior's rule, which also emphasizes a simultaneous increase in the nickel concentration in the metallic (iron) phase of chondrites, can be schematically represented in the form of the following continuous mineral reaction:

$0.75Mg_{1,6}Fe_{0,4}SiO_4 + 0.25Mg_{0,8}Fe_{0,2}SiO_3 + 0.25Fe + 0.25H_2O = Mg_{1,4}Fe_{0,6}SiO_4 + 0.25H_2$.

This reaction reflects an increase in the iron mole fraction with increasing H_2O/H_2 ratio in the fluid and the simultaneous decrease in the content of metallic iron in chondrites. LL chondrites contain little iron, which is characterized in them by the highest concentrations of nickel. Chondrites were originally formed is the iron-nickel cores of their giant parent planets, which were similar to Jupiter and lost their hydrogen under the effect of the Sun, in agreement with the increase in the water/hydrogen ratio in their fluid shells of the planets. These shells exerted a huge pressure on the chondritic cores, which differentiated under this effect into a nickel-iron (matrix) and silicate (chondrule) phases that further evolved autonomously. This differentiation is shown in the diagram as diverging arrows. The huge fluid pressure induces the crystallization of tiny diamond crystals in chondrites. These diamonds abound in fluid inclusions, and their apparent density is thus as low as 2.2 g/cm^3 (whereas the density of diamond itself is 3.5 g/cm^3). The nickel-iron matrix melt, which contained much fluid, crystallized after the silicate melt of chondrules. The former actively replaced chondrules and transformed them into amoeba-shaped inclusions and other relics, which display continuous transitions between the chondrules and matrices of chondrites. Chondrules crystallized mostly after the loss of the giant fluid envelopes by the parent planets, when the chondritic cores of these planets were transformed into independent chondritic planets. Their evolution in environments resembling volcanic ones preceded the explosive breakup of the chondritic planets into asteroids. Chondrules crystallized in chondrites mostly under equilibrium conditions, as follows from systematic compositional relations between the olivine and orthopyroxene in the diagram. Consequently, so-called equilibrium (plutonic) chondrites (III) were produced. In spite of the homogeneous composition of the crystals, more rapid cooling caused deviations from equilibrium and the appearance of glass, i.e., chondrites of type II. The type II is transitional from equilibrium to volcanic chondrites (I) with strongly zoned silicate crystals and volcanic glass. This glass is mostly residual, rich in Ca, Na, Al, and Si, and corresponds to the *CPx + Pl + Q* assemblage in composition (see diagram). In this diagram, all types of chondrites are in essence magmatic polyfacies rocks that were variably reworked by overprinted metamorphism. The highest temperature alterations of these rocks gave rise to the crystallization of olivine of much more ferrous composition than that of the olivine shown in the diagram. Its formation was associated with oxidation under the effect of aqueous fluids and the ensuing disappearance of the metallic phase with the origin of secondary R chondrites bearing olivine close to fayalite in composition. The lowest temperature hydrothermal metamorphic alterations occur in carbonaceous chondrites (particularly in C1), which nearly completely consist of secondary phases (chlorite, sericite, serpentine, and carbonaceous matter) with rare remnants of primary (magmatic) high-temperature minerals.

Acknowledgments: This work was supported by the Russian Foundation for Basic Research, grant 04-05-64880 and the Program "Support of Scientific Schools".

References:

[1] Catalog on Antarctic Meteorites (1995) Nat. Inst. Polar Res. Tokyo. 230 p. (ed. by Yanai K. and Kojima H.); [2] Marakushev et al. (2003) *Kosmicheskaya Petrologiya*, Moscow, Nauka-press, p. 387 (in Russian).

THE USE OF GEOGRAPHIC REMOTE SENSING, MAPPING AND AERIAL PHOTOGRAPHY TO AID THE RECOVERY OF BLUE ICE SURFICIAL METEORITES IN THE ANTARCTIC. A. A, Mardon[1], A. S. C. Lau[2] and J. A. Greenspon[3], [1]Antarctic Institute of Canada (Member, Post Office Box 1223, Main Post Office, Edmonton, Alberta, Canada. T5J 2M4 Email: amardon@shaw.ca), [2]Antarctic Institute of Canada (Director, Post Office Box 1223, Main Post Office, Edmonton, Alberta, Canada. T5J 2M4 Email: laua63@hotmail.com) and [3]StarGate Research (President, 3700 Quartz Canyon, # 41, Riverside, California, USA. 92509-1115 Email: jon.a.greenspon@stargateresearch.com)

Summation: This paper describes the contribution of geography through the use of cartography, remote sensing and aerial photography to the ongoing recovery of meteorites in the Antarctic.[1], [2] It gives details of the first geographer to go on an Antarctic meteorite recovery expedition experiment relating to the aerial detection of meteorites from aerial photography and the ground truth experiment comparing meteorites and other surficial terrestrial rocks. While that experiment was null it did point to using criteria to select sites for the recovery of meteorite placers along the Trans-Antarctic mountain range.[3] Meteorites have been estimated in the Antarctic to amount to over 100,000 potentially recoverable ones over the last 30 years and the next 20 years.[4], [5]

Problem: How to describe the contribution of geography through mapping, remote sensing and aerial photography to the international Antarctic meteorite recovery effort?

Introduction: The largest source of extraterrestrial materials has come from the Antarctic over the last 30 odd years as meteorites. Our major source of rock samples from Mars comes from the over 10,000 meteorites that have come from the Antarctic meteorite surface placers. The pristine condition of Antarctic meteorites and the varied nature of the fall sources has meant that the United States of America Antarctic meteorite recovery program is a scientific priority. The first Antarctic meteorite was recovered in the early 20th century by the famous Australian Antarctic explorer Douglas Mawson.[6] Meteorites have been estimated in the Antarctic to amount to over 100,000 potentially recoverable ones over the last 30 years and the next 20 years. Antarctic meteorites have become a major source of materials from Mars, the Moon, from Near-Earth objects and from the Asteroid belt. Geography can and has contributed to the recovery of meteorites in the Antarctic thus benefiting the sum of mankind's knowledge of the inner Solar system.

History of research: The author in 1986[7] was the first geographer to go on an Antarctic meteorite recovery expedition. He was a field member for just under two months at the Lewis Cliff Ice tongue meteorite placer site. The USARP team recovered over 700 meteorites in that locale over the season of 1986-1987. Their was an aerial over flight where photographs of the Lewis Cliff IceTongue were taken. In the field during the season their was ground truth images taken.[8] The first aerial photographs that were taken of the Lewis Cliff ice tongue that were taken were in the late 1940's related to Operation Highjump and American expedition.[9] Those images and successive images are archived at the USGS in Reston, Virginia, USA. The purpose of the research was to see if it would be possible to detect meteorites from the air so that later they could be recovered knowing exactly where they were. Sadly this experiment was unsuccessful.[10] But in other areas such as looking for sites where meteorites can be recovered from geography through its disciplines of cartography, aerial photography and remote sensing. Certain areas of the Antarctic seem to concentrate meteorites and they are also exposed at these locales. Geographic tools can be used to select these sites for field reconnaissance.

Purpose: At the first stage of selection of a potential field site to look for meteorites the researcher looks for the characteristics of an Antarctic meteorite placer area. They have over-flights, look at maps and examine aerial photographs and other remote sensing images. The majority of meteorites that have been recovered by the US Antarctic meteorite recovery program are along the Trans-Antarctic Mountain Range. The meteorites are concentrated along the edge of this mountain range and are exposed by the ablating process of katabatic winds along this mountain range. The criteria of selection along this range of blue ice meteorite placers is fairly consistent. Once meteorites are found maps of where they are exactly found is mapped out and maps of these meteorite placers are made.[11] New sites are selected based on the criteria that has been deduced from previous locations where meteorites have been found is made. Cartography contributes to the recovery using maps to discover meteorites and also contributes by mapping out the locations of where the meteorites are found in the field.[11]

Methods: The author will examine the techniques that have been taken from the discipline of geography and examine and contrast how they have been used to enhance the recovery of meteorites from the Antarctic. Ground truth was taken in the field and mapping techniques were done.[12] There was examination of geographic

techniques. Field mapping was done of the Lewis Cliff Ice Tongue.

Results: The primary result is that thousands of meteorites are being recovered from the Antarctic. Cartography is used to find locales that meteorite placers occur at. Maps are made of meteorite placers and the meteorites that are found there are located on these maps. Remote sensing systems are used to find the blue ice placers where meteorites that fall all over the interior of Antarctic are found.[12] The size of meteorites that are recovered can not be distinguished from photographs taken from airplanes at heights averaging 500 feet.[13] Criteria of selection of areas that receive ground reconnaissance use cartography, aerial photography and remote sensing. The author has proposed the increase in the number of countries Antarctic programs that hunt for meteorites to include the French[14} and Russian[15], [16]_Antarctic programs. Patterns of recovery can be replicated in other areas of the world such as North America or Russia. Previously glaciated regions of the world might have meteorites that might be able to be recovered.[17] The geology of the placer deposits can be known to a greater extent such as the process of deposition of meteorites in Antarctic placers.

Contribution of the writers: The authors will describe the method and process of exploration that is used to find Antarctic meteorites using geographic techniques. Geographic techniques have been used from the beginning when Japanese Antarctic explorers first recovered meteorites.[18] The author will examine how geography has been used and will be used. An example is the mapping out of meteorite recovery locations within each of the placers such as the Lewis Cliff Ice Tongue complex. The second author flew in an over flight of the Lewis Cliff Ice Tongue, Antarctica and examined the last 50 years of aerial photography and remote sensing of the Lewis Cliff Ice Tongue, Antarctica in Washington, D.C. The second author was the first geographer to go on an Antarctic meteorite recovery expedition in 1986.[19]

Conclusion: The meteorite recovery program is a priority because it is filling in the gap of getting samples from planets and bodies that have not yet had sample return missions. Currently the majority of samples from Mars have been recovered from the Antarctic. Techniques of exploration that have been used in other locales such as cartography and map reading are used to select sites for exploration and reconnaissance and then after the meteorites are recovered their location is mapped out. Geography can be used to benefit the recovery of the precious meteorites from the Antarctic.

References: [1] Cassidy W. A. (1986) *Private Communication.* [2] Cassidy W. A. et al (1987) *Meteoritics* 22, 4, 353. [3] Mardon A. A. (1987) *Proceedings of the Association of American Geographers* April. [4] Cassidy W. A. (2003) *Meteorites, Ice and Antarctica* Cambridge University Press. [5] Whillans I. & Cassidy W. A. (1983) *Science*. [6] Bayly and Stillwell (1923) *Science Reports Series* A, 4, 1-13. [7] Mardon A. A. (1987) *The Explorers Journal* September, 41. [8] Mardon A. A. (1987) *LPSC XIX* 723. [9] Roscoe J. H. (1986) *Personal Communication.* [10] Mardon A. A. (1988) *Proceedings of the American Association of the Geographers* April, 121. [11] (AMLAMP) www.lpi.usra.edu/research/amlamp/intro/intro.html [12] Mardon A. A. (1988) *Proceedings of the American Association of the Geographers* April, 121. [13] Mardon A. A. (1989) *Proceedings of the Association of American Geographers* April. [14] Mardon A. A. (2003) *Annual Meteoritical Society Meeting* July. [15] Mardon A. A. (1992) *LPSC XXIII.*. [16] Mardon A. A. (1988) *ESO Workshop on Minor Bodies in the Outer Solar System* November. [17] Mardon A. A. (1988) *Meteoritics* 30, 5. [18] Nagata T. (1982) *Antarctic Geosciences* 1049-1058. [19] Mardon A. A. (1988) *Meteor News* 80.

Acknowledgements: This paper was prepared with the support of the Antarctic Institute of Canada and StarGate Research.

Dedication: To M. G. Knowler, C. A. Curry, & M. C. Chao.

THE IMPORTANCE OF METEORITE RECOVERY FOR INNER SOLAR SYSTEM DEVELOPMENT. A. A. Mardon[1] and J. A. Greenspon[2], [1] Antarctic Institute of Canada (Director, Post Office Box 1223, Main Post Office, Edmonton, Alberta, CANADA.. T5J 2M4. Email: amardon@shaw.ca), [2]StarGate Research (President, 3700 Quartz Canyon, # 41, Riverside, California, USA. 92509-1115 Email: jon.a.greenspon@stargateresearch.com)

Discussion: It has been proposed that an eventual non-terrestrial source of strategic mineral resources could come from the asteroid belt.[1] The only significant material geological samples from the asteroid belt are from meteorites. They can compare the spectral signature of the meteorite samples and then compare it to the spectral signature of the large asteroids in the asteroid belt. The asteroid belt is closer to Low Earth Orbit then the surface of the Earth in terms of the energy required to move mass. Ts being based on the Delta Velocity force that is required to get to low Earth Orbit from the Earth's surface compared to the Delta Velocity force needed to get to Low Earth Orbit from the Asteroid belt. Long term resource and distribution and development of inner solar system geological resources depend on an understanding of the chemical and geochemical nature of objects that would be mined in the inner solar system especially the asteroid belt. Terrestrial sources of strategic minerals is decreasing and ultimately the only new source of new mineral deposits for Earth and Earth orbit is the asteroid belt. The gravitational well from the Moon's surface to Low Earth Orbit is also more costly then from the Asteroid Belt.

Trojans as Resource: The Trojan asteroids are also a potential source of materials. Also we would like to not have all of eggs in one basket in case of a cosmic disaster on the Earth. Within the next several centuries space could be utilized for the development of resources that could be used to develop build energy producing systems such as Solar Power Satellites that could beam energy back down to the Earth from Low Earth Orbit. The infrastructure in Low Earth Orbit to develop Solar Power Satellites would need substantial construction materials that might be acquired from the Asteroid belt. It might seem very speculative but meteorites are a '*Poor Man's Space Probe*' and with the over 30,000 distinct separate meteorite samples that have been recovered it would seem that we have just to today enough separate samples to do geochemical analysis for several generations. With the advent of Antarctic meteorites the mass of material is the problem the samples are being recovered quicker then they can be looked at by scientists in detail.

Conclusion: Space to any extent will only be colonized when there is a need for the resources of the inner solar system for mans push out to find new planetary homes. Sadly, the push and pull of the history of exploration shows that true colonization not just exploration occurs when economic incentives and/ or geo-political considerations occur: not because of any potential scientific benefits.

References: [1] Mardon A. A. et al. (1990) *Canadian Mining Journal*, April, 43.

Research Support: This abstract was supported with the generous support of the Antarctic Institute of Canada and StarGate Research. Dedicated to C. A. Curry & M. G. Knowler.

Minor Elements in Nakhlite Pyroxenes: Cr in MIL00346. G. A. McKay[1], C. Schwandt[2], L. Le[2], J. Makishima[3], T. Mikouchi[3], and T. Kurihara[3], [1]Mail Code KR, NASA Johnson Space Center, Houston, TX 77058, [2]ESC Group, NASA Johnson Space Center, [3]Dept. of Earth and Planetary Science, Univ. of Tokyo, 7-3-1 Hongo, Tokyo 113-0033, Japan.

Introduction: Nakhlites are olivine-bearing clinopyroxene cumulates [e.g., 1]. Based on petrographic characteristics, they may be divided into groups that cooled at different rates and may have been formed at different depths in a single flow [e.g., 2, 3]. The order of cooling rate from slowest to fastest is NWA998<Lafayette < Governador Valadares ~ Nakhla < Yamato000593 < NWA817 ~ MIL03346. Nakhlite cumulus pyroxene grains consist of large cores that are nearly homogeneous in major element composition surrounded by thin rims that are zoned to Fe-rich compositions. Detailed study of these pyroxenes is important because they retain a record of the crystallization history of the nakhlite magma. Moreover, because the composition of the nakhlite parent melt cannot be directly determined, "inversion" of the major and minor element composition of the cumulate pyroxene cores can be used to estimate the composition of that melt. Thus it is important to understand the major and minor element zoning in the cumulus pyroxenes. While major elements are nearly homogeneous, minor elements exhibit distinctive zoning patterns that vary from one nakhlite to another [e.g., 3,4]. This abstract reports unusual Cr zoning patterns in pyroxenes from MIL03346 (MIL) and contrast these with pyroxenes from Y593.

Minor Element Zoning: Nakhlite pyroxenes are zoned in Al, Ti, and Cr. Al and Ti are strongly correlated, but Cr is not correlated with these elements. Pyroxenes from slowly cooled nakhlites generally exhibit a bimodal zoning pattern for Al and Ti, but rapidly-cooled sample MIL has a single mode of Al concentrations (Fig. 1) [3]. The origin of this zoning is not completely understood. However, by analogy with pyroxenes from our experimental runs, we believe that it is likely produced by sector zoning during growth.

In contrast, Cr in slowly cooled samples exhibits only minor Cr zoning, but rapidly-cooled MIL pyroxenes are strongly zoned in Cr (Fig. 3). Cr is depleted in the central portions of the pyroxene grains, but enriched in the outer portions of the homogeneous cores, and then strongly depleted in the Fe-enriched outer rims. Cr zoning is not correlated with Al zoning. Except for the outer Fe-enriched rims, this zoning pattern is in marked contrast to that expected during normal fractional crystallization. Typically, early-formed, central portions of crystals are enriched in Cr and outer portions are depleted because Cr is a highly compatible element in olivine, pyroxene, and spinel, and is thus depleted from the melt during the course of crystallization, leading to decreases in Cr from core to rim. In contrast, MIL

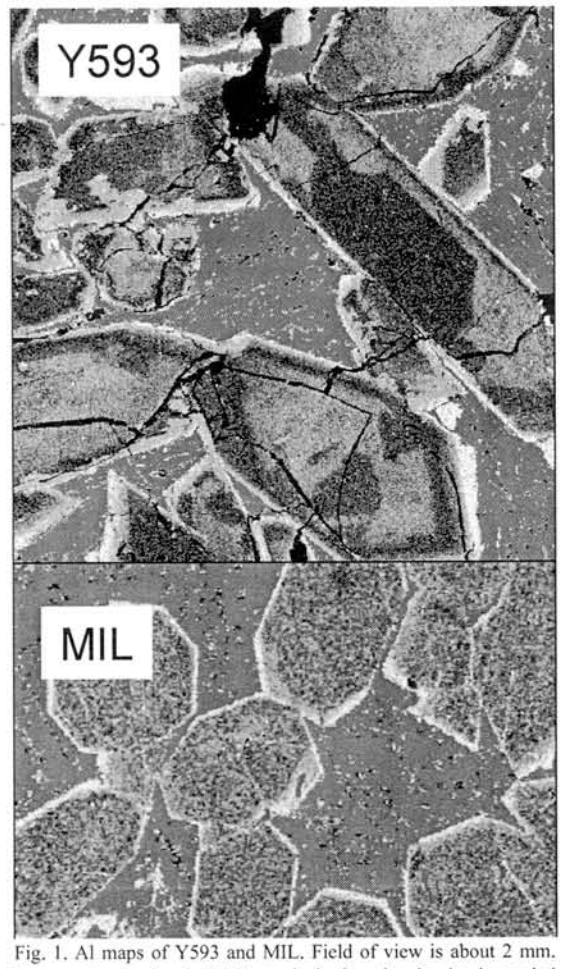

Fig. 1. Al maps of Y593 and MIL. Field of view is about 2 mm. Note patchy zoning in Y593, typical of zoning in slowly cooled nakhlites, and lack of zoning in MIL.

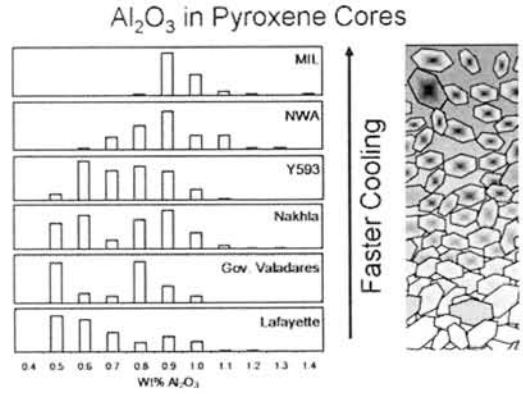

Fig. 2. Histograms of Al content in nakhlite pyroxenes, arranged according to estimated cooling rates [2].

pyroxenes exhibit an abrupt increase near the outer portion of the homogeneous core, then show the expected depletion in the late-stage Fe-enriched outer rim (Fig. 3).

Discussion. The source of the unusual Cr zoning is difficult to understand. Fractional crystallization would be expected to produce the opposite pattern, i.e. Cr depletion from core to rim. One possibility is that the Cr zoning might reflect a change in oxidation state of the magma during crystallization of the pyroxenes. Average D(Cr,Px/L) in our experiments increases by nearly a factor of 3 as oxygen fugacity increases from IW to QFM (Fig. 5). This probably reflects the ease of charge balancing in the presence of increased amounts of Fe^{+3}. MIL has been reported to have large amounts of trivalent Fe compared with other nakhlites [5,6]. Whether this effect is responsible for the unusual zoning in MIL is yet to be determined.

Fig. 3. Cr map of MIL pyroxenes. Note Cr depletion in center of grains relative to margin. Cr-enriched portion is outer part of core that is homogeneous with respect to major elements. Arrow shows location of microprobe profile in Fig. 4.

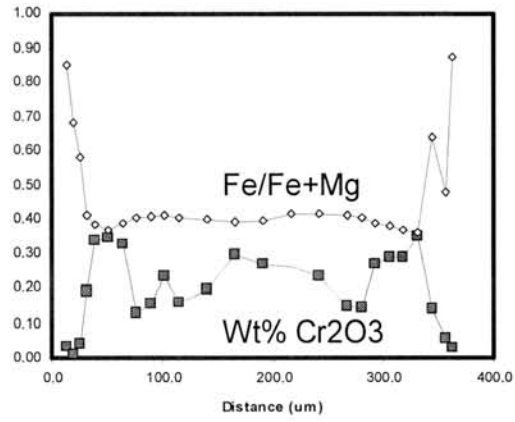

Fig. 3. Microprobe profiles across MIL pyroxene in Fig. 3. Note that Cr enrichment is within homogeneous core (constant Fe/Fe+Mg).

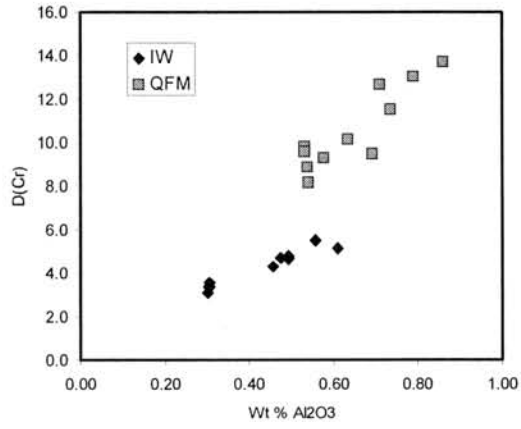

Fig. 5. Pyroxene/melt partition coefficients from nakhlite crystallization experiments. Note that average D values increase from ~4 to ~12 as oxygen fugacity increases from IW to QFM.

References: [1] Wadhwa (2001) Science 291, 1527. [2] Mikouchi *et al.* (2006) LPSC 37, #1865. [3] McKay *et al (2005), MAPS 40, 5335.* [4] McKay *et al.* (2006) LPSC 37, #2435. [5] Morris *et al.* (2006) LPSC 37, 1594. [6] Dyar M.D. et al. (2005) *JGR, 110*, doi:10.1029/2005JE002426.

SHOCK METAMORPHISM OF THE DHOFAR 378 BASALTIC SHERGOTTITE. T. Mikouchi[1] and G. McKay[2], [1]Dept. of Earth and Planet. Science, University of Tokyo, Hongo, Bunkyo-ku, Tokyo 113-0033, JAPAN, [2]Mail Code KR, NASA Johnson Space Center, Houston, TX 77058, USA, E-mail: mikouchi@eps.s.u-tokyo.ac.jp.

Introduction: Shock metamorphism is one of the most fundamental processes in the history of Martian meteorites, especially shergottites, which affect their mineralogy and chronology [e.g., 1]. The formation of "maskelynite" from plagioclase and shock melts is such major mineralogical effects. Dhofar 378 is one of the recently found desert shergottites that is mainly composed of plagioclase and pyroxene [e.g., 2-3]. This shergottite is important because of its highly shocked nature and unique plagioclase texture, and thus has a great potential for assessing a "shock" age of shergottites. We have been working on a combined study of mineralogy and chronology of the same rock chip of Dhofar 378. This abstract reports its mineralogical part. Chronological studies are reported somewhere in this abstract volume [4,5].

Petrography: Two thin sections were prepared from a rock chip of Dhofar 378. After the thin sections were made, the rest part was used for chronological study. The sections studied (5 x 3 mm, respectively) are mainly composed of plagioclase with smaller amounts of clinopyroxenes (Fig. 1). Plagioclase areas comprise about 50-60 % of the sections and the largest plagioclase area reaches 3 x 2 mm in size probably because it is a composite of several "grains" (Fig. 1). These "grains" are however composed of fibrous minute crystalline plagioclase needles usually ~100 μm long and <10 μm wide. These plagioclase grains often contain vesicles (~500 μm) with dirty halos around them. Although most parts of the grains show crystalline fibrous plagioclase, several grains contain glass areas that are isotropic under optical microscope. These glass areas are present as thin bands (~50 μm wide and ~500 μm long) in many cases near the center of plagioclase grains. Brown to black shock melt veins are observed. Plagioclase grains show a flow texture near these veins. Pyroxene grains show mosaic or undulatory extinction. Thin (~1 μm) exsolution lamellae are common, but they are usually deformed probably by shock. The FEG-SEM observation of pyroxene edges adjacent to plagioclase grains showed fairly sharp boundaries and no intergrowth of pyroxene was observed unlike the section previously studied [3].

Mineral Compositions: Most plagioclase "grains" do not show igneous chemical zoning in major elements, instead zoning patterns are complex (Fig. 2). The plagioclase composition ranges from $An_{58}Or_1$ to $An_{40}Or_7$. The glass areas in plagioclase grains are enriched in Na and K (Fig. 2). Some of them have a chemical composition identical to the plagioclase stoichiometry, but most of them are not. The ranges of K_2O and Na_2O are 0.5-6.5 wt% and 5-11 wt%, respectively. There is no clear correlation between Na and K abundances of the K-rich glass. The abundance of FeO and MgO in all feldspathic phases is less than 1 wt%, suggesting little contamination with surrounding minerals (pyroxene) during plagioclase crystallization.

Discussion: Petrography and mineral compositions of the Dhofar 378 sections studied are generally similar to the section that we previously studied [3]. The presence and chemical compositions of K-rich glass are almost identical to the previously studied section. However, the shock textures of the previously studied section are more extensive than those of sections studied this time. In fact, it appears that the sections studied here show intermediate shock metamorphism between [2] and [3]. Probably, shock effects were heterogeneous even in a small meteorite (total recovered mass: only 15 grams).

Heating experiment of Zagami "maskelynite":

As we already reported [3], the fibrous plagioclase needle is possibly a product of recrystallization from originally large plagioclase grains. The presence of both recrystallizing plagioclase rims and the inner K-rich feldspathic glass areas is similar to experimentally heated "maskelynite" in Zagami [6]. We performed these experiments only at 900 °C (for 1, 4, 8, 12, 24, 72 hours). In order to see textural and mineralogical changes of maskelynite at higher temperatures, we performed additional experiments at 1000 °C and 1100 °C. The sample heated at 1100 °C shows nearly complete plagioclase recrystallization (formation of fibrous plagioclase) even only for 1 hour. We could find thin partial melt areas between pyroxene and plagioclase, and pyroxene grains look somewhat rounded. The sample heated for 24 hours at 1100 °C shows drastic changes. The plagioclase grains are turned into clear brown glass and large vesicles formed. Only small areas show recrystallizing plagioclase. In this sample, we could not find any Ca phosphates probably because they were melted. We also found that K-rich feldspathic melt intrudes into cracks of pyroxenes. In contrast, the sample heated at 1000 °C shows no evidence of partial melting and rather similar to samples heated at 900 °C. However, the sample heated for 1 hour already shows nearly complete recrystallization of plagioclase. In this sample, thin K-rich glass bands are present in plagioclase grains. The

sample heated for 24 hours does not significantly change from the sample heated for 1 hour.

Shock heating and cooling of Dhofar 378:

In our previous study [3], we discussed the origin of recrystallizing plagioclase in Dhofar 378 and concluded that a strong shock event (possibly during impact ejection from Mars) caused plagioclase shock melting and subsequent cooling from high temperature allowed partial recrystallization of plagioclase. We ruled out the possibility that maskelynite was already present by an early shock event and later it was somehow reheated on Mars causing recrystallization of maskelynite, and another shock event ejected it from Mars, because Dhofar 378 shows heterogeneous shock metamorphism in a cm scale [2,3].

Our additional heating experiment of Zagami suggests that the texture of recrystallizing plagioclase and K-rich glass in Dhofar 378 is most similar to the heated Zagami at 1000 °C for 1-24 hours. Because no obvious partial melting is observed in the sections studied, the peak temperature during shock was lower than 1100 °C, probably ~1000 °C. This is consistent with the presence of Ca phosphates and the absence of feldspathic glass in pyroxene cracks in Dhofar 378. The cooling rate of Dhofar 378 after the shock event is difficult to estimate from our present results. If the peak shock temperature was 1000 °C, we know that 1 hour is enough to recrystallize most plagioclase grains, but this does not give quantitative cooling rate. We plan to perform cooling experiments of Zagami from 1000 °C and 1100 °C to constrain a post-shock cooling rate of Dhofar 378. However, another information about its cooling rate is reported in [7], which performed crystallization experiment of Los Angeles. As is already pointed out [2,3], Dhofar 378 is similar to Los Angeles in many respects except for different degrees of shock metamorphism. In our previous study [3], we interpreted that the absence of pyroxferroite breakdown products in Dhofar 378 was due to its shock melting and euhedral fayalite with pyroxene and the mesostasis in some areas of Dhofar 378 are products of recrystallization from shock melt of pyroxferroite breakdown products. Because the 2.5 °C/hour cooling experiment of the Los Angeles synthetic composition could produce similar fayalite textures, this cooling rate may be comparable to post-shock cooling history of Dhofar 378 [7]. If we take this cooling rate, it is 40 hours from 1000 °C to 900 °C. This duration is consistent with the recrystallization of plagioclase with only small amounts of K-rich glass left. However, 2.5 °C/hour cooling is very slow for shock environment, and we expect that Dhofar 378 cooled slightly faster than 2.5 °C/hour.

The strong shock event and "slow" post-shock cooling rate of Dhofar 378 is unique among shergottites. The Ar-Ar age obtained from the same rock chip used for this study gave ~143 Myr, which is interpreted as an earlier impact event rather than the ejection event from Mars [4]. The Sm-Nd result also shows a similar age of 157 Myr [5]. The strong shock metamorphism observed in Dhofar 378 may record this ~143 Myr event.

Acknowledgment: We thank Drs. D. D. Bogard, J. Park, and L. E. Nyquist and Profs. H. Takeda and Y. Ikeda for useful discussion.

References: [1] Bischoff A. and Stoffler D. (1992) *Eur. J. Mineral., 4*, 702-755. [2] Ikeda Y. et al. (2002) *Antarct. Meteorites XXVII*, 40-42. [3] Mikouchi T. and McKay G. (2003) *LPS XXXIV*, #1920. [4] Park J. and Bogard D. D. (2006) *Antarct. Meteorites XXX* (in this volume). [5] Nyquist L. E. et al. (2006) *Antarct. Meteorites XXX* (in this volume). [6] Mikouchi T. et al. (2002) *MAPS, 37*, A100. [7] Koizumi E. et al. (2005) *LPS XXXVI*, #2015.

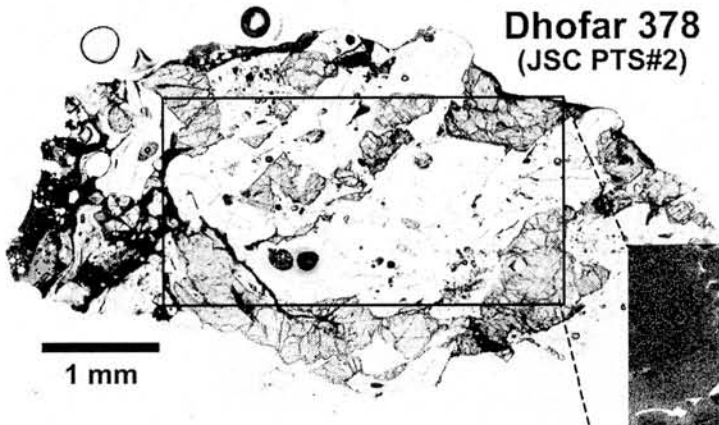

Fig. 1 (Left) Optical photomicrograph of one of the thin sections studied. This section contains a large area of plagioclase grains near the center. Shock melt is present at the left edge. Pyroxenes show sharp outer edges at the boundary to the plagioclase grains.

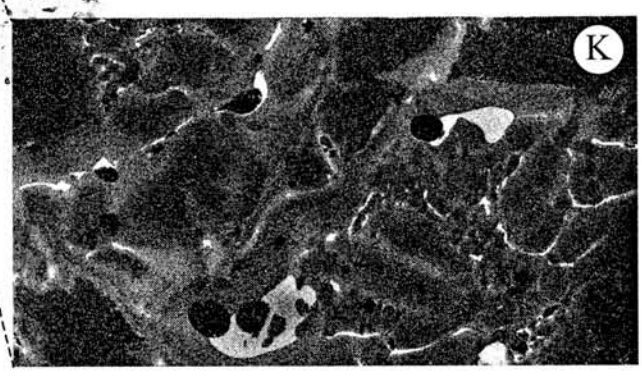

Fig. 2 (Right) K X-ray map of the area shown in Fig. 1. Note the presence of thin K-rich glass bands near the center of the plagioclase grains. These K-rich glasses contain 0.5-6 wt% K_2O. Plagioclase areas also show heterogeneous distribution of K.

New lherzolitic shergottites from the Yamato Mountains. K. Misawa[1], N. Iwata[2], N. Imae[1], I. A. Franchi[3], R. C. Greenwood[3] and H. Kojima[1]. [1]Antarctic Meteorite Research Center, National Institute of Polar Research, Tokyo 173-8515 (misawa@nipr.ac.jp), [2]Yamagata Univ., Koshirakawa, Yamagata 990-8560, [3] Open University, Walton Hall, Milton Keynes, GB-MK7 6AA United Kingdom

The Wintering Party of the 41st Japanese Antarctic Research Expedition (JARE) conducted a meteorite search around the Yamato Mountains area, Antarctica. Among 3550 meteorite samples found, Yamato 000027 (hereafter Y000027), Y000047 and Y000097 are newly identified as lherzolitic shergottites [1]. Up to now eight lherzolitic shergottites are identified: two (NWA 1950 and NWA 2646) are from hot desert and the rests (ALH 77005, LEW 88516, Y-793605, GRV 99027, GRV 020020 and Yamato 00) are from Antarctica [1,2].

On 26th November 2000, Y000027 (9.68 g) and Y000047 (5.34 g) were collected in the bare ice field a few km north from the northern end of the JARE IV Nunataks. Next day Y000097 (24.48 g) was found. Three lherzolitic shergottites were collected in a small area, within ~2 x 4 km^2, suggesting they are paired (Fig. 1). Samples are partly covered with fusion crust and inner portions of green colored are visible with the naked eye (Fig. 2).

The PTSs (Y000027,41, Y000047,41 and Y000097,51) show distinct textures, poikilitic and non-poikilitic (Fig. 3). In poikilitic areas, low-Ca pyroxene crystals up to several mm in size enclose rounded olivine (up to 1 mm) and euhedral chromite grains, and plagioclase glass (maskelynite) is rarely observed (Fig. 3b). In non-poikilitic areas, olivine and plagioclase glass are more abundant (Fig. 3c). Olivine grains contain magmatic inclusions (~80 μm in size). Shock effects are prevalent. Plagioclase is totally isotropic. Some olivine grains adjacent to a shock-melt pocket show strong mosaicism. The meteorites contain shock-melt pockets (Fig. 3c). Y000027 contains a shock-melt vein (Fig. 3a).

Oxygen isotopic compositions were determined by the method described in [3]. Duplicate analyses of each sample clearly show that three meteorites are Martian in origin (Table 1). In terms of oxygen isotopic compositions, there is a good possibility that the three samples are paired.

We are now planning a consortium study to better understand its crystallization history, to make comparison with other lherzolitic shergottites and to constrain evolutional history of Mars. A homogeneous powdered sample, Y000097,21 (1.985 g), was prepared from interior chips. For bulk chemical analysis this sample is available upon request.

References: [1] *Meteorite Newsletter* (2006) **14**, (edited by Kojima H.), NIPR. [2] *The Mars Meteorite Compendium*. (2006) (compiled by Meyer C.), ARES, NASA, JSC. [3] Miller M. F. et al. (1999) *Rapid Comm. Mass Spectrometry*, **13**, 1211-1217.

Table 1. Oxygen isotopic compositions of Yamato 00 lherzolitic shergottites.

sample	$\delta^{18}O$ (‰)	$\delta^{17}O$ (‰)	$\Delta^{17}O$
Y000027,91	4.129	2.446	0.299
(52 mg)	4.079	2.409	0.288
Y000047,91	4.178	2.481	0.308
(53 mg)	4.273	2.536	0.314
Y000097,91	4.178	2.471	0.298
(81 mg)	4.157	2.481	0.319

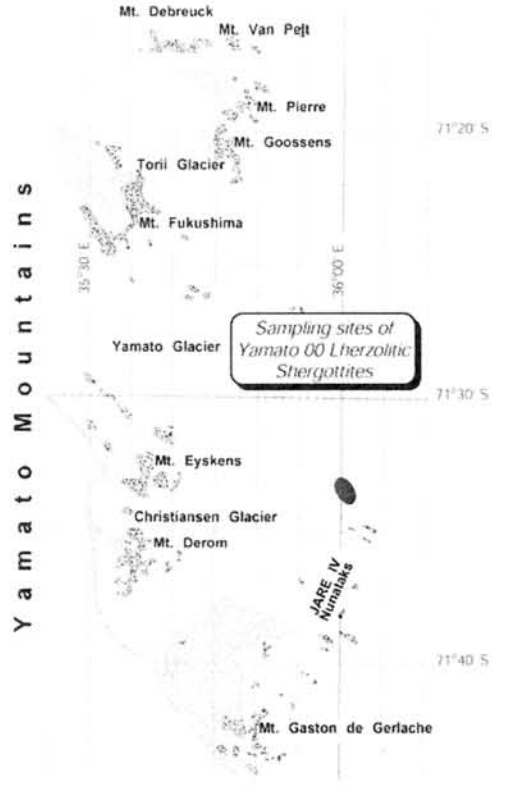

Figure 1. Sampling sites of Yamato 00 lherzolitic shergottites.

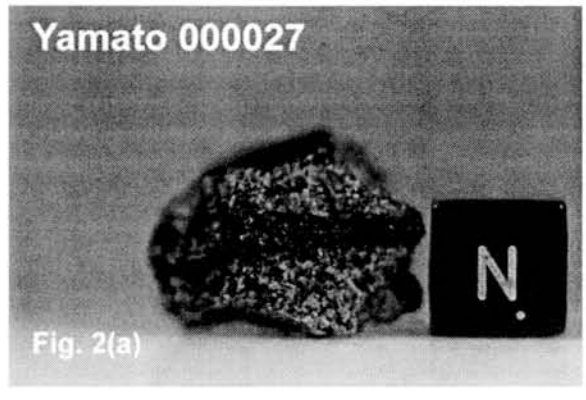

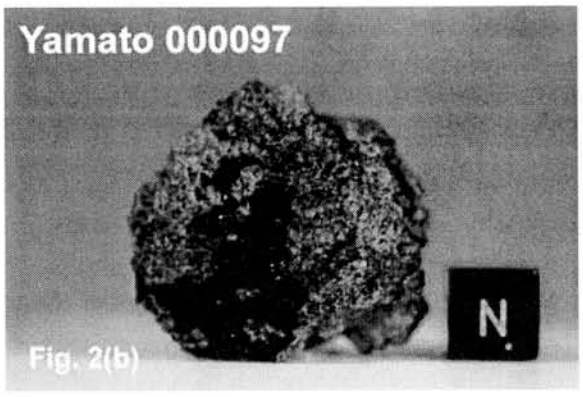

Figure 2. Photographs of (a) Yamato 000027 and (b) Yamato 000097. Yamato 000027 contains a shock-melt vein (~2 mm width) which is cutting through the rock. The samples are partly covered with fusion crusts. Cubes are 1 cm.

Figure 3. Photomicrographs of thin sections of (a) Yamato 000027,41-1, (b) Yamato 000047,41-1 and (c) Yamato 000097,51-1. Transmitted plane polarized light. Scale bar is 1 mm.

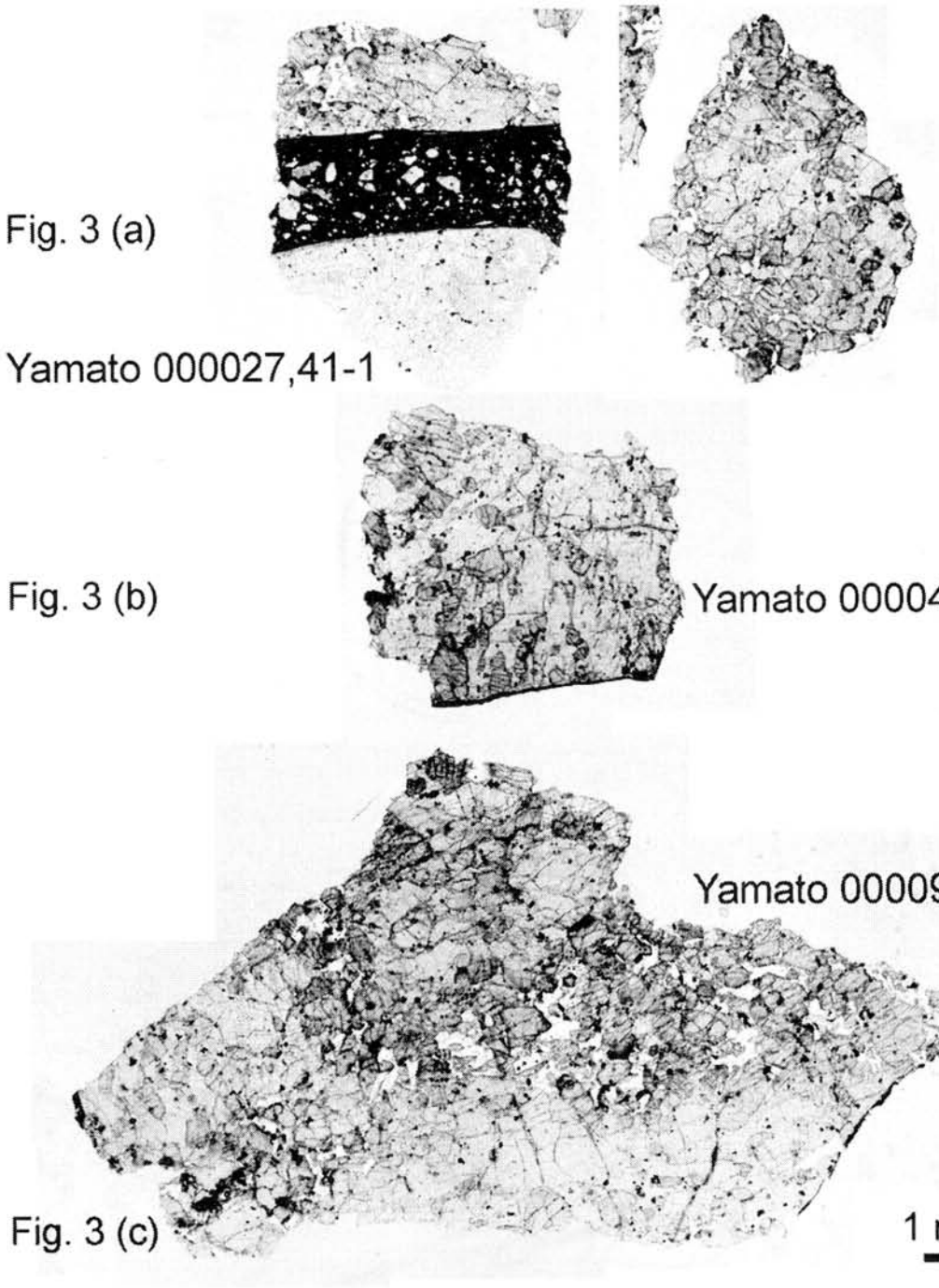

Molten Droplet in Gas Flow: Diversity of Chondrule Shapes. H. Miura[1,2] and T. Nakamoto[3], [1]Theoretical Astrophysics Group, Department of Physics, Kyoto Univ., [2]Research Fellow of the Japan Society for the Promotion of Science, [3]Center for Computational Sciences, Univ. of Tsukuba, E-mail:miurah@tap.scphys.kyoto-u.ac.jp

Introduction:

Tsuchiyama et al. (2003) [1] studied three-dimentional shapes of chondrules using X-ray microtomography. The external shapes of chondrules were approximated as three-axial ellipsoids with a-, b-, and c-axes (axial radii are A, B, and C ($A \geq B \geq C$), respectively) using the moments of inertia of the chondrules. They found that the shapes are diverse from oblate ($A \sim B > C$), general three-axial ellipsoid ($A > B > C$) to prolate ($A > B \sim C$).

Shock-wave heating model is considered to be one of the most plausible models for chondrule formation and has been investigated theoretically by many authors. One of the special features of this model is that chondrule precursor dust particles are heated and melt in a high-velocity rarefied gas flow. Therefore, it can be considered that the gas frictional force works on the molten dust particles from a certain direction. In this case, it is naturally expected that the droplet is dented in the direction of the gas flow and swells toward other two perpendicular directions (Sekiya et al. 2003 [2]). If it re-solidifies keeping the shape, we obtain an "oblate" chondrule. However, Tsuchiyama et al. (2003) showed the existence of prolate chondrules. How can we explain the origin of prolate ones?

Purpose:

In addition to the gas frictional force, the effect of the dust rotation can be considered in the shock-wave heating model. It is thought that the precursor dust particles are not perfect sphere and have many bumps on its surface before melting. The asymmetrical structures would cause the net torque in the gas flow and the precursor dust particles should begin to rotate. By the simple order of magnitude estimation, we found that the expected angular velocity is about a few hundreds s^{-1} or higher. Notice that the rotation axis should be perpendicular to the direction of the gas flow. In this study, we assume that the rotation continues during the melting phase and consider how the rotating molten droplets deform in the high-velocity gas flow.

Method & Results:

Let's assume that the gas frictional force is acting on the rotating molten droplet. We also assume that the droplet shape can be deformed much faster than the droplet rotates. We define that the gas flow is along the x-axis and the rotation axis is the z-axis. If we consider only the effect of the gas frictional force, the droplet radius along the x-axis, r_x, becomes shorter by the gas ram pressure, while other radii (r_y and r_z) get longer because the volume of the droplet does not change. On the contrary, if only the effect of rotation is considered, r_x and r_y get longer by the centrifugal force, while r_z becomes shorter. If we simply superpose the radius changes by above two effects, the shapes of rotating droplets exposed to the gas flow can be imagined. Figure 1 schematically shows how the radius of the droplet for each direction changes as the rotation becomes faster. The strength of the gas frictional force is fixed here. It is found that the droplet shape changes from oblate, general three-axial ellipsoid, to prolate as the rotation velocity increases. Although this picture shows a general three-axial ellipsoid at faster rotation region, our hydrodynamic simulations of droplets (Miura & Nakamoto, in prep.) predict that such fast rotation produces a prolate shape whose major axis is longer than that of slower case. We estimate the degree of the deformation of molten droplets based on the physical conditions expected from the shock-wave heating model, and found that the trend of the droplet shapes is very similar to the chondrule data measured by Tsuchiyama et al. (2003).

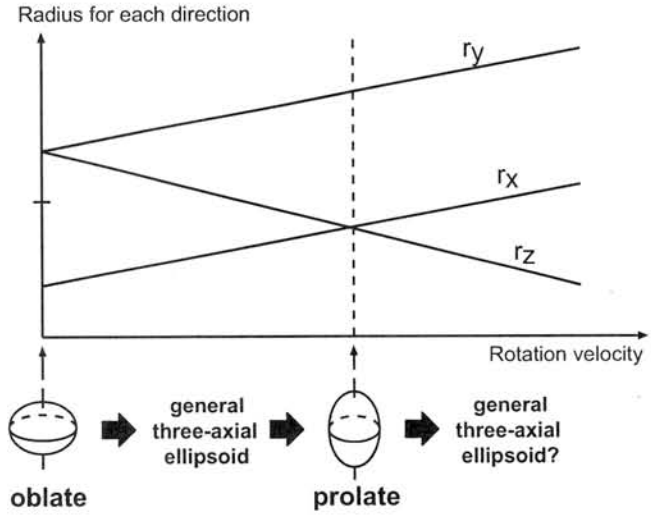

Figure 1: Droplet radius of each direction on which the gas frictional force takes place is plotted as a function of the rotating velocity. It is assumed that the gas flow is along the x-direction and the rotation axis is the z-axis. The strength of the gas frictional force is fixed.

Discussion & Summary:

In this study, we implicitly assumed that the droplet shape can be deformed much faster than the droplet rotates. However, when the droplet re-solidifies to form chondrules in the cooling phase, the viscosity of the droplet would become higher and higher as the temperature falls down. It would result into the longer timescale of deformation. Moreover, the rotation speed of the droplet and the gas frictional force gets smaller (or weaker) as a result of the momentum exchange with ambient gas molecules. In future works, we would have to take into account above effects in order to discuss the final shapes of the molten chondrule precursor dust particles.

However, we would like to note the possibility that the diversity of chondrule shapes can be explained in the framework of the shock-wave heating model. If our attempt about the re-production of chondrule shapes succeeds, it would be a strong evidence that chondrules have been formed in the shock-wave heating events.

Reference: [1] Tsuchiyama et al. (2003) *LPS XXXIV*, 1271-1272. [2] Sekiya et al. (2003) *Progress of Theoretical Physics, 109,* 717-728.

Noble gases in the lunar meteorite Yamato 983885, a KREEP-rich lunar regolith breccia.

Y. N. Miura[1], T. Arai[2], Y. Karouji[3] and M. Ebihara[3], [1]Earthquake Research Institute, University of Tokyo, Japan. [2]Antarctic Meteorite Research Center, National Institute of Polar Research, Tokyo, Japan. [3]Department of Chemistry, Tokyo Metropolitan University, Japan.

Introduction:

The Yamato (Y) 983885 is a polymict lunar regolith breccia containing KREEP basalt, Mg-suite, high-Al basalt, very low-Ti basalt, granulite and Si, Na-rich impact spherules [1]. Simultaneous occurrence of such minerals constrains that the source region of Y 983885 is most likely the KREEP-rich Procellarum terrane on the Moon [1]. The chemical composition of matrix in Y 983885 reveals similarity to those of Apollo 16 soil and regolith breccias except for FeO and Al_2O_3 [2]. The substantial contribution (>30 %) of VLT basalts in the bulk composition further infers the Schiller-Schickard region south of the PKT, where the mafic geochemical anomaly due to the underlying VLT basalts has been reported [2]. In this study, we determined noble gas elemental and isotopic compositions in order to investigate cosmic-ray exposure and regolith histories of this meteorite.

Sample and experimental method:

About 1.3 g of powder specimen was prepared at NIPR, of which 0.062 g was allocated to us for noble gas measurement. Another fraction of the powder was used for chemical analyses [2], whose data are referred as target element abundances to calculate cosmogenic production rates. Noble gases were measured twice. Stepwise gas extractions by 3 steps (#1 using 3.781 mg sample) and 12 steps (#2 using 13.963 mg sample) were applied, respectively (Table 1). Noble gas analyses were performed with a mass spectrometer (MS-II) at Laboratory for Earthquake Chemistry, University of Tokyo.

Solar noble gases:

Y 983885 contains large amounts of solar noble gases (Table 1 and Fig. 1). Results from two analyses well agree with each other, implying that the data determined for the powder specimens are representatives of bulk Y 983885 in spite of small sample sizes for analyses. Murty et al. [3] reported noble gas data of the meteorite, which also plotted on Fig. 1. One specimen measured by [3] shows somewhat higher abundances than the other one by [3] and the samples in this study. This may reflect heterogeneous distribution of solar noble gases in Y 983885. The concentrations of solar noble gases in Y 983885 are within the range of bulk Apollo lunar soils [4] and lunar meteorites [5], but near the high end of the variation for these lunar materials as shown in Fig. 1.

The release profiles of #2 show that the largest amounts of ^{4}He, ^{20}Ne, ^{36}Ar, ^{84}Kr and ^{132}Xe were released at 700, 700, 1300, 1300 and 1300°C, respectively. Release of ^{36}Ar shows bimodal peaks (the peak at 1300°C with a small peak at 900°C). Most fractions in the analyses reveal solar noble gas isotopic compositions.

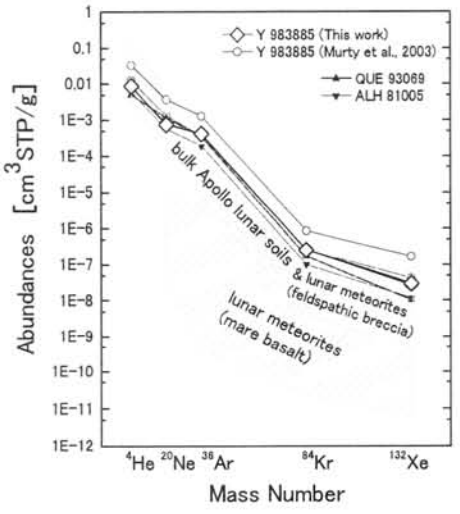

Fig. 1. Abundances of noble gases for Y 983885 measured in this work and [3]. A typical range of bulk Apollo lunar soils [4] and lunar meteorites (feldspathic breccia) [5] (upper hatched area), that of lunar meteorites (mare basalts) [5] (lower hatched area) and two lunar meteorites with abundant solar noble gases [6, 7] are shown.

Three isotope plot of Ne is shown in Fig. 2. Ne data of #1 and below 1200 °C of #2 plot close to the SW-SEP line, whereas those above 1300 °C of #2 plot towards cosmogenic from SEP-Ne. We evaluate cosmogenic ^{21}Ne as excess from the SEP-SW line.

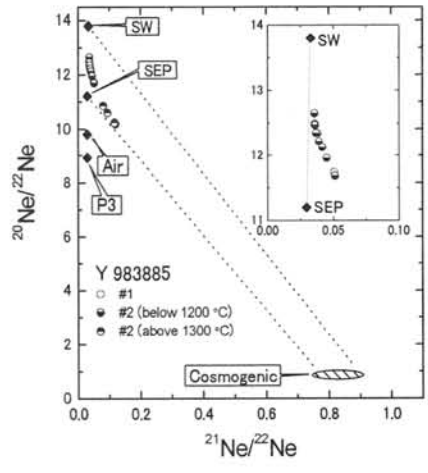

Fig. 2. Three isotope plot of Ne. Trapped Ne is referred from [8]. The cosmogenic Ne area was calculated using production rate parameters [9] and the chemical compositions [2]. The area covers shielding conditions from 10 to 500 g/cm^2.

Cosmogenic noble gases:

Cosmogenic Ne, Kr and Xe are remarkable. Although He and Ar are also likely contained, they are masked by trapped noble gases. It was difficult to calculate amounts precisely. As shown later, the concentrations of cosmogenic noble gases are too high to be attributed to space irradiation of 4π-geometry. Therefore most cosmogenic nuclides can be considered as productions on the Moon. In order to clarify shielding depth, we first examine cosmogenic $^{131}Xe/^{126}Xe$ ratios. Fig. 3 presents a diagram of $^{126}Xe/^{130}Xe$ vs. $^{131}Xe/^{130}Xe$. The measured Xe of Y 983885 plot between cosmogenic Xe with shielding depths of 40 and 65 g/cm^2, from which we estimated an average shielding depth during exposure for Y 983885 to be ~50 g/cm^2.

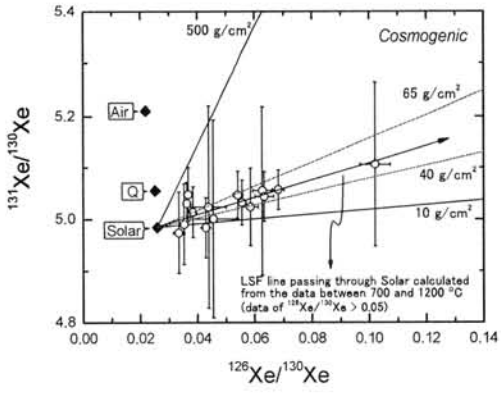

Fig. 3. $^{126}Xe/^{130}Xe$ vs. $^{131}Xe/^{130}Xe$. Directions of cosmogenic Xe with various shielding depths are shown, which were calculated from production rate parameters given in [9] and chemical composition determined for the same powder sample [3], where 113 ppm of Ba and 11 ppm for La are adopted.

Assuming the shielding depth of ~50 g/cm^2, the production rates of ^{21}Ne, ^{83}Kr and ^{126}Xe are calculated to be 1.2×10^{-9}, 5.2×10^{-13} and 1.1×10^{-13} cm^{3}STP/g, respectively (the Kr production rate parameters are referred from [10] and the other ones from [9]). The concentrations of cosmogenic noble gases and calculated cosmic-ray exposure ages are summarized in Table 2. The obtained exposure ages range from 470 and 1100 Ma. Because He and Ne are easier released by diffusion, the short T_{21} might be due to partial loss of cosmogenic ^{21}Ne. From the observed internal consistency of Xe isotope systematics, T_{126} seems to be most plausible.

Summary:

A large amount of solar noble gases and long duration for cosmic-ray irradiation, ca 700 Ma, at an average depth of ~50 g/cm^2 (a few 10 cm) indicate that Y 983885 is the usual mature lunar regolith sited near surfaces. A similarity with Calcalong Creek and SaU 169 was argued based on chemical compositions [2]. However, solar noble gas abundances and duration of cosmic-ray exposure are different between Y 983885 and these meteorites; only the duration of Calcalong Creek, showing several hundred Ma [11], is more or less close to that of Y 983885.

References:

[1] Arai T. et al. (2005) *Antarct. Meteorite Res., 18*, 17-45. [2] Karouji Y. et al. (2006) *LPS XXXVII*, 1919. [3] Murty S. V. S. et al. (2003) *Antarct. Meteorites, XXVII*, 92-93. [4] Fegley B. Jr. and Swindle T. (1993) in *Resources of near-Earth space*, 367-426. [5] Schultz L. and Franke L. (2004) *Meteorit. Planet. Sci., 39*, 1889-1890. [6] Thalmann C. et al. (1996) *Meteoritics, 31*, 857-868. [7] Eugster O. et al. (1986) *Earth Planet. Sci. Lett., 78*, 139-147. [8] Wieler R. (2002) in *Reviews in Mineralogy and Geochemistry, Vol. 47*, 21-70. [9] Hohenberg C. M. et al. (1978) *Proc. Lunar Planet. Sci. Conf., 9th*, 2311-2344. [10] Regnier S. et al. (1979) *Proc. Lunar Planet. Sci. Conf., 10th*, 1565-1586. [11] Swindle T. et al. (1995) *Meteoritics, 30*, 584-585.

Table 1. Measured concentrations and isotopic ratios of noble gases in Y 983885.

Sample	^4He (10^{-3})	$^3He/^4He$	^{20}Ne (10^{-4})	$^{20}Ne/^{22}Ne$	$^{21}Ne/^{22}Ne$	^{36}Ar (10^{-4})	$^{38}Ar/^{36}Ar$	$^{40}Ar/^{36}Ar$	^{84}Kr (10^{-7})	^{132}Xe (10^{-8})
#1	8.8	3.69	8.2	12.28	0.03963	4.2	0.1882	1.079	2.5	2.8
3 steps		±.01		±.0.01	±.0.00007		±.0.0006	±.0.003		
#2	8.8	3.65	7.5	12.26	0.03988	4.2	0.1886	1.087	2.5	3.0
12 steps		±.03		±.0.01	±.0.00007		±.0.0003	±.0.001		

Concentrations are given in the unit of cm^{3}STP/g.
Extraction temperatures are 600, 1000 and 1750 °C for #1, and 400, 600, 700, 800, 900, 1000, 1100, 1200, 1300, 1400, 1500 and 1750 °C for #2, respectively.

Table 2. Cosmogenic noble gases and cosmic-ray exposure ages (2π) for Y 983885.

Sample	^{21}Ne (10^{-7})	^{83}Kr (10^{-10})	^{126}Xe (10^{-11})	T_{21}	T_{83}	T_{126}
				(Ma)		
#1	5.7	5.5	8.3	490	1100	770
#2	5.4	-	7.6	470	-	710

Concentrations are given in the unit of cm^{3}STP/g.

Material evidences of catastrophe at the end of the Permian Period : Carbon- rich spherules with Fe and Ni, Yasunori Miura, Inst. Earth Sciences, Graduate School of Sci. & Eng., Yamaguchi University, Yoshida 1677-1, Yamaguchi, 753-8512, Japan, yasmiura@yamaguchi-u.ac.jp

Introduction:

The end of the Permian Period (ca.250Ma, used as PTB) is the largest known mass extinction of fossil record on the Earth, as ca.96% of all species on the Earth was died out shown in Fig.1[1, 2, 3, 4]. The main purpose of present paper is to show material evidences of impact by textures and compositions of the spherules, especially carbon and iron-nickel contents. The samples are used from Meishan sections (the PTB) in Southern China, and compared samples of Akiyoshi limestone (the Permian in Japan) [1-7].

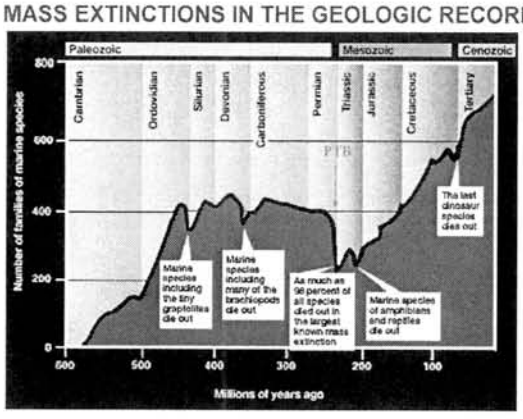

Fig.1. Mass extinction with geological time on the Earth. The PTB is shown by arrow (250Ma ago).

Composition of spherules of the PTB samples:

The composition of the spherules of the Meishan PTB samples are summarized as follows (Figs.2 & 3):

1) Almost all spherules (95 % form 20 spherules) are Fe-rich, together with silica spherules.
2) Fe-rich spherules contain considerable contents of Si-Al at impact event from basement rocks.
3) Silica-rich spherule can be found also in the PTB samples.
4) S is contained only in FeS grains of spherules.
5) Ni-rich spherules contain Fe and C-Al-Si-K-Ca-Co-Cu as mixed phases.
6) Carbon-rich spherules are found in 10% of all spherules.

The compositions of the spherules indicates that magnetic spherules of Meishan PTB samples are considered to be impact origin on target rocks of the crust rocks on the Earth. This is mainly because there are no mantle-derived rocks with much Mg. All elements found at the present spherules can be explained by impact event on limestone and silica-rich target rocks on the crust.

Carbon spherules of the Meishan PTB sample:

It is summarized as follows (Fig.3):

1) Carbon spherules are varied from 1μm to 20μm in size, though nanostructure of 10nm size is observed.
2) Carbon contents of spherules from the Meishan PTB are ranged from 56wt.% C to 90wt.%C with in-situ ASEM (JEOL7000F) which are coexisted with Fe contents of 2 to 36wt%.
3) C-Fe diagram of 7 carbon-rich spherules shows that carbon phases are mixed with Fe. Analyzed data of carbon 90wt.% from spherule and the PTB samples are obtained in this study.
4) Small contents of Si, Al and Ca are related with C content.
5) Carbon-rich samples are found in magnetic fragments and direct in red-layered at the PTB sample.
6) Carbon contents within a spherule are almost homogeneous, but heterogeneous among spherules. Fe contents of spherules are not found in network-type nano-carbon from backscattering image (BEI) of the high-resolution ASEM data. This suggests that mixed elements of Fe, Si, Al and Ca are remained during impact relation with major carbon at sea-deposit of limestone and Si-rich rock.
7) There are few Mg contents of the Meishan PTB spherule, as well as localized S content on each grain in the spherule. This indicates that these spherules are formed on surface rocks (without direct mantle or volcanic rocks).

Carbon grains of the drilled Akiyoshi limestone breccias samples:

It is summarized as follows (Fig.3):

1) Drilled Akiyoshi breccias of limestones from Yamaguchi, Japan are used as related limestone with Meishan PTB samples originally from Southern Equator transported by continental-drift after impact event. Carbon spherules and grains are varied from 0.5μm to 30μm in size, though nanostructure of 10nm size is observed.
2) Carbon contents of spherules from the Akiyoshi breccias are ranged from 41wt.% C to 93wt.%C with in-situ ASEM (JEOL7000F) which are coexisted with Ca contents of 2 to 54wt% .
3) C-Fe diagram of 11 carbon-rich spherules shows that carbon phases are mixed with Ca. It is first detailed report for carbon ca.90wt.% from the Akiyoshi.
4) Small contents of Fe, Si, Al, Na, K and S are related with C content (as shown in Fig.3).

5) Carbon-rich samples are found in spherules and vein fragments of the drilled samples to 243m in depth (which are offered from the Akiyoshi Science Museum, Japan).
6) There is few Mg content of the Permian Akishoshi limestone breccias, which indicates that these spherules are formed on surface rocks (without mantle or volcanic rocks).
7) Origin of carbons in the Akiyoshi breccias can be derived from limestone during impact reaction due to strong correlation with C and Ca.

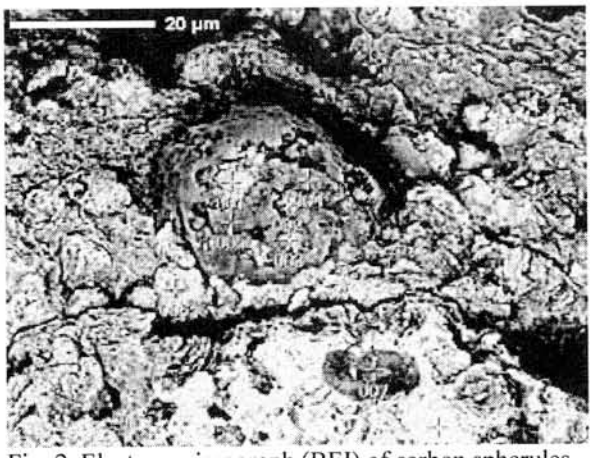

Fig. 2. Electron micrograph (BEI) of carbon spherules (89C%) with Fe, Ca and Si elements. The samples are the Meishan PTB sample from China. Red-layered PTB sample from the Meishan was collected and analyzed by author.

Bulk contents of Fe, Ni Co elements:

The bulk samples of Meishan PTB and Akiyoshi limestone breccias at two analyses are Fe=1.89, 2.98 (%), Ni=15, 8 (ppm), and Co= 3, 2 (ppm) in the Meishan samples, and Fe= 0.21, 0.05 (wt.%), Ni=3, 3 (ppm), and Co=1, 1 (ppm) in the Akiyoshi samples by the ICP analyses.

Ni-Fe rich spherules from the Meishan PTB sample:

The detailed images of Ni-rich spherules are obtained in the Meishan PTB sample as follows (Fig.4).
1) Ni-Fe-rich spherules as aggregates are varied from 100nm to 5μm in size.
2) Ni and Fe contents of spherules from the Meishan PTB are ranged from 24 to 31wt.%NiO, and from 29 to 33 wt% FeO with in-situ ASEM (JEOL) which are coexisted with C and Cu.
3) Ni and Fe rich spherules are obtained from the Meishan PTB spherules at each grain.

Summary:

The present results are summarized as follows:
1) The Meishan PTB spherules contain C-rich (up to ca.90%C) and Ni-Fe rich spherules (31%Ni and 29%Fe).
2) Akiyoshi drilled limestone breccias contain C-rich grains with Ca from limestone target rocks.
3) These data are similar evidences for the PTB impact.

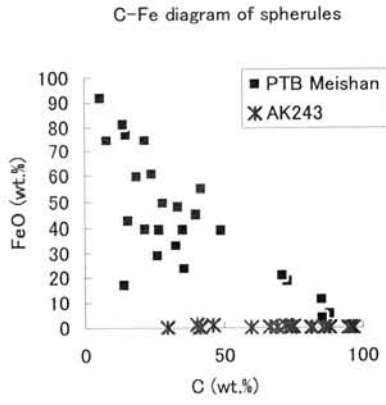

Fig3. C-FeO diagram of spherules from PTM Meishan, China and Akiyoshi drilled 243m in depth. Data are from in-situ analytical scanning electron micrograph.

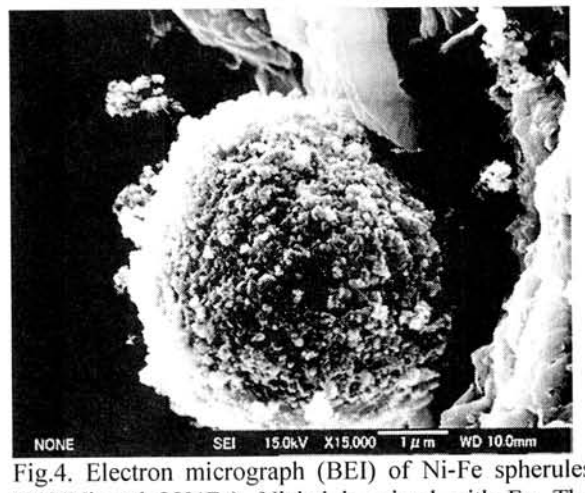

Fig.4. Electron micrograph (BEI) of Ni-Fe spherules (31%Ni and 29%Fe). Nickel is mixed with Fe. The samples are the same in Fig.2.

Reference:

[1] Kaiho Y et al. (2001): *Geology,* 29, 815-818.
[2] Kaiho,K. et al. (2002): *Geology,* 30, 856-856.
[3] Miura Y. (2003): *Yamaguchi Chigaku kaishi* (Japanese) , 50, 13-18.
[4] Miura Y. (2003): *LPS XXXIV*,abstract #2150.
[5] Miura Y. Ed.(2003): *IEJSAP'03 symp abstract* (Yamaguchi University, Yamaguchi), 21-30.
[6] Miura Y. (2006): *LPS XXXVII*,abstract#2441.
[7] Miura Y. (2006): ICEM2006 (Yamaguchi),pp.2.

GEOLOGY, PETROLOGY AND MINERALOGY OF TAKAMATSU IMPACT CRATER IN JAPAN.

Yasunori Miura, Dept. Earth System Sci., Fac. Sci., Yamaguchi University, Yoshida 1677-1, Yamaguchi, 753-8512, Japan (yasmiura@yamaguchi-u.ac.jp)

Introduction: Center of Takamatsu buried structure with ca.8km size is located in Busshozan - Cho, Takamatsu City, Kagawa Prefecture, Shikoku Islands, Japan as in Latitude 34.3° and Longitude 134.05° . The main purpose of this paper is 1) to describe geological, petrological and mineralogical data on surface and 1,750m in depth, 2) to show shocked quartz and corona (necklaces) texture , and 3) probable broken site of shocked rocks in Japan islands [1-9].

Geological map of the surface: Geological map of Takamatsu crater is drawn by considering analyzed data of surface and drilled samples. Surface soils of Alluvium sediment are covered completely which indicate that Takamatsu crater was broken and buried under sea-sediments after its formation. Four types rocks in X-ray fluorescence (XRF) compositions are found on surface, that is, S1 (Miocene andesite intrusion), S2 (granites and shocked granite with shocked quartz at 4km and 8km wide), S3 (altered rock by buried metamorphism within 8km wide) and S4 (altered rocks with shocked rocks). Five types of surface rocks are found as Quaternary sediments of Mitoyo group layer, andesite of the Sanuki group layer at Miocene Tertiary as S1 type, fine-grained breccias with altered melt glasses I of Miocene Tertiary as S3 and S4 types, melt breccias mixed with altered melt glasses II of Miocene Tertiary as S4 and S3 types, and Rhyoke granite of Late Cretaceous in Mesozoic Period as S2 type (Fig.1). From topographic and gravity anomaly data indicate that the Takamatsu formation by andesite instrusions squeezes the original open crater structure (before filling out completely) to southeast direction to form present ellipsoidal shape of NE-SW direction and deeper shape in gravity anomaly 3D map, as 8kmx4km in surface, and 1.1km in depth.

Geology of drilled sample studies: Alluvium sediments are found in 45m in depth from the surface. Conglomerate and clay of the Quaternary Mitoyo group layer with 125m in thickness. Crater sediments I of crater flow sediments are round granite and blocks and crystal minerals formed by flowing process in water environments for 285m in thickness. Crater sediment II are melt breccias with brownish and black

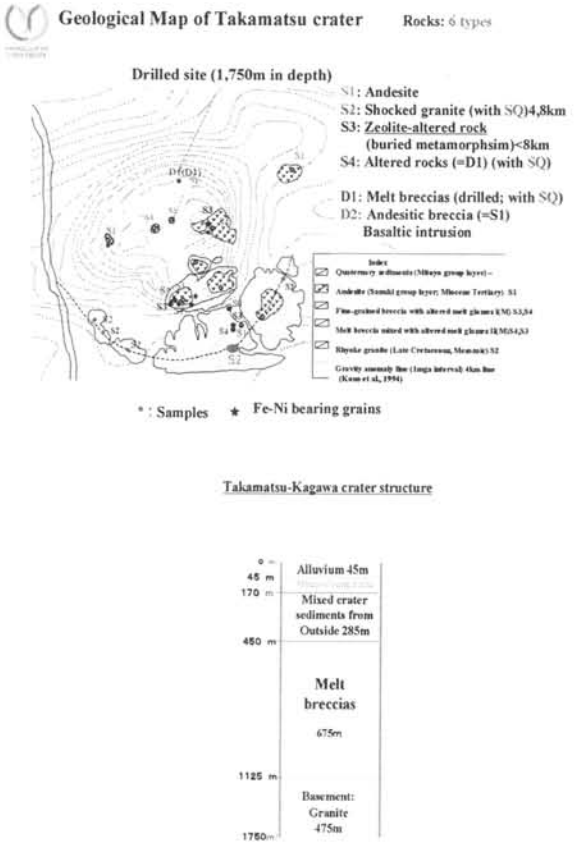

Fig.1 Geology surface map and drilled log of Takamatsu crater in Japan.

colors for 675m in thickness. All rocks are granitic rock from 1,125m in depth for 625m in thickness. Drilled samples of 1,750m in depth at northern part of the crater structure are found as many sediment layers in crater structure with shocked quartz grains, Fe-Ni rich grains and melted glasses. Below 1,125m in depth there are basement rocks of granitic rocks (Fig.1). Drilled and surface samples analyzed by the XRF are summarized as follows: Twenty-one drilled samples from 180 to 1400m in depth show all granitic compositions of higher silica and lower CaO and Fe, though there are some rocks of andesitic compositions (S1) which are considered to be intrusion along the crater structure [1,2,3]. Eight glassy samples at the surface (with red, black and grey colors) are consistent

with melt data of granitic compositions which suggest many melt events during crater formation. From different site near Takamatsu crater, there are no melted rock until drilled samples of 1,700m in depth at southern plateau of volcanic Koshikidai plateau.

Bulk chemical change of drilled crater sediments: Bulk XRF data of the drilled samples indicate original crater sediments are ca.450m in depth (i.e. ca.675m in thickness) with difference from magmatic crystallization trend (for example, Al_2O_3 to SiO_2). There is sharp change of these bulk XRF composition at 450m to 470m in depth to higher silica-rich composition which suggest that original crater sediments after impact event are 450m depth, though there are ca.20m thick volcanic flow from smaller andesitic intrusions in deeper crater sediments due to intrusions by followed crustal movements of XXXI form Japan islands.

Location of shocked quartz: Shocked quartz with planar deformation features (PDFs) can be found in three localities of granitic basement rock S2 in surface rims (south at 8km in diameter), drilled melted breccias D1 (450m to 1120m in depth) and melt breccias at surface around the andesitic intrusions. Shocked quartz minerals with PDFs (one to three directions) are found at granitic basements (S2), though there are many cracks after formation of the PDFs texture due to movements of primordial Japan islands (Fig.2).

Fe-Ni grains: There are three types of Fe-Ni rich grains, that is, Fe-rich (49-79wt%), FeNi-rich (20-40Fe%, 15-35Ni%) and Ni-rich (43-49Ni%) in drilled samples. These types are considered to be separated during impact reaction (Fig.2). These grains found in granitic compositions are not from volcanic or mantle originated due to less magnesium contents of the samples.

Corona texture: There are complicated flow-shapes of elongated corona (necklaces)-in-corona texture of K-feldspar K (clasts as rim) and quartz Q (matrix as core) as various elongated sizes with 0.1mm to 0.4mm size, which is formed by less evaporated components of silica coated more evaporated component of K-feldspar after impact reaction (Fig.2).These grains in corona texture is impact origin, due to no large volcanic elements.

Proposed separation of impact blocks: Impact blocks of Takamatsu crater was formed near sea-coast which is considered to transported for ca.500km along the Median Tectonic Line (MTL) as sea-sediments to find blocks at South Alps of Japan [10,11] (Fig.3).

Summary: 1) Takamatsu crater has original impact rocks, melt breccias and later volcanic rocks. 2) Three types of shocked quartz with PDFs and Fe-Ni rich micro-grains are found both in surface and drilled samples. 3) Complicated "corona-in-corona texture" is found as clasts (rim) of K-feldspar, and matrix (core) of quartz. 4) Broken blocks will be found at separated parts along the Miedian Tectonic Line in Japan.

References: [1] Kono Y.et al. (1994): Report of Kaken B (Japan), 36pp. [2] Miura Y. Ed. (1999): PIECE'99 Symposium paper abstract volume (Yamaguchi University, Yamaguchi, Japan), 94pp. [3] Miura Y. Ed. (2000): IFIE'00 Forum paper abstract volume (Yamaguchi University, Yamaguchi, Japan), 30pp. [4] Miura Y. (2003): IEJSAP'03 symposium abstract paper volume (Yamaguchi University, Yamaguchi), 10-20. [5] Miura Y. (2005): LPSXXXIVI, abstract #2394. [6] Miura Y. (2002): Proc. NIPR Antarctic Meteorites (NIPR, Tokyo), 25, 35-38. [7] Miura Y. (2002): LPSXXXIII, abstract# 1231. [8] Miura Y. (2006) LPSXXXVII, abstract# 1239. [10] Miura Y. et al. (1991) Symp. NIPR Antarctic Meteorites (NIPR, Tokyo), 16, 10-12. [11] Miura Y. et al. (1991) Meteoritics, 26, 374.

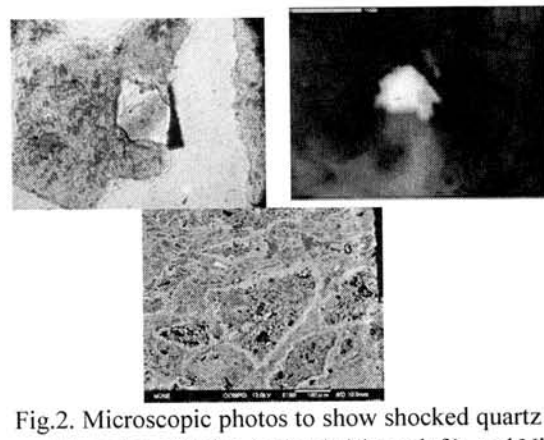

Fig.2. Microscopic photos to show shocked quartz with melt breccias at 910m in depth (above left), and Ni-rich grains of 520m in depth (above right), corona-in-corona texture in 610m in depth (below) of the Takamatsu crater in Japan.

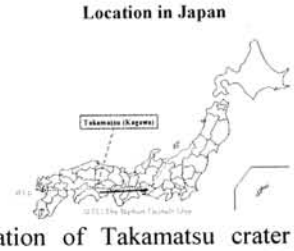

Fig.3. Location of Takamatsu crater in Japan and proposed transportation of impact blocks along the MTL to the East of Japan as sea-sediment [10,11].

Carbon contents of Nio meteorite and Hiroshima atomic bomb explosions in atmosphere of the Earth,
Yasunori Miura, Inst. Earth Sciences, Graduate School of Science & Engineering, Yamaguchi University, Yoshida 1677-1, Yamaguchi, 753-8512, Japan, yasmiura@yamaguchi-u.ac.jp

Introduction:

There are three types of carbon at meteorite, spherules. First type of carbon is found at various meteorites determined by composition of parent body of the asteroids. Second type of carbon is carbon-bearing spherules formed by impact on limestone target rock on the Earth. Third source of carbon on meteorite or melted fragments is considered to be originated from atmosphere of the Earth [1]. The third type of carbon has been used for determination of terrestrial ages of meteorite to distinguish with carbon-rich gases from terrestrial and cosmogenic origins by accelerator mass spectrometry (AMS) [2]. However there is no report to observe carbon-bearing impact spherules and glasses formed from carbon-rich gases during explosions in atmosphere, because of rare collection of such type of spherules. Main purpose of the paper is to discuss carbon contents of the third type of carbon materials as in-situ analyses of analytical scanning electron microscopy.

Spherules of Nio chondritic meteorite:

Nio (H3/4) chondrite fallen in Niho in Yamaguchi city in 1898 was exploded at ca.20km above to form meteoritic shower. Four meteorite fragments reveal soft landings with main bodies and many spherules formed by explosion on the sky which are collected from wet rice-paddy. Spherules formed by explosion in air show Fe- rich composition as shown in Fig.1, where carbon contents increase from core to rim of the spherule.

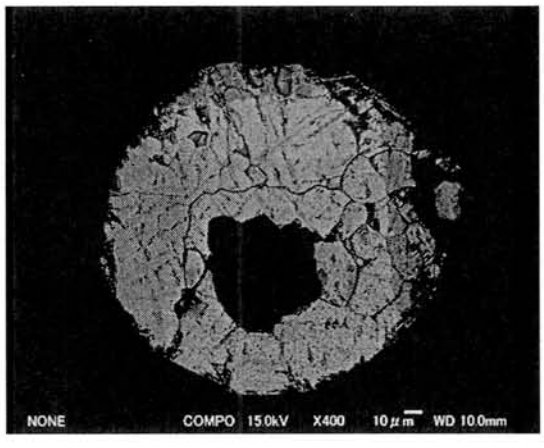

Fig.1. Electron micrograph of spherule from Nio meteorite explosion in atmosphere. Carbon content is increased from core to rim of the spherules.

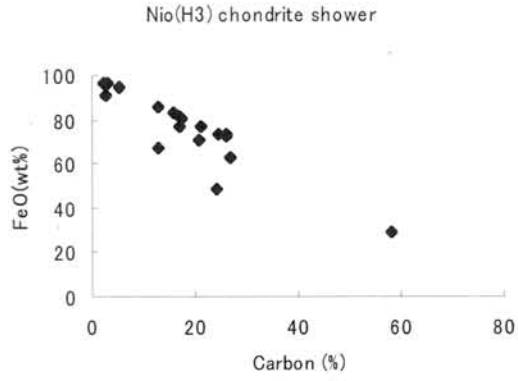

Fig.2. Carbon – iron oxide diagram of Nio chondritic spherules. Carbon content of chondritic spherules is not so high in composition.

In order to describe the composition of spherules, iron and carbon are selected to make relation in diagram due to their stable elements at high temperature condition. Figure 2 indicates C-FeO relation of Nio chondritic spherules have high contents of iron and low content of carbon from 2 to 30%C, though the highest content of carbon is found as 60%C.

Considerable contents of carbon in Nio spherules are considered to be supplied from carbon-rich gas of atmosphere.

Spherules of roof-tiles at A-bomb explosion:

Watanabe et al. (1954) [3] reported that Hiroshima granite rocks based at Hiroshima city have no strong effect of shock metamorphism by the Hiroshima atomic bomb (A-bomb) on August 8, 1945 in Japan, together with Nagasaki A-bomb explosion, but remarkable effect of remained melted roof-tiles based on naked eyes or optical microscope.

Huge PT condition was produced on nuclear explosion at 580($\pm$20) m above from surface of Hiroshima city. Original roof-tiles with quartz, kaolinite, orthoclase, albite, hematite and rutile minerals as 2 to 100 μ m in size are changed to mixed glasses of K-Fe-rich, Ca-Na-rich, Fe-K-Na- rich and Fe-Ti-K-Na-rich feldspars, ilmenite, and silica in compositions by in-situ analytical scanning electron microscopy (ASEM-JEOL7000F), as shown in Fig.3 [4].

Although there are no carbon contents of roof-tiles, carbon contents of spherules are remarkable from 2 to 21 C atom.% (Fig.4). The carbon contents are

considered to be deposited from carbon dioxide of atmosphere during the A-bomb explosion [4]. This is mainly because the A-bomb explosion in carbon-bearing atmosphere produces dynamic reaction of vaporization and melting. This is short cut of carbon-cycle on the Earth from atmosphere direct to solid deposition during the A-bomb explosion (skipped liquid condition). Similar data of carbon are found in Nagasaki A-bomb explosion.

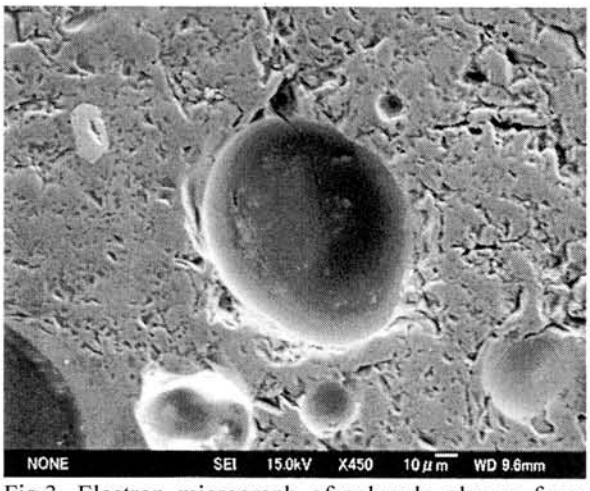

Fig.3. Electron micrograph of spherule glasses from roof-tile at the Hiroshima A-bomb explosion. Sample is used from the Hiroshima Peace Memorial Museum.

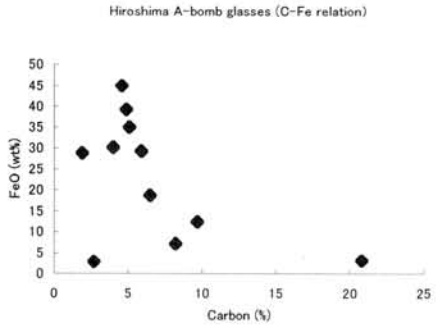

Fig.4. Carbon – iron oxide diagram of spherules of roof-tile at the Hiroshima A-bomb explosion. Samples are used from the Hiroshima Peace Memorial Museum.

Summary:

The present results are summarized as follows:

1) Direct carbon cycle from atmosphere to solid state can be found at spherules of the Nio meteorite shower, and of roof-tiles at the Hiroshima A-bomb explosion.

2) Carbon contents of Nio chondritic spherules are varied from 2 to 30%C, though the highest content of carbon is found as 60%C.

3) Carbon contents of spherules of the Hiroshima A-bomb explosion are varied from remarkable from 2 to 21 %C.

Acknowledgements:

Author thanks to Mr. K. Maeda and Ms. M. Shimomura of the Hiroshima Peace Memorial Museum, and to Ms. M. Kagoshima of the Nagasaki Atomic bomb Museum for sample preparations.

References:

[1] Watanabe T. et al. (1954), *Japanese Journal of Geology and Geography,* Vol. XXIV, 161-170.

[2] Miura Y. (1991), *The Future of AMS Requirements in Canada* (Ed. by Carlisle)1, 45.

[3] Miura Y. (2006): *ICEM2006 symposium abstract paper volume* (Yamaguchi University, Yamaguchi, Japan), pp.2 (in press).

Debris migration on the surface of Itokawa: implications to regolith formations and future sample-return missions. H. Miyamoto[1, 2], H. Yano[3], D. Scheeres[4], S. Sasaki[5], O. Barnouin-Jha[6], R.W. Gaskell[7], A. Cheng[6], H. Demura[8], A. Fujiwara[3], T. Hashimoto[3], N. Hirata[9], C. Honda[3], M. Ishiguro[10], T. Kubota[3], T. Michikami[11], A.M. Nakamura[9], R. Nakamura[12], J. Saito[3], Y. Yokota[3], and Hayabusa Team, [1]Department of Geosystem Engineering, University of Tokyo, Tokyo, Japan (miyamoto@geosys.t.u-tokyo.ac.jp), [2]Planetary Science Institute, 1700 E. Ft. Lowell Rd., Suite 106, Tucson, AZ 85719, [3]The Institute of Space and Astronautical Science, [4]University of Michigan, [5]National Astronomical Observatory of Japan, [6]The Johns Hopkins University Applied Physics Laboratory, [7]JPL/CALTECH, [8]Aizu University, [9]Kobe University, [10]Seoul University, [11]Fukushima National College of Technology, [12]National Institute of Advanced Science and Technology

Introduction:

Whether smaller asteroids are covered by regolith or not was a significant unanswered question in understanding the evolution of asteroids [1-3]. Regolith on an asteroid is considered as a pile of debris formed by impacts. Although the impacts happen regardless the size of asteroids, a smaller body may lack in regolith due to the lower escape velocity. The presence of regolith on small objects is technically difficult to observe from Earth, thus the Hayabusa mission, which observed a sub-kilometer size asteroid, provides significant opportunity to the above question. Thus, detailed studies of the nature of Itokawa's regolith would provide an important key in understanding the origins and the evolutions of regolith materials on asteroids.

The AMICA imaging camera of the Hayabusa spacecraft reveals that the asteroid Itokawa has a variety of features [4], which suggest its complex evolutional history. Most notably in images at distance, two types of terrains (rough and smooth terrains) are recognized. In this talk we will report the results of our preliminary analysis of the smooth terrains.

Smooth terrains:

The smooth terrains are featureless, flat part of Itokawa with almost uniform brightness. These characteristics indicate that the smooth terrains are likely covered by fine particulates. In this paper, we practically called the fine particles "regolith".

The regolith of Itokawa is not globally distributed; the smooth regolith terrains partially cover the surface of Itokawa. We identified several smooth terrains, whose detailed geological mappings are undergoing. Using three-dimensional shape model of Itokawa [5,6], we measured the areas of each smooth area by carefully comparing the shape model and the images. We found that areally 20 % of the surface of Itokawa is covered by regolith.

The close-up images at altitudes lower than several hundred meters reveal that gravel-like grains uniformly cover the part of Muses Sea [8], which is the largest and the most distinctive smooth terrain. Preliminary analyses of these images suggest that the grain size of the gravel-like deposits likely ranges from sub-centimeter to centimeter scale, which is coarser than those of the "pond" deposits on Eros.

Debris migrations:

Important findings related to the formations of smooth terrains include: (1) Although the boundary between the smooth and rough terrains is generally sharp, there is a ~10 m-scale "transition zone" between them; (2) Boulder alignments along the boundary can be seen inside and near the transition zone; (3) The size of boulders inside the regolith area seems to become smaller gradually, as a function of the distance from the transition zone, when measured based on the lengths of shadows; (4) The depth of regolith may be several meters if the boulders inside the regolith are the remnants after the deposition of regolith; (5) The depth of the regolith appears to be shallower at the boundary between rough and smooth terrains than the middle of the Muses Sea; (6) Measured by the shades, the grain size of the regolith systematically becomes finer from the boundary to inside the Muses Sea.

All of these observations collectively indicate that the evolutions of smooth terrains likely involve processes of grain-size sorting. We also noticed that certain dynamical interactions between regolith and boulders would have been present, although the transport/deposition mechanisms are subject to further investigation.

References:

References: [1] Asphaug, E. et al. (2002) *in Asteroid III*, 463-484. [2] Scheeres, D. et al. (2002) *in Asteroid III*, 527-544. [3] Cheng, A.F. (2004) *Icarus*, 169, 357-372. [4] Saito, J. (in press) *Science*. [5] Demura et al (in rev.) *Science* [6] Gaskell, R. (2006) *LPS* XXXIII, Abst. #1876. [8] Yano, H. (in rev.) *Science*.

CONDENSATION ORIGIN OF CHONDRULES IN ORDINARY CHONDRITES: EVIDENCE FROM BULK CHEMICAL COMPOSITION AND MASS-DEPENDENT OXYGEN ISOTOPIC FRACTIONATION

H. Nagahara[1], K. Ozawa[2], and N. T. Kita[3], [1]Dept. Earth Planet. Sci., Univ. Tokyo, Hongo, Tokyo 113-0033, Japan. E-mail: hiroko@eps.s.u-tokyo.ac.jp., [2]Dept. Earth Planet. Sci., Univ. Tokyo. [3]Dept. Geol. Geophy., Univ. Wisconsin, Madison.

Introduction: Although chondrule formation by melting of precursor materials has been favored since the finding of relict olivine [1], the model has a fundamental disadvantage that the diversities of bulk compositions are not well explained. Recent review by [2] has complied bulk chemical compositions and oxygen isotopic compositions of chondrules in various chemical group of chondrites, however, they pointed out the secondary modification and analytical uncertainty of those results and has failed to show the origin of compositional and isotopic diversities of chondrules.

Critical observation: [3] carried out a precise and comprehensive analysis of chondrule compositions for primitive ordinary chondrites, Krymka and Bishupur, and revealed following characteristics of their compositions. Tthe refractory element abundances are constant, which is less than the solar value. There is large Mg/Si fractionation on both higher and lower sides of the solar ratio; type I chondrules tend to have higher values and type II lower values. These variations could not be inherited from the precursors, evaporation residue, or equilibrium condensation. They are explained only by kinetic condensation of silicate melt in dust-enriched systems [3].

Recently, some of those chondrules were studied for precise oxygen isotopic analysis. They show mass-dependent isotopic fractionation, where type I chondrules are lighter with wide variation, whereas type IIs are heavier with a limited range [4]. Because ilt has already been known that all metallic elements do not show notable mass-dependent isotopic fractionation, oxygen is the only element that shows mass dependent isotopic fractionation. Mass-dependent isotopic fractionation is the direct evidence for open system behavior of chondrules formation, which has been pointed out by many indirect petrological evidence for a decade.

Here, we discuss which process is responsible for and which conditions are necessary to generate the observed chemical and isotopic characteristics of chondrules.

Model: The quantitative evaporation / condensation model by [3, 5] was modified to investigate the conditions where chemical diversity of bulk compositions with oxygen isotopic variations for type I and II chondrules are formed through evaporation and condensation of melt droplets under various cooling conditions and dust enriched systems.

Result and discussion: Because mass - dependent isotopic fractionation suggest the role of evaporation/condensation in the formation of chondrules, the role of evaporation and condensation were evaluated. It is shown that type I chondrules are explained by rapid condensation of silicate melt from the gas with the solar compositions with dust enrichment by more than about hundred. The presence of more oxygen in the gas than metallic elements formed chondrules with light oxygen compositions. Because lighter isotopes have chances to condense more easily than heavy isotopes, the oxygen isotopically light type I chondrules should have formed earlier than isotopically heavy type II chondrules. The oxygen isotopic variation among type I chondrules was caused by rapid chemical isolation of chondrules from the residual gas, otherwise rapid exchange of oxygen between chondrules surface and ambient gas should have homogenized their isotopic compositions. The fairly low Mg/Si composition and homogeneous and heavier oxygen isotopic compositions of type II chondrules are explained by condensation of residual gas to melt droplets after type I chondrule isolation, which kept chemical and isotopic equilibrium during condensation to lower temperatures, and which eventually got volatile components with almost the solar ratios.

The present model explains the systematic chemical and isotopic compositions of type I and type II chondrules in ordinary chondrites. The systematic difference of abundances of refractory elements in carbonaceous chondrites where the abundance of refractory elements increases with Mg/Si ratio [2] would suggests either equilibrium condensation or the role of evaporation. The difference between ordinary and carbonaceous chondrules would be due to the degree of dust enrichment, which changed the degree of kinetics for condensation.

References: [1] Nagahara, H., 1981. *Nature* **292** 135-146. [2] Jones, R. H. et al., 2005. *Astron. Soc. Pac. Conf. Ser.* **341** 251–285. [3] Nagahara, H. et al., 2005, *Astron. Soc. Pac. Conf. Ser.* **341** 456-468. [4] Kita, N. T. et al. 2006. 37th *Lunar & Planetary Science Conference*. Abstract #1496. [5] Ozawa, K. and Nagahara, H., 2001. *GCA* **65** 2171-2199.

Noble gas isotopic composition of Vaca Muerta: Implication for complex history of mesosiderite.

K. Nagao and K. Bajo, Laboratory for Earthquake Chemistry, Graduate School of Science, University of Tokyo, Hongo 7-3-1, Bunkyo-ku, Tokyo 113-0033, Japan. (nagao@eqchem.s.u-tokyo.ac.jp)

Introduction:

Vaca Muerta is classified as a mesosiderite, a breccia of approximately equal mixture of silicate and metal. It was found in 1861 in the Atakama desert, Chile [1]. The brecciated texture of mesosiderites suggests collision event(s) between differentiated asteroidal bodies for its formation. Chemical and mineralogical compositions of eucritic clasts from the Vaca Muerta have been studied and indicated several compositionally different clasts in the meteorite [e.g., 2-4]. Based on the concentrations of He, Ne and Ar as well as ^{36}Cl in metal of the Vaca Muerta, Begemann et al. [5] gave a cosmic-ray exposure age of 133±12 Ma. Sm-Nd ages of basaltic and gabbroic clasts of Vaca Muerta were obtained as 4.4-4.5 Ga by Stewart et al. [6]. ^{39}Ar-^{40}Ar ages have been measured for mesosiderites by Bogard et al. [7, 8]. The ^{39}Ar-^{40}Ar ages are in the range of 3.77-4.13 Ga with average of 3.94±0.10 Ga [8]. Early differentiation of parent body and regolith breccia formation through impact gardening followed by mixing of molten Fe-Ni metal with the regolith had occurred within 100-150 m.y. after the solar system formation [6]. Mild heating probably by impact metamorphism at about 4 Ga is required to reset K-Ar system for mesosiderites [6, 7, 8].

We measured noble gases of a eucritic pebble and bulk sample from the Vaca Muerta mesosiderite by stepwise heating method. Unusual isotopic compositions of Ar have been observed, which would be a result of complex formation history of this meteorite.

Samples and noble gas analysis:

Several chips taken from a slice of Vaca Muerta were used as a bulk sample (0.2086 g). Chips named as Clast-1 (0.4844 g), Clast-2 (0.4829 g) and Clast-3 (0.2129 g) were separated from the single eucritic pebble (ca. 3cm x 3 cm x 0.5cm in size) of Vaca Muerta. The Clast-2 was reached with H_2O_2 to remove weathering products prior to noble gas analysis. Stepwise heating with 13 steps from 400 to 1800°C was applied to the bulk and the Clast-1, and 8 steps to the Clast-2. The Clast-3 was heated at 1800°C after preheating at 300°C to measure ^{81}Kr for Kr-Kr exposure age. Noble gases released from the samples at each temperature step were purified with Ti-Zr getters and separated into four fractions, He-Ne, Ar, Kr, and Xe, then measured on a modified-VG5400(MS-II) noble gas mass spectrometer.

Sensitivities and mass discrimination correction factors of the mass spectrometer were calibrated by measuring known amount of atmospheric noble gases and a ^{3}He-^{4}He mixture with

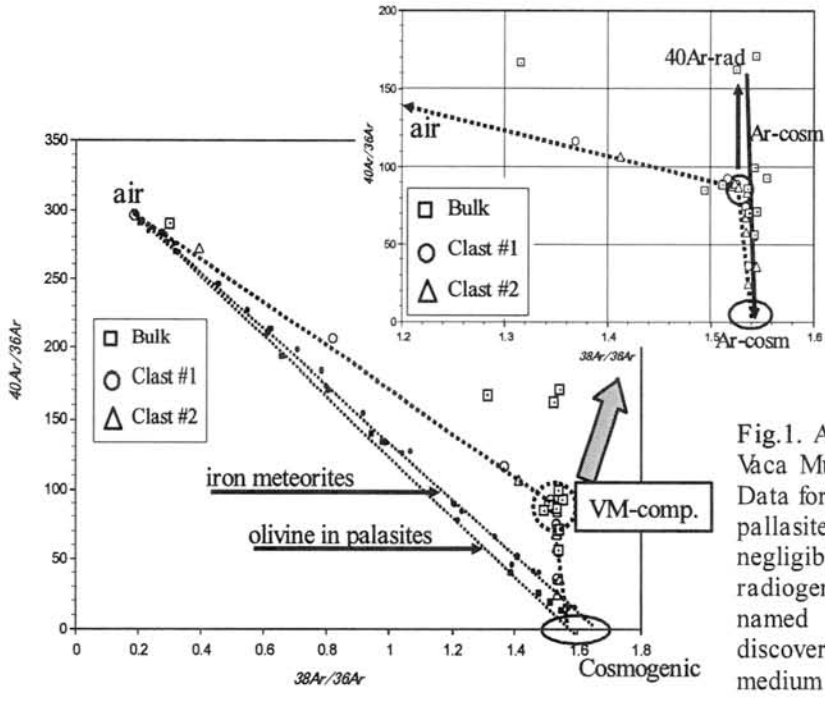

Fig.1. Ar isotopic compositions of the Vaca Muerta mesosiderite are plotted. Data for iron meteorites and olivines in pallasites are plotted as examples with negligible amounts of trapped Ar and radiogenic ^{40}Ar. Unusual Ar component named as "VM-component" was discovered for the samples at the medium heating temperatures.

$^{3}He/^{4}He = 1.71x10^{-4}$. Blank corrections have been applied for the noble gas data, although the blank levels were negligible in the most cases.

Results and discussion:

Ar isotopic ratios obtained for Bulk, Clast-1 and Clast-2 are plotted in Fig. 1. Data points at the lowest temperature (400°C) are plotted close to the terrestrial atmosphere, and then move toward the cosmogenic Ar. The data points for Clast-1 and Clast-2 at the medium temperatures, however, are plotted in a narrow range named here as "VM-component". At the higher temperatures data are plotted on a line connecting the VM-component and the cosmogenic Ar. Contrary to the Vaca Muerta, Ar for iron meteorites and olivine crystals from pallasites (unpublished data) are plotted just on the straight lines between terrestrial atmospheric Ar and cosmogenic Ar. This is due to extremely low concentrations of trapped Ar and radiogenic ^{40}Ar in these meteorites. The different mixing lines for iron meteorites and olivines reflect different target elements producing cosmogenic Ar. Data points of the bulk sample plotted above the line connecting air and VM-component should be due to radiogenic ^{40}Ar produced from ^{40}K.

Approximate values of isotopic ratios based on the data points in Fig. 1 are $^{38}Ar/^{36}Ar=1.53$ and $^{40}Ar/^{36}Ar=87$ for the VM-component, and $^{38}Ar/^{36}Ar=1.54$ for the cosmogenic Ar. We suppose at present that the VM-component was produced as a mixture between cosmogenic Ar and radiogenic ^{40}Ar accumulated in surface layers of differentiated parent body under the thermal metamorphic event which could have reset K-Ar system at about 4 Ga determined by ^{39}Ar-^{40}Ar method [7, 8]. If this is the case, the data points plotted above the line between terrestrial Ar and VM-component can be interpreted as the in situ produced radiogenic ^{40}Ar after the heating event occurred at 4 Ga. Due to the production of cosmogenic Ar during the transit from parent body to the Earth, data points were shifted to the point of cosmogenic Ar. The VM-component formation should not have occurred on the parent body through brecciation in the early sage of solar system described by Stewart et al. [6], because accumulation of sufficient amount of radiogenic ^{40}Ar needs interval of several Ga. Mixing of Ar with primordial $^{38}Ar/^{36}Ar\sim0.188$ and cosmogenic Ar with $^{38}Ar/^{36}Ar=1.54$ implies very high $^{40}Ar/^{36}Ar$ of about 10,000 to produce the VM-component. This reflects a well degassed parent body. Almost undetectable concentrations of trapped noble gases in the Vaca Muerta samples support this view.

Based on the model, concentrations of radiogenic ^{40}Ar and cosmogenic ^{38}Ar for the VM-component and those produced after 4 Ga are calculated for Clast-1 and Clast-2 as $^{40}Ar=(610\text{-}690)x10^{-8}$cc/g and $^{38}Ar=(11\text{-}12)x10^{-8}$ cc/g for the 1st stage (>4 Ga), and $^{40}Ar=(1\text{-}4)x10^{-8}$ cc/g and $^{38}Ar=(3.5\text{-}4.3)x10^{-8}$ cc/g for the 2nd stage (<4 Ga). For bulk sample, which shows clear excess in ^{40}Ar, concentrations of ^{40}Ar are roughly estimated as 380 and 140 ($x10^{-8}$ cc/g) for the 1st and the 2nd stages, respectively. The concentrations of ^{38}Ar imply cosmic-ray exposure age of about 30 m.y. for the 2nd stage and 90 m.y. for the 1st stage assuming production rate of $0.15x10^{-8}$ cc/g/m.y. Real exposure age for the 1st stage must be longer than the 90 m.y., because we do not know the condition of cosmic-ray irradiation and amount of loss during the thermal event at 4 Ga. Concentration of ^{81}Kr in the Clast-3 sample was $4.8x10^{-14}$ cc/g, and the ^{81}Kr-Kr exposure age was calculated as 180 m.y. In the calculation, decay of ^{81}Kr during the residence time in the Atakama desert was not considered. Because the ^{81}Kr concentration gives a recent production rate in the meteorite, the ^{81}Kr-Kr exposure age would be a lower limit because of a partial loss of cosmogenic Kr accumulated in the 1st stage irradiation. Based on the exposure ages obtained above, we can estimate that the Vaca Muerta mesosiderite had been irradiated by cosmic-rays for more than 150 m.y. before thermal metamorphism occurred at 4 Ga, and the meteoroid was excavated and sent to Earth-crossing orbit 30 m.y. ago.

Concentrations of cosmogenic ^{3}He, ^{21}Ne, ^{38}Ar and ^{83}Kr in the Clast-1 and Clast-2 samples are almost twice those in the bulk sample. This may indicate longer duration and/or shallower shielding depth of the cosmic-ray exposure for the eucritic pebble (Clast-1 and Clast-2 samples) than for the bulk materials of this meteorite.

As can be seen in Fig 1, excess ^{40}Ar concentrations produced in the eucritic pebble in the 2nd stage are very low compared with those of the bulk sample. The ^{40}Ar concentration of $(1\text{-}4)x10^{-8}$ cc/g for the Clast samples as given above indicate a very low concentration of 2-7 ppm K for the eucritic pebble assuming 4 Ga for Ar retention. This may compatible with the low concentration of K (13 ppm) observed for the Vaca Muerta Pyx. (#5) sample by Bogard and Garrison [8]. For bulk sample 240 ppm K is suggested from the similar calculation.

Noticeable amounts of excessive ^{129}Xe from ^{129}I could not detected in the samples, which indicates that volatile degassing occurred or continued until the ^{129}I extinction in the parent body.

References:

[1] Grady M. (2000) Catalogue of Meteorites (5th ed.). [2] Rubin A.E. and Jerde E.A. (1988) EPSL **87**, 485-490. [3] Ikeda Y. et al. (1990) Proc. NIPR Symp. Antarctic Meteorites **3**, 99-131. [4] Kimura M. et al. (1991) Proc. NIPR Symp. Antarctic Meteorites **4**, 263-306. [5] Begemann F. et al. (1976) GCA **40**, 353-368. [6] Stewart B.W. et al. (1994) GCA **58**, 3487-3509. [7] Bogard D.D. et al. (1990) GCA **54**, 2549-2564. [8] Bogard D.D. and Garrison D.H. (1998) GCA **62**, 1459-1468.

Compound Chondrule Formation in Shock Wave Heating Model.

T. Nakamoto[1], [1]Center for Computational Sciences, University of Tsukuba, Ibaraki, 305-8577, Japan: nakamoto@ccs.tsukuba.ac.jp.

Introduction:

It is usually thought that chondrules were formed in the solar nebula by some heating events. However, the temperature of the solar nebula is not high enough to melt silicate material. Thus, it is thought that some transient heating processes should be present. The shock wave heating mechanism has been proposed as the chondrule forming heating process [1].

Shock wave heating mechanism works as follows: when a shock wave is present in the solar nebula, the relative velocity between gas and dust particles is generated, and it causes the gas drag heating on the dust particle. This mechanism can explain many features of chondrules, for example, rapid heating and melting, appropriate cooling and re-solidifying, chondrule sizes, and 3-dimensional shapes of chondrules [2]. Thus, it is thought that the shock wave heating mechanism is a promising model for chondrule formation [1].

Compound chondrules consist of two or more independent single chondrules. A number ratio of them to single chondrules in chondrites is about 10 %. Compound chondules are thought to be formed by collisions of two partially molten particles. However, previous work on the compound chondrule formation based on the shock wave heating model was very limited. In this study, we examine the compound chondrule formation in the framework of the shock wave heating model.

Constraint on Compound Chondrule Formation:

To collide two particles and coalesce together, some physical quantities should meet appropriate conditions. For example, a product of the particle number density, the relative velocity, the cross section, and the elapsed time of the partial molten state becomes the average number of collisions for a dust particle. This collision number should be larger than a certain value to form compound chondrules. Or, if the collision velocity is too large, the collision leads to destruction. Key physical quantities to form the compound chondrules are the number density of dust particles, the collision velocity, and the elapsed time of the partial molten state.

Compound Chondrule Formation by Shock Wave Heating:

The velocity of dust particles entering the post-shock region from the pre-shock region (here, we call those particles as the primary particles) is mainly determined by the deceleration due to the gas drag in the post-shock region. The deceleration depends on the dust particle size. So if the sizes of two particles are different each other, the relative velocity between them is yielded, and it could be as large as several km s^{-1}. In this case, the collision would become destruction [3]. On the contrary, if they collide with the small relative velocity, the collision can lead to compound chondrule formation. A process that can produce small relative velocity among dust particles will be introduced below.

The number density of dust particles in the post-shock region should be enhanced locally, because it has been shown that the global high density state cannot form chondrules [3]. The primary particles could be destructed mechanically by the ram pressure [4]. And the partially molten part of the particle can be stripped off from the particle [5]. In addition, the collision between primary particles can lead to collisional destruction and produce a number of fragments. Those processes generally produce many dust particles, which we call here secondary particles. Then, the number density is enhanced locally. Moreover, the relative velocity among those secondary particles as well as between the primary and secondary particles could be small enough.

It should be noted that the silicate particles are likely to experience supercooling [6]. In addition, when the secondary particles are produced, they can be melted at a different timing with the primary particles. Thus, the order of re-solidification should be independent of the liquidus temperature of the particles.

Taking into account above factors, it is expected that collisions between secondary particles and the primary and the secondary particles should take place and can form compound chondrules.

Summary:

Compound chondrule formation in the context of the shock wave heating model was examined. It was found that the dust particle destruction, collisional fragmentation, and the stripping off of the molten part can take place in the post-shock region, and those processes produce large number of dust particles with low relative velocity. Then, the produced low relative velocity particles can form compound chondrules.

References:

[1] e.g., Desch S. J. *et al.* (2005) *Chondrites and the Protoplanetary Disk,* 849–872. Jones R. H. *et al.* (2000) *Protostars and Planets IV,* 927-962. [2] Miura H. and Nakamoto T. (2005) *LPS 36,* #1248. Miura H. and Nakamoto T. (2006) *LPS 37,* #1765. [3] Nakamoto T. and Miura H. (2004) *LPS 35,* #1847. [4] Susa H. and Nakamoto T. (2002) *ApJL 564,* L57. [5] Kato T. *et al.* (2006) *MAPS 41,* 49. Kadono T. and Arakawa M. (2005) *Icarus 173,* 295. [6] Nagashima K. (2006) Dissertation, Tohoku Univ.

Experimental Hydrothermal Alteration of Anhydrous Interplanetary Dust Particles.

K. Messenger[1,2], S. Messenger[2], M.E. Zolensky[2] and L.P. Keller[2] [1]ESCG Jacobs-Sverdrup, [2]Astromaterials Research and Exploration Science, NASA Johnson Space Center, Houston TX 77058

Introduction:

Chondritic interplanetary dust particles (IDPs) are subdivided as (1) particles that form highly porous aggregates (chondritic porous 'CP' IDPs), and (2) smooth particles ('CS' IDPs) [1-3]. Infrared (IR) spectroscopy has been a valuable tool for non-destructively determining the bulk mineralogy of IDPs. Most IDPs fall within three distinct IR groups: (1) olivine-rich particles, (2) pyroxene-rich particles, and (3) phyllosilicate-rich particles [4]. In the IR study, IDPs dominated by anhydrous minerals tend to be fine grained (CP) [5], while phyllosilicate-rich IDPs are mostly CS [4]. CP IDPs have been linked to cometary sources based on their compositions, spectral properties, and atmospheric entry velocities [6]. Since no spectral signatures of hydrated minerals have been detected in comets, CS IDPs are thought to derive from primitive asteroids [6].

Detailed mineralogical studies of IDPs by transmission electron microscopy (TEM) have revealed that the mineralogical distinctions between CP and CS IDPs are not always clear. Amorphous silicates and small amounts of saponite occur in both phyllosilicate-rich IDPs and anhydrous IDPs [7,8]. A better understanding of these particles will help to elucidate whether there is a genetic relationship between anhydrous and hydrated IDPs, provide insight into the earliest stages of aqueous alteration of primitive materials, and may help to determine whether comets have experienced any aqueous processing.

We reported an unusual IDP whose mineralogical and isotopic characteristics are mostly typical of anhydrous cometary IDPs but also contained minor hydrated phases [9]. Two possible origins for this IDP should be considered: (1) primitive (anhydrous) asteroidal material not represented in the meteorite collections, or (2) a short-period comet that experienced a brief and incomplete aqueous alteration episode. To test these hypotheses, we carried out a series of hydrothermal alteration experiments on anhydrous IDPs.

Methods:

Sample Preparation: To study mineralogy and chemical compositions before and after the hydrothermal experiments, anhydrous cluster IDPs L2009O2*13 (8μm in size) and U2097A19 (9μm in size) were individually embedded in epoxy and 50 nm-thick sections were obtained by ultramicrotomy. The sections were then transferred to C-coated Au grids. 12 TEM grids with 5 thin-sections each on top (total 60 thin sections) were prepared from each of the IDPs for subsequent TEM study.

Hydrothermal experiments: After the initial TEM observations, the grids were individually sealed in small Teflon containers (7ml) with aqueous solutions of differing pH:

1) Deionized pure water
2) 0.01 M NaOH solution
3) 0.10 M NaOH solution

These samples were heated at 120~160°C for 12 to 72 hours. This method provides 12 different conditioned experiments from one single IDP.

The sections were observed before and after the hydrothermal experiments by TEM for precise mineralogical and crystallographic studies of individual phases.

Results:

Initial observations: Both of the IDPs L2009O2*13 and U2097A19 had mineralogy typical of anhydrous IDPs including olivine, enstatite and Fe-sulfides. GEMS (glass with embedded metal and sulfide) grains are also ubiquitous.

After 24 hours in 120°C deionized water (pH not controlled): No mineralogical changes observed. The thin sections survived remarkably well given the harsh experimental conditions, and the C film actually became smoother.

After 12 hours in 160°C deionized water (pH not controlled): Previously Si-rich glass area in GEMS grains showed alteration. The chemical composition and 7Å basal spacing indicate that the phyllosilicates are poorly-crystallized Fe-rich serpentine, and fewer than 30 layers were observed. Metal and sulfide inclusions in GEMS and other anhydrous components such as enstatite and olivine grains were not altered.

After 24 hours in 160°C deionized water (pH not controlled): The outer rims of most of enstatite crystals and some amorphous silica in GEMS grains in the IDPs were replaced by fine-grained phyllosilicate serpentine (7Å basal spacing). Olivine grains in the IDPs showed minor alteration. GEMS grains were easily altered: - as quick as 12 hours and as low as 160 ° C, replaced by serpentine, but not all GEMS were altered in this condition.

After 72 hours in 160°C deionized water (pH not controlled): Samples were completely hydrated except a few GEMS grains.

After 24 hours in 160°C 0.1 M NaOH solution: IDP thin sections were thoroughly replaced to serpentine, leaving no traces of previous grain

boundaries.

Discussion and Conclusions:
All three major components (En, Fo, GEMS) in CP IDPs are aqueously altered preferably in order of: GEMS > En > Fo during our hydrothermal experiments. GEMS were easily altered as quickly as 12 hours and at temperatures as low as 160 °C replaced by serpentine. However, not all GEMS were altered in these experiments. This may due to the wide variety of chemical composition of GEMS, which complimentarily covers serpentine solid solution [10]. Alteration of these IDPs proceeded much more rapidly than similar experiments on meteorites [e.g. 11-13]. This is likely due to unique compositions [10] and fine grain sizes of IDPs (~200nm). Using alkaline condition (0.1 M) NaOH is too violent and not appropriate for cometary condition simulation. Further work will be required to constrain the conditions necessary to induce aqueous alteration in cometary materials .

References:

[1] Brownlee D.E., (1978) *In Protostars & Planets*. (Gehrels T. ed) Univ. Arizona Press, 134-150. [2] Schramm L.S., Brownlee D.E. & Wheelock M.M. (1989) *Meteoritics* **24**, 99-112 [3] Mackinnon I.D.R. & Rietmeijer F.J.M. (1987) *Reviews Geophys.* **25**, 1527-1553 [4] Sandford S.A. & Walker R.M. (1985) *ApJ* **291**, 838-851 [5] Bradley J.P. & Brownlee D.E. (1986) Science 231, 1542-1544 [6] Bradley J.P. et al. (1996) *MAPS* **31**, 394-402 [7] Zolensky M.E. & Lindstrom D.J. (1992) *Proc. LPSC* **22**, 161-169 [8] Gibson E.K.Jr. & Bustin R. (1994) *AIP Proc.* **310**, 173 [9] Nakamura K., Messenger S. and Keller L.P (2005) *LPSC* 36, #1824 [CD-ROM] [10] Keller L.P. and Messenger S. (2003) *LPSC* 34, #1985 [CD-ROM] [11] Jones C.L. and Brearley A.J. (2000) *LPSC* 31, #1204 [CD-ROM] [12] Cohen B.A. et al (2004) *LPSC* 35, #1423 [13] Ohnishi I. and Tomeoka K. (2003) NIPR Evolution of Solar System Material p.109

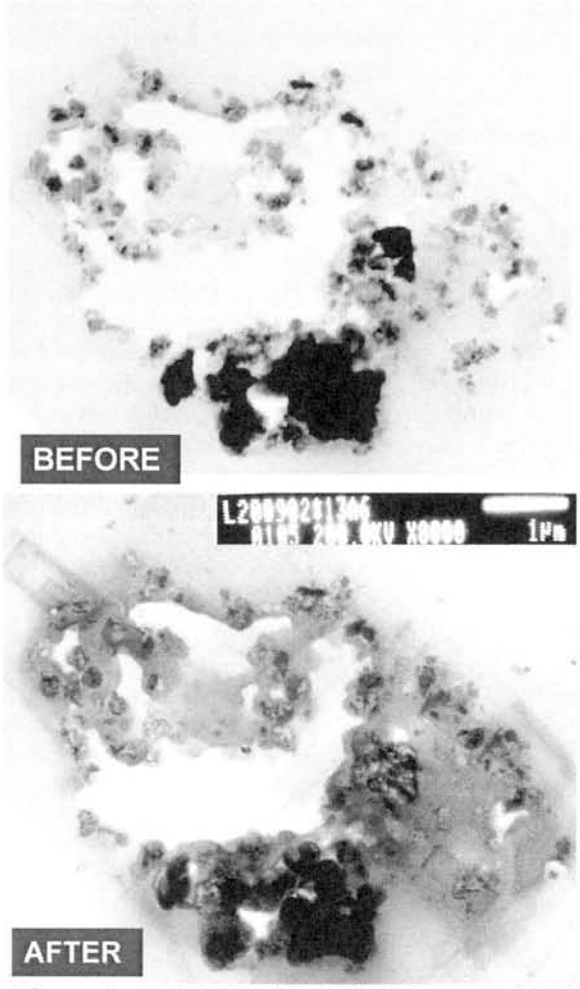

Figure 1: (top) TEM bright field image of IDP L2009O2*13 before hydrothermal experiment, showing a typical texture of an anhydrous IDP. (bottom) TEM bright field of image of the same field of view after 24 hours in 160C deionized water.

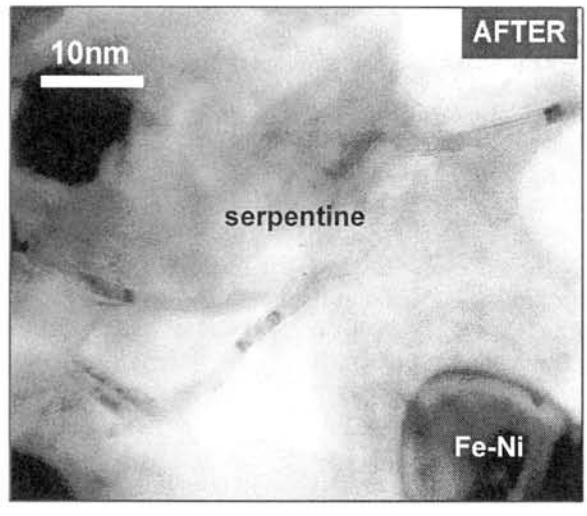

Figure 2: TEM bright field image of a GEMS grain after 24 hours in 160C deionized water.

Raman spectra of carbon minerals in Antarctic ureilites. Y. Nakamuta, Kyushu University Museum, Kyushu University, Fukuoka 812-8581, Japan, nakamuta@.museum.kyushu-u.ac.jp.

Introduction:

Ureilites are unique in containing relatively large amounts of C occurring as graphite or diamond [1]. The mode of occurrence and X-ray properties of carbon minerals in ureilites show that diamond in ureilites formed by high-pressure conversion of graphite that crystallized during igneous or metamorphic processes on an ureilite parent body or bodies [2]. Nakamuta et al. [3], [4] suggested that catalytic mechanism dominated in the diamond formation in some ureilites and non-catalytic one in others. Their results are mainly based on X-ray diffraction patterns of each C-rich grain. In this study, *in-situ* observation of graphite and diamond crystals in each grain was made by Raman spectroscopy in order to confirm the formation mechanisms of diamond in ureilites.

Sample and Experiment:

Polished thin sections of six Antarctic ureilites, Y-74123, A 77257, Y-8448, A 881931, Y-74659 and Y-74130, among which X-ray properties of graphite and diamond vary in a wide range, were observed under an optical microscope and MicroRaman spectra of graphite and diamond in each C-rich grain were obtained.

MicroRaman spectra were recorded with a Jobin-Yvon T64000 triple-grating spectrometer equipped with confocal optics and a nitrogen-cooled CCD detector. A microscope was used to focus the 514.5 nm Ar excitation laser beam to a 1 μm spot and to collect the Raman signal in the back-scattered direction. Accumulations lasting 120 to 600 seconds were made. The laser power on the sample was 2 mW.

Results:

C-rich grains in Y-74123, A 77257 and Y-74659 show amoeboid shapes and those in Y-8448, A 881931 and Y-74130 show blade-like shapes. The sizes of C-rich grains are about 1-2 mm in length and 0.1-0.05 mm in width. In each grain, diamond crystals can be observed in high relief under an optical microscope of high magnification. Raman spectra of diamond crystals in high relief and graphite crystals in low relief were recorded.

Raman spectra observed at three positions in each C-rich grain of Y-74123, A 881931 and Y-74130 are shown in Figs. 1-3, respectively. Based on the X-ray analysis, diamonds in Y-74123 and A 881931 were though to have formed by catalytic mechanism and Y-74130 by non-catalytic one [4]. All C-rich grains contain graphite, as shown by the spectra at the tops of each figure, together with diamond, as shown by the spectra at the bottoms of each figure. The spectrum showing intermediate properties

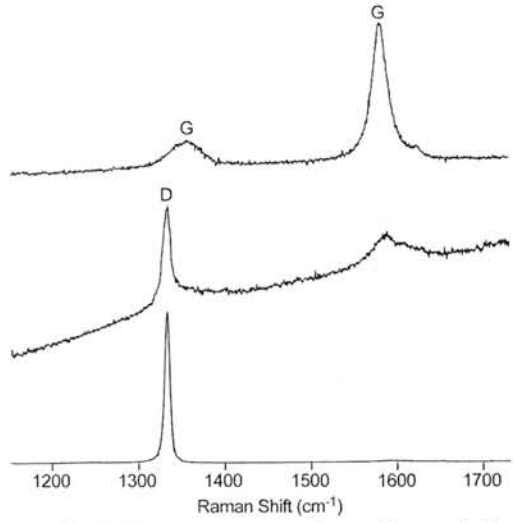

Fig. 1 Raman spectra of graphite and diamond in a C-rich grain of Y-74123.

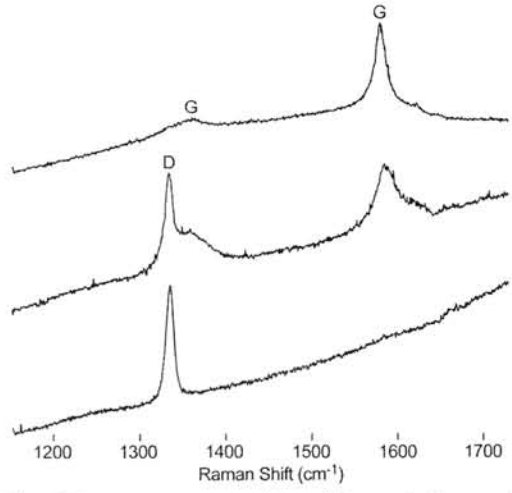

Fig. 2 Raman spectra of graphite and diamond in a C-rich grain of A 881931.

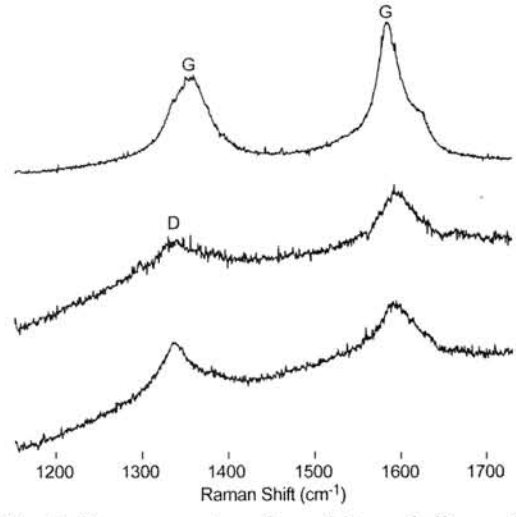

Fig. 3 Raman spectra of graphite and diamond in a C-rich grain of Y-74130.

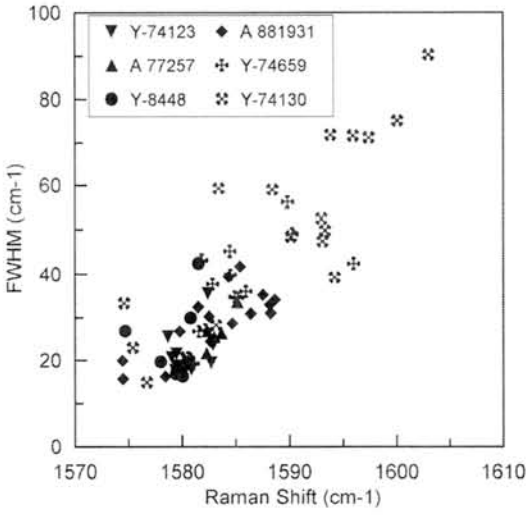

Fig. 4 Plots of Raman shift vs. FWHM of graphite E2g band.

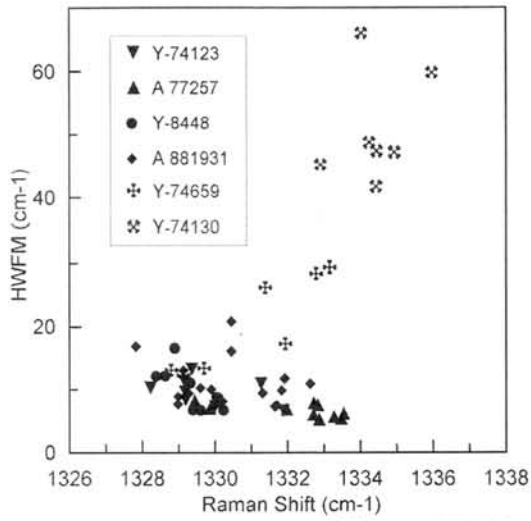

Fig. 5 Plots of Raman shift vs. FWHM of Raman band of diamond.

between the spectra of the top and the bottom of each figure is shown at the middle.

Raman spectra of graphite in all samples are composed of E_{2g} band at 1580-1600 cm^{-1} and D band at about 1350 cm^{-1} and agree well with that of relatively well crystallized graphite [5]. The full width of half maxima (FWHM) and peak positions of the E_{2g} bands vary among ureilites and also among crystals in a grain. The intensity ratio between D and E_{2g} bands is known to be used as an index of crystal size of graphite [5]. However, the intensity ratio is largely affected by grinding when a polished thin section is prepared [6]. Then, the intensity ratio is not considered as an index of crystal size of graphite in this study.

The Raman spectra of diamonds in each sample appear around 1332 cm^{-1}. The FWHM of the Raman band vary among ureilites and also among crystals in a grain. The band of Y-74130 is conspicuously broader than those of others. Raman spectra of diamonds in Y-74123 and A 881931 are similar to that of diamond synthesized by static experiments with a catalyst or by a CVD method and the spectra of Y-74130 to that of diamond synthesized by shock or detonation experiments.

The spectra at the middle of each figure suggest that the parts where the spectra were obtained are composed of an intimate mixture of graphite and diamond, of which spectra are similar to those obtained from the parts where graphite or diamond exclusively exists.

Plots of Raman shift vs. FWHM of graphite E_{2g} band from six ureilites are shown in Fig. 4. The band positions vary in the range from 1575 to 1600 cm^{-1} and FWHM in the range from 10 to 90 cm^{-1} and the band positions correlate positively with FWHM. Some of graphite crystals in Y-74659 and Y-74130 show distinguishably broader bands than others.

Plots of Raman shifts vs. FWHM of spectral bands of diamond from six ureilites are shown in Fig. 5. The Raman shift varies in the range from 1328 to 1336 cm^{-1} and FWHM from 5 to 65 cm^{-1}. The FWHM of Y74123, A 77257, Y-8448 and A 881931 correlate negatively and those of Y-74659 and Y-74130 correlate positively with the band positions. It is known that cluster diamond with a small crystal size shows a broader Raman spectrum at a smaller wave number position than that with a large crystal size [7]. Then, the negative correlation between spectrum positions and FWHM is due to the variation in crystal sizes of diamond observed. The positive correlation between the spectrum positions and FWHM observed in Y-74659 and Y-74130 can not be interpreted as the variation of crystal sizes of diamond. As diamonds in Y-74659 and Y-74130 are accompanied by graphite, the positive correlation may be apparent one due to overlap between diamond spectrum and graphite D band.

The results of Raman spectroscopy suggest that diamonds in Y-74659 and Y-74130 may have formed by shock at the conditions near to those of shock or detonation experiments and those in Y-74123, A 77257, Y-8448 and A 881931 have formed at the conditions near to those of static experiments with a catalyst or at a high temperature and a high pressure near to a melting point of graphite. These results agree well with the results obtained by X-ray analyses of C-rich grains [4].

References:

[1] Goodrich C. A. (1992) *Meteoritics, 27, 327-352.* [2] Nakamuta Y. and Aoki Y. (2000) *Meteorit. Planet. Sci., 35, 487-493.* [3] Nakamuta Y. and Aoki Y. (2001) *Meteorit. Planet. Sci., 36, A146.* [4] Nakamuta Y., Aoki Y. and Kojima H. (2002) *27th Symposium on Antarctic Meteorit. (abstract), 117-119.* [5] Tuinstra F. and Koenig J.L. (1970) *J. Chem. Phys., 53, 1126-1130.* [6] Pasteris J. D. (1989) *Appl. Apectrosc., 43, 567-570.* [7] Yoshikawa M. et al. (1995) *Appl. Phys. Lett., 67, 694-696.*

δD variation of macromolecular organic matter from carbonaceous chondrites.

Hiroshi Naraoka and Yasuhiro Oba, Dept. of Earth Sciences, Okayama Univ. Okayama, Japan

Introduction:

Various organic compounds such as amino acid, carboxylic acid and polycyclic aromatic hydrocarbon have been detected from carbonaceous chondrites. However, a solvent-insoluble and high-molecular organic matter is the major component of the total organic matter in chondrites. The macromolecular organic matter is consisted mainly of aromatic structure with minor aliphatic carbon as well as heteroelements(N, O, S)-linked carbon. In the previous study [1], we reported an H/C-N/C chemical sequence of well-purified macromolecules from nine Antarctic and non-Antarctic carbonaceous chondrites as a sensitive indicator for thermal alteration. On the other hand, many studies revealed extreme D-enrichment of the macromolecules (up to ~+1000‰ relative to SMOW; *e.g.* [2]). Such meteoritic D-enrichment is generally recognized as a signature of presolar, interstellar-cloud material which survived incorporation into the forming solar system (*e.g.* [3, 4]). Hydrogen isotope distribution of macromolecular organic matter has not been understood with respect to thermal alteration of chondrites. In this study, we have conducted δD measurement of several macromolecules to investigate the δD distribution for CM chondrites.

Samples and methods:

Hydrogen isotopic compositions of the purified macromolecule from seven CM chondrites (Yamato (Y)-791198, Y-793321, Belgica-7904, Asuka(A)-881280, A-881334, A-881458, and Murchison) were determined using an isotope ratio mass spectrometer coupled with a high temperature elemental analyzer at 1440°C with graphite in on-line mode. The purification procedure and CHN chemical composition of these macromolecule are given elsewhere [1]. The δD value was calibrated with three international isotope standards (SMOW, GISP and SLAP), and expressed by δ notation relative to SMOW.

Results and discussion:

The δD value of macromolecule ranges widely from +133‰ to +986‰. Although the extreme D-enrichment in Murchison (+986‰) is consistent with a previous report [2], much less δD values are observed from Y-793321 (+133‰) and A-881334 (+257‰). δD-H/C (atomic) relationship is shown in Fig. 1, being divided into two groups: the high δD with high H/C group (Y-791198, A-881458 and Murchison) and the low δD with low H/C group (Y-793321, B-7904, A-881280 and A-881334). Generally, the hydrogen enriched macromolecules show D-enrichment in this study. A ^{13}C NMR study of these macromolecules [5] clarified the various ratio of aliphatic to aromatic carbon, where the high H/C group contained more aliphatic carbon. This observation suggests that the D-enrichment occur in the aliphatic hydrogen, being consistent with previous studies [2, 4].

The high δD group yielded abundant soluble organic compounds such as amino and carboxylic acid, while the low δD group was extremely depleted in these organic compounds. In the previous study [1], the thermal alteration could cause the H/C decreasing associated with loss of labile solvent-extractable organic compounds. It is likely that D-enriched aliphatic hydrogen of macromolecule was lost during the thermal alteration, as well as aromatic hydrogen exchanged with environmental water hydrogen during hydrothermal activity on meteorite parent bodies, as supported by a hydrothermal experiment of macromolecule [6].

Conclusions:

We determined hydrogen isotopic compositions of macromolecules from CM chondrites including Antarctic and Murchison. The δD value ranges widely from +133‰ to +986‰, where the high H/C macromolecule shows the high δD value in general, probably due to D-enrichment in aliphatic hydrogen in the structure. The δD variation of macromolecule in CM chondrites may depend on the chemical structure and isotopic changes associated with the thermal alteration process.

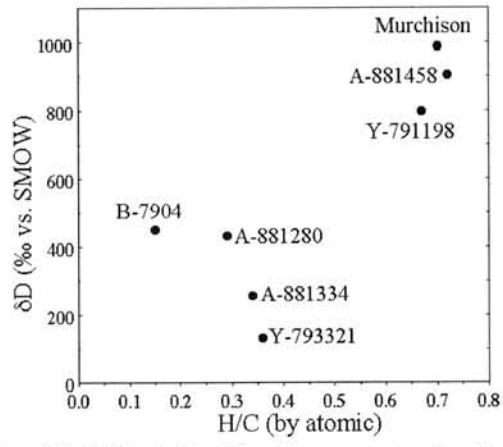

Fig.1 δD-H/C relationship of macromolecules from CM carbonaceous chondrites

References:

[1] Naraoka H. et al. (2004) *Meteorit. Planet. Sci., 39,* 401–406. [2] Kerridge J. F. et al. (1987) *Geochim. Cosmochim. Acta, 51,* 2527-2540. [3] Kerridge J. F. (1999) *Space Sci. Rev., 90,* 275-288. [4] Pizzarello S. and Huang Y. (2005) *Geochim. Cosmochim. Acta, 69,* 599-605. [5] Yabuta H. et al. (2005) *Meteorit. Planet. Sci., 40,* 779–787. [6] Oba Y. and Naraoka H. (2005) *Antarctic Meteorites XXX,* 59-60.

THERMOLUMINESCENCE STUDY OF JAPANESE ANTARCTIC METEORITES IX

K. Ninagawa[1], T. Kuyama[1], N. Imae [2], H. Kojima[2], and K. Yanai[3]

[1]Okayama University of Science, [2] National Institute of Polar Research, [3] Iwate University.

Natural TL (thermoluminescence), the luminescence of a sample that has received no irradiation in the laboratory, reflects the thermal history of the meteorite in space and on Earth. Natural TL data thus provide insights into such topics as the orbits of meteoroids, the effects of shock heating, and the terrestrial history of meteorites. Induced TL, the response of a luminescent phosphor to a laboratory dose of radiation, reflects the mineralogy and structure of the phosphor, and provides valuable information on the metamorphic and thermal history of meteorites. The sensitivity of the induced TL is used to determine petrologic type of type 3 ordinary chondrites.

As reliable pairing approach, TL properties within large chondrites were analyzed, taking advantage of the fact that serial samples from these meteorites is known to be paired [1]. Then a set of TL pairing criteria: 1) the natural TL peak height ratios, LT/HT, should be within 20%; 2) that ratios of raw natural TL signal to induced TL signal should be within 50%; 3) the TL peak temperatures should be within 20℃ and peak widths within 10℃ was proposed. This set of TL pairing criteria is less restrictive than previously used [1].

We have measured TLs of 82 Yamato and 100 Asuka unequilibrated ordinary chondrites so far [1,2,3,4]. This time we measured TL of more 26 Asuka chondrites. Eight of them are from 20km east of point A233 (D4), and 18 of them are from point A233 (D3) of around the Sør Rondane Mountains. The TL data of them are listed in Table. The petrologic subtype was determined from their TL sensitivity. Six chondrites, A-881742 (LL3), A-881628 (LL3), A-881647 (LL3), A-881915 (L3), A-881749 (L3), and A-881837 (LL3) were primitive below subtype 3.4. They are on main trend of correlation between TL sensitivity and olivine heterogeneity as shown in figure 1.

Above pairing criteria were also applied to the 26 samples. We found 5 TL potential paired fragments as shown in Table 2. .A group of L3 at D3 site comprises a chain of paired fragments. A L3 chondrite might shower near the D3 site.

References: [1] Ninagawa et al. (1998): Antarctic Meteorite Res., 11, 1-17. [2] Ninagawa et al. (2000): Antarctic Meteorite Res., 13, 112-120. [3] Ninagawa et al. (2002): Antarctic Meteorite Res., 15, 114-121. [4] Ninagawa et al. (2005): Antarctic Meteorite Res., 18, 1-16.

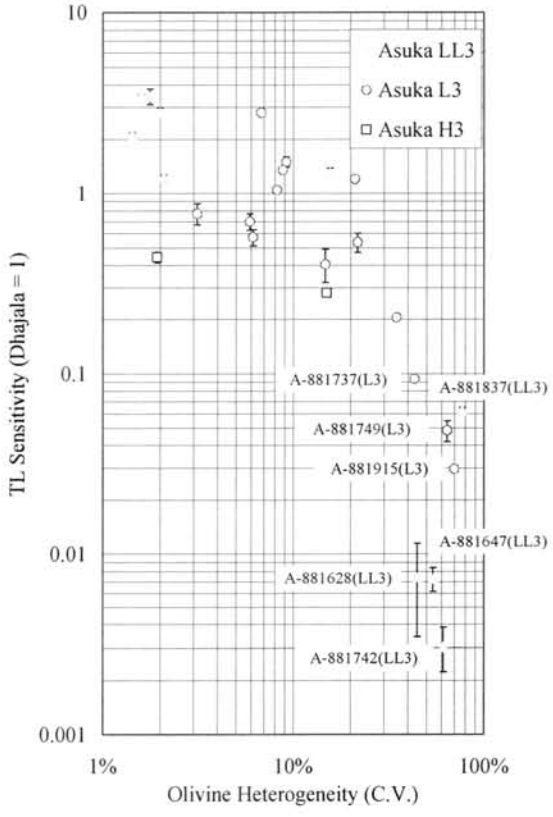

Fig.1. Correlation between TL sensitivity and olivine heterogeneity

Table 2. Paired fragments

Sampling site	Meteorite	Paired fragments
D3	A-881640	A-881634
	A-881634	A-881636 A-881643
	A-881636	A-881643
	A-881643	A-881695

Table Thermoluminescence data of Okayama for twenty-six unequilibrated Japanese ordinary chondrites

Meteorite	Class	Natural TL						Induced TL										LT			Low Ca-Py	Ol	Ol	Recom-	Sampling
		LT/HT			LT			TL Sensitivity			Peak Temp.			Width			TL	/TL Sens.			Heterogenity	Heterogenity	Ol	mended	site
					(10^3 counts)			(Dhajala=1)			(℃)			(℃)			Subtype	($x10^3$)			(C.V.)†	(C.V.)‡	Subtype	Subtype	
A-881628	LL3							0.007	±	0.004	360	±	17	144	±	17	3.0-3.2				72%	45%	3.5	3.0-3.2	D3
A-881634	L3	2.27	±	0.06	106.4	±	6.9	1.20	±	0.05	187	±	11	141	±	10	3.8	89	±	7	36%	21%	3.5		D3
A-881636	L3	2.38	±	0.01	306.3	±	6.9	2.80	±	0.10	187	±	0	143	±	1	3.9	109	±	5	25%	7%	3.9	3.9	D3
A-881640	L3	1.96	±	0.08	94.5	±	6.5	1.34	±	0.04	191	±	0	146	±	0	3.8	70	±	5	33%	9%	3.9		D3
A-881643	L3	2.70	±	0.01	167.6	±	23.6	1.49	±	0.10	193	±	4	147	±	3	3.8	112	±	17	31%	9%	3.9		D3
A-881647	LL3							0.007	±	0.001	146	±	4	147	±	5	3.1				67%	54%	≤3.4	3.1	D3
A-881649	LL3	5.11	±	0.05	146.9	±	0.2	1.24	±	0.02	194	±	5	148	±	1	3.8	118	±	2	30%	2%	3.9		D3
A-881653	L3	0.28	±	0.01	0.8	±	0.1	0.20	±	0.01	159	±	13	179	±	2	3.5-3.6	4	±	0	52%	35%	3.6	3.6	D3
A-881683	L3							0.70	±	0.07	190	±	1	156	±	1	3.7				27%	6%	3.9		D3
A-881686	LL3	0.98	±	0.03	36.6	±	2.8	1.30	±	0.07	193	±	5	167	±	3	3.8	28	±	3	52%	16%	3.8		D3
A-881695	L3	2.98	±	0.19	124.7	±	10.4	1.04	±	0.04	189	±	1	142	±	1	3.8	120	±	11	32%	8%	3.9		D3
A-881696	L3							0.77	±	0.10	191	±	3	160	±	1	3.7-3.8				36%	3%			D3
A-881709	L3							0.54	±	0.06	189	±	0	160	±	5	3.6-3.7				39%	22%	3.7	3.7	D3
A-881726	H3	1.15	±	0.06	5.3	±	0.7	0.28	±	0.01	178	±	7	155	±	1	3.6	19	±	3	34%	15%	3.8		D3
A-881737	L3							0.094	±	0.004	114	±	4	69	±	1	3.4-3.5				86%	43%	3.5	3.5	D3
A-881742	LL3							0.003	±	0.001	192	±	20	228	±	52	3.0-3.1				95%	61%	≤3.4	3.0-3.1	D3
A-881749	L3							0.05	±	0.01	78	±	2	68	±	1	3.3-3.4				75%	64%	≤3.4	3.3-3.4	D3
A-881759	LL3	1.79	±	0.02	62.4	±	1.0	2.13	±	0.05	145	±	0	126	±	0	3.8-3.9	29	±	1	24%	1%			D3
A-881770	L3	3.25	±	0.02	35.3	±	9.7	0.41	±	0.09	156	±	0	143	±	1	3.6-3.7	87	±	30	40%	15%	3.8		D4
A-881811	LL3	1.38	±	0.04	70.0	±	5.3	3.44	±	0.35	154	±	1	129	±	0	3.9	20	±	3	16%	2%			D4
A-881837	LL3	0.26	±	0.00	0.4	±	0.0	0.063	±	0.002	144	±	15	162	±	0	3.4	6	±	1	66%	77%	≤3.4	3.4	D4
A-881841	LL3	1.89	±	0.02	117.2	±	3.2	2.81	±	0.16	146	±	1	123	±	4	3.9	42	±	3	20%	2%			D4
A-881866	LL3	1.69	±	0.02	150.4	±	12.6	3.53	±	0.00	146	±	0	133	±	1	3.9	43	±	4	12%	2%			D4
A-881875	H3	2.86	±	0.38	32.5	±	3.1	0.44	±	0.03	147	±	1	143	±	0	3.6-3.7	73	±	9	31%	2%			D4
A-881915	L3				0.2	±	0.0	0.030	±	0.001	75	±	8	62	±	0	3.3	7	±	1	79%	70%	≤3.4	3.3	D4
A-881919	L3							0.57	±	0.06	163	±	0	146	±	1	3.7				41%	6%	3.9		D4

†: Coefficient of variation (σ as percentage of the mean) of ferrosilite in the low Ca pyroxene.

‡: Coefficient of variation (σ as percentage of the mean) of fayalite in the olivine.

Micrometeorites discovered from surface snow near the Dome Fuji station, Antarctica.

Takaaki Noguchi[1], Miki Osonoi[1], Tomoki Nakamura[2], Akira Tsuchiyama[3], Naoya Imae[4], [1]Department of Materials and Biological Sciences, Ibaraki University, [2]Department of Earth and Planetary Sciences, Faculty of Science, Kyushu University, [3]Department of Earth and Space Sciences, Osaka University, [4]Institute of Polar Research.

Introduction:

Antarctic micrometeorites (AMMs) have been collected by melting bare ice. Their mineralogy strongly suggests that vast majority of them were derived from asteroids experienced heavy aqueous alteration [e. g. 1, 2, 3] although quite small amounts of primary anhydrous ultracarbonaceous AMMs were recognized by our group [4] and it was revealed that they contain high abundances of presolar silicates (about 1200~3300 ppm [4]) that are comparable with the highest value found among IDPs (~5500 ppm) [5]. On the contrary, it has been well known that interplanetary dust particles (IDPs) captured in the stratosphere are composed mainly of almost equal amounts of anhydrous and hydrated particles [e. g. 6, 7]. Obviously mineralogical population of fine-grained extraterrestrial particles is different between two loci of sample collection. One explanation for this difference is primary anhydrous AMMs that were deposited in snow would have been selectively destroyed during compaction of snow. Recently some porous AMMs were discovered among fine-grained samples collected by melting snow near Dome C Station by European researchers [8, 9]. However, the majority of the collected AMMs are similar to conventional AMMs. In this study, we report characteristics of AMMs collected among fine-grained precipitate after filtering of melted snow fell near Dome Fuji Station. Their morphological and mineralogical features of our new AMM collection strongly suggest that it is a "missing link" between conventional AMM and IDP collections.

Sampling procedures and analytical methods:

Surface unconsolidated snow collected in the vicinity of Dome Fuji Station was returned to the National Institute of Polar Research in 2004. It was transferred to a clean room (class 1000) at Ibaraki University. During transfer, the snow sample was kept well below 0 °C. The snow was melted and filtered by using a multiple suction filtration in the clean room. It took about 2 months to filter the entire snow sample. 743 fine-grained residual particles were picked up and placed on platinum plates under a stereomicroscope in a clean bench (class 100) in the clean room. The particles were observed by scanning electron microscope (SEM) and chemical compositions were measured by energy dispersive spectrometer (EDS) equipped on the SEM to find AMMs. After SEM/EDS observation and analysis, 49 particles including 8 spherules were recognized as AMMs. Their average diameter is 63 μ.m. After identification of AMMs, micro-Raman spectroscopy was performed at Ibaraki University to investigate carbonaceous materials and coexisting minerals in the AMMs. Bulk mineralogy of individual AMMs was determined by synchrotron radiation X-ray diffraction (SR-XRD) at KEK-PF and SPring-8. 3D-structure investigation by micro-CT at SPring-8 and transmission electron microscope (TEM) observation and EDS analysis are just started [10].

Results:

Partially melted AMMs and cosmic spherules occupy 8 and 18 %, respectively. These populations contrast starkly with those of conventional AMMs. Conventional AMMs contain 37 % scoreaceous (weakly to heavily melted) ones and 48 % spherules based on our unpublished data on 3000 AMMs collected at Tottsuki Point near Syowa Station. The majority of the AMMs in this study experienced weak to slight heating based on their surface textures. Most of them are highly to moderately porous morphology (Figs. 1 and 2). Figure 1 is a secondary electron image (SEI) of one of the most porous AMMs found in this study. SEM observation of its surface revealed that submicrometer-sized grains compose this AMM. There is also irregular shaped material (indicated by an arrow in Fig. 1). These features are comparable with CP IDPs. This type of AMMs has not been found before. 3D internal structure of one AMM of this type shows that they are truly porous even in its interior and as porous as anhydrous IDPs [10].

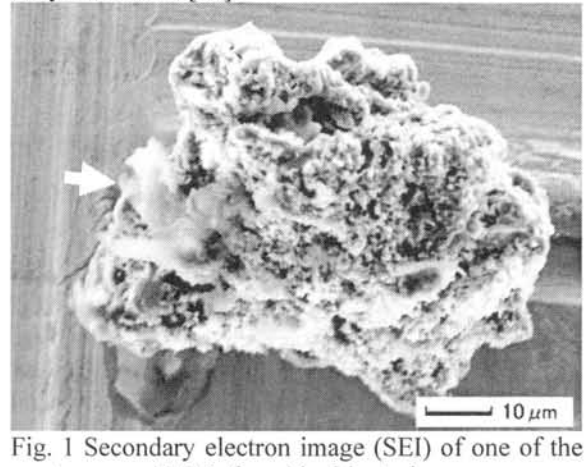

Fig. 1 Secondary electron image (SEI) of one of the most porous AMMs found in this study.

There are also less porous AMMs. Figure 2 shows a SEI of this type of AMMs found in this study. The sizes of monomers that constitute the AMM are larger than 1 μm. Compact and/or melted

partially particles that are typical among conventional AMMs are less common.

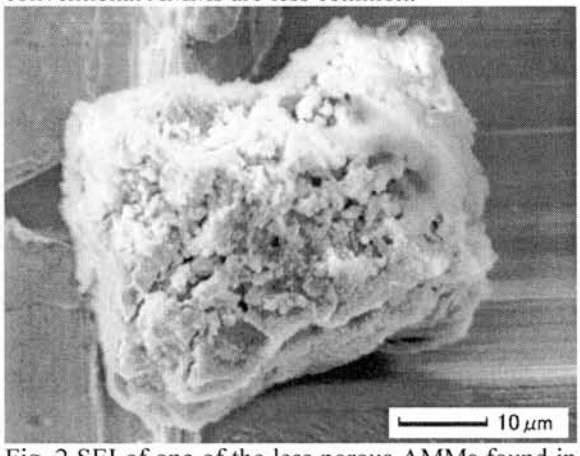

Fig. 2 SEI of one of the less porous AMMs found in this study.

SR-XRD data of weakly heated AMMs have some unique features that have not been reported by previous studies of conventional AMMs. (1) Primary olivine and low-Ca pyroxene, and pyrrhotite are common among them. Especially abundant pyrrhotite was identified from 14 AMMs among 20. The presence of pyrrhotite is rare among conventional AMMs. (2) 11 AMMs among 20 are thought to have primary anhydrous mineralogy. Two AMMs of this type contain plagioclase that has not been identified from conventional AMMs. 5 AMMs contain saponite as phyllosilicates and no serpentine was identified. The abundance of serpentine is very low if present. In the other AMMs, phyllosilicates are though to have been decomposed by heating.

Two AMMs were investigated by TEM. One has primary anhydrous mineralogy and another contains phyllosilicates. TEM observation of ultrathin sections of the anhydrous AMM shows that they experienced heating probably during atmospheric entry because there are some submicrometer-sized recrystallized aggregates composed of Fa_{50} olivine and magnetite. However, it contains magnesian olivine and low-Ca pyroxene and Si-rich glass (amorphous silicate material). Each low-Ca pyroxene grain is composed of an intimate mixture of low-Ca clino- and ortho-pyroxene. Another one is the AMM shown in Fig. 2. In spite of its morphology, it is composed mainly of saponite with a small amount of magnetite and rare low-Ca pyroxene and olivine. Its mineralogy is common to phyllosilicate-rich AMMs collected from ice.

Raman spectroscopy of the 32 unmelted AMMs shows that 60 % of them have remarkable Raman shift bands of amorphous carbon (D and G bands) and the others do not show the bands. However, EDS spectra of these AMMs show that area intensity of the D and G bands does not correlate with intensity of C Kα normalized by that of O Kα in the AMMs and CI (Orgueil). No Raman bands from silicates were detected from all the unmelted AMMs except for one particles, which has weak bands from olivine.

Discussion:

Morphology and bulk mineralogy of the most porous AMMs found in this study are almost identical to those of anhydrous IDPs. Therefore, we believe that this type of AMMs is large IDPs that fell on the ground. Most of their SR-XRD data show that the AMMs contain magnetite and that kamacite was not identified. These facts suggest that they experienced heating during atmospheric entry. Even in such heated AMMs, Si-rich glass that is often included in anhydrous IDPs was identified. Such amorphous material has not been discovered from AMMs until this study. At least two of the most porous AMMs contain kamacite as well as olivine, low-Ca pyroxene, and pyrrhotite. And one of them contains plagioclase. They may contain GEMS (glass embedded metal and sulfides) [e. g. 7].

Based on the SR-XRD data of 20 AMMs, population of primary anhydrous AMMs is 55 %, which is similar to the value for anhydrous IDPs, 45 % [e. g. 6, 7]. Because we have not analyzed the other 20 AMMs by SR-XRD, the abundance of the primary anhydrous AMMs may change. If all the other 20 AMMs were hydrated AMMs, this value will decrease to 27 %. If we take this value, it is still comparable with the value of IDPs. Higher proportion of this type of AMMs probably resulted from the use of Millipore® filters instead of stainless sieve during filtering of water. The use of Millipore® filters would have served to preserve fragile AMMs.

Features of micro-Raman spectra of the unmelted AMMs in this study are similar to those of IDPs [11]. Raman shift bands of silicates are masked by carbonaceous materials in them like the case of IDPs. Well ordered carbonaceous material was not found among the unmelted AMMs. The average CI-normalized C/Si ratio of the primary anhydrous AMMs is 3.6 and that of hydrated AMMs is 1.6. These features of carbonaceous materials are also consistent with those of IDPs.

Acknowledgement:

We thank Drs. Obinata, Fujita, and Kurisaki for sampling surface snow near Dome Fuji Station. Messers. Mori, Akaki, and Yokoyama are appliciated for technical assistance during XRD analysis.

References:

[1] Kurat G. et al. (1994) GCA, 58, 3874-3904, [2] Noguchi T. and Nakamura T. (2002) EPSL, 202, 229-246, [3] Nozaki W. et al. (2006) MAPS, in press, [4] Yada T. et al. (2006) LPS XXXVII, #1470, [5] Messenger S. (2003) Science, 300, 105-108,[6] Jessberger E. K. (2001) In: Cosmic Dust, [7] Bradley J. P. (2004) In: Treatise on Geochemistry, [8] Dupart J. et al. (2005) LPS XXXVI, #1678,[9] Duprat J. et al. (2005) EAS, 14, 51-56, [10] Tsuchiyama A. et al. (2006) LPS XXXVII, #2001,[11] Wopenka B. (1988) EPSL, 88, 221-184.

Sm-Nd Age and Nd- and Sr- Isotopic Evidence for the Petrogenesis of Dhofar 378. L. E. Nyquist[1], Y. Ikeda[2], C.-Y. Shih[3], Y. D. Reese[4], N. Nakamura[5], and H. Takeda[6], [1]Mail Code KR, NASA Johnson Space Center, Houston, TX 77058-3696, USA, laurence.e.nyquist@nasa.gov, [2]Dept. of Material and Biological Sci., Ibaraki University, Mito 310-8512, Japan, y-ikeda@mx.ibaraki.ac.jp, [3]Mail Code JE-23, ESCG/Jacobs Sverdrup, P.O. Box 58477, Houston, TX 77258-8477, USA, [4]Mail Code JE-23, ESCG/Muniz Engineering, Houston, TX 77058, USA, [5]Dept. of Earth and Planet. Sci., Kobe University, Nada, Kobe 657-8501, Japan, [6]Research Institute, Chiba Institute of Technology, Narashino 257-0016, Japan.

Introduction:

Dhofar 378 (hereafter Dho 378) is one of the most ferroan lithologies among martian meteorites, resembling the Los Angeles basaltic shergottite in lithology and mineral chemistry, although it is more highly shocked than Los Angeles [1,2]. All plagioclase (Pl) grains in the original lithology were melted by an intense shock in the range 55-75 GPa. Clinopyroxenes (Cpx) sometimes show mosaic extinction under a microscope showing that they, too, experienced intense shock. Nevertheless, they zone from magnesian cores to ferroan rims, reflecting the original lithology. Cpx grains also often contain exsolution lamellae, showing that the original lithology cooled slowly enough for the lamellae to form. Because all plagioclase grains were melted by the intense shock and subsequently quenched, the main plagioclase component is glass (Pl-glass) rather than maskelynite. Like Los Angeles, but unlike most basaltic shergottites, Dho 378 contains approximately equal modal abundances of Cpx and Pl-glass. The grain sizes of the original minerals were comparatively large (~1 mm). The original plagioclase zoning has been severely modified. Following shock melting, the plagioclase melts crystallized from the outside inward, first forming outer rims of Cpx-Pl intergrowths (~10 μm) followed by inner rims (10's to 100 μm) of An_{40-50} feldspar, and finally Pl-gl cores of compositions An_{33-50} with orthoclase compositions up to Or_{12} [2].

Sample Preparation:

At JSC two bulk aliquants weighing 26 and 31 mg, resp., were taken from the 340 mg remainder of 550 mg of finely ground material used for major element analyses [2]. The smaller aliquant was analysed directly, the larger was sonicated for 10 min. in 2 N HCl prior to analysis. Mineral separates were prepared from a second ~400 mg sample. A PTS was made from an ~70 mg piece of this sample. The remainder was powdered and sieved to obtain fractions of grain size <74 μm and 74-149 μm, respectively. A 17 mg Pl-gl sample was obtained from the <74 μm fraction by repeated separations with liquids of density 3.32 and 2.85 g/cm^3, resp. A sample of Pl-gl from the 74 -149 μm fraction was used for the Ar-Ar study [3]. Pyroxene samples, Px1 and Px2, resp., were obtained as more magnetic and less magnetic subsamples of density >3.45 g/cm^3.

Sm-Nd Age:

Measured Sm and Nd concentrations in the whole rock powder were 1.12 and 2.83 ppm, respectively, in good agreement with 1.13 and 2.7 ppm previously reported for another 97 mg bulk sample [4]. $^{147}Sm/^{144}Nd$ = 0.239 is similar to 0.234 for Zagami ([5] and unpublished JSC data), and 0.232 for a bulk sample of Los Angeles Stone 1 (LA1, unpub. JSC data). The Sm and Nd abundances in our sample of LA1 were 4.5 and 11.8 ppm, significantly higher than those in Dho 378. Our analysis of LA1 may have been unrepresentative, however. Rubin et al. [6] report Sm = 1.94 ppm in LA1, but Sm = 3.4 ppm in LA2. Zagami, Dho 378, LA1, and LA2 show an approximately linear correlation of La to P_2O_5; i.e.; La (ppm) ~ 3 x P_2O_5 (%). P_2O_5 = 0.77 wt% in Dho 378 [2], in good agreement with 0.66 wt% in a 352 mg sample of LA1, but about ½ that of a 207 mg sample of LA2 [6].

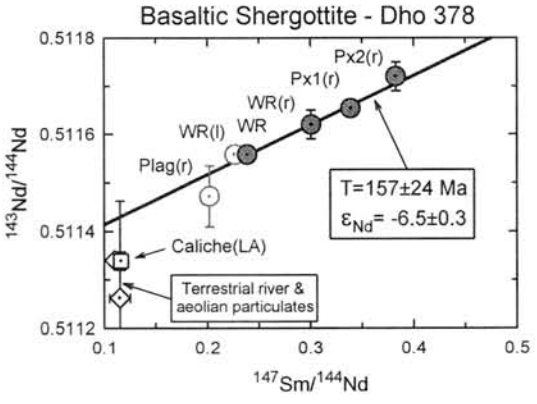

Figure 1. Sm-Nd isochron for Dho 378.

Sm and Nd concentrations in the two pyroxene separates are 0.30-0.35 and 0.53-0.55 ppm, respectively. These values are similar to 0.33-0.34 and 0.32-0.63 [2] for SIMS analyses of augitic cores; rim values are slightly lower [2]. They also are similar to Sm = 0.19-0.33 ppm and Nd = 0.26 –0.50 ppm in Zagami pyroxene separates and to Sm = 0.12-0.31 ppm and Nd = 0.17-0.42 in LA pyroxene separates. $^{147}Sm/^{144}Nd$ = 0.38 for the most Fe-rich Dho 378 pyroxene, Px 2, is similar to values obtained for Zagami and LA. Wadwha et al. [7] showed that REE abundances in shergottite pyroxenes are the result of closed system igneous crystallization. Mg/Fe zoning profiles and exsolution textures in Dho 378 pyroxenes were retained during the shock event. Nd = 0.3 ppm in the Dho 378 plagioclase residue after leaching is similar to Nd = 0.2 ppm for a plagioclase separate of LA2. The plagioclase and

whole rock leachate (WR(l)) data lie within error limits of an isochron determined primarily by the pyroxene and whole rock data. The WR(l) data are dominated by Sm and Nd from Dho 378 phosphates. Thus, we interpret the Sm-Nd isochron age of 157±24 Ma for Dho 378 as its crystallization age.

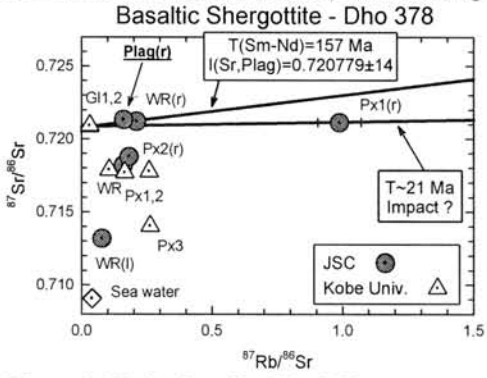

Figure 2. Rb-Sr data for Dho 378.

Rb-Sr Data

Rb-Sr data obtained at JSC and in prior analyses at Kobe University are shown in Fig. 2. The data from both laboratories show the pervasive effect of terrestrial weathering and contamination. The effect of contamination was minimized by leaching four samples of high Sr content: two Pl-gl samples analysed at Kobe, and Plag(r) and WR(r) analysed at JSC. The data for these samples, combined with the the Sm-Nd age of 157 Ma, yields initial $^{87}Sr/^{86}Sr$ = 0.720779±14. Combining this initial $^{87}Sr/^{86}Sr$ value with data for Px1(r) gives an apparent age of ~21 Ma. Possibly this "age" is that of a minor Rb-rich phase produced during shock melting and contained within the Px1 separate. The possibility that the Px1 analysis simply shows less contamination than evident for the other pyroxenes cannot be excluded.

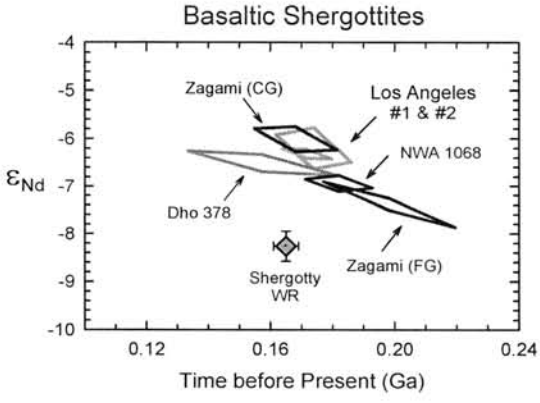

Figure 3. (T, ε_{Nd}) plot for Dho 378.

Initial ε_{Nd}

Negative ε_{Nd} = -6.5±0.3 at T = 157 Ma ago for Dho 378 is similar to that of other shergottites of its class (Fig. 3). NWA 1068 is classified among the Ol-bearing doleritic type of the Ol-phyric subgroup [1]. Negative ε_{Nd} values indicate assimilation of LREE-enriched crustal materials by basaltic shergottite magmas. The occurrence of the same REE and isotopic signatures among different shergottite subgroups shows the REE- and P-rich "crustal" component has no detectable impact on the major element composition of the magma, suggesting contamination by metasomatic fluids. The (T, ε_{Nd}) data for Dho 378 data match most closely to those of NWA 1068 and Los Angeles.

Initial $^{87}Sr/^{86}Sr$

Initial $^{87}Sr/^{86}Sr$ (Fig. 4) confirm Los Angeles as the closest isotopic match to Dho 378. They were either co-magmatic or derived from similar source regions via similar petrogenetic processes.

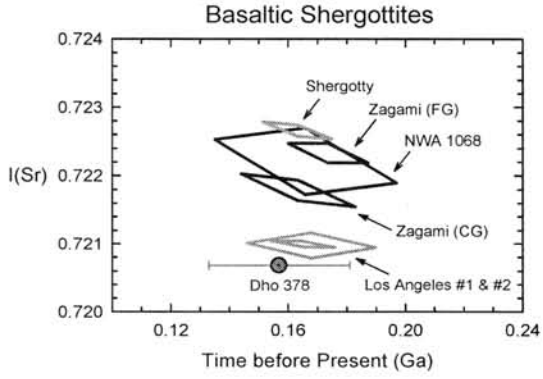

Figure 4. (T, ISr) plot for Dho 378.

Discussion

The similarity in lithology and mineralogy of Dho 378 and Los Angeles has already been noted [2]. This study extends the similarity to include Nd- and Sr- isotopic systematics. If the three stones, LA1, LA2, and Dho 378 were indeed co-magmatic, the slightly younger Sm-Nd age of Dho 378 compared to previously determined Sm-Nd ages of 172±8 Ma and 174±12 Ma for LA1 and LA2, respectively, may reflect some resetting during shock melting. Park and Bogard [3] suggest that an Ar-Ar isochron age of 143(+18,-10) Ma for Dho 378 may date Ar outgassing in an impact event predating the ~ 3 Ma ejection event. If so, the Sm-Nd age may have been partially reset at that time. However, some other volatile species show no evidence of post-magmatic losses. Bulk Na_2O = 2.08 wt% [2] is nearly the same as for LA1 (2.22 wt%) and LA2 (2.13 wt%). The more refractory alkali, K, also is lower in Dho 378: K_2O = 0.17 wt% in Dho 378 vs 0.24 and 0.31 wt% in LA1 and LA2, resp. The K/Rb ratio has been shown to be a sensitive indicator of *in vacuo* volatile loss of alkalis. The K/Rb ratio of Dho 378 (~256) is nearly identical to that of LA2 (~245). The possibility that the Ar-Ar age approximates the age of crystallization of very high K phases (alkali feldspar, rhyolitic glass) stochastically enriched in the feldspar sample used for Ar-Ar analysis merits thorough evaluation.

References:

[1] Ikeda Y. (2004) *Antarctic Met. Res., 17,* 35-54. [2] Ikeda Y. (2006) et al. *Antarctic Met. Res., 19,* (in press). [3] Park J. and Bogard D. D. (this vol.) [4] Dreibus G. et al. (2002) *MAPS, 37,* A43. [5] Nyquist L. E. et al. (1995) *LPS XXVI,* 1065-1066. [6] Rubin A. E. et al. (2000) *Geology, 28,* 1011. [7] Wadhwa M. et al. (1994) *GCA, 19,* 4213-4229.

Elemental composition of asteroid Itokawa by remote X-ray fluorescence spectrometry and its relation to meteorite types. T. Okada[1,2], K. Shirai[1], Y. Yamamoto[1], T. Arai[1,3], K. Ogawa[1,4], T. Inoue[1,2], and M. Kato[1,2,4], [1]Institute of Space and Astronautical Science, Japan Aerospace Exploration Agency, [2]University of Tokyo, [2]Graduate University for Advanced Studies (Soekndai), [4]Tokyo Institute of Technology.

Introduction:

The asteroid-meteorite connection is among the most important problems to be solved for understanding the origin and evolution of our solar system. There has been a paradox that the most frequently observed asteroids are classified as S type in taxonomy whose reflectance spectra are not suited to ordinary chondrites, the most commonly found meteorites on Earth. Recent progress in Earth based observations and laboratory experiments in visible to near-infrared spectroscopy possibly provides more detailed identification of the relation of asteroids and meteorites [1, 2].

X-ray fluorescence or XRF spectrometry of an S (IV) class near-Earth asteroid 25143 Itokawa has been conducted by the CCD-based X-ray spectrometer (XRS) onboard Hayabusa [3] during the rendezvous phase in 2005. X-ray fluorescence emissions excited by solar X-rays were detected for some major elements. Major elemental ratios (Mg/Si, Al/Si) and the upper limit of S/Si are obtained. In this study, some constraints of the elemental composition of Itokawa are discussed.

Hayabusa:

The Japanese Hayabusa mission is an engineering asteroid explorer to demonstrate technologies for asteroid sample return [4]. It still has a high scientific significance including remote sensing of the asteroid during the rendezvous. Sample return will provide, if successful, the most important scientific progress [5].

The target asteroid of Hayabusa is a near-earth asteroid 25143 Itokawa, characterized by ground based observations as an S (VI) and its composition proposed as an LL-chondrite [3], 550m x 250m in shape [6], and the rotation period of 12.1 hours [7]. The key scientific objectives of Hayabusa are to understand what the asteroid is made of and what its origin is.

Hayabusa (renamed from MUSES-C) was launched in 2003 and arrived at Itokawa in 12 September 2005. The rendezvous phase lasted three months. The first two months were used for remote observaions of Itokawa, and the last month was used for trial of sample collection with rehearsal descents and two successful touchdowns.

XRS:

The XRS is one of the remote instruments onboard Hayabusa for major elemental analysis of Itokawa by measuring X-rays off the asteroid surface excited by solar X-rays [8]. Remote XRF technique has been proven by the Apollo missions to determine major elemental composition of the uppermost 100 micron of the surface of atmosphere-free planets [9].

The XRS [8] is based on charge-coupled device (CCD) with high energy resolution (FWHM 160eV @5.9KeV). In addition, it has a standard sample plate aboard to concurrently calibrate X-rays excited by the Sun. Since the intensities and spectral profiles of the solar X-rays drastically changes, the compared analysis by using the standard sample has much improved the accuracy of elemental compositions.

XRF Spectrometry of Itokawa:

During the rendezvous phase, the XRS performed XRF spectrometry of the surface of Itokawa. X-ray intensities excited from the asteroid strongly depend on solar activity. During the period, solar X-rays were faint and not favored for XRF spectrometry. But some times late in November, solar X-rays became brighter enough to excite XRF of major elements of Mg, Al, and Si [3]. With the cooled CCD, these line emissions are clearly detected and discriminated each other, both for X-rays from the asteroid and from the standard sample. S detection is marginal with low signal to background ratios, so that only the upper limit of S/Si is estimated. For our method of preparation for the glassy plate standard sample, sulfur was almost escaped when heated. Thus the compared method is not able to be applied to S/Si analysis.

Elemental composition of Itokawa:

The surface composition of Itokawa has been analyzed by compared method [10] between the X-rays off the asteroid and the standard sample for Mg/Si and Al/Si. We have calculated the surface elemental ratios of Mg/Si and Al/Si for some sites. There are relatively small regional variations in composition and regional average of Mg/Si = 0.78 ± 0.09 and Al/Si = 0.07 ±0.03. This result shows that the elemental composition of Itokawa is more like an ordinary chondrite than any other types. Among the ordinary chondrites, LL- or L- chondrites are more likely. But H-chondrites or primitive achondrites cannot be rejected within the error bars [3]. S/Si appears lower than that of typical ordinary chondrites, although there is uncertainty due to instrumental errors. This may imply that a little bit of surface process occurred if the parent bodies are chondrites. But the loss of sulfur might be caused by many

possible processes such as thermal processes or meteorite impact processes. There is no information on the loss of sulfur is happened for the whole asteroid or only in the uppermost surface. This result that Itokawa is basically in chondritic composition but some processes might occur is consistent with other studies by near-infrared studies [11, 12]. Since the results are still preliminary and have relatively large uncertainties, further analysis should be needed, especially for heavier elements other than Mg, Al, Si, and S.

References:

[1] Binzel, R. et al.,(2001) *Met. Planet. Sci.* **36**, 1167. [2] Gaffey, M. J., et al., (1993) Icarus, **106**, 573-602. [3] Okada T. et al. (2006) *LPSC* **37**, 1596. [4] Kawaguchi, J. *et al.*, (2003) *Acta Astronautica* **52,** 117. [5] Fijiwara, A. et al.,(2003) *Adv. Space Res.*, **25**, 231-238. [6] Ostro, S.J. et al.,(2004) *Met. Planet. Sci.*,39(3):407-424. Muller et al. (2005) , *A&A* 443, 347-355. [7] Kaasalasinen, M. et al. (2003) *A&A*, **405**,L29-32. [8] Okada, et al., (1999) *Adv. Space Res.* **23**, 345-348. [9] Adler, I.J. and Trombka, J.I.,. *Phys. Chem Earth.*, **10**, 10-43,1977. [9] Trombka J. I. *et al.*, (1997) *JGR*, **102**, 23729. [10] Masuda, E. (2002), Master's thesis. Tokyo Inst. Tech., pp.76. [11] Abe, M. et al. (2006), *LPSC* **37**, 1547. [12] Abell, P. A., et al., (2006), *LPSC* **37**, 1513.

Mg-number Mapping of Mare Serenitatis with a Hyper-spectral Telescope

H. Okuno[1], Y. Yamanoi[1], and K. Saiki[1]
[1]Department of Earth and Space Science, Graduate School of Science, Osaka University, 1-1 Machikaneyama-cho, Toyonaka, 560-0043, Osaka, Japan.

Introduction:

The Clementine mission [1] and Lunar Prospector mission [2] are leading to significant new views of the structure and distribution of materials in the crust and upper mantle of the Moon. Lucey *et al.* [3] proposed the distribution map of iron and titanium of the moon, using Clementine UV/VIS data. These achievements offer a significant refinement to previous models for the compositional asymmetry of the moon, which has been recognized for many years. Mg# (=atomic Mg/(Mg+Fe)) serves as an important petrologic discriminator when analyzing and understanding lunar rocks and crustal evolutionary models. Mg# variation of the pyroxene shifts the wavelength of the absorption spectra of ferrous iron with their peaks at around 1000 nm and 2000 nm. If there really exist Mg# variations on the lunar surface materials, the shift of the absorption peak could be detected. However, the shift had not been detected by remote sensing because it is limited to a very small range. Pieters *et al.* [4] reported that small variations between spectra for different mare craters had also been observed at visible wavelengths as well as near the 1000 nm absorption feature obtained with Earth –based telescope and the center of absorption spectra ranges 980 nm –1000 nm in the lunar mare. However, there was no description about the shifts caused by Mg# variations in the lunar mare. In this study, we obtained reflectance spectra of lunar near side surface with an Earth-based hyper-spectral telescope and succeeded to detect the shifts by comparing a large number of spectra of mare basalts in Mare Serenitatis. Mare Serenitatis was selected as a test region because the pixels there have little variation in photometric geometry.

Method:

The spectral data of the lunar surface were obtained by Advanced Lunar Imaging Spectrometer (ALIS). ALIS is a kind of hyper-spectral imaging telescope. ALIS divides lunar near side surface into about 80,000 small areas and gains a hyper-spectral image cube of the each small area covering the visible and near-infrared regions (VIS-system: 380-1100 nm, NIR-system 1000-1700 nm) at high spectral resolutions (VIS: 5 nm and NIR: 9 nm) [5]. The location of the observation was Science City at the peak of Mt. Haleakala, Maui, Hawaii, USA. The dates of observation were from 15 to 26 Aug. 2005 and from 12 to 18 Dec. 2005. The observations were carried out by ALIS users group including authors. ALIS and its peripheral devices were transported from Japan. An observation dome, which had been constructed by Okano Lab. at Tohoku University, Japan, and the observation supporting facilities were served by Mees Solar Observatory at University of Hawaii.

Image processing:

In order to detect slight shift of the absorption peak, we analyzed the image cube of the moon by taking the following steps; (1) dark and flat field correction, (2) 5-points moving (20 nm width) smoothing, (3) normalization of all mare spectra with the same standard highland spectrum to reduce the influence of atmospheric absorption and that of the difference of relative sensitivity of CCD pixels at each wavelength, (4) 5-points moving (20 nm width) smoothing again, (5) baseline correction with line which starts from 693 nm and ends at 1059 nm to reduce the influence of lunar space weathering, (6) 3x3-pixels spatial smoothing. All smoothing are carried out to reduce the fluctuation of CCD pixels.

Result:

Comparing the resultant spectra, we detected the slight shift of the absorption spectra. For example, Figure 1 shows the spectra of three small areas of Mare Serenitatis (MS A, B, and C) after all data processes except for 3x3-pixels spatial smoothing. The locations of the points are shown in Fig. 2. The wavelengths of the absorption peak of them are 984 nm, 968 nm, and 973 nm. The wavelength of the absorption peak of spectrum of MS A shifts slightly longer than that of MS B and MS C. Using the processed spectrum of each point, the map of the wavelength of the absorption peak was made (Fig. 2). In Mare Serenitatis, most of the absorption peak ranges from 968 nm to 984 nm. In the middle of Mare Serenitatis, the absorption peak at around 1000 nm is the longest (984 nm) within Mare Serenitatis. The eastern area of the mare has shorter (973 nm) than the middle area. In the western area of the mare, the value gradually changes from east (973 nm) to west (968 nm).

Discussion:

In addition to Mg# variation, there are two major factors shifting the wavelength of absorption spectrum of ferrous iron; space weathering and calcium in pyroxene. When the both can be regarded as constant in some limited area, the shift can be interpreted as Mg# change and the absorption-peak map can be regarded as Mg# map of the area. Mg#s of Apollo 17 basalt samples range 0.37 – 0.54 under the assumption that the samples include all variations

of basalt lavas in Mare Serenitatis. 16 nm wavelength shift detected in this study corresponds approximately to 0.17 Mg# variation.

Acknowledgment:

We would like to express our thanks to Dr. Mike Maberry and Mr. Daniel O'Gara of Hawaii Univ. and ALIS users group for their kind assistance at Haleakala site. We also wish to thank Drs. Shoichi Okano and Hiroaki Misawa of Tohoku Univ. They allowed us to use their astronomical dome at the site and gave us helpful advice. ALIS was developed through Phase-IA research of "Ground-based Research Announcement for Space Utilization" (PI: K. Saiki) promoted by Japan Space Forum. Ground-based observations were supported by the Japanese Ministry of Education, Science, Sports, and Culture, Grant-in-Aid for Young Scientists (PI: K. Saiki).

Reference:

[1] Nozette S. *et al.* (1994) Science, 266, 1835-1839. [2] Binder, A. (1998) Science, 281, 1475-1476. [3] Lucey P. G. *et al.* (2000) J. Geophy. Res. 105: 20297-20305. [4] Pieters *et al.* (1993) Remote Geochemical Analysis: Elemental and Mineralogical Composition, Cambridge, 594pp. [5] Saiki K. *et al.* (2003) LPSC XXXV, #1483

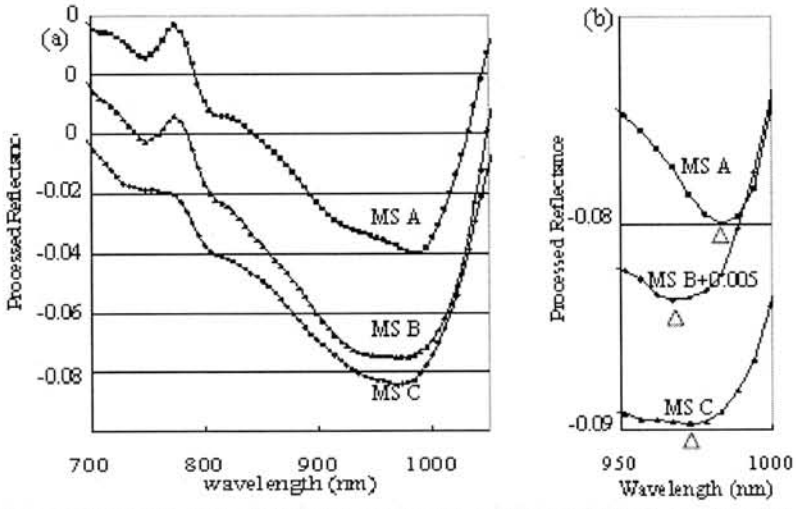

Fig. 1. The processed spectra of Mare Serenitatis. MS A, MS B, and MS C are three small example areas located in Mare Serenitatis (shown in fig. 2). Spectra (b) are parts of spectra (a) on large scale at around absorption-peak wavelength. Each triangle indicates the wavelength of the absorption peak.

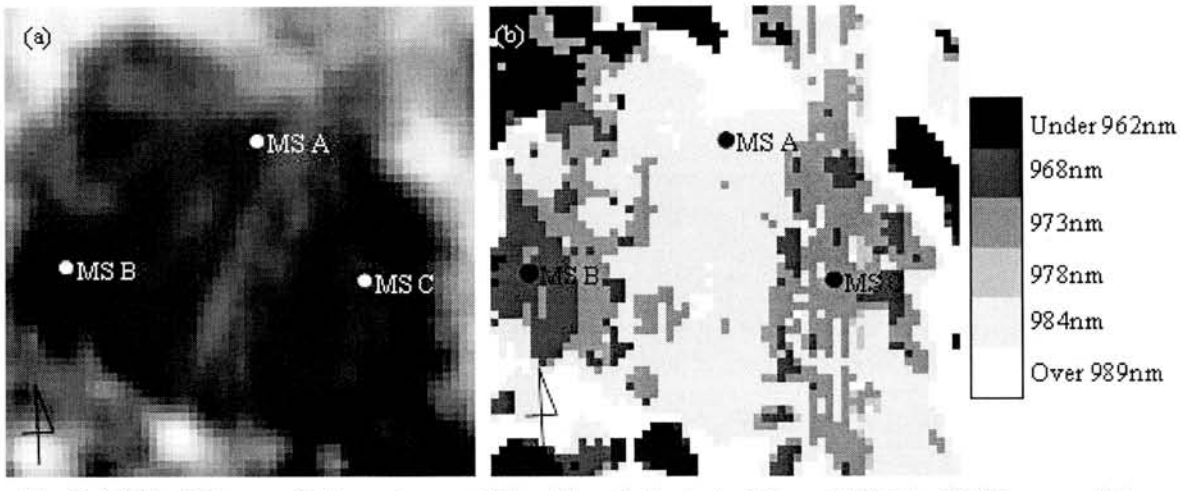

Fig. 2. (a) The 700 nm reflectance image of Mare Serenitatis derived from ALIS data. (b) The map of the wavelength of the absorption peak in Mare Serenitatis.

High-pressure minerals in shock melt veins of L6 chondrites: constraints on their P-T history

S. Ozawa[1], E. Ohtani[1], A. Suzuki[1], T. Kondo[1], M. Kimura[2]
[1]Institute of Mineralogy, Petrology and Economic Geology, Graduate School of Science, Tohoku University, Sendai 980-8578, Japan
[2]Institute of Astrophysics and Planetary Science, Faculty of Science, Ibaraki University, Mito 310-8512, Japan

Introduction:

The accretion of the terrestrial planets from asteroid collisions and delivery of meteorites to the Earth has been studied extensively. Investigations of meteorites that experienced such shock events are useful for understanding of mechanism of planetary impact events and formation of terrestrial planets.

Shock metamorphism has been studied to understand the shock conditions on meteorites and impact craters. Stöffer et al. (1991) developed a shock classification scheme (Shock Stage S1 toS6) and pressure calibration for ordinary chondrites based on the comparison of shock features between natural and experimentally shocked samples [1]. However, pressure calibration based on shock recovery experiments is problematic for some features, such as phase transformation that depend on kinetics. Recent studies of shock melt veins show that melt vein mineralogy and phase diagrams obtained from static high-pressure experiments can be used to constrain the shock conditions [2].

In this study, we investigated the mineralogy of shock melt veins in two L6 chondrites (Sahara98222 and Yamato74445) and estimated the P-T conditions during their impact events.

Samples and Experimental methods:

Sahara98222 was found in 1998 in the Sahara desert and classified as L6 chondrite. Previously, Grossman (1999) reported that Sahara98222 contains ringwoodite and should be classified as Shock Stage S6 [3]. Yamato74445 was also classified as L6 chondrite and reported to contain maskelynite [4]. Both of these meteorites have shock metamorphic features such as pervasive shock melt veins and high-pressure phases.

In this study, we used thin sections of Sahara98222 and Yamato74445 containing shock melt veins. The mineralogical features and the texture of rock were investigated with combination of optical petrography using transmitted and reflected light and scanning electron microscopy (SEM). Mineral phases in shock melt veins of these meteorites are identified using micro-Raman spectroscopy. Chemical compositions of minerals were analyzed using an energy dispersive (EDS) and a wavelength dispersive (WDS) EPMA.

Results:

Sahara98222 L6 chondrite consists of chondritic portion and shock melt veins. The maximum width of the shock melt vein is about 2.5 mm. In shock melt veins, chondritic fragments are surrounded by fine-grained minerals which look dark under transmitted light. The major minerals in Sahara98222 include olivine, orthopyroxene, clinopyroxene and plagioclase with minor amounts of iron-nickel alloy, troilite and other minor minerals. Olivine and pyroxenes show irregular fractures, planar fractures and undulatory extinction. Almost plagioclases have been transformed to optically isotropic maskelynite. In shock melt veins, minerals in fragments have partially or totally transformed into high-pressure phases such as wadsleyite, jadeite and tuite. We found no ringwoodite that reported in the previous work [3]. Tuite is a phosphate mineral recently found in a shocked meteorite [5]. Tuite is thought as a high-pressure polymorph of phosphate minerals such as whitlockite and merrillite [5]. In Sahara98222, We also found merrillite from chondritic portion adjacent to the shock melt veins.

In terms of basic petrography and shock features, Yamato74445 L6 chondrite is similar to Sahara98222 and the maximum width of the shock melt veins is about 1 mm. Olivine and pyroxenes adjacent to the shock melt veins show weak mosaicism as well as irregular fractures, planar fractures and undulatory extinction. Almost plagioclases have transformed into maskelynite.In shock melt veins, minerals in fragments have transformed into high-pressure phases such as wadsleyite, ringwoodite and akimotoite.

Discussions:

We found that shock melt veins of Sahara98222 contain olivine, wadsleyite, orthopyroxene, clinopyroxene, jadeite and tuite. According to the phase diagram of Akaogi at al. (1989), olivine-wadsleyite phase transition with composition of olivine in Sahara98222 occurs at the pressure around 13 to 15 GPa [6]. In terms of $MgSiO_3$ phases, shock melt veins of Sahara98222 contain only low-pressure phases and no high-pressure polymorphs was identified, which indicates that the shock pressure was lower than 16 GPa [7]. Therefore, we estimated the shock pressure of Sahara98222 to be about 13-15 GPa.

Shock veins of Yamato74445 contain olivine, wadsleyite, ringwoodite, orthopyroxene, clinopyroxene and akimotoite. Olivine, wadsleyte and ringwoodite assemblage constrains the shock pressure to be around 15 to 20 GPa [6]. The

existence of akimotoite indicates that shock pressure is up to 23-24GPa [7]. Therefore we estimated the shock of Yamato74445 to be around 15-24 GPa.

These meteorites contain pervasive shock melt veins, which indicate they experienced above liquidus temperature of meteorites. However, there are little experimental data for high-pressure melting of L chondrite compositions. The most complete data available are for the Allende CV carbonaceous chondrite and for KLB-1 peridotite. On the basis of liquidus temperature of these compositions, the shock temperatures experienced by Sahara98222 and Yamato74445 were estimated to be around 2000-2200 ℃ at 13-15GPa and 2000-2400 ℃ at 15-24GPa, respectively [8, 9, 10].

References:

[1] Stöffer et al. (1991) *Geochim. Cosmochim. Acta.*, 55, 3845-3867.

[2] Xie Z. and Sharp T. G. (2004) *Meteorit. Planet. Sci.*, 39, 2043-2054.

[3] Grossman J. N. (1999) *Meteorit. Planet. Sci.*, 34, A169-A186.

[4] National Institute of Polar Research (2000) *Catalog of Antarctic Meteorites*

[5] Xie X., Minitti M. E., Chen M., Mao H. K., Wang D., Shu J. and Fei Y. (2003) *Eur. J. Mineral.*, 15, 1001-1005.

[6] Akaogi M., Ito E. and Navrotsky A. (1989) *JGR-Solid Earth and Planets*, 94 (B11), 15671-15685.

[7] Ohtani E., Kagawa N. and Fujino K. (1991) *Earth Planet. Sci. Lett.*, 102, 158-166.

[8] Agee C. B., Li J., Shannon M. C. and Circone S. (1995) *JGR.*, 100, 17725-17740.

[9] Asahara Y., Kubo T. and Kondo T. (2004) *Phys. Earth Planet.* Inter., 143-144, 421-432.

[10] Zhang J. and Herzberg C. (1994) *JGR.*, 99, 17729-17742.

Ar-Ar dating of Martian meteorite, Dhofar 378: An Early Shock Event? J. Park[1] and D. D. Bogard[1], [1]ARES, code KR, NASA Johnson Space Center, Houston TX 77058. jisun.park1@jsc.nasa.gov

Introduction: Martian meteorite, Dhofar 378 (Dho378) is a basaltic shergottite from Oman, weighing 15 g, and possessing a black fusion crust [1]. Chemical similarities between Dho378 and the Los Angeles 001 shergottite suggests that they might have derived from the same Mars locale. The plagioclase in other shergottites has been converted to maskelenite by shock, but Dho378 apparently experienced even more intense shock heating, estimated at 55-75 GPa [2]. Dho378 feldspar (~43 modal %) melted, partially flowed and vesiculated, and then partially recrystallized [3]. Areas of feldspathic glass are appreciably enriched in K, whereas individual plagioclases show a range in the Or/An ratio of ~ 0.18-0.017 [2], [3].

Radiometric dating of martian shergottites indicate variable formation times of ~160-475 Myr, whereas cosmic ray exposure (CRE) ages of shergottites indicate most were ejected from Mars within the past few Myr (e.g., [4]). Most determined ^{39}Ar-^{40}Ar "ages" of shergottites appear older than other radiometric ages because of the presence of large amounts of martian atmosphere or interior ^{40}Ar [5]. Among all types of meteorites and returned lunar rocks, the impact event that initiated the CRE age very rarely reset the Ar-Ar age. This is because a minimum time and temperature is required to facilitate Ar diffusion loss. It is generally assumed that the shock-texture characteristics in martian meteorites were produced by the impact events that ejected the rocks from Mars, although the time of these shock events (as opposed to CRE ages) are not directly dated.

Here we report ^{39}Ar-^{40}Ar dating of Dho378 plagioclase. We suggest that the determined age dates the intense shock heating event this meteorite experienced, but that it was not the impact that initiated the CRE age.

Ar-Ar Results: The ^{39}Ar-^{40}Ar ages and K/Ca ratios for 16 stepwise temperature extractions of a 2.8 mg sample of Dho378 plagioclase are shown in Fig. 1, as a function of cumulative release of ^{39}Ar. The first extraction released significant terrestrial Ar, and these age data are not further considered. Changes in the K/Ca ratio and in the differential rate of ^{39}Ar release with extraction temperature suggest three distinct, but overlapping Ar diffusion domains, which, expressed as cumulative ^{39}Ar release, are: <13%, 13-45%, and >45%. Based on compositional data of [2] we tentatively identify these three phases as rhyolitic glass, milky glass (both part of the mesostasis), and plagioclase glass with crystallized rims. The youngest Ar-Ar age, ~162-165 Myr observed at ~28-40% ^{39}Ar release, is similar to the Sm-Nd age of 157 ±24 Myr [6]. Other extractions (of the plag.) suggest older Ar-Ar ages and indicate release of trapped martian ^{40}Ar.

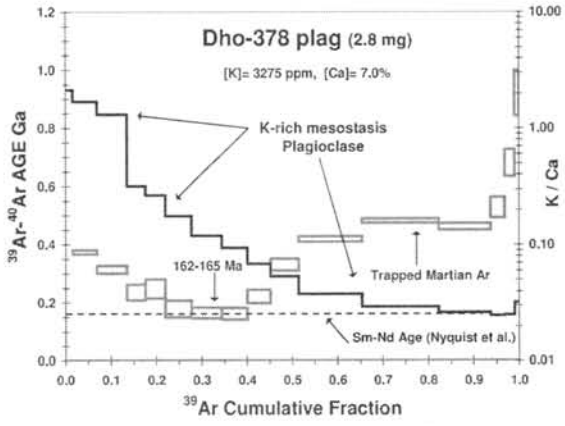

Fig. 1. ^{40}Ar-^{39}Ar ages and K/Ca ratios as a function of ^{39}Ar released during stepwise degassing of Dho378 plagioclase.

To separate trapped ^{40}Ar from ^{40}Ar resulting from in situ decay of ^{40}K, we utilize isochron plots of ^{40}Ar/^{36}Ar vs. ^{39}Ar /^{36}Ar, for which the Ar-Ar age is proportional to the isochron slope. Because Ar components with different compositions appear to be present for extractions releasing <45% of the ^{39}Ar and those releasing >45% of the ^{39}Ar, we examine these two data sets in separate isochron plots. Further, for an isochron plot to represent a linear mixing relationship between two components, ^{40}Ar from in situ decay and a trapped Ar component, cosmogenic ^{36}Ar must be subtracted from the total ^{36}Ar. To do this we use the measured ^{36}Ar/^{37}Ar ratio and assume specific values of this ratio produced by nuclear processes. (^{37}Ar is produced in the reactor from Ca; cos-^{36}Ar is produced in space from Ca; and this nuclear ratio is expected to remain approximately constant during Ar extraction.) Trapped ^{36}Ar for each extraction is obtained by subtracting the abundance of $^{36}Ar_{cos}$ from total ^{36}Ar. We adopted three values of nuclear-(^{36}Ar/^{37}Ar) to make this correction. First the minimum measured ^{36}Ar/^{37}Ar is taken as an upper limit to $(^{36}Ar/^{37}Ar)_{nuclear}$. Secondly, we used the abundance of $^{36}Ar_{cos}$ measured in an unirradiated sample of Dho378 plag. [7] to determine $(^{36}Ar/^{37}Ar)_{nuclear}$. Thirdly, we assumed a $^{36}Ar_{cos}$ only one-half as large as that directly measured.

The isochron plot for 8 extractions, releasing 3-45% of the ^{39}Ar and corrected for $^{36}Ar_{cos}$ using directly measured $^{36}Ar_{cos}$, is shown in Fig. 2. The Ar-Ar age corresponding to this isochron is 143±4 Myr (where the ± ignores the uncertainty in applying a correction for $^{36}Ar_{cos}$). Applying a

correction assuming only one-half of the measured $^{36}Ar_{cos}$ gives an age of 159 ±2 Myr. Using the minimum measured $^{36}Ar/^{37}Ar$ to apply the correction gives a minimum possible age of 138±5 Myr. All of these ages are within combined uncertainties of the Sm-Nd age [6]. The trapped $^{40}Ar/^{36}Ar$ ratio obtained from the isochron is largely defined by the highest [K] data. The intercepts corresponding to these three $^{36}Ar_{cos}$ corrections are 146 ±16, 150±15, and 119±21, respectively.

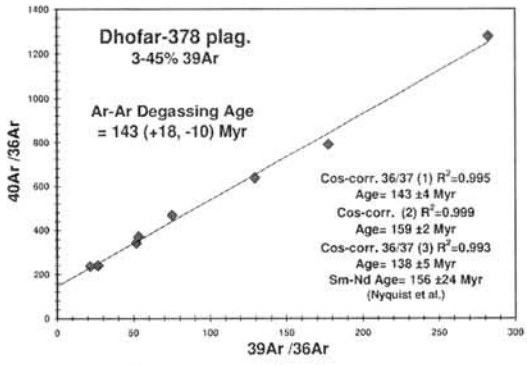

Fig. 2. Trapped $^{40}Ar/^{36}Ar$ ratios against $^{39}Ar/^{36}Ar$ for Dho378 plagioclase.

The isochron plot for extractions releasing 45-98% of the ^{39}Ar scatter considerably and do not define an isochron using any of these applied corrections for $^{36}Ar_{cos}$. These data cannot represent both a constant age and a constant trapped $^{40}Ar/^{36}Ar$ ratio. One of these parameters, or both, must be variable in these extractions.

Ar-Ar Age Interpretation: To interpret the Ar-Ar age results for Dho378 plag. we must consider differences in Ar diffusion characteristics of the two Ar "components" discussed above (<45% and >45% ^{39}Ar). From the release of ^{39}Ar as a function of temperature we calculated the diffusion parameter, D/a^2, and examined these in an Arrhenius plot (Fig. 3). The first ~45% of the ^{39}Ar released shows much greater ease of diffusion loss compared to the last ~55% of the ^{39}Ar released, and the first ~13% of the ^{39}Ar release, which occurred from the high-K glass phase, appears to diffuse even more readily. This finding is consistent, during shock heating, with much greater retention of trapped martian ^{40}Ar in the plagioclase releasing at highest temperature, where Ar diffusion is more difficult, compared to the melted mesostasis material.

We used these diffusion data in a thermal model that compares the cooling rate of bodies of given sizes with various fractional losses of Ar by diffusion [8]. The Ar-Ar isochron (Fig. 2) suggests that no more than ~10% of the ^{40}Ar that accumulated after the degassing event ~143 Myr ago could have been lost in the ~3 Myr CRE initiation event. If we assume Dho378 was 10 cm in diameter when ejected into space, this thermal

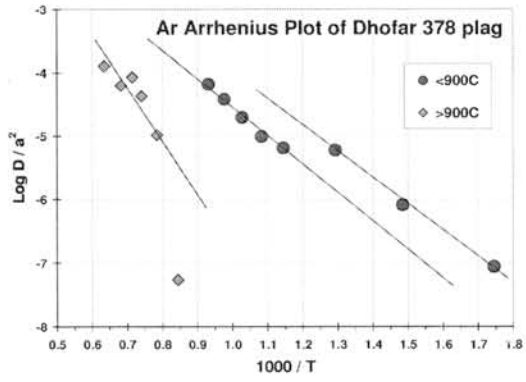

Fig. 3. Arrhenius plot of diffusion parameter D/a^2 vs. reciprocal temperature (in Kelvin) of Dho378. ^{39}Ar diffusion has two distinct phase at the temperature of 900 °C.

model and Fig. 3 imply that the low-temperature "phases" (those releasing <45% of the ^{39}Ar) could not have been heated above ~500°C. Yet, the plagioclase texture implies heating to 1000-1100°C, and the mesostasis apparently melted [2, 3, 9]. If we use the value of D/a^2 at a temperature of 1000°C implied by Fig. 3 ($\sim 2\times10^{-4}$) and examine this in our thermal model, we conclude that to retain ~90% of the ^{40}Ar in the low-temperature phase during heating to 1000°C ~3 Myr ago, Dhofar378 would have to substantially cool in a time of seconds.

Conclusion: We suggest that the ~143 Myr Ar-Ar age determined from the Dho378 isochron may not date the impact that ejected the meteorite into space ~3 Myr ago, but a much earlier impact at ~143 Myr. The relationship between the similar Ar-Ar and Sm-Nd ages is not clear. For the Ar-Ar isochron not to have been reset ~3 Myr ago would require one of two conditions. Either the mesostasis yielding the Ar-Ar age was not heated above ~500°C, in spite of the observation that plagioclase was melted, or alternatively, those K-rich phases heated to melting cooled so rapidly, on the order of seconds over distances of mm, such that ^{40}Ar diffusive loss did not occur. This last explanation would require that pyroxene was not significantly shock-heated.

Acknowledgements: We thank H. Takeda for supplying the Dho378 sample, C-Y Shih for separating the plagioclase analyzed, D. Garrison for lab support, and T. Mikouchi, G. McKay, L. Nyquist, and F. Hörz for helpful discussions.

References: [1] Russell S. S. et al. (2002) *MAPS. 37 (suppl.)* A157-A184. [2] Ikeda et al. (2006) *Antarctic Met. Res., 19,* (in press). [3] Mikouchi T. and McKay G. (2003) *LPS XXXIV,* #1920. [4] Nyquist L. E. et al. (2001) *Space Science Reviews. 96,* 105-164. [5] Bogard D. D. and Garrison D. H. (1999) *MAPS, 34,* 451-473. [6] Nyquist et al. (2006) *NIPR,* this volume. [7] Park J. and Nagao K. (2003) *MAPS, 38,* A79. [8] Dixon E. T. et al. (2004) *GCA, 68,* 3779-3790. [9] Mikouchi T. and McKay G. (2006) *NIPR,* this volume.

COMPARISON OF THE CRYPTOBIOTIC-CRUSTS AND SURFACE MINERAL CRUSTS ACCORDING TO THEIR MAIN CHARACTERISTICS IN HELPING LIFE SUPPORT MECHANISMS AND THEIR IMPLIED ROLE FOR MARTIAN LIVING ORGANISMS. ***T. Pócs*** *(1,6),* ***Gánti T.****(1),* ***A. Horváth*** *(1,2),* ***Sz. Bérczi*** *(1,3),* ***A. Kereszturi*** *(1,4),* ***A. Sik*** *(1,4),* ***E. Szathmáry*** *(1,5); (1)* Collegium Budapest (Institute for Advanced Study),, H-1014 Budapest, Szentháromság tér 2. Hungary, *(2)* Konkoly Observatory, H-1525 Budapest Pf. 67, Hungary, *(3)* Eötvös University, Dept. G. Physics, Cosmic Mat. Sp. Res. Gr. H-1117 Budapest, Pázmány 1/a. Hungary, *(4)* Eötvös University, Dept. Physical Geography, H-1117 Budapest, Pázmány 1/c. Hungary, *(5)* Eötvös University, Dept. of Plant Taxonomy and Ecology, H-1117 Budapest, Pázmány 1/c. Hungary (bercziszani@ludens.elte.hu, *(6)* Eszterházy College, Dept. of Botany, Eger, Pf. 43, H-3301, Hungary.

Introduction: On MGS MOC images we studied *defrosting spotting process* at the Martian South Polar Regions. In the interpretation of the defrosting process we involved living organism activities of putative *Martian Surface Organisms (MSOs*) operating in the surface soil environment. In this study we compared two possible soil environment types in order to approach understanding the mechanisms, which may help life support abilities of the surface mineral and biotic layers.

Materials: Both mineral crusts and cryptobiotic crusts are widely occurring on the surface of the bare soil or rocks at the Earth, various climatic conditions may contribute to their main characteristics and the constituent mineral and biotic components may give a double characterization for them. Many types of the crypto-biotic crusts (CBC) were summarized as candidate counterparts for the Martian life in 2003 by [1]. The surface mineral crusts (SMC) were overviewed in 2006 by [2]. The main purpose of this paper to compare them for common characteristics and markers.

CBC: On dark dunes characteristic, growing splotches, called *dark dune spots* appear at the end of the winter or in early spring [3]. We worked out an interpretation exclusively for the DDSs [4]. In a detailed sequence of interactions with the soil components we showed that development and characteristic features of these spots involve many kinds of materials where soil, water, snow coverings all serve the main actors, the MSOs. The seasonal water supply results in interrupted life cycle of MSOs. We focused the search on terrestrial counterparts with such interrupted life cycle and also with harsh climatic conditions. This way we found the CBC crusts as candidates.

For crypto-biotic crusts their interrupted life cycle, fitting to various environments, extremal conditions were the main reasons for selection as Martian Surface Organism counterparts on the Earth. The active life cycle of the CBC consortia in desert areas is restricted to the short wet season, when the water is present. After one-two months of active period the CBC dries out and waits for the next wet season.

The terrestrial CBC in central *Australia* has violet-brown color. This is due to the *scytonemin pigment* of cyanobacteria, which are most important component of this crust. This dark pigment is accumulated in the gelatinous sheath of the cyanobacteria and it is protecting the living cells and its assimilating pigments from the overdose of intensive UV radiation, and in such a way makes the survival of the cells possible.

Scytonemin is the most successful against the deteriorating effect of long UV-A radiation. The protective role of this pigment was studied mainly by *Garcia-Pichel* and his collaborators [5, 6 and 7]. Other cyanobacteria, especially those living in the CBC of rock surfaces, have another protective pigment too, gloeocapsin, with an intense reddish-violet color. In fact, cyanobacteria cells also have an internal protective system too, first of all in the form of *Mycosporin* like compounds (MAA), which are colorless, water-soluble aminoacid derivates. The MAA is most effective, according to *Oren and Seckbach* [8], against the shorter wavelength UV-B radiation.

Because the cyanobacteria are capable to survive also in extreme cold or heat, and moreover dry conditions, it is probable that according to this analogous situation, they also can survive the hard Martian conditions as it was proposed already by *Friedmann* [9].

SMC: The mineral crust studying group focused their studies on the role of mineral components together with water as main supplies from the soil or rock surface. The role of water is: transporting solutes, (for mineral growing), containing dissolved ions as nutrients for living organisms, the previous two roles unified to entrap organic components. The mutual interaction between the water solutes and the supposed living organisms produces various processes to be studied. Climatic events allow to conclude the evidence of the presence of the various forms of water precipitates on the Earth and also on Mars (weathering products as surface mineral crusts, observation of the precipitating events as fog, snow and long staying frosted surfaces).

In the Houghton crater various mineral crusts with carbonate, gypsum and iron rich crusts are described [2]. On the carbon chain molecule content of these SMCs they conclude that the remnant molecules are characteristic markers of the cyanobacteria.

Discussion: Search for CBC and SMC crust types on soils contribute to the understanding the processes which may important in Martian life formation and preservation, moreover probably to the survival of the Martian life. Recent MER probes studied some SMCs along their pathway and revealed the weathering history of these surfaces. Joint effort of search both CBC and SMC crust types may emphasize the role of the living – mostly cyanobacterial – bacterial components in forming these crusts and these interactions may contribute to the development of new measuring methods of Martian life to. Till that epoch we must use the recent comparative possibilities in which water using, mineral (and biotic) crust forming living organisms act on soil and rocky surfaces. In this aspect the joint use of the CBC, SMC and MSO model data may give the best testifyable model.

The MSO model: During Martian spring defrosting the precipitated water ice component is producing partly fluid water, partly adsorbed water on the surface of soil grains, in the uppermost layer of the subsurface. This amount of water is the source of the life activity of the putative MSOs in our model. This amount of water may contribute to the production of other observed traces of liquid water associated with the DDSs [10, 11].

Acknowledgments: Authors thank for the worthy discussions with professors I. Friedmann and D. Möhlmann.

References: [1] Pócs, T., Horváth, A., Gánti, T., Bérczi, Sz., Szathmáry, E. (2004) Possible Crypto-Biotic-Crust on Mars? *Proc, of the III. European Workshop on Exo-Astrobiology. Mars: The search for Life, Spain, 18-20 November 2003. ESA SP-545*, March 2004, p. 265. [2] Parnell, J.; Bowden, S. A.; Cockell, C. S.; Osinski, G. R.; Lee,P. (2006): Surface Mineral Crusts: A Priority Target in Search for Life on Mars. *Lunar Planet. Sci. XXXVII*, #1049, Houston; [3] Gánti, T., A. Horváth, Sz. Bérczi, A. Gesztesi, E. Szathmáry (2003): Dark Dune Spots: Possible Biomarkers on Mars? *Origins of Life and Evolution of the Biosphere* **33**: pp. 515-557, Kluwer Academic Publishers, Netherlands. [4] Gánti, T., A. Horváth, Sz. Bérczi, A. Gesztesi, E. Szathmáry (**2003**) Evidence for water by Mars Odyssey is compatible with a biogenic DDS-formation process. *Lunar Planet. Sci.* **XXXIV, #1134**, Houston. [5] Garcia-Pichel, F., Bebout, B. M., 1993, The penetration of UV radiation into shallow water sediments: high exposure for photosynthetic communities. *Mar. Ecol. Progress Ser.,* 257-261:13-31. [6] Garcia-Pichel, F., Castenholz, R. W., 1993, Occurrence of UV-absorbing, mycosporine like compounds among cyanobacterial isolates and an estimate of their screening capacity. *Appl. Environ. Microbiol.,* 59, 163-169. [7] Garcia-Pichel, F., Castenholz, R. W. (1994): On the significance of solar ultraviolet radiation for the ecology of microbial mats. In Stal, L. J., Camuette, P. (eds): *Microbial mats. Structure, Development and Environmental Significance.* Springer, Heidelberg, 77-84. [8] Oren, A., Seckbach, J. (2001): Oxygenic photosynthetic microorganisms in extreme environments. *Nova Hedwigia,* , Beiheft 123, Garcia-Pichel, F., Castenholz, R. W. : Characterization and biological implications of scytonemin, a cyanobacterial sheath pigment. *J. Phycol.,* 1991, 27, 395-409. [9] Friedmann, E. I., 1986, The Antarctic cold desert and the search for traces of life on Mars. *Adv. Space Res.*, 6, 265-268. [10] Möhlmann, D.T.F. (2004): Water in the upper Martian surface at mid- and low-latitudes: presence, state and consequences. *Icarus*, **168**, pp. 318-323. [11] Bibring, J.-P.. Langevin, Y., Poulet, F., Gendrin, A., Gondet, B., Berthé, M., Soufflot, A., Drossart, P., Combes, M., Bellucci, G., Moroz, V., Mangold, N., Schmitt, B. and the OMEGA team, (2004) Perennial water ice identified in the South Polar Cap of Mars, *Nature*, **428**, p. 627-630.

The role of Antarctic meteorites in defining new chondrite groups and enhancing our understanding of the early solar system. K. Righter, Mailcode KT, NASA Johnson Space Center, Houston, TX 77058; kevin.righter-1@nasa.gov

Introduction

Ordinary, enstatite, and carbonaceous chondrite groups define a solar nebula with distinct compositional characteristics that range from reduced (E) to oxidized (C), but mainly metal-bearing hydrous minerals relegated to low temperature minerals such as sheet silicates. Our understanding of the conditions prevailing in the early solar nebula has been enhanced by new chondrite groups such as the metal-rich and heavily shocked CB, the oxidized and metamorphosed CK, and the oxidized and perhaps now hydrous R chondrites. These groups have been defined by meteorites found by both the Japanese (e.g., NIPR; Y-693 - CK and Y-75302 – R) and the US collection programs (QUE94411 – CB, ALH85002 – CK). The new constraints provided by these unusual samples are not only important in defining conditions not represented by the common groups of meteorites (E, O, traditional C chondrites) , but also in defining the boundary conditions in the early solar system, that help guide our modelling and understanding.

CB chondrites

The recovery of metal-rich chondrites from Antarctica (QUE94411, 94627, 99309, and MAC 02675) augmented the number of samples with affinities to Bencubbin. This unusual group is now recognized for several distinctive features, including zoned metal grains, young and cryptocrystalline chondrules, heavily shocked matrix (Fig. 1) and a large proportion of FeNi metal [1,2].

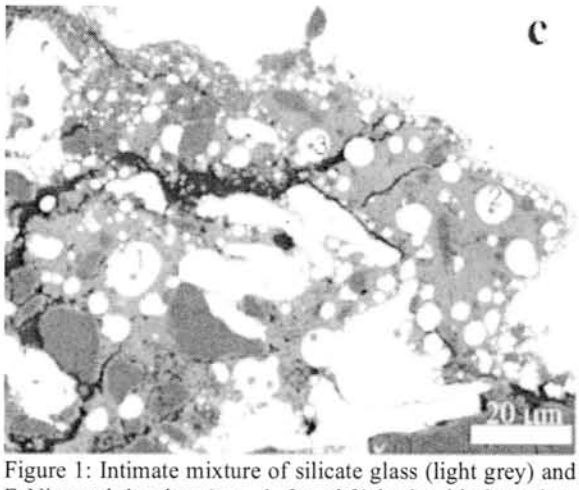

Figure 1: Intimate mixture of silicate glass (light grey) and FeNi metal droplets (e.g., 1, 2 and 3) in the thin boundary zone between chondrules, metal grains and CAIs in QUE94411 (from [3]).

CK chondrites

A metamorphosed carbonaceous chondrite was discovered in Antarctica in December 1969 (Y-693; [4]). Many additional have been recovered around the world and as of May 2006, there are now 140 CK chondrites, 94 (~70%) of which are from Antarctica. Although CK chondrites are assigned petrologic grades 3 through 6 similar to enstatite and ordinary chondrites, many of the highest grade CKs do not record temperatures higher than ~600 °C [5]. Nonetheless, they have abundant petrographic evidence for oxidation, such as the absence of FeNi metal, and the presence of magnetite [6,7,8]. The latter frequently surround chondrules. Additionally, ilmenite-magnetite intergrowths (Fig. 2) record temperatures and oxygen fugacities that are as high as 4 log fO_2 units above the FMQ buffer. Darkened matrix in CK's is thought to be due to shock darkening and fine grained magnetites within olivines [9].

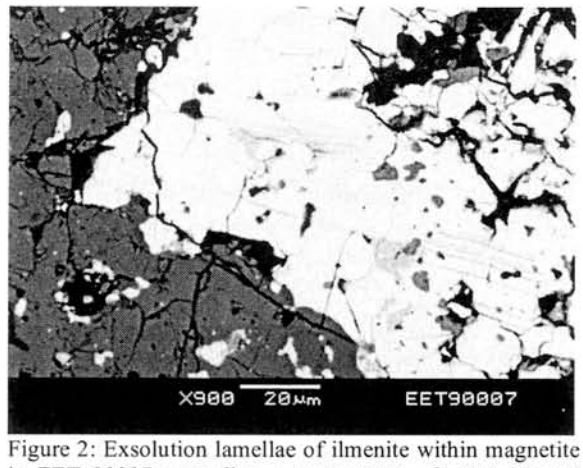

Figure 2: Exsolution lamellae of ilmenite within magnetite in EET 90007, recording a temperature of ~500 °C and relative fO_2 of FMQ+3.2 (from [5]).

R chondrites

Only recognized as a group in the 1990's (Carlisle Lakes), the distinctive R chondrites have quickly become a large and fascinating group of chondrites [10,11,12]. R chondrites are distinctive in that some of R3 chondrites contain oxidized minerals, indicating that they formed in an oxidized environment. On the other hand there are also some reduced R3's,

demonstrating heterogeneity among the group as a whole. This is also reflected in their diverse mineralogy which includes metal, graphite, magnetite, and chromite. In fact, a newly discovered R chondrite contains calcic hornblende (Fig. 3) and is metamorphosed to grade 6, certainly a unique meteorite to world collections as well as to Antarctica [13].

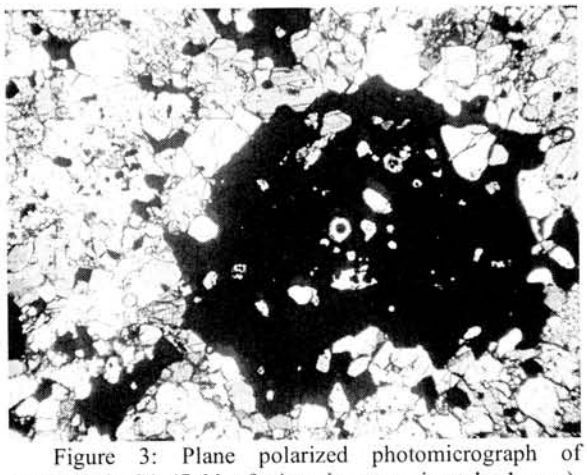

Figure 3: Plane polarized photomicrograph of LAP04840 ,24 (field of view is approximately 1 mm). Opaque phase is magnetite, brown phase is hornblende and clear phases are olivine, plagioclase, and pyroxene.

Ungrouped chondrites

Finally, there are a small but significant number of ungrouped chondrites from Antarctica. The unique carbonaceous chondrites MAC 87300 and 87301 have properties distinct from those of other CC groups. The unique chondrite LEW85332 may be a petrologic type 3.0 to 3.1 and related to CR chondrites [14]. Framboidal magnetite is associated with hydrous alteration in Y-86720, an unusual C1/2 chondrite [15]. LEW87232 is a Kakagari-type chondrite, with petrologic and mineralogic characteristics that are intermediate to E, O and C chondrites [16]. Finally, QUE94204 (and 7 pairs from the 97 and 99 seasons) is an ungrouped chondrite with affinities to enstatite chondrites. A detailed study of this sample has not been undertaken, but it may have similarities to Itqiy [17].

Implications

Connections between oxidation and water and in the early solar system have not been straightforward. CV, CK and R chondrites all offer new insights into these processes and suggest that some materials in the early solar nebula were a) initially reduced and later oxidized on the parent body new groups, whereas, and b) initially oxidized. In addition, it is now apparent that some water can be stored at the higher temperatures of metamorphism (LAP 04840), in addition to the more common hydrated matrices of carbonaceous chondites. These two realizations have implications for H/O, dust/gas ratios, and the condensation and accretion of materials of a wide range of Fe/Mg (e.g., [18]). A diversity of shock features in CK and CB chondrites will most certainly add to out understanding of shock textures in a broader range of planetary materials. And finally, the existence of chondrite groups (K) that break the trend of variation of metal content, silicate Mg#, and oxidation, indicates that simple models of variation with distance from the Sun are unlikely to be correct (also noted by [16]). Unusual chondrites are present in both the US and Japan collections – careful petrologic and petrographic studies can help elucidate features that allow recognition of new and interesting groups of chondrites.

References

[1] Petaev, M. et al. (2002) MAPS 36, 93-106; [2] Krot, A.N. et al. (2005) Nature 436, 989-992; [3] Meibom, A. et al. (2005) MAPS 40, 1377; [4] Yanai, K. (1979) Catalog of Yamato Meteorites, first edition, NIPR, Tokyo; [5] Neff , K.E. and Righter, K. (2006) LPSC XXVI, #1320; [6] Geiger, T. and Bischoff, A. (1994) Planetary and Space Science 43, 485-498. [7] Kallemeyn, G.W. et al. (1991) GCA 55, 881-892; [8] Nakamura, T. et al. (1993) Proc. Symp. Antarct. Meteorites 6, 171-185; [9] Tomeoka et al. (2001) MAPS 36, 1535-1545; [10] Weisberg, M.K. et al. (1991) GCA 55, 2657-2669; [11] Kallemeyn, G.W. et al. (1996) GCA 60, 2243-2256; [12] Imae, N. et al. (1999) Antarctic Meteorites XXIV, 24th Symp. Ant. Meteorites, 47-49; [13] Satterwhite, C.E. and Righter, K. (2006) Ant. Met. Newslett. 29, no. 1, February; [14] Wasson, J.T. et al. (2000) GCA 64, 1279-1290; [15] Tomeoka, K. et al. (1989) Proc. Symp. Antarct. Meteorites 2, 55-74; [16] Weisberg, M.K. et al. (1996) GCA 60, 4253-4263; [17] Patzer, A. et al. (2001) MAPS 36, 1495-1505.

Al-Mg isotope systematics in chondrules from UOC ALHA76004 (LL3.3). N. G. Rudraswami and J. N. Goswami, Physical Research Laboratory, Ahmedabad-380 009, India. E-mail: gowda@prl.res.in

Introduction:

Fossil records of now-extinct radionuclide ^{26}Al that decays to ^{26}Mg with a half life of 0.72Ma have been studied extensively to infer relative chronology of events taking place during the first few million years of the solar system history. In recent years ^{26}Al has been used as a chronometer to understand the time difference in formation of the two early formed solar system objects, CAIs (Ca-Al rich inclusions) and chondrules, and also the duration of CAI and chondrule formation in the solar nebula [1-5]. ^{26}Al also serves as the major source of heat during the early evolution of planetisimals [6]. The one time presence of ^{26}Al is determined by identifying ^{26}Mg excess and its correlation with Al/Mg ratio in Al-rich phases.

In order to further our understanding of the duration of chondrule formation, we have started a systematic study of ferromagnesian chondrules from unequilibrated ordinary chondrites (UOC) of low metamorphic grades ranging from 3.0 to 3.3 belonging to both L and LL groups. Petrographic studies suggest that these meteorites were not subjected to temperature >250^{0}C and >450^{0}C for UOCs belonging to metamorphic grade 3.0 and 3.4, respectively, during their residence in their parent bodies [7]. Such temperatures are not sufficient to induce diffusion of ^{26}Mg in glass or anorthite over distances of tens of microns even when one considers time scales of several million years or more [8]. Thus we expect to see the imprint of pristine records of ^{26}Al in chondrules from the meteorites chosen for this study.

Sample Description and Analytical Techniques:

Three thin sections of Antarctica meteorites of LL-type received from the National Institute of Polar Research (NIPR), namely Y-793596, Y-791324, ALHA76004 having metamorphic grade LL3.0, 3.1 and 3.3, respectively, have been studied by us. In addition, we have also studied chondrules from Semarkona (LL3.0) and Bishunpur (LL3.1) as well as four L-type chondrites with different metamorphic grade, namely LEW86134 (L3.0), QUE97008 (L3.4 redesignated as L3.05 [9]), LEW86018(L3.1) and ALHA77176 (L3.2) from the NASA collection of Antarctic meteorites [10]. We present here initial results obtained from the study of chondrules in ALHA76004 that extend our work to metamorphic grade up to 3.3.

The carbon coated polished thin section of ALHA76004 was mapped and analyzed using a scanning electron microscope equipped with energy dispersive X-ray spectrometer to identify suitable chondrules that have Al-rich phases (Al/Mg>20) that are greater than ten micron in size. The Al-Mg isotope systematics in these phases, primarily glassy mesostasis, were studied using a Cameca ims-4f secondary ion mass spectrometer. A low intensity (a few nA) primary $^{16}O^-$ ion beam with energy of 12.5 kV was used to sputter secondary positive ions from the carbon coated sample surface kept at a potential of 4.5 kV. Ion imaging of areas around spots identified as having high Al/Mg ratios from SEM analysis allowed us to choose areas for isotopic analysis. Suitable field apertures are used to ensure transmission of secondary ions from such areas for mass analysis that was carried out at a mass resolution (M/ΔM) of ~4000, adequate to resolve hydride and other molecular interferences at the masses of interest. The measurements were carried out in the peak jumping mode by cycling the magnet through the mass sequence ^{24}Mg, ^{25}Mg, ^{26}Mg and ^{27}Al. Standards such as Burma spinel, anorthositic glass and Lake County plagioclase as well as phases with low Al/Mg ratio such as olivine and pyroxene within the analyzed chondrules were also analyzed to ensure instrument stability and reproducibility. The measured Mg isotopic ratios were analyzed to detect possible presence of radiogenic ^{26}Mg from the decay of ^{26}Al.

Results and Discussion:

From more than a dozen chondrules identified for analysis, we were successful in obtaining meaningful results in three chondrules at present. Presence of Mg-rich microcrystalites within the Al/Mg rich phases makes it difficult to carry out meaningful analysis in most of the other cases. The Al-Mg isotope data for these three chondrules are shown in Fig.1. All the chondrules have well defined isochron that yielded initial $^{26}Al/^{27}Al$ [$(^{26}Al/^{27}Al)_0$] of $(1.06\pm0.16)\times10^{-5}$ [CH#1; Fig1a], $(7.1\pm1.0)\times10^{-6}$ [CH#11; Fig1b] and $(1.15\pm0.17)\times10^{-5}$ [CH#2; Fig1c]. Repeated analyses were conducted on each of the ion probed areas, as long as the Al/Mg ratio remained nearly constant, to improve analytical precision of the measured isotopic ratios.

The $(^{26}Al/^{27}Al)_0$ values found in ALHA76004 [LL3.3] chondrules are close to those seen in chondrules from Semarkona (LL3.0) [2] and

Bishunpur (LL3.1) [4] and also in LEW86134 (L3.0), QUE97008 (L3.05), LEW86018 (L3.1) and ALHA77176 (L3.2) [10]. We could not detect obvious signature of disturbance in the Al-Mg isotope system in chondrules having phases with reasonably high Al/Mg ratio (Fig. 1a, 1b). Although more data will be needed to rule out absence of chondrule with initial $^{26}Al/^{27}Al < 4\times10^{-6}$ in ALHA76004, the present data reinforces the suggestion that parent body metamorphism is not the prime cause for low values of initial $^{26}Al/^{27}Al$ seen in chondrules from UOCs of lower metamorphic groups such as Semarkona (LL3.0) and Bishunpur (LL3.1) [12], Krymka (LL3.1) [3], Adrar-003 (LL3.2) [11] and LEW86134 (L3.0) [10].

References:

[1] Russell S. S. et al. (1996) *Science* 273:757-762. [2] Kita N. T. et al. (2000) *Geochimica et Cosmochimica Acta* 64, 3913–3922. [3] Huss G. R et al. (2001). *Meteoritics & Planet. Sci.*36, 975–997. [4] Mostefaoui S. et al. (2002) *Meteoritics & Planet. Sci.* 37:421-438. [5] Bizzaro M. et al. (2004) *Nature*, 431, 275-278. [6] Srinivasan. G et al. (1999) *Science*, 284, 1348-1350. [7] Sears. D. W. G et al. (1991) *21st Lunar and Planet. Sci. conf.*, 493-512. [8] LaTourette T. and Wasserburg. G. J (1998) *Earth Planet. Sci. Lett.*, 158, 91-108. [9] Grossman J. N and Brearley. A (2005) *Meteoritics & Planet. Sci.*, 40, 87-122. [10] Rudraswami N. G et al. (2005) *MAPS*, 5071. [11] Rudraswami N.G. et al. (2004) *Lunar and Planet. Sci.*, Abstract# 1236. [12] McKeegan K. D. et al. (2000) *LPS XXXI*, #2009

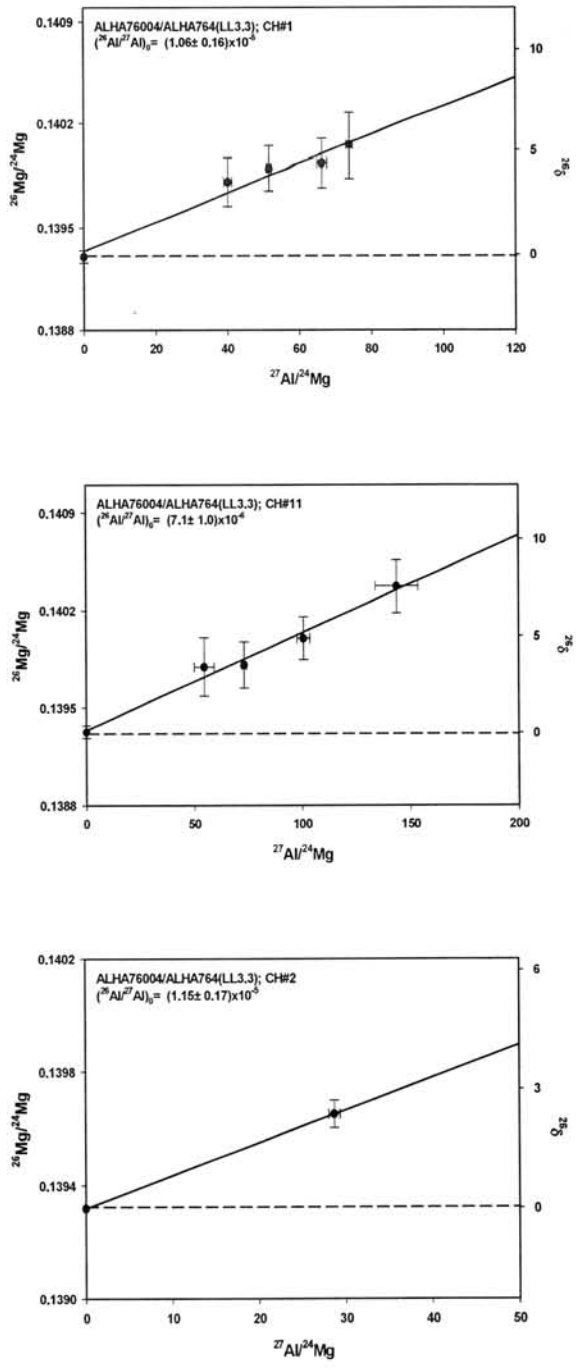

Figure1: Al-Mg isotope systematics of chondrules from ALHA76004 (LL3.3). Inferred $(^{26}Al/^{27}Al)_0$ value is given in each case.

Space weathering and movement of surface materials of Itokawa as observed by Hayabusa. S. Sasaki[1], M. Ishiguro[2#], N. Hirata[3], M. Abe[2], H. Demura[3], T. Hiroi[4], H. Miyamoto[5], T. Nimura[2], J. Saito[2], A. Yamamoto[6], [1]RISE Project Office, National Astronomical Observatory of Japan, Oshu, Iwate 023-0861, Japan (sho@miz.nao.ac.jp), [2]The Institute of Space and Astronautical Science, JAXA, Sagamihara, Kanagawa 229-8510, Japan, [3]School of Computer Science and Engineering, Aizu University, Fukushima 965-8580, Japan, [4]Department of Geological Science, Brown University, Providence, RI 02912, U.S.A., [5]Department of Geosystem Engineering, University of Tokyo, Tokyo 113-8656, Japan, [6]Remote Sensing Technology Center of Japan, Roppongi, Tokyo 106-0032, Japan, [#]Now at School of Earth Environmental Sciences, Seoul National University, Seoul 151-742, Korea

Introduction: Hayabusa is an engineering spacecraft by ISAS/JAXA (The Institute of Space and Astronautical Science of Japan Aerospace Exploration Agency) aiming at sample return from the surface of S-type asteroid (25413) Itokawa [1]. Between September and November 2005, Hayabusa observed Itokawa's surface by Asteroid Multiband Imaging CAmera (AMICA) and Near Infrared Spectrometer (NIRS). A filter wheel of AMICA has a wide bandpass filter and a set of seven ECAS-compatible narrowband filters: 380 (ul), 430 (b), 550 (v), 700 (w), 860 (x), 960 (p), and 1010 nm (zs) [2]. From the Home Position (HP) (7km), AMICA observed the whole surface of Itokawa with nominal resolution 70 cm at the solar phase angle around 10 degree. Observations from closer distances were also performed with spatial resolution less than 1cm during touchdown phases [3].

Brightness difference on Itokawa: Observation by AMICA revealed that Itokawa is heterogeneous in both color and brightness [3]. The brightness difference is approximately 10-20% on distant images and as high as 30% on close-up images. Brighter areas are usually situated at locally elevated zones and at gravitationally steep zones, although steep zones are not always bright. AMICA color observations and NIRS observations show that brighter areas are bluer and darker areas are redder in color [4, 5].

Figure 1 shows the Muses Sea area where landing operations of Hayabusa were performed. In Fig. 1, Shirakami is one of the distinctly brightest regions on Itokawa. Here in Shirakami, the brightest area (a) has very steep slope, which is steeper than a typical angle of repose of granular materials. The elevated zone (b) consists of boulder-covered dark areas (10m-scale patched areas) and boulder-poor bright areas. Typical boulder size on the dark patched area is about 1m. On the other hand, the adjacent darker area (c) is covered continuously with numerous boulders. Obscure lineaments probably of boulder imbrications trend from the area (c) to the area (b). The morphology here suggests that the bright surface of Shirakami was formed by removal of the superposed dark boulder rich layer. The area (a) is a totally excavated whereas the area (b) is partially excavated due to boulder movements.

Yatsugatake (d) is a distinct ridge between the Muses Sea and Shirakami. The brightness of the summit area of Yatsutagake might be also explained by excavation of a darker superposed layer. At the foot of Shirakami and Yatsugatake (d) extends a darker and boulder-rich zone (denoted by e). But no distinct flow front or talus structure is observed.

Figure 2 is a close-up image of the area to the north of the Muses Sea. Here are observed bright patched surfaces of a few meter scale. Some boulders on brighter surface are dark, which would suggest darker materials should superpose on brighter materials.

In comparison with color observation [4, 5] and experimental data [6, 7], we interpret that the darker materials experienced more space weathering than brighter materials. High resolution images indicate that boulders are firmly covered with weathered fine particles or boulders' surface are optically weathered.

After the emplacement of boulders, the surface of Itokawa was weathered by micrometeorite impacts (and irradiation by high-energy particles such as solar wind). Then, dark weathered boulder-rich surfaces were removed by shaking caused by impacts or planetary encounters, leading to the exposure of underlying relatively fresh bright area.

Weathering of rocky surface: Using spectral slopes of near-Earth asteroids obtained through ground-based observations, Binzel et al. advocated the size dependent transition from Q-type (ordinary chondrite-like) asteroids to S-type asteroids around the size range 0.1 to 5km [8]. Smallest asteroids with low gravity might be regolith-free; it was considered that presence of regolith should enhance the space weathering, and that regolith is scarce (abundant) on objects smaller (larger) than the transition size. However, the observation of Itokawa by Hayabusa suggested that even regolith-free rocky surface should have been weathered.

To examine the possibility of weathering of rocky surface, we irradiate pulse laser (simulating micrometeorite impact heating) on meteorites NWA1794 (LL5) and Bensour (LL6) [9]. As

shown in Fig. 3, rocky meteorite surface is darkened and reddened by space weathering simulation. Ordinary chondrites usually have microscopic porosity with much more surface area than a flat plane. Upon laser irradiation, evaporated material may condense on nearby surface of grains. This process would form weathered coating on the rock surface.

We consider that the darker boulder-rich zone of Itokawa is made up with dark boulders with weathered coating, which is also suggested from highest resolution image. Small (sub-km) less-regolith asteroids with silicate composition may also change its brightness and color by space weathering, although their weathering degree would be weaker than regolith-covered asteroids.

References: [1] Fujiwara A. et al. (2006) Science, in press. [2] Nakamura T. et al. (2001) EPS 53, 1047-1063. [3] Saito J. et al. (2006) Science, in press. [4] Abe M. et al. (2006) Science, in press. [5] Ishiguro M. et al. LPSC XXXVII #1533. [6] Sasaki S. et al. (2001) Nature 410, 555-557. [7] Hiroi T. and Sasaki S. (2001) M&PS 36, 1587-1596. [8] Binzel R. P. et al. (2004) *Icarus* **170**, 259-294. [9] Sasaki S. et al. (2006) LPSC XXXVII #1705.

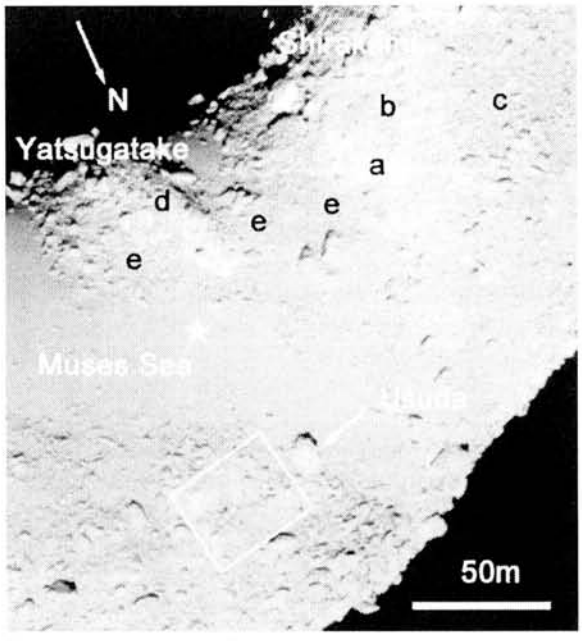

Figure 1 The Muses Sea area on Itokawa where detailed feature of Yatsugatake-Shirakami region is involved. The smooth area is the Muses Sea which includes possible landing spot of Hayabusa (denoted by a white stellar mark). Yatsugatake is a bright rough ridge to the west of the Muses Sea. A white rectangle is the area of Fig. 2. (ST_2474731509)

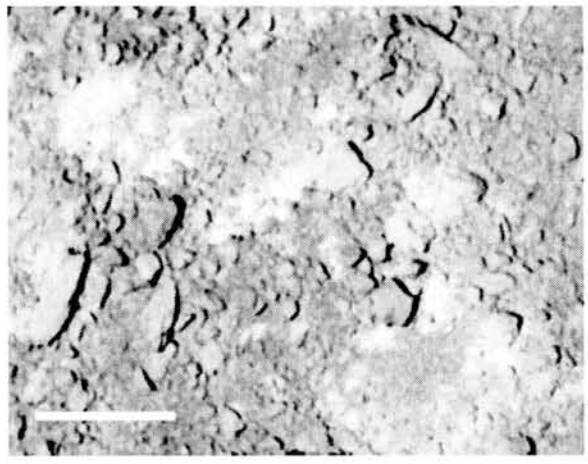

Figure 2 Close-up v-band image of a region to the north of the Muses Sea (just to the east of Usuda boulder). Scale in the figure is 10 m. The brightness contrast is enhanced in this image for clarity. (ST_2530292409).

Figure 3 A rock sample of NWA1794 (LL5) after nano-second pulse laser irradiation. The laser pulse power was 15 mJ. The size of darkened irradiated area is 6 mm.

The petrogenesis of nakhlites inferred from chemical compositions of nakhlites. N. Shirai and M. Ebihara, Department of Chemistry, Tokyo Metropolitan University, Hachioji, Tokyo 192-0397, Japan (shirai@comp.metro-u.ac.jp)

Introduction: Nakhlites are mostly composed of augite, with olivine and mesostasis as minor mineral phases. A total of seven nakhlites have been identified so far. They show similar chemical compositions, petrology and isotopic compositions, suggesting that they experienced similar formation histories. Considering that the formation process for nakhlites is still less understood, we conducted a chemical study of nakhlites to place constraints on the petrogenesis of nakhlites based on their chemical compositions.

Analytical procedures: We analyzed three nakhlites (Nakhla, Y 000593 and MIL 03346). Bulk major, minor and trace element compositions were measured by using PGA, INAA, IPAA and ICP-MS. For Y 000593, six powdered samples were prepared by grinding g-scale of samples located at different positions [1].

Comparison among nakhlites: A part of incompatible element abundances are shown in Fig. 1. Elements are ordered with increasing compatibility during igneous processes (partial melting and/or fractional crystallization) of Earth upper mantle. CI-normalized abundances of incompatible elements for nakhlites are downward with increasing of compatibility. It can be seen that incompatible element abundances of Nakhla, Lafayette, Governador Valadares and Y 000593 are similar to each other, and are systematically lower than those of MIL 03346 and NWA 817. Petrographically, Nakhla, Lafayette, Governador Valadares and Y 000593 were reported to have lower abundances of mesostasis than MIL 03346 and NWA 817 [2]. Considering that incompatible elements are relatively enriched in mesostasis, chemical and petrographical characteristics are consistent with each other. For compatible elements (Mg, Cr, Mn, Co and Ni), MIL 03346 and NWA 817 have lower abundances than Nakhla, Lafayette, Governador Valadares and Y 000593, which were reported to have higher abundance of olivine and augite than MIL 03346 and NWA 817 [2]. Thus, major, minor and trace elements abundances for nakhlites reflect their modal abundances of major constituent mineral phases.

There can be seen an interesting chemical characteristics in Zr/Hf ratios among nakhlites as shown in Fig. 1. Zr/Hf ratios increase with increasing of Zr and Hf abundances. Moreover, Zr/Hf ratios are found to increase with decreasing of Sc abundances (not shown). An experimental partitioning study indicates that Zr is more incompatible than Hf in a system of clinopyroxene-melt [3]. In consideration of petrographical and experimental partitioning studies [2, 3], observed correlations among Zr/Hf ratios and element abundances (Zr and Sc) are controlled by the precipitation of clinopyroxene. Thus, Zr/Hf ratios for nakhlites reflect a modal abundance of its major constituent mineral (clinopyroxene). According to [4], majorite is also responsible for the fractionation of Zr and Hf in nakhlites.

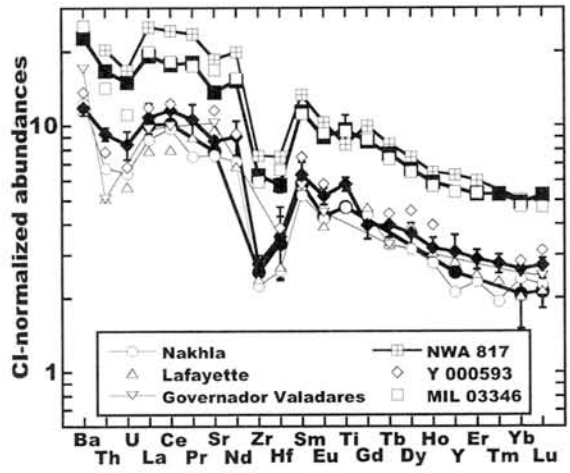

Fig. 1. CI-normalized abundances of incompatible elements for nakhlites. Solid and open symbols represent our data and literature values, respectively.

Petrogenesis of nakhlites and chassingites: As shown in Fig. 1, Th-U and Zr-Hf are depleted relative to neighboring rare earth elements (REEs) in nakhlites. Hf and Sm have similar degrees of compatibility during igneous processes of Earth upper mantle [5]. However, with the presence of some minerals such as majorite, Mg-perovskite and ilmenite, Hf and Sm are fractionated from each other. Shirai and Ebihara [4] suggested that majorite is responsible for the fractionation of Hf and Sm in nakhlites and chassignites and further that the source material for nakhlites was supplied as an ascending plume from the deep region of the Martian mantle where majorite was partly melted.

Figure 2 shows data of La/Th and La/Yb ratios for Martian meteorites including nakhlites. As shown in Fig. 2, La/Th ratios for nakhlites and chassignites are superchondritic while those of shergottites are chondritc or subchondritic. In contrast with the fractionation of Hf and Sm, which doesn't occur in Earth upper mantle region, Th can be fractionated from La during Earth upper mantle processes. In case of Earth, La/Th ratios of the depleted mantle are superchondritc while those of the continental crust are subchondritic. In this sense, the depleted mantle and the continental crust are complementary. In Fig. 2, shergottites display a negative correlation between

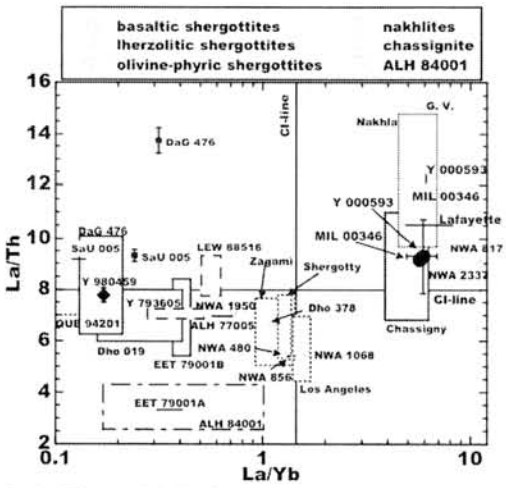

Fig. 2. La/Th vs. La/Yb for Martian meteorites. Symbols are the same as those in Fig. 1. Smaller symbols show Martian meteorites found in hot desert

La/Th and La/Yb ratios. Since the bulk partition coefficient of La (denoted as D_{La}) is lower than D_{Yb} for dominant minerals of Martian mantle (olivine, orthpyroxene, clinopyroxene and garnet) [6], a negative correlation between La/Th and La/Yb ratios in shergottites indicates that D_{Th} is lower than D_{La} for the dominant minerals. As shown in Fig. 2, La/Th and La/Yb ratios for nakhlites and chassignites are not on this observed trend. Given bulk partition coefficients for the dominant minerals, igneous processes including such dominant minerals cannot produce the chemical characteristics for nakhlites and chassignites. Then, we consider whether accessory minerals control the chemical characteristic for nakhlites and chassignites, and if so, which accessory minerals are responsible for the fractionation of Th and La in nakhlites and chassignites.

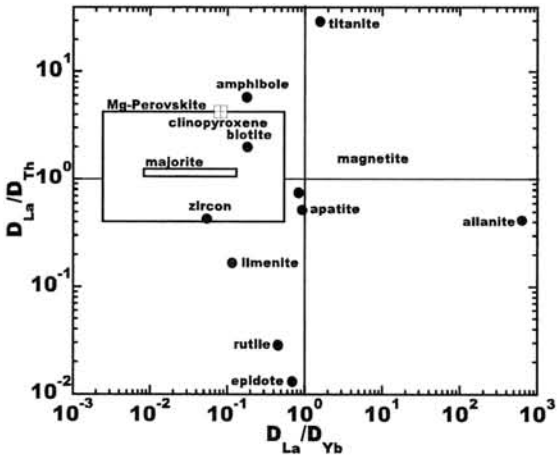

Fig. 3. Partition coefficient ratios for La/Th and La/Yb for several minerals. La, Yb and Th partition coefficients for clinopyroxene are from [7], those for majorite and Mg-perovskite are from [5] and those for the other minerals are from [8]. Squares indicate ranges of partition coefficients.

Figure 3 shows a correlation of partition coefficient ratios of La/Th and La/Yb for several minerals. It is clear that any mineral can fractionate Th from La except majorite and Mg-perovskite. Assuming that La/Th and La/Yb fractionations in nakhlites are controlled by only one mineral, igneous processes including any mineral of titanite, magnetite, apatite, zircon, ilmenite, rutile and epidote can produce chemical characteristics for nakhlites and chassignites. These minerals are considered to be accessory minerals in Martian mantle. In consideration of constituent minerals of Martian mantle [6], clinopyroxene largely hosts incompatible elements. Assuming that its precursor material is constituted by both clinopyroxene and any accessory mineral described above, we calculate the bulk partition coefficient of La, Yb and Th for the precursor material. Corresponding bulk partition coefficients of several possible precursor materials are shown in Fig. 4. As D_{La}, D_{Yb} and D_{Th} for apatite, epidote and zircon are much higher than those of clinopyroxene, bulk partition coefficient ratios of La/Th and La/Yb of the precursor materials are largely controlled by those for such accessory minerals (apatite, epidote and zircon), leading bulk partition coefficient ratios of La/Th and La/Yb of the precursor materials to be less than unity, as shown in Fig. 4. Thus, we conclude that igneous processes including apatite, epidote and/or zircon control the fractionation of La and Th in nakhlites and chassignites.

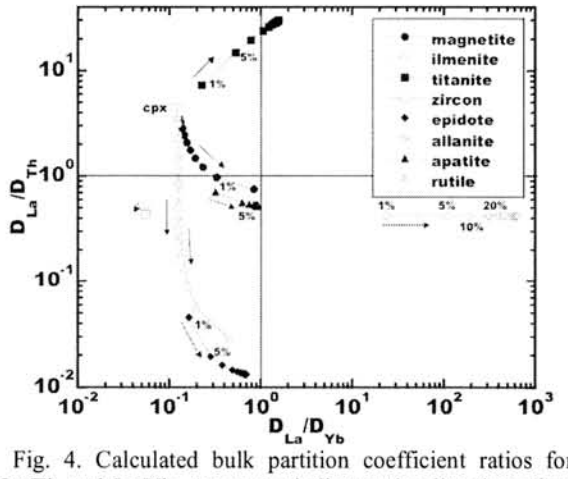

Fig. 4. Calculated bulk partition coefficient ratios for La/Th and La/Yb. An arrow indicates the direction of an increment of mineral abundance (in %) for each accessory.

References: [1] Misawa K. et al. (2003) *Antarct. Meteorite Res., 16,* 1-12. [2] Treiman A. H. 2005. *Chemie der Erde Geochemistry, 65*, 203-270. [3] Salters V. J. M. and Longhi J. (1999) *Earth Planet. Sci. Lett., 166,* 15-30. [4] Shirai N. and Ebihara M. (2005) *Meteorit. Planet. Sci., 40*, A140. [5] Xie Q. and Kerrich K. (1994) *JGR, 99,* 15799-15812. [6] Longhi J. et al. 1992. *Mars*, 184-208. [7] Hauri E. H. et al. (1994) *Chem. Geol., 117,* 149-166. [8] Bédard J. H. (2006) *Geochim. Cosmochim. Acta., 70*, 1188-1214.

Evaporation of forsterite in vacuum: anisotropic isotopic fractionation of Mg. S. Tachibana, M. Yamada, H. Nagahara and K. Ozawa, Department of Earth and Planetary Science, University of Tokyo, 7-3-1 Hongo, Tokyo 113-0033, Japan.

Introduction:

Evaporation of condensed materials at low pressures plays important roles in chemical and isotopic fractionations in protoplanetary disks or in circumstellar environments. Numerous studies attempted to reveal chemical evolutions of the planetary materials from the chemical and isotopic signatures of kinetic processes combined with a model on kinetic evaporation and condensation and accompanying chemical and isotopic fractionation. For instance, isotopic fractionations of Mg and Si in CAIs [1] have been attributed to kinetic isotopic fractionation during evaporation of CAI-melts, and several studies have attempted to reproduce chemical and isotopic signatures of such CAIs based on a kinetic evaporation and condensation [e.g., 2]. Because kinetic aspects of evaporation and condensation cannot be understood from theoretical studies alone, many laboratory studies on minerals and melts have been carried out and the obtained kinetic parameters have been applied to chemical evolution models for planetary materials. However, such kinetic parameters have been obtained only under limited conditions, and fundamental mechanisms have not yet be fully understood.

In this study, we have studied anisotropy of isotopic fractionation of Mg during evaporation of forsterite (Mg_2SiO_4) in vacuum to understand the fundamental surface processes related to evaporation.

Methods:

Magnesium isotopic compositions of the evaporated forsterite were measured using an ion microprobe, Cameca ims-6f. The procedure of depth profiling is mostly the same as that described in [3] except for several analytical conditions such as energy distributions of analyzed secondary ions and primary beam settings.

The evaporated samples were pressed into indium filled in cylindrical stainless-steel bullets (~8 mm in diameter) and were coated with Au of 20 nm thickness. A polished chip of starting forsterite was also prepared in the same way to be used as a reference. The primary ion of $^{16}O^-$ with an accelerating voltage of 12.5 kV and intensity of 5-25 nA was focused to a 50 μm spot and scanned over an area of ~150 μm x 150 μm. Secondary ions were extracted at a voltage of 10 kV with an offset voltage of -120 V. Secondary ions of ^{24}Mg, ^{25}Mg and ^{26}Mg were collected from the central flat part (~50 μm x 50 μm) of the scanned area using digital and mechanical apertures and were counted for 0.7, 5, and 5 sec, respectively, on the electron multiplier at a mass resolving power of ~4000. The mass resolving power of 4000 was sufficient to avoid the interference of ^{24}MgH to ^{25}Mg. A typical count rate for ^{24}Mg was (2-5) x 10^4 cps. The mean of 150-cycle measurements through ^{24}Mg, ^{25}Mg, and ^{26}Mg was used for a single data point in depth profiling. It took ~13 hours to obtain a single depth profile.

The depth of the scanned area, measured using the DEKTAK surface profiler, was ~4-7 μm for the ~13-hour sputtering. Because the depth was proportional not only to the sputtering time but to the primary beam intensity, the primary ion beam intensity was monitored before and after each 150-cycle analysis in order to correct the fluctuation of the primary beam intensity when the sputtered time was converted to the depth.

Results:

The evaporated samples showed positive $\delta^{25}Mg$ and $\delta^{26}Mg$, and heavier isotopes are most enriched nearby the evaporated surface (10-30 ‰ for $\delta^{26}Mg$ and 5-15 ‰ for $\delta^{25}Mg$) along all the crystallographic directions (Fig. 1). The degree of enrichment of heavier isotopes becomes smaller with depth, and the isotopic composition approaches to that of unevaporated forsterite (Fig. 1). The value of $\delta^{26}Mg$ is twice as large as that of $\delta^{25}Mg$ at any depth for most samples, indicating mass-dependent isotopic fractionation. The observations are consistent with those for forsterite evaporated along the a-axis by [3], and suggest that preferential evaporation of lighter isotopes causes enrichment of heavier isotopes nearby the surface and that relatively slow self-diffusion of Mg in forsterite prevents the evaporation residue from isotopic homogenization.

The depth profiles along the a-, b-, and c-axes of forsterite, evaporated under the same conditions, show clear anisotropy in isotopic fractionation profiles in terms of both the slope of the profile and the degree of fractionation at the surface (Fig. 1). The degree of isotopic fractionation at the surface was largest along the c-axis and smallest along the b-axis. On the other hand, in the interior of the sample, the fractionation along the b-axis becomes larger than that along the a-axis. This is due to much gentler slope of the profile along the b-axis, suggesting faster diffusion along the b-axis than along the a-axis. The difference in depth profiles of isotopic compositions along different crystallographic orientations thus reflects anisotropy both in the isotopic fractionation at the surface by evaporation and in diffusion within the residue.

Discussion:

We applied a one-dimensional, semi-infinite diffusion controlled isotopic fractionation model [3] to isotopic zoning profiles by the least-squares

method with experimentally obtained evaporation rates (V) [e.g., 4], by which we could obtain the self-diffision coefficient of Mg in forsterite (D) and the isotopic fractionation factor of Mg for kinetic evaporation of forsterite (β).

The obtained D is fastest and slowest along the c- and a-axis, respectively ($D_{//c} > D_{//b} > D_{//a}$) (Fig. 2). The $D_{//a}$ in this study agrees well with that obtained by [3] in the temperature range of 1500-1800°C with the same technique. The largest D along the c-axis has been found for Mg self-diffusion in forsterite at lower temperatures by different techniques [e.g., 5]..

A non-linear weighted least squares regression was applied to estimate the activation energies for diffusion, which gives 674 ± 94, 627 ± 99, and 559 ± 29 kJ/mol along the a-, b-, and c-axes, respectively. The activation energies along all of the three axes in this study are larger than those at lower temperatures (<1450°C) in previous studies [e.g., 5] by ~120-300 kJ/mol. The differences in activation energies at high and low temperatures for diffusion along all the crystallographic orientations may be interpreted by the change of the diffusion regime from extrinsic diffusion at lower temperatures to intrinsic diffusion at higher temperatures, where thermally activated vacancies are dominant and thus the activation energy of diffusion should include the formation enthalpy of vacancies.

The β along all the crystallographic orientations is closer to unity than that expected from the kinetic theory of gases, a square root of the inverse mass ratio of evaporating gas species containing different isotopes (Fig. 3). Although the predicted β should be constant irrespective of crystallographic orientations, we found that β depends both on crystallographic orientations and on temperature. The β seems to be largest and smallest along the c- and b-axis, respectively, especially at higher temperatures.

We propose that the isotopic fractionation factor for kinetic evaporation can be expressed by the ratio between detachment rates of isotopes, which depend on vibrational frequencies between an adatom and a surface atom (or atomic cluster). If the vibration mode with a maximum frequency is responsible for detachment of adatoms, the isotopic fractionation factor can be expressed by the inverse ratio of reduced mass of the vibrating system. If we assume an adsorbed Mg isotope vibrates with a surface O atom or a SiO_4 tetrahedron, β corresponds to the range of the β obtained in this study and in previous studies. Anisotropy may also be explained by the difference of the surface atom (or atomic cluster) vibrating with Mg: the surface O atom may be the dominant species vibrating with Mg at the (010) surface with the largest bond density.

We relate such surface processes to the evaporation rate in vacuum, which is usually expressed only by the velocity of gas species detaching from the evaporating surface.

References:

[1] Clayton R. N. et al. (1988) *Phil. Trans. Roy. Soc. A, 325,* 483-501. [2] Grossman, L. and Fedkin, A. V. (2003) *Geochim. Cosmochim. Acta, 67,* 4205-4221. [3] Wang J. et al. (1999) *Geochim. Cosmochim. Acta, 63,* 953-966. [4] Ozawa K. et al. (1996) *Lunar. Planet. Sci., XXVII,* 989-990. [5] Chakraborty, S. et al. (1994) Phys. Chem. Miner., 21, 489-500.

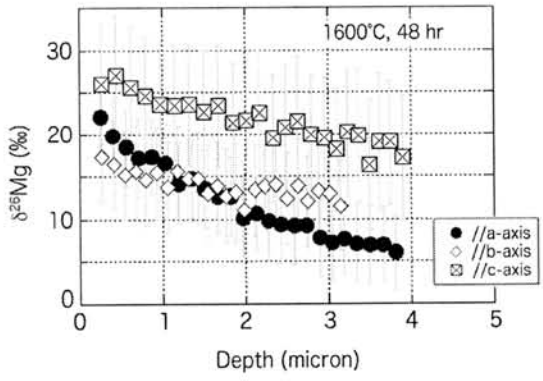

Fig. 1. Depth profiles of δ^{26}Mg of evaporated forsterite

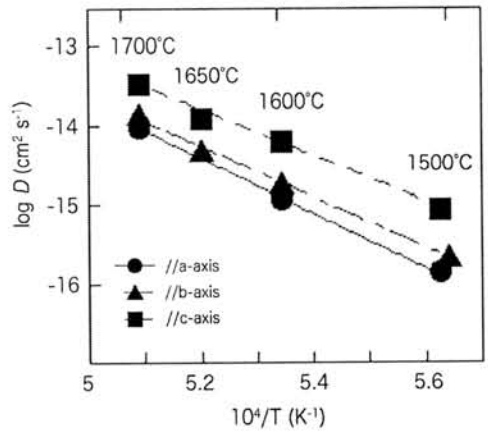

Fig. 2. Mg self-diffusion coefficient in forsterite

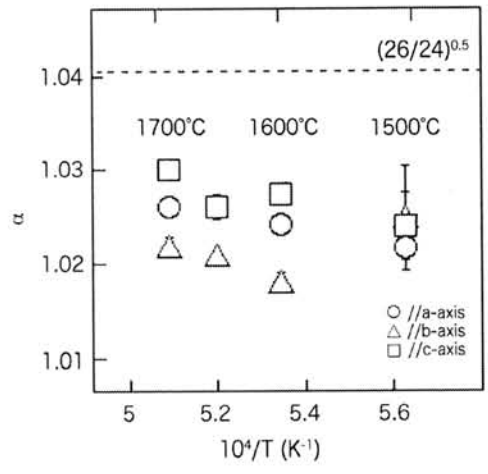

Fig. 3. Mg isotopic fractionation factor for evaporation of forsterite

Asteroidal processes related to strongly recrystallized chondritic materials and augite-bearing lodranite-like meteorites. H. Takeda[1], A. Yamaguchi[2] and M. Kusakabe[3], [1]Chiba Inst. of Technology, [2]National Inst. of Polar Research, and [3]Inst. for Study of the Earth's Interior, Okayama Univ.

Introduction:

The Hayabusa (MUSES-C) spacecraft of ISAS/JAXA observed global properties of 25143 Itokawa from September to November, 2005 [1]. The Itokawa is an Apollo type asteroid with the longest dimension, 548m. The surface of Itokawa is divided into two distinct types of terrain: "the rough terrain", which exhibits rough topography mostly due to the existence of numerous, large boulders, and "the smooth terrain", which is mainly comprised of flat regolith region.

Before the Hayabusa mission, Itokawa was classified as an S(IV)-type asteroid with olivine and pyroxene as the main components, based on telescopic observations [2]. Spectra obtained by the near-infrared spectrometer (NIRS) [3], covering the wavelength range 0.76 to 2.25 μm, shows that Itokawa's surface shows strong phase reddening, similar to that observed at Eros. Preliminary analyses of NIRS data suggest that Itokawa is an object that contains a significant amount of olivine and pyroxene on its surface [4].

X-ray fluorescence spectrometry (XRS) of the Itokawa has been performed by the CCD-based X-ray spectrometer [5]. The first results of the XRS observation indicate that the surface of Itokawa has chondritic composition and that LL- or L-chondrites are most likely but H-chondrites or primitive achondrites cannot be ruled out so far.

With reference to these data obtained by Hayabusa and presented at the 37*th* Lunar and Planetary Science Conference, we present asteroidal processes deduced from the evidence of meteorites, related to the possible formation of the parent asteroid of Itokawa. Because of the existence of "the rough terrain" with numerous, large boulders, we reexamined strongly melted and recrystallized chondritic materials including the type LL7 chondrites [6] and a new lodranite-like meteorite [7] recovered from the hot desert [8].

Samples and Experimental Methods:

NWA2235, a 64 g stone found within 100km of Alnif, Morocco in 2000 [8]. Samples were supplied from NIPR. The PTSs of NWA2235 were studied by an optical microscope and an electron probe micro-analyzer (EPMA) at Ocean Res. Inst. (ORI) of Univ. of Tokyo. The Area Analysis technique of the JEOL 8900 EPMA was applied to obtain elemental and mineral distribution maps (Fig. 1) at ORI. The modal abundance (vol. %) of silicate minerals was derived from these maps. Chemical compositions of minerals were obtained with EPMA, JEOL JCXA-733 at ORI with WDS. We reexamined digital images of strongly melted or recrystallized LL chondrites and lodranites stored in the Planetary Material Database of Univ. of Tokyo.

Results:

The PTS of NWA2235 shows a coarse-grained aggregate (ca. 0.5 to 2 mm in the longest dimension) with triple point juncture, consisting mainly of olivine (Fo88), orthopyroxene (Ca2Mg85Fe13), Fe-Ni-metal, troilite, augite (Ca40Mg54Fe6) and chromite [Cr/(Cr+Al)=0.85 atomic ratio, Fe/(Fe+Mg) =0.63]. The mineral compositions are within the range reported for lodranites [7], but amounts of opaque minerals are less than Lodran. It is weakly shocked, with rare mosaicism in olivine. The textures and mineral distribution are similar to those of Yamato 791491 [6], in that the amounts of opaque minerals are less than Lodran, and those of augite are higher than the most of lodranites. MAC88177 contains 6% of augite. Modal abundance of minerals are: Olivine 55 vol.%, Opx 17, Aug. 7, metal 8.5, troilite 1, chromite 2.5, Others 9.

The oxygen isotopic compositions of NWA2235 ($\delta^{17}O$ = 1.62, $\delta^{18}O$ = 4.94, $\Delta^{17}O$ = -0.96) are roughly plotted along the extension of slope-1 trend on the oxygen 3-isotope plot of the lodranite-acapulcoite trend, with near the highest $\Delta^{17}O$ values, and below the winonaite-IAB group. The O-isotopic data are in line with the high augite contents, which suggest extensive transport of materials.

Yamato-74160 has been described as LL7 chondrite [7], because it experienced partly melting at temperature well above 1090°C and euhedral pyroxene crystals in albite grew from melt pockets in one area of the PTS. Most other parts show textures of brecciation and extensive recrystallization in solid state. Siderophilic and chalcophilic elements were lost by extraction into partial melt that drained away. Chmical zoning in albite crystals and mobile element loss suggest shock as the most likely heat source.

Y-790964 and Y-790143 [9] are unusual impact-melted LL chondrites, and experienced nearly total melting, yet partly preserve chondritic textures. Olivine and chromite grains in Y790964 and olivine in Y-790143 are the only relicts of the precursor materials. The chondrule ghosts were melted and crystallized in situ, without significant mixing with less viscous melts. Evidence of complex injection of troilite, Fe-Ni-metal and feldspathic glass into relict minerals suggests that the precursor rock was shocked in situ. Shock ages of these meteorites are ca. 1.2 Ga [10].

Discussion:

We examined geographical features and chemical characteristic of Itokawa observed by Muses-C, in terms of evidence we gathered from the extensively modified chondritic meteorites, as described above and reported in literatures. This idea is based on the facts that hard, rocky materials are abundant at the surface of Itokawa.

The appearance of the surface of Itokawa [1] is different from any other asteroids previously observed by spacecraft, which are much larger than Itokawa and globally covered with thick regolith layers and many craters. Two types of terrains are recognized by AMICA [11]: (1) rough terrain, which is covered with numerous boulders, and (2) smooth terrain, whose surface is apparently flat.

These features have not been interpreted in terms of proposed models of the chondrite parent bodies [e.g., 12]. An onion-shell model assumes heating by rapid decay of the short-lived isotope of Al produced a metamorphosed (petrologic type 6) interior, but the surface layers remain relatively cool (type 3). A brecciated rubble pile model assumes formation by accretion of smaller, already metamorphosed planetessimals, or formation by gravitational reassembly of a larger onion-shell body that had been disrupted by a large impact. However, a model applicable for Itokawa with two terraines, may involve mixing of two or more (type 6, 3) large fragments formed by disruption of the onion-shell by a large impact on the same parent body.

Extensively recrystallized or melted chondrites we presented in this study were fromed by heating by a local impact. The lodranite-acapulcoite and winonaite-IAB groups were formed very early by inhomogeneous segregation of partial melts and the grain-coarsening mechanism from chondritic source materials [13]. These asteroidal processes would contribute to produce hard, rocky, crystalline materials in interior by ^{26}Al decay, and near surface by shock heating by repeated impacts. Mixing of these hard rocks and fragile materials of the low metamorphic grade would promote formation of two different terrains. However, the observation by AMICA [11] proposed more physical processes are important.

These characteristics of the surface features observed by AMICA are consistent with the view that the smooth terrains are mantled by fine materials. These likely indicate the existence of certain surface processes to concentrate the regolith materials on the smooth terrains after the formation of Itokawa. The most distinctive smooth terrain is called the Muses Sea, whose location may indicate its depositional origin [11]. This fact may imply the gravitationally-induced movements of the finer materials after the formation of the asteroid. Smooth terrains, including the largest smooth terrain always locate at the local lows of gravity, however, the local lows of gravity do not always have smooth deposits. This may suggest that the regolith on Itokawa is not a direct result of impact re-accumulation but may have experienced complicated evolutional history.

The AMICA [14] detected large variation in the degree of "space weathering" on the surface of Itokawa. Some lodranites show reflectance spectra similar to that of "space weathering". Olivine crystals in them include fine dusty inclusions along dislocations, which were produced during cooling after break-up of a hot parent body [15].

The results of the XRS observation [5] show that the surface of asteroid has chondritic Mg/Si and Al/Si ratios. There are relatively small regional variations in composition. Regional average of Mg/Si=0.78±0.09 and Al/Si= 0.07±0.03 of Itokawa [5], are in good agreements with the wt % ratios of Mg/Si=0.82 and Al/Si= 0.072 of Y-74160, which are close to Mg/Si=0.82 and Al/Si=0.063 of mean LL chondrites. Mg/Si=1.09 and Al/Si=0.029 of the Y-791493 lodranite are more deviated. The XRS group [5] stated that LL- or L- chondrites are most likely but the H-chondrites or primitive achondrites cannot be rejected.

Further studies are required to interpret asteroidal processes to better understand the features observed by Muses-C in terms of meteorite samples.

We thank NIPR, ORI (T. Ishii and M. Otsuki), CIT and Univ. of Tokyo for support of this study.

References:

[1] Fujiwara A. et al. (2006) *LPS XXVII,* #1575. [2] Binzel, R.P. et al. (2001) *Meteorit. Planet. Sci., 36,* 1167- 1172. [3] Kitazato K. et al. (2006) *LPS XXVII,* #2258. [4] Abe M. et al. (2006) *LPS XXVII,* #1547. [5] Okada T. et al. (2006) *LPS XXVII,* #1596. [6] Takeda H. et al. (1984) *Earth Planet. Sci. Lett. 71,* 329-339. [7] Takeda H. et al. (1994) *Meteorit. 29,* 830-842. [8] Takeda H. and Yamaguchi A. (2005) *Meteorit. Planet. Sci., 39, Suppl.* A232. [9] Yamaguchi A. et al. (1998). *Antarct. Meteor. Res. 11,* 18-31. [10] Nakamura N. and Okano O. (1985) Nature, 315, 563-566. [11] Miyamoto H. et al. (2006) *LPS XXVII,* #1686. [12] Miyamoto M. et al. (1981) *Proc. LPSC 12,* 1145-1152. [13] Bogard D. D. et al. (2005) *Meteorit. Planet. Sci., 40,* 207-224. [14] Ishiguro M. et al. (2006) *LPS XXVII,* #1533. [15] Miyamoto M. and Takeda H. (1994) *JGR 99,* 5669–5677.

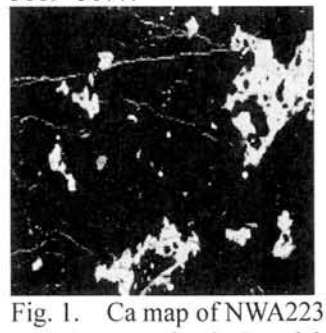

Fig. 1. Ca map of NWA2235. Width is 6 mm. Green region is Ca –rich pyroxene.

Chemical Composition of Micrometeorites collected from Tottuki Point, Soya Coast, Antarctica

Y. Tazawa[1], T. Fukuoka[2], N. Hoshi[2], Y. Fukushi[2, 6], Y. Saito[3], T. Noguchi[4] and T.Yada[5] [1]Department of Physics and Astrophysics, Graduate School of Science, Kyoto University., Kyoto 606-8502, (tazawa@cr.scphys.kyoto-u.ac.jp), [2]Department of Environmental Systems, Faculty of Geo-Environmental Science, Rissho University, Kumagaya 360-0914, [3]Radio Isotope Laboratory, College of Science and Engineering, Aoyama Gakuin University, Sagamihara 229-8551, [4]Department of Materials and Biological Science, Ibaraki University, Mito 310-8512, [5]Department of Earth and Planetary Science, University of Tokyo, Tokyo 113-0033, [6](Present Address) Department of Earth and Planetary Science, Tokyo Institute of Technology, Tokyo 152-8551.

Introduction

Micro particles of cosmic origin collected from the Earth have more or less survived from the heating during the Atmospheric entry and the weathering after the settling on the Earth. The typical of them are fully molten droplets called "Cosmic Spherules (CSs)"[1]. Scarcely affected extraterrestrial particles were firstly mass-collected from the Stratosphere, typical of which are fragile aggregates of chondritic constituents, called "Interplanetary Dust Particles (IDPs)", and thought as of cometary origin [2,3]. Those from the Polar Regions, especially from Antarctica, "Antarctic Micrometeorites (AMMs)", have been collected in large quantities [4, 5, 6] and also examined, especially on "Unmelted Micrometeorites (UMMs)" in recent years [7, 8, 9, 10]. Instrumental neutron activation analysis (INAA) is one of the most effective means to measure abundances of many elements of a single microscopic sample (heavier than sub-μg in weight) in quantitative, simultaneous, and non-destructive ways. So far, we have been studying chemical features of individual AMMs by means of INAA [10, 11, 12]. We report here recent INAA results of AMMs.

Samples and Experimental

AMMs studied here are twenty-one stony type spherules (SSs) provided by National Institute for Polar Research (NIPR); *i.e.*, ten fully melted MMs (NA6, ND7, NI5, NJ5, NN5, NO7, NP5, NR6, NS5, and NS7) and eleven unmelted MMs (UM1, UM2, UM3, UM4, UM5, UM6, UM7, UM8, UM9, UM10, and UM11), however NS7 and UM3 were lost during sample preparations for the second neutron irradiation (for long-lived nuclides). They were collected from the bare ice at the N7 point near Tottuki Point on the Soya Coast (68°55.3'S, 39° 51.0'E) by JARE-41 in 2000[13]. Assortments and preliminary investigations of the AMM collection have been also performed by the AMM initial examination team organized by NIPR.

INAA were performed on the individual MMs and tiny chips of standard materials; *i.e.*, glass made from a GSJ standard rock, JB-1 (basalt) for lithophile elements (LPEs: Na, Mg, Al, Ca, Sc, Ti, V, Cr, Mn, La, Ce, Sm, Eu, Dy, Yb, Lu, *etc.*, and Fe, Co as well) and metal wire, Al-Au (IRMM-530) and Pt (SRM-680a) for siderophile elements (SPEs: Au, Ir, Os, *etc.*). Each of the samples was weighed by an electro micro-balance (Mettler: UMT2) prior to the INAA. The procedures were applied after [14] and as follows.

INAA for short half-life nuclides (SN series): Each of the MMs and the standards was heat-sealed in each small (ca. 2 x 2 mm) bag made of ultra pure polyethylene sheet (to handle easily) and irradiated by neutron for 10 min at 20 MW ($2x10^{13}$ neutrons/cm^2/sec) in a pneumatic pipe (PN-3) of the reactor JRR-3M, Japan Atomic Energy Research Institute (JAERI). The first count series were done individually for 400 sec (live-time) after 2 ~ 10 min cooling, using a gamma-ray counting facility at PN-3. The second count series were done individually for 1000 sec at several hours after the first series using a facility at the Inter-University Laboratory for the Joint Use of JAERI Facilities, Research Center for Nuclear Science and Technology (RCNST, Tokai Branch), University of Tokyo. In these procedures, Na, Mg, Al, K, Ca, Ti, V, Mn, and Dy are determined.

INAA for long half-life nuclides (LN series): After the SN series mentioned above, the samples were picked out from the polyethylene bags and encased again individually in ultra-pure synthetic quartz vials. They were irradiated again all together by neutrons for 100 hr at 20 MW (1×10^{14} neutrons/cm^2/sec) in a hydraulic rabbit irradiation facility (HR-1) of the JRR-3M. After the irradiation and a few days cooling, each of them was unsealed and put on a small plastic plate for setting into a well type detector. They were counted sequentially according to the half-lives and activities of nuclides of respective elements, *e.g.*, (Na, K), Cr, Fe, Sc, rare earth elements (REEs: La, Ce, Nd, Sm, Eu, Tb, Yb, Lu), SPEs (Co, Au, Ir, Os), *etc.*, using the counting facilities of Aoyama Gakuin University and Institute for Cosmic Ray Research (ICRR), University of Tokyo. Counting durations and cooling times were about for 2 ~ 12 hours after 4 ~ 8 days (1st sequence), for 6 ~ 24 hours after 2 ~3 weeks (2nd sequence), 1 day ~ 1 week after more than 1 month (3rd sequence), respectively.

Results and Discussion

As listed in Table and shown in Figures, all the MMs, not only unmelted but also melted ones, are confirmed to be S-type MMs similar to chondrite;

Unmelted MMs: (1) Abundances of 13 elements (Al, Ca, Ti, V, Mg, Cr, Mn, Na, La, Sm, Yb, Lu, Sc) range between 0.2 and 3 times of CI, except lack of Ca (in U1, U5, U6 and U10) and Ti (in U6). Mean abundances (and relative errors:σ/M) of 10 MMs are ranging from 0.61 (92%) for Ca to 1.99 (23%) for Lu. Mean abundances of the 13 elements of the MMs is

Table. INAA results of Micrometeorites collected from Bare ice at Tottuki Point, Soya Coast, Antarctica

Sample	weight	Na	Mg	Al	Ca	Ti	V	Cr	Mn	La	Sm	Yb	Lu	Sc	Fe	Co	Au	Ir
	μg	%	%	%	%	%	ppm	ppm	%	ppm	ppm	ppm	ppm	ppm	%	ppm	ppb	ppb
NA6	6.4	0.05	19.0	1.93	1.7	–	77.2	613	0.331	0.60	0.385	0.383	0.056	10.4	12.80	191	27.1	77.8
ND7	20.5	0.03	18.5	1.34	1.4	0.10	93.1	3540	0.510	0.28	0.199	0.256	0.038	11.2	13.00	245	19.8	68.9
NI5	14.9	0.60	17.7	1.43	1.8	0.08	78.4	1090	0.304	0.22	0.161	0.174	0.038	13.1	5.19	8.03	–	14.8
NJ5	4.7	0.03	15.0	1.75	–	–	115	3900	0.217	0.62	0.332	0.269	0.052	11.6	19.60	127	2.2	133
NN5	5.1	0.05	13.4	0.588	–	–	80.3	2120	0.181	0.78	0.049	–	–	5.68	19.00	400	6.3	64.4
NO7	4.5	0.03	13.0	1.10	1.6	–	83.7	3390	0.263	0.27	0.188	0.263	–	9.55	26.40	526	5.1	55.7
NP5	10.8	0.08	10.6	1.05	–	0.14	103	3710	0.197	0.18	0.099	–	0.026	8.39	28.58	340	95.3	177
NR6	13.3	–	30.6	0.415	0.46	–	164	726	0.134	0.13	0.065	0.154	0.036	13.9	3.13	40.9	–	26.7
NS5	24.4	0.58	18.8	1.64	0.92	0.10	54.7	899	0.296	0.16	0.058	0.102	0.026	8.84	9.34	26.2	3	15.5
TPU1	2.9	0.47	7.7	1.04	–	0.10	71.6	3620	0.091	0.35	0.133	0.160	0.068	6.13	27.64	128	387	236
TPU2	59.0	0.31	15.4	1.27	1.2	0.08	88.0	4880	0.199	0.39	0.217	0.231	0.048	11.8	23.83	307	179	401
TPU4	8.9	0.37	13.1	1.15	1.0	0.09	65.4	3470	0.198	0.34	0.187	0.235	0.036	7.66	22.92	258	218	185
TPU5	1.4	0.4	6.2	1.25	–	0.1	49	2490	0.10	0.16	0.123	0.13	0.05	5.82	19.79	82.9	173	165
TPU6	1.1	0.2	4.8	0.88	–	–	40	1360	0.08	0.2	0.085	0.11	0.03	3.53	10.85	40.0	137	77
TPU7	11.2	0.19	10.5	1.29	1.0	0.09	68.4	3460	0.184	0.30	0.198	0.204	0.056	7.29	31.09	215	221	299
TPU8	8.5	0.44	13.9	1.06	1.1	0.06	58.8	3380	0.273	0.30	0.186	0.166	0.037	7.14	23.42	218	228	183
TPU9	15.5	0.40	8.69	1.06	0.69	0.06	63.1	3500	0.108	0.31	0.130	0.133	0.055	7.28	24.79	57.4	305	186
TPU10	0.6	0.1	6.5	0.75	–	0.1	47	1830	0.04	0.2	0.095	0.11	0.05	3.45	9.75	28.1	177	100
TPU11	4.1	0.43	8.45	1.56	0.61	0.10	63.2	3310	0.161	0.33	0.184	0.225	0.054	8.72	25.57	323	305	400
% Error		1–36%	3–18%	<5%	10–35%	10–50%	4–20%	<3%	3–22%	5–50%	5–14%	5–29%	5–21%	<3%	<3%	<3%	2–29%	<6%
CI		0.50	9.89	0.868	0.93	0.0436	56.5	2660	0.199	0.235	0.147	0.163	0.0243	5.82	19.04	502	140	481

1.13 times of CI (43%). (2)Except for the depletion of Ca and Ti in some samples and somewhat lower Na abundances, LPEs of the unmelted MMs are quite similar to chondrite. (3) The abundance ratios of Na/Al are ranging from 0.26 to 0.78, and the mean of 10 MMs is 0.50 (43%), which indicate that the MMs have not been so fractionated. (4) Mean abundances of SPEs (Fe,Co, Ir and Au) of the MMs are 0.48 (33%) for Ir, 1.15 (31%) for Fe, 0.33 (68%) for Co, and 1.59 (50%) for Au. Mean of the 4 elements for the unmelted MMs is 0.89 (52%). (5) Contrast to the high abundances of Au, abundances of Co and Ir are about 1/5 and 1/3 of the Au.

Melted MMs: (6) Abundances of 13 elements of the melted MMs (9 samples) are ranging from 0.32 times of CI (151% of relative error) for Na to 1.77 (25%) for Sc, despite lack of Ca, Ti, Yb and Lu in some MMs. (7) Mean abundance and the relative error of 13 elements for all the melted MMs are 0.80 and 64%, respectively. (8) The Na/Al ratios are ranging from 0 to 0.61, the mean and the relative error are 0.22 and 156%, respectively. (9) The SPE abundances are 0.15 (77%) for Ir, 0.80 (58%) for Fe, 0.42 (86%) for Co, and 0.13 (173%) for Au. Mean of the SPE for the melted MMs (9 samples) is 0.37 (102%). (10) Contrast to the unmelted MMs, the melted ones rather deplete SPEs.

Types of abundance patterns: As shown in Figures, abundance patterns normalized to CI and Mg for LPEs and REEs, and CI and Fe for SPEs are classified into 4 types.

References:

[1] Murray J. and Renard A.F. (1883), *Proc. Roy. Soc. Edinburgh*, *12*, 474-495. [2] Brownlee D.E. et al. (1976), *NASA Tech. Mem.*-TMX-73152, 1-42. [3] CDPET (1981-1996), *Cosmic Dust Catalog,* NASA/ JSC, Vol. *1-16*. [4] Maurette M. et al. (1986), *Science*, *233*, 869-872. [5] Maurette M. et al. (1991), *Nature*, *351*, 44-47. [6] Nakamura T. et al. (1999), *Antarct. Meteorite Res.*, *12*, 183-198. [7] Noguchi T. and Nakamura T. (2000), *Antarct. Meteorite Res.*, *13*, 285-301. [8] Nakai I. et al. (2000), *ibid.*, 302-310. [9] Osawa T. et al. (2000), *ibid.*, 322-342. [10] Fukuoka T. et al. (1999), *Antarct. Meteorites XXIV*, 24-25. [11] Fukuoka T. et al. (2000), *Antarct. Meteorites* **XXV**, 10-11. [12] Tazawa Y. et al. (2003), *Int. Sym. Evolution of solar System Materials*, Sept. 3-5, 138-139. [13] Yada T. and Kojima H. (2000), *Antarct. Meteorite Res.*, *13*, 9-18. [14] Fukuoka T. and Tazawa Y. (1996), *Antarct. Meteorites* **XXI**, 33- 34.

Figure: Abundance Patterns normalized to CI and Mg for LPE/REE, and CI and Fe for SPE.

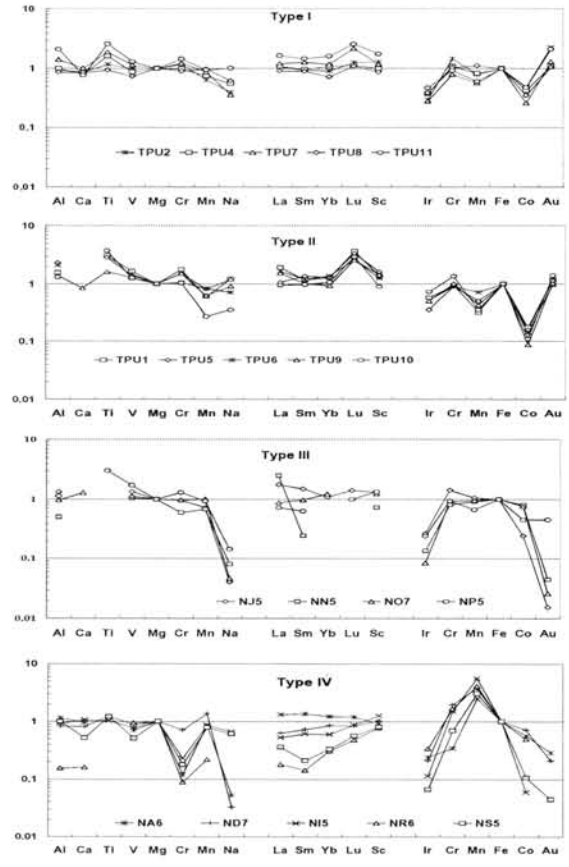

Speculations on the slow neutron capture process in AGB stars based on the isotopic analyses of SiC grains from the Murchison Meteorite. K. Terada[1], T. Yoshida[2], N. Iwamoto[3], W. Aoki[2] and I. S. Williams[4], [1] Department of Earth and Planetary Systems Science, Hiroshima University, JAPAN (terada@sci.hiroshima-u.ac.jp). [2] National Astronomical Observatory, JAPAN, [3] Japan Atomic Energy Agency, JAPAN. [4] Research School of Earth Sciences, The Australian National University, AUSTRALIA

Introduction:

It is generally agreed that Asymptotic Giant Branch stars (AGB stars) are the main contributors of the slow neutron capture process (s-process) elements. According to the recent stellar evolution models of thermally pulsing AGB stars [1-4], the best candidate reactions for the neutron source are $^{13}C(\alpha, n)^{16}O$ and/or $^{22}Ne(\alpha, n)^{25}Mg$. The former reaction operates at temperatures from about 8 keV up to 10keV in the ^{13}C-pocket at the top of the He inter-shell during the inter-pulse phase, where the neutron density is low (up to 10^7 cm^{-3} in solar-metallicity stars). This phase is followed by He-shell flash episodes which are characterized by higher temperatures of 25–30 keV. In this flash phase, the $^{22}Ne(\alpha, n)^{25}Mg$ reaction is activated and gives rise to a higher neutron density (10^8–10^{11} cm^{-3} in the case of solar-metallicity stars).

Several approaches based on the chemical and isotopic composition of the bulk of Solar system materials have been used to try and understand the "origin of the s-process element in the Solar system" [e.g. 5-8]. For example, based on the σ N curve of isotopes produced only by the s-process, Howard et al. [5] calculated average neutron densities of N_n = 1.1 (+0.6, -0.3) x 10^8 cm^{-3} at an optimum temperature of T = (2.7±0.3) x 10^8 K and a mean neutron exposure of $\tau_0 = 0.26 \pm 0.01$ mbarn^{-1}. Wisshak et al. [6] and Toukan et al. [7] suggested that neutron densities were possibly N_n = (4.1±0.6) x 10^8 cm^{-3} and N_n = (3.8±0.6) x 10^8 cm^{-3}, respectively, based on the $^{148}Sm/^{150}Sm$ isotopic ratio of bulk solar materials. Moreover, Wisshak et al. [8] suggested a temperature of 28–33 keV based on the $^{152}Gd/^{154}Gd$ ratio of solar materials. They suggested that this higher temperature and neutron density might result from the $^{22}Ne(\alpha, n)^{25}Mg$ reaction being the neutron source.

In contrast, a series of studies of relict presolar grains in primitive meteorites has provided a different point of view of nucleosynthesis in AGB stars (for a general review, see [9]). For example, the enhancements of ^{25}Mg expected as a result of the $^{22}Ne(\alpha, n)^{25}Mg$ reaction are uncommon, even in the presolar grains rich in s-process elements [10], indicating that the $^{13}C(\alpha, n)^{16}O$ reaction is a more likely neutron source. Nicolussi et al. [11] suggested, based on Mo and Zr measurements, that most of the SiC grains condensed around low-mass AGB stars where the $^{13}C(\alpha, n)^{16}O$ reaction is the principal neutron source. Moreover, Nicolussi et al. [12] suggested that neutron densities in most parent stars were lower than 10^7 cm^{-3}, based on the observation that the measured $^{88}Sr/^{86}Sr$ ratios in most SiC grains indicated the dominant β decay of short-lived ^{85}Kr. To better understand the physical parameters of nucleosynthesis in parent stars prior to formation of the Solar system, we focus here on the *s*-process parameters reflected in Eu isotopic compositions.

Analytical methods and results:

Presolar SiC grains were recovered from the Murchison meteorite using the procedure of Amari and others [13]. The grains remaining after acid digestion and density separation, corresponding to the KJ fraction [13], were mounted by pressing them onto a copper plate. They were analyzed for major elements and identified by the Electron Probe Micro Analyzer at Hiroshima University, then the three largest SiC grains (>5 μm) were selected for isotopic study.

First the Si and C isotopic compositions of individual grains were measured on the SHRIMP II at the Australian National University, using a Cs^+ primary ion beam. The Eu isotopic compositions of same grains were then measured on the SHRIMP II at Hiroshima University, using an O_2^- primary beam. Details of the experimental procedures and calibrations are given in [14].

Among three grains, grain SiC35 and SiC67 have slightly lower $^{12}C/^{13}C$ than the terrestrial reference value of 89. They are also slightly enriched in ^{29}Si and ^{30}Si relative to ^{28}Si. These are the characteristics of Mainstream grains [15], considered to originate from low-mass AGB stars with a solar metallicity. On the other hand, grain SiC39 is depleted in ^{12}C and has a large excess in ^{30}Si relative to ^{28}Si and ^{29}Si ($^{12}C/^{13}C$ = 55, $\delta(^{30}Si/^{28}Si)$ = 278 and $\delta(^{29}Si/^{28}Si)$ = 12), indicating that it is a Z-grain [9]. It is proposed that such grains come from low-mass stars of much lower metallicity (approximately less than one-third solar) [15, 16].

The measured $^{153}Eu/^{151}Eu$ ratios in Mainstream grains SiC35 and SiC67 are 1.29 ± 0.24 and 1.33 ± 0.24, within error of the solar value of 1.09 [17], but significantly higher than the ratios of 0.85 and 0.71 predicted for products of the *s*-process by the stellar and classical models respectively [18]. In contrast, the Eu content of Z-grain SiC39 was so low that a precise isotopic analysis could not be obtained (0.97 ± 0.52). This might be concerned with the parent AGB star for this type of grain being a low-metallicity star. The discussion below is based on an

average $^{153}Eu/^{151}Eu$ ratio of 1.3 ± 0.2 in the two Mainstream grains, which were considered to originate from low-mass AGB stars with a solar metallicity.

Discussion:

To further investigate the s-process by using Eu isotopes, we have calculated expected Eu isotopic ratios as a function of nucleosynthetic conditions, in accordance with [19]. Here, in order to simply understand complicated nuclear flows (which are realized in the s-process of an AGB model) in wide ranges of temperature and neutron density, we adopted simple assumptions (constant temperature and neutron density conditions, in which recurrent neutron exposures are followed) for the usual s-process with the two major neutron sources. To follow the nuclear flow around the Nd-Pm-Sm-Eu-Gd region, we have used a nuclear network code in which the temporal variation of nuclides is solved with updated neutron capture rates [20], beta-decay rates and electron capture rates [21] under with various temperature and neutron density conditions. We used the recently reported neutron capture cross section for the unstable nucleus ^{151}Sm ([22], [23]). The new $^{151}Sm(n,\gamma)$ rate is a factor of 2 larger than previous theoretical predictions (e.g., [24]).

Figure 1 illustrates the changes in $^{153}Eu/^{151}Eu$ as a function of temperature and neutron density for different neutron exposures (τ_0 = 0.3 mbarn^{-1} and τ_0 = 0.03 mbarn^{-1}, respectively). As shown in Figure 1, the predicted $^{153}Eu/^{151}Eu$ ratios are sensitive to temperature (T) and neutron density (N_n), so the observed $^{153}Eu/^{151}Eu$ ratio could be a good probe for the values of these s-process parameters in the He-layer. On the other hand, the differences between $^{153}Eu/^{151}Eu$ ratios at τ_0 = 0.3 and 0.03 mbarn^{-1} are less than 2%, indicating that the Eu isotopic ratio is not sensitive to the neutron exposure.

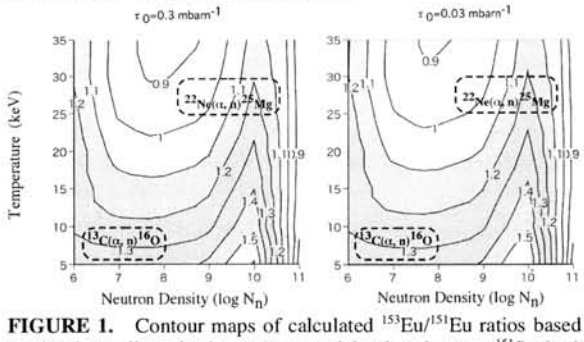

FIGURE 1. Contour maps of calculated $^{153}Eu/^{151}Eu$ ratios based on the thermally pulsed s-process model using the new $^{151}Sm(n,\gamma)$ reaction rate.

The observed $^{153}Eu/^{151}Eu$ ratio of the Mainstream grains (average 1.3 ± 0.2) constrains the possible *s*-process temperature and neutron density conditions to the gray area in Figure 1; that is, (i) T < 15 keV for 10^7–10^9 cm^{-3}, and/or (ii) T > 10 keV for 10^{10} cm^{-3}. The plausible regions of $^{13}C(\alpha, n)^{16}O$ and/or $^{22}Ne(\alpha, n)^{25}Mg$ based on the recent stellar evolution models of thermally pulsing AGB stars [1-4], are also shown as dashed enclosures. It should be noted that $^{153}Eu/^{151}Eu$ values previously predicted by the stellar model (0.85) and the classical model (0.71) assuming that N_n = 4.1 x 10^8 cm^{-3} [18] are out of range of not only the possible neutron sources of $^{13}C(\alpha, n)^{16}O$ and $^{22}Ne(\alpha, n)^{25}Mg$, but also of the extended region of Figure 1 (5–35 keV and 10^6–10^{11} cm^{-3}). This discrepancy is possibly due to the different reaction rate previously used for $^{151}Sm(n,\gamma)$.

Both the recent theoretical studies [4] and the analysis of individual presolar grains [11] shows that *s*-process elements in the solar system are derived predominantly from $^{13}C(\alpha, n)^{16}O$ sources. It should be noted that our data closely match the current ^{13}C-pocket model (<10 keV at about 10^7 cm^{-3}), but the neutron source of $^{22}Ne(\alpha, n)^{25}Mg$ is still possibly about 10^{10} cm^{-3}. For tighter constraints on the *s*-process conditions, much higher precision analyses of $^{153}Eu/^{151}Eu$ ratios, coupled with analyses of isotopic compositions of other heavy elements sensitive to s-process branchings in the same grains, would be required.

References:

[1] Gallino R. et al. (1998) ApJ **497**, 388-403 [2] Busso M., Gallino R. and Wasserburg G. J. (1999) *Annual Review of A&A* **37**, 239-309 [3] Goriely S. and Mowlavi N. (2000) *A&A* **362**, 599-614. [4] Lattanzio J. C. and Lugaro M. A. (2005) *Nuc. Phy. A* **758**, 477c-484c. [5] Howard W. M. et al. (1986) *ApJ* **309**, 633-652. [6] Wisshak K. et al. (1993) *Nuc. Phy. C* **48**, 1401-1419. [7] Toukan K. A. (1995) *Nuc. Phy. C* **51**, 1540-1550. [8] Wisshak K. et al. (1995) *Nuc. Phy. C* **52**, 2762-2779. [9] Zinner E. K. (2005) "Presolar Grains", in *Meteorites, Comets, and Planets*, edited by A. M. Davis, Vol. 1 *Treatise on Geochemistry, Oxford, Elsevier-Pergamon, pp. 17-39.* [10] Amari S. (private communication) [11] Nicolussi G. K. et al. (1998) *GCA* **62**, 1093-1104. [12] Nicolussi G. K. et al. (1998) *Phy. Rev. Lett.* **81**, 3583-3586. [13] Amari S., Lewis R. S. and Anders E. (1994) *GCA* 58, 459-470. [14] Terada K. et al. (2006) New Astronomy Rev. submitted. [15] Hoppe P. et al. (1997) *ApJ Lett.* **487**, 101-104. [16] Lugaro M. et al. (1999) *ApJ Lett.* 527, 369-394. [17] Anders E. and Grevesse N. (1989) *GCA* 53, 197-214. [18] Arlandini C., Käppeler F. and Wisshak K. (1999) *ApJ* 525, 886-900. [19] Aoki W. et al. (2003) *ApJ Lett.* **592**, 67-70. [20] Bao Z. Y. et al. (2000) *At. Data Nucl. Data Tables* **76**, 70-154. [21] Takahashi K. and Yokoi K. (1987) *At. Data Nucl. Data Tables* **36**, 375-409. [22] Marrone S. et al. (2005) *Nuc. Phy. A* **758**, 533c- 536c. [23] Abbondanno U. et al. (2004) *Phy. Rev. Lett.* **93**, 161103. [24] Best J. et al. (2001) *Phy. Rev. C* **64**, 015801.

Chromium isotopic systematics of ureilite. T. Ueda[1], K. Yamashita[2] and N. Kita[3], [1] Graduate School of Science and Technology, Kobe University, Nada, Kobe 657-8501, Japan, [2] Department of Earth and Planetary Sciences, Kobe University, Nada, Kobe 657-8501, Japan, [3] Department of Geology and Geophysics, University of Wisconsin Madison, 1215 W. Dayton Street, Madison, WI 53706-1692, USA.

Introduction:

Ureilite is a unique class of igneous ultramafic achondrites that preserves signatures of primitive meteorites (e.g. oxygen isotope [1]). This unique characteristic makes it very important to investigate their origin and their relationship with other meteorite classes. Determining their absolute ages, however, is often very difficult as they are depleted in elements such as U, Th, Sm, and Rb, which are used in conventional geochronology. Although the recent Mn-Cr and Al-Mg investigations on the felsic clasts in polymict ureilites have shown that these clasts are old [2, 3], the age constraints for the ultramafic monomict ureilites are still limited [4].

In this study, we have undertaken a detailed Cr isotopic analysis of three ureilites, ALH77257, Y791538 and MET78008. ALH77257 is a typical olivine-pigeonite ureilite with moderate Mg#, MET78008 is the Ca-rich ureilite containing olivine, low Ca pyroxene and augite, and Y791538 is a magnesian ureilite containing olivine and orthopyroxene. The primary goal of this study is to place chronological constraints on the formation of monomict ureilite. However, we would also like to examine the existence of $\varepsilon^{54}Cr$ anomaly presented earlier [5], which may be used as a tracer to investigate the precursor of the ureilite parent body.

Analytical procedure:

As an initial step, we have removed fragments weighing 8~18mg from each meteorite for Cr isotopic analyses (WR). While these fragments may not be representative of the whole rock sample in terms of Mn/Cr ratio and $\varepsilon^{53}Cr$, their $\varepsilon^{54}Cr$ (which do not change since their last equilibration) is expected to be representative. For ALH77257, we have further separated a second fragment weighing ~80mg for magnetic separation and leaching experiment. This fragment was coarsely ground and the magnetic fraction (~47%) was separated using a hand magnet. Both the magnetic (MG) and the non-magnetic fractions (NM) were further separated into two fractions, one of which was dissolved using $HF+HNO_3$ without further treatment (-B), and the other leached with 0.1N HCl prior to $HF+HNO_3$ dissolution (-R).

Our analytical procedure for Cr isotope is broadly similar to that of Lugmair and Shukolyukov [6], and has already been described in some detail [5]. In order to eliminate the effect of residual mass fractionation, we have made a large number of repeated measurements for WR samples (>40 sets of 300 ratios). For the leaching experiment, the number of repeated measurements is much smaller, and we have so far analyzed the Cr isotopic ratios for ALH77257 NM-B and NM-R.

Results and discussion:

The results for the three WR samples are shown in Fig. 1. The results show that the $\varepsilon^{53}Cr$ values of these ureilites vary from 0.04 to 0.29, and $\varepsilon^{54}Cr$ values from -0.73 to -1.16. There is a clear correlation between the $\varepsilon^{53}Cr$ and $\varepsilon^{54}Cr$ values and the slope of the correlation is similar to that of the line defined by the repeated measurements of the terrestrial standards (broken line in Figure 1). When the $\varepsilon^{53}Cr$ values are plotted on an isochron diagram, the data show a scatter without defining an isochron (Fig. 2).

The variation in the $\varepsilon^{53}Cr$ and $\varepsilon^{54}Cr$ values may indicate that (1) these samples are derived from isotopically distinct reservoirs, or (2) despite the relatively large number of repeated measurements made, the effect of residual mass fractionation still remains. At this point, it is difficult to distinguish between the two possibilities and further repeated analyses are required. However, if we assume that this scatter is a result of residual mass fractionation effect, we can correct for this by applying a second order fractionation correction using $^{54}Cr/^{52}Cr$ ratio as suggested by Lugmair and Shukolyukov [6]. There is, however, a problem in that we are unable to assume that the $^{54}Cr/^{52}Cr$ ratios of these samples are normal, or similar to that of the terrestrial standard. To overcome this problem, we have estimated the $\varepsilon^{54}Cr$ value of the ureilite parent body (assuming that they are from isotopically homogeneous reservoir) by taking the average of all the $\varepsilon^{54}Cr$ values determined from the three WR samples. Our current best estimate for such ureilite parent body is $\varepsilon^{54}Cr = -0.93 +/- 0.23$. Using this value, we can then apply a second order fractionation correction to calculate the corrected $\varepsilon^{53}Cr$ values ($\varepsilon^{53}Cr$-normalized). When the $\varepsilon^{53}Cr$-normalized values are plotted on an isochron diagram, the WR ureilites defines a linear trend with a slope of nearly zero (Fig. 3). This suggests that if the variation in the $\varepsilon^{54}Cr$ values is a result of residual mass fractionation effect, the ureilite parent body must have equilibrated after all the ^{53}Mn had decayed (i.e. >20 m.y. after the solar system formation).

We have taken a similar approach for the leached and untreated samples of the ALH 77257 NM fraction (ALH77257 NM-R and ALH77257 NM-B, respectively), and the results are also shown in Fig. 3. The smaller number of repeated measurements for these samples makes the scatter of the data somewhat larger, but both of these data plot on a line defined by the WR samples ($\varepsilon^{53}Cr$-normalized = +0.16), suggesting that the

Mn-Cr system for these samples may have also reached equilibrium after ^{53}Mn had decayed. This result disagrees with the recent Mn-Cr and Al-Mg studies [2, 3], as well as the U-Pb age of MET78008 (4.563 +/- 0.006 Ga [4]). However, we feel that additional data, in particular, the internal isochron data using pure mineral separates, are required to fully address this issue. It is also noteworthy that the Mn-Cr ratio of the leached and the untreated fractions are similar, implying that the Mn/Cr ratio of the NM fraction has not been disturbed by the event(s) that formed HCl soluble phase(s).

Perhaps the most interesting finding of this study is the discovery of ε^{54}Cr deficit in all ureilite samples analyzed so far. The current result strongly support our earlier data [5]. At first glance, the negative ε^{54}Cr values of the ureilites may indicate that the precursor(s) of the ureilite parent body was isotopically distinct from those of carbonaceous chondrites (with positive ε^{54}Cr) and Earth (ε^{54}Cr = 0). However, it has been shown by Rotaru [7] that carbonaceous chondrites, with bulk ε^{54}Cr > 0, are actually a mixture of phases with both positive and negative ε^{54}Cr values. In particular, CI and CM chondrites contain phases with extreme deficit in ε^{54}Cr. Thus, preferential melting of these phases relative to the high ε^{54}Cr phases may produce melts with ε^{54}Cr deficit. If such melts were somehow incorporated into the ureilite parent body, it may be possible to produce the Cr isotopic signatures of the ureilite parent body from the CI and/or CM chondrite-like precursor. Clearly, further Cr isotopic investigations of these meteorites are necessary to address this issue.

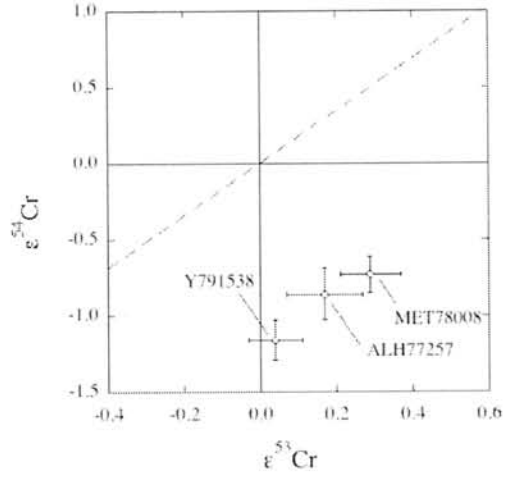

Fig. 1 Results of the Cr isotopic analyses of the whole rock (WR) ureilite samples plotted on an ε^{53}Cr versus ε^{54}Cr diagram. Shown in broken like is a linear trend defined by repeated measurements of terrestrial standards.

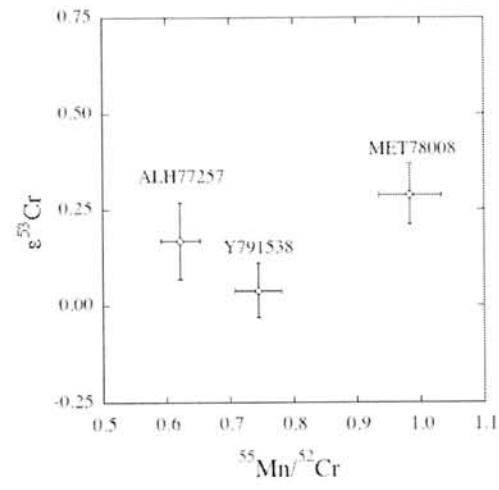

Fig. 2 The Cr isotopic results of the whole rock samples without the application of second order fractionation correction.

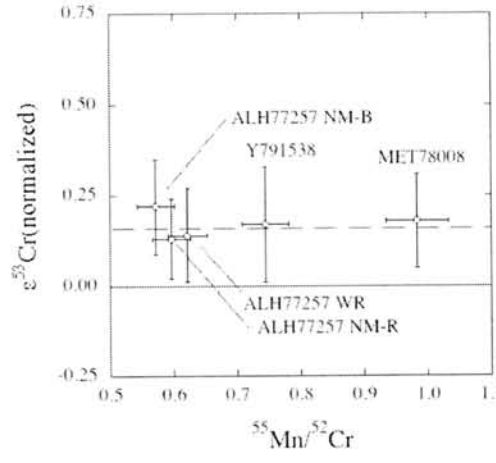

Fig. 3 ε^{53}Cr values normalized to ε^{54}Cr = -0.93.

Summary:

We have undertaken a detailed Cr isotopic investigation of three ureilites ALH77257, Y791538 and MET78008. The WR fractions of all three samples, as well as the leached and untreated non-magnetic fractions of ALH77257, show deficit in ε^{54}Cr. When normalized to our current best estimate of ε^{54}Cr = -0.93, the ε^{53}Cr values of all samples analyzed so far plots on a line of ε^{53}Cr = ~+0.16, regardless of their Mn/Cr ratio.

References:

[1] Clayton R. N. and Mayeda T. K. (1988) *GCA, 52,* 1313-1318. [2] Goodrich C. A. et al. (2002) *MAPS, 37,* A54. [3] Kita N. et al. (2003) *LPS XXXIV,* #1557. [4] Torigoye-Kita N. et al. (1995), *GCA*, 59, 2319-2329. [5] Yamashita K. et al. (2005) Antarctic Meteorites *XXIX*, 100-101. [6] Lugmair, G.W. and Shukolyukov A. (1998) *GCA, 62,* 2863–2886. [7] Rotaru et al. (1992) Nature, 358, 465-470.

Application of X-ray computed micro-tomography (μCT) to the observation of chondrite chips. M. Uesugi and K. Uesugi, Japan Synchrotron Radiation Research Institute (JASRI) 1-1-1 Kouto, Sayo-cho, Sayo-gun, Hyogo 679-5198, Japan.

Introduction:

Three-dimensional observation of meteorites provides us important information, such as true radii of chondrule and iron grain, and mutual structure of them. However, the method of observation and analysis are less constructed compared to those of two-dimensional observations. X-ray computed tomography (CT) method can provide a means to quantify the three-dimensional structure. This method has several advantages than other method, such as freeze-thaw disaggregation method. At first, generally, the matrixes, chondrules and iron grains have largely different value of X-ray linear attenuation coefficient (LAC), mainly originate from their Fe contents. So we can easily separate them using image-processing schemes. Secondly, we obtain three-dimensional internal information of the meteorites that is fully digitized. And also, this method is essentially non-destructive method. We can re-examine the result of X-ray CT measurement by making thin sections of the meteorites, or use samples for another studies, such as mass spectrometric analysis.

Tsuchiyama et al. [1] shows the observation of Kobe meteorite chip with X-ray μCT. They also noticed that the possibility of three-dimensional curation of meteorite samples. Recently, some authors observed iron grains in meteorites using X-ray CT [2-5]. However, because of the limitation of CT analysis that mainly based on the low signal to noise (S/N) ratio and lack of spatial resolution, small objects around a few tens μm, especially chondrules in meteorite chips, were not well identified in those studies.

X-ray μCT in SPring-8 (SP-μCT) achieved high spatial resolution, which has pixel size 3.14 μm x 3.14 μm for 4 mm x 3 mm Field of View, and 0.2 μm x 0.2 μm for 400 μm x 260 μm Field of View. Here, we show an example for the observation of chondrite chip using SP-μCT, and application for the observation of compound chondrules in meteorites.

Method:

A meteorite chip Y-791717 (CO3) was measured by SP-μCT, whose size is 2 mm x 3 mm x 1 mm. The meteorite chip is fixed on the rotation stage. Number of projections are 5000 in a half rotation of sample stage. X-ray energy is 35 keV in this experiment, and exposure time is 3 seconds for a projection from each rotational angle. Obtained projection images are reconstructed into CT images by Convolution-BackProjection (CBP) method with Chesler filter. Format of the obtained CT images is 1344x1344 and the number of slices is 670. Pixel size of all directions is 3.14 μm. Five-sets of the CT images are reconstructed from the projection images. The CT images, called set A, are reconstructed using only 500 projections in a half rotation of the stage. In the same way, set B, C, D and E are reconstructed using 1000, 1666, 2500 and 5000 projection data, respectively.

We used a program series called "Slice" developed at SPring-8, for identifying the structure of meteorite chip. Figure 1 shows one of the images obtained by the "Slice" using set E data.

Results:

As shown in Fig. 1, we could identify the chondrules, which appear as black globules in the images, even for those have small radii (~30 μm) and not have iron rims. The S/N ratio is significantly increased with increasing of the projection number. Thus, we obtained highest quality of the S/N ratio for spatial and density by data set E (see Fig. 3).

Using data set E, we found some compound chondrules in the meteorite chip. Though they have low difference of LAC value between the constituent chondrules, we could identify the boundary for some of them. Figure 2 shows a compound chondrule that composed of a primary chondrule that has high LAC and secondary chondrule that has lower LAC value than primary stuck on the surface of the primary chondrule. Though the primary chondrule has nearly same range of the LAC value to that of matrixes, the chondrule could be clearly identified.

Uesugi et al. [6] showed that about 50% of compound chondrules in CV3 chondrite shows that the primary chondrule has lower liquidus temperature than that of secondary chondrule. It is highly unlikely that the constituent chondrules of those compounds are formed in a same heating event. There are two possibilities for the origin; very small scale of the heating event of chondrule formation and very rapid cooling after the heating.

The compound chondrule in Fig. 2 shows that the secondary chondrule is much smaller than primary. And also, if the difference of LAC value of the compound originates from the difference of their Fe contents, their liquidus temperature would also be different, i.e. the primary chondrule has lower liquidus temperature than secondary. So, secondary chondrule should solidify prior to primary chondrule, if they were formed in a same heating event with rapid cooling. This is clearly inconsistent with the formation of compound chondrule, and thus the compound might indicate the chondrules were formed in heating events with very small scale. We will report the chemical composition analysis of this compound chondrule.

Thus, our experiment shows that CT imaging by SP-μCT with proper number of the projection (Fig. 3) provides us effective way of the three-dimensional observation of meteorites.

References:

[1] Tsuchiyama A. et al., (2002) *Geochemical Journal.*, *36*, 369-390. [2] Kuebler K. E. et al., (1999) *Icarus.*, *141*, 96-106. [3] Netteles J. W. and McSween Jr H. Y. (2004) *LPS XXXV*, 2004-2005. [4] Netteles J. W. and McSween Jr H. Y. (2005) *LPS XXXVI*, 2018-2019. [5] Netteles J. W. and McSween Jr H. Y. (2006) *LPS XXXVII*, 1996-1997. [1] Uesugi M. et al., (2005) *Antarctic Meteorites XXIX*, 90-91.

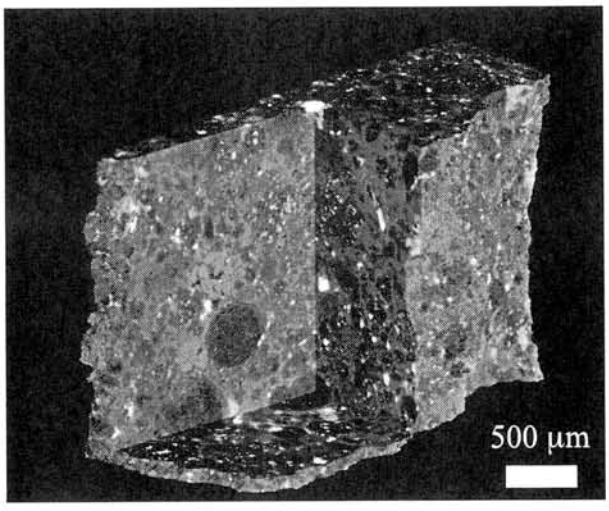

Fig. 1 A bird-eye view of Y-791717 (CO3) meteorite chip. White globules in the figure are metallic iron grains, and dark spherical objects are chondrules.

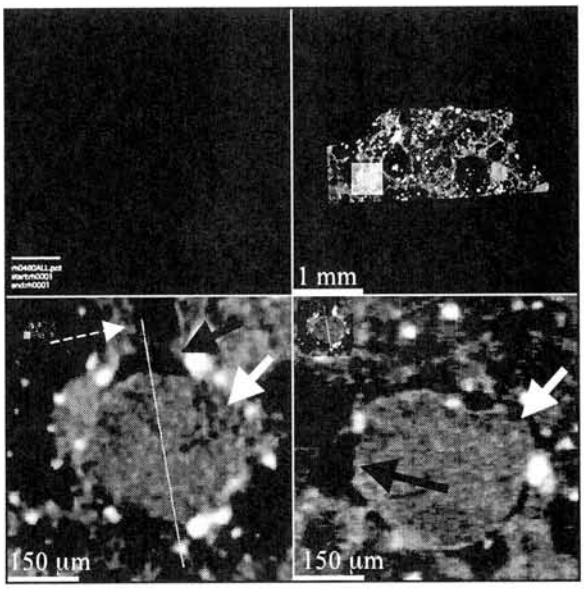

Fig. 2 Images of a compound chondrule in Y-791717. Upper right: View of a slice of the chip. Lower left: An enlarged view of the white square in upper right part of the image. A gray spherical object is primary chondrule (white arrow) and dark object attached on the surface of the chondrule is secondary chondrule (black arrow) that has lower Fe contents than primary chondrule. Lower right: A cross sectional view of the chondrule that appears in the lower left of the image. The line of the cross section is shown as the white line and direction of cross section is shown by a dotted arrow.

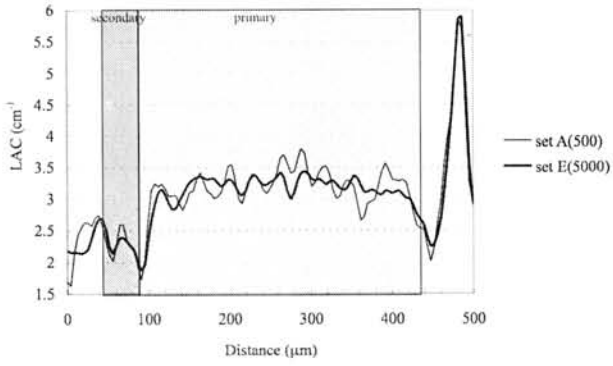

Fig. 3 Line profiles of LAC value along the white line shown in lower left image of Fig. 2. Solid line shows for the case of data set A (with 500 projections) and bold line shows for the case of data set E (with 5000 projections). Light gray zone in figure shows the LAC profile for the primary chondrule and dark gray zone shows the LAC profile for the secondary chondrule. This plot shows that the data set E has planer profile inside of the primary chondrule, and then easy to identify the outer boundary of the chondrule.

Thermal history of highly metamorphosed eucrites and basaltic clasts in mesosiderites: A comparison. A. Yamaguchi[1,2], M. Tamaki[1,2], H. Kaiden[1,2], K. Misawa[1,2], and M. Ebihara[1,3]. [1]Antarctic Meteorite Research Center, National Institute of Polar Research, Tokyo 173-8515, [2]Department of Polar Science, School of Multidisciplinary Science, Graduate University for Advanced Studies, Tokyo 173-8515. [3]Department of Chemistry, Tokyo Metropolitan University, Hachioji, Tokyo 192-0397.

Introduction:

The howardites, eucrites, and diogenites (HEDs) are a suite of achondrites, formed by extensive melting on a parent body ~4.56 Ga ago [1]. The parent body is tentatively assigned to a large asteroid, 4Vesta. Mesosiderites are mixtures of silicates and FeNi metals. The silicate portions are broadly similar to HEDs. The FeNi metals are inferred to be derived from core materials. Thus, mesosiderites are products of impact mixing of crustal and core materials. The HEDs and mesosiderites have O-isotopic compositions similar to one another, indicating the formation of similar regions in the solar system [2,3].

Whether mesosiderites and HEDs were derived from the same parent body has been a subject of debate. Complicated igneous processes inferred from the bulk compositions of mesosiderite silicate clasts suggest that they are originated from a different parent body from the HED parent body (HPB) [4]. One of the complications is that mesosiderite silicate clasts are strongly metamorphosed rocks, and some of the clasts experienced partial melting, which might have changed the compositions and mineralogy of mesosiderite silicates [5,6].

Basaltic eucrites were metamorphosed in a varying degree (e.g., type 1-6) [7]. Eucrites with the highest metamorphic degrees could have experienced partial melting during thermal metamorphism [8,9]. The partial melting events may have been related to impact cratering events into hot crust as early as ~4.5 Ga [9]. These events may be related to the formation of metal silicate mixing [10]. Thus, detailed petrologic comparison between two meteorite groups is necessary.

We performed a mineralogical and geochemical comparison between the highly metamorphosed basaltic eucrites (HMEs) (EET90020 and Y-86763) and basaltic clasts in the Mt. Padbury mesosiderite and other poblished data. We particularly focused on the textural and mineralogical changes caused by thermal metamorphism.

Petrologic comparison

HMEs (EET90020 and Y-86763) and the basaltic clast in Mt. Padbury are composed of pigeonite, plagioclase, and minor minerals such as tridymite, Ca-phosphates, ilmenite, Ti-rich spinel, troilite, Fe-metal, and/or zircon [8-12]. EET90020 is a recrystallized breccia composed of coarse-grained subophitic portion and fine granulitic portion. Y-86763 has a subophitic texture resembling EET90020. Although recrystallized, the basaltic clast in Mt. Padbury shows a relict basaltic texture, similar to that in Ibitira [13].

In these meteorites, pyroxene is pigeonite having fine (several μm thick) exsolution (001) lamellae with homogeneous distribution. This pyroxene is similar to those in type 5 eucrites [7]. The pyroxene in these meteorites is not inverted into orthopyroxene. Chemical compositions of the pyroxene and plagioclase are within those of typical basaltic eucrites [1,7]. Compositional variations of the plagioclase are narrower, compared to types 1-6 basaltic eucrites.

These meteorites lack mesostasis portions, which are typically observed in basaltic eucrites. In basaltic eucrites, mesostasis is composed of very fine-grained or glassy phases, and occurs interstitially between pyroxene and plagioclase [7]. In the HMEs and basaltic clasts in mesosiderites, the minerals which typically occur in mesostasis (e.g., Ti-rich phases and silica minerals) scattered heterogeneously. Ti-rich spinels are often associated with ilmenite, in some cases forming a euhedral to subhedral shapes, suggesting that they are decomposed products from ulvöspinel [15]. Spinels have Ti-Cr trend commonly observed in metamorphosed eucrites [14]. Silica phases occur as tridymite, and are also distributed heterogeneously, in some cases, forming lath shapes. In EET90020, there are large massive grains up to a few mm. Ca-phosphates are observed, but not always associated with tridymite. These Ca-phosphates have lower REE abundances compared to those of eucrites [8,9], which are attributed to remobilization of the REE from Ca-phosphates to the REE-poor silicates [8,9].

Thermal history

The textures and compositions of pyroxene and metamorphic minerals (e.g., tridymite, Ca-phosphates, Ti-rich chromite and ulvöspinel) in HMEs and basaltic clast in Mt. Padbury are very similar. The similar mineralogy suggests that these meteorites experienced high temperature metamorphism.

Yamaguchi and Mikouchi [16] performed melting experiments of an unbrecciated basaltic eucrite near the solidus (~1050°C). The partial melts are enriched in P, Ti with high Fe# due to the melting of silica phases, Ca-phosphate, ilmenite, and probably the rims of pyroxenes. Thus, ulvöspinel and Ca-phosphates observed in the HMEs and

basaltic clasts in Mt. Padbury [8] and Vaca Muerta [6] were likely crystallized from such partial melts.

However, those metamorphic minerals are not always associated with one another. For example, Ti-rich spinels occur as large grains, in some cases enclosing surrounding minerals (e.g., in EET90020) [9]. These facts do not argue against the presence of partial melt. The distribution of these minerals depend on the locations of nucleation sites, and coarsened with presence of small amounts of partial melts, as proposed for the origin of heterogeneous mineral distribution in primitive achondrites [17]. In spite of evidence of partial melting (melting of mesostasis) and crystallization of the metamorphic minerals, textures of pyroxene and plagioclase are roughly preserved. The melting is limited in a small degree.

Plagioclases in the HMEs and basaltic clast in Mt. Padbury have the limited chemical variations, compared to type 1-5 basaltic eucrites. The equilibration of plagioclase seems unlikely because of extremely slow diffusion rates of Na in plagioclase. The limited variation could be due to partial homogenization during high temperature metamorphism. It is also possible that Na-rich rims were melted and lost during partial melting events.

These lines of evidence suggest that HMEs and basaltic clast in Mt. Padbury experienced high temperature metamorphism near the solidus (~1060°C) and relatively rapid cooling to preserve pigeonite phase. The question is whether similar thermal histories are coincidental.

The peak metamorphic temperatures of eucrites are typically less than ~1060°C. Metamorphic degrees of basaltic eucrites, EET90020 and Y-86763 rank among the highest. In contrast, the metamorphic degree of the basaltic clast in Mt. Padbury could be the lowest among mesosiderites. Mesosiderites were typically metamorphosed at 800-1200 °C, with the highest one which experienced large degrees of melting [e.g., 5]. Thus, silicate clasts in mesosiderites more extensively altered by heating events. It is possible that theses thermal histories can be explained by different sites of large impact craters formed by metallic projectiles.

Rubin and Mittlefehldt [4] suggested that some gabbroic and basaltic clasts (polygenic basalts) in mesosiderites experienced multi-stage igneous history to account for the anomalous bulk chemistry characterized by positive Eu anomaly and La/Lu ratios <1. They suggested that these rocks were formed by remelting of a mixed basalt-cumulate gabbro-metal source region near the parent body surface. Impact is not effective heat source for large-scale melting on asteroids, but impacts on a hot crust would have caused remelting effectively. Thermal metamorphism, partial melting, mobilization of partial melt, crystallization of metamorphic minerals caused by impact events may have changed the mineralogy and bulk compositions.

Implication

Thermal history of mesosiderites may have varied considering the diversity in sizes and temperatures of the components in metal-rich and metal-poor regions after metal-silicate mixing. The degrees of metamorphism and siderophile contamination could have been varied considerably. Thus, some silicate clasts in mesosiderites may be indistinguishable from eucrites. Therefore, it is possible that both eucrites and mesosiderites were derived from the same parent body. They came from different sites in impact craters on HPB. Recent high precision O-isotopic analyses support this idea [3].

Two other eucrite-like basalts, NWA011 [19] and Ibitira [20] with distinct O-isotopic compositions have similar thermal history to that of HMEs and basaltic clasts in mesosiderites [6,12]. These eucrite-like basalts could have experienced partial melting by heating during metamorphism [20,21,22]. It is suggested that these eucrites were formed by large impacts into hot primary crust of the parent bodies. As suggested for the petrologic origin of some primitive achondrites [17], impacts event on asteroids heated internally may have been common processes in the early solar system.

References:

[1] Takeda H. (1997) MAPS 32, 841-853. [2] Clayton R.N. and Mayeda T.K. (1996) GCA 60, 1999-2017. [3] Greenwood R.C. (2006) LPSC 37, #1768. [4] Rubin A.E. and Mittlefehldt D.W. (1992) GCA 56, 827-840. [5] Delaney J.S. et al. (1981) PLPSC 12B, 1315-1342. [6] Wadhwa M. et al. (2003) GCA 24, 5047-5069. [7] Takeda H. and Graham A.L. (1991) Meteoritics 26, 129-134. [8] Floss C. et al. (2000) AMR 13, 222-237. [9] Yamaguchi A. et al. (2001) GCA 65, 3577-3599. [10] Yamaguchi A. et al. (2006) MAPS, in press. [11] Yamaguchi A. et al. (1997) AMR 10, 431-453. [12] Tamaki M. et al. (2006) MAPS, submitted. [13] Steele I.M. and Smith J.V. (1976) EPSL 33, 67-78. [14] Yamaguchi A. (2000) MAPS 35, A174. [15] El Goresy A. and Ramdohr P. (1975) PLPSC 6, 729-745. [16] Yamaguchi A. and Mikouchi T. (2005) LPSC. [17] Takeda H. et al. (1994) Meteoritics 29, 830-842. [18] Yamaguchi A. et al. (1996) Icarus 124, 97-112. [19] Yamaguchi A. et al. (2002) Science 296, 334-336. [20] Mittlefehldt D.W. (2005) MAPS 40, 665-677. [21] Yamaguchi A. et al. (1996) LPSC 27. 1469. [22] Floss C. et al. (2005) MAPS 40, 343-360.

Noble gases in the Moorabie L3 chondrite: comparison with sub-Q gas in the enstatite chondrites. Yukio Yamamoto and Keisuke Nagao, Laboratory for Earthquake Chemistry, Graduate School of Science, University of Tokyo, 7-3-1 Hongo, Bunkyo-ku, Tokyo 113-0033, Japan.

Introduction:

Primordial noble gases, which were incorporated into meteorites during their formation, include mainly three components: exotic, Q, and subsolar (Ar-rich) noble gases. In addition to these components, there are many minor components of primordial noble gases such as sub-Q gas [1]. This component is found in solar-gas-free EH3 chondrites [1]. Sub-Q gas has low $^{36}Ar/^{132}Xe$ (37.0 ± 18.0 [1]) ratio relative to Q gas (76.2 [2]). This component is thought to originate from fractionated Q gas [1].

Moorabie chondrite is closely related to reduced L chondrite on the basis of the texture of chondrules and siderophile abundance pattern [3]. The texture and the distribution of olivine and low-Ca pyroxene compositions indicate that this chondrite is classified to 3.8 types [4]. On the other hand, TL sensitivity indicates type 3.5 [3].

In this study, sub-Q like noble gas was found in the Moorabie L3 chondrite. We discuss about noble gas signatures of this chondrite and make comparison with sub-Q gas in the EH3 chondrites.

Experimental Method:

A 0.1357 g of Moorabie was prepared for stepwise heating analysis. Noble gases were extracted at ten temperature steps of 400, 600, 800, 1000, 1100, 1200, 1300, 1400, 1600, and 1800 °C for 30 minutes each. The concentrations and isotopic compositions of the noble gases were determined with a mass spectrometer (modified MM5400, MS-II) at University of Tokyo. The configurations of noble gases analyses are described in Park et al. (2003) in detail [5].

Results and Discussion:

Noble gas concentrations and isotopic ratios in Moorabie L3 chondrite are given in Table 1. Figs. 1 and 2 show the xenon three-isotope diagram and elemental ratios, respectively. The noble gases released at 400 °C may contain some atmospheric noble gases in respect of both the xenon isotopic composition (Fig. 1) and the elemental ratios (Fig. 2). The noble gases released at 1800 °C are large contribution of blank because of low concentration of noble gases. For the reason mentioned above, the noble gases released at the both 400 °C and 1800 °C are not taken into consideration below. Helium and neon isotopic compositions are close to those of cosmogenic components through the all temperature steps, suggesting that large parts of helium and neon in this chondrite are dominated by cosmogenic component. Xenon isotope compositions obtained by stepwise heating analyses shows that noble gases in Moorabie chondrite are same isotopic composition of Q gas (Fig. 1). Krypton isotope compositions also show that almost all of krypton is Q gas.

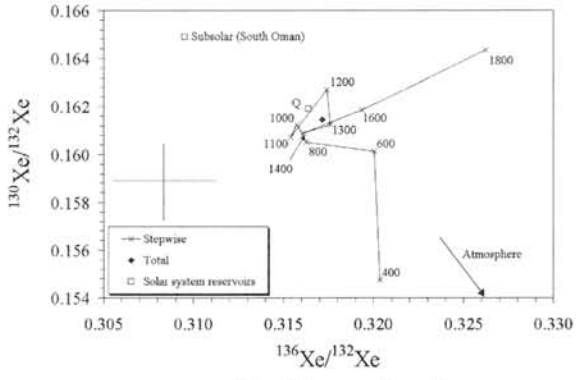

Fig. 1. The change of $^{136}Xe/^{132}Xe$ vs. $^{130}Xe/^{132}Xe$ ratios of Moorabie L3 chondrite during stepwise heating analysis. Numerals near the points are temperature in °C. The typical error is shown in left side of the figure. The elemental ratios of Q gas and subsolar are from Busemann et al. (2000) [2] and Crabb and Anders (1981) [9], respectively.

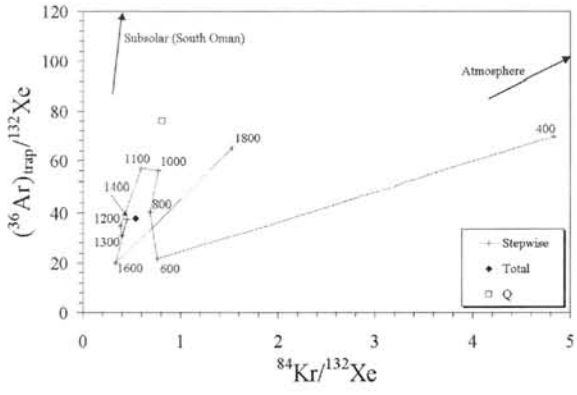

Fig. 2. The change of $^{36}Ar/^{132}Xe$ and $^{84}Kr/^{132}Xe$ ratios of Moorabie L3 chondrite during stepwise heating. Numerals near the points are temperature in °C. The elemental ratios of Q gas and subsolar are from Busemann et al. (2000) [2] and Crabb and Anders (1981) [9], respectively.

The concentrations of cosmogenic ^3He (^3He_c), ^{21}Ne ($^{21}Ne_c$) and ^{36}Ar ($^{36}Ar_c$) are calculated based on the isotopic ratios (Table 1). In this calculation, these ratios were used for cosmogenic (c) and trapped (t) components: $(^3He/^4He)_c$=0.192, $(^3He/^4He)_t$ =1.43×10^{-4}, $(^{21}Ne/^{22}Ne)_c$=0.9, $(^{21}Ne/^{22}Ne)_t$=0.024. Cosmic ray exposure ages are calculated from concentrations of cosmogenic component obtained above with formulae given by Eugster (1988) [6] for T_3 and T_{21} and Marti and Graf (1992) for T_{38}. $(^{22}Ne/^{21}Ne)_c$ (1.11) is used for the shielding parameter. We assumed that this meteorite was exposed to cosmic rays with 4π geometry and with

an average shielding. Derived exposure ages are given in Table 2. The short cosmic-ray exposure age calculated from ^{3}He is explained by diffusive loss of cosmogenic ^{3}He probably due to solar heating during transit to earth. The majority of L-chondrite exposure ages are >10 Ma [7]. Therefore, the cosmic ray exposure age of Moorabie chondrite is relatively short among the L chondrites.

^{40}K-^{40}Ar age is estimated to 0.93 Ga by the ^{40}Ar concentration and potassium content (0.085 wt % [3]). This is shorter age than typical age of L chondrite (1-4 Ga [8]).

The elemental ratios of noble gases in the Moorabie L3 chondrite differ from those of Q gas. The change of elemental ratios of noble gases released by stepwise heating is shown in Fig. 2. For the same reason mentioned above, the noble gases released at the both 400 °C and 1800 °C are not taken into account below. The $(^{36}Ar)_{trap}/^{132}Xe$ ratio of total noble gas released from this chondrite is 37.8 and the lowest ratio is 20.0 at 1600 °C (Fig. 2). In the all temperature steps, except 1000 °C and 1100 °C, the $(^{36}Ar)_{trap}/^{132}Xe$ ratios are in the range of sub-Q gas [2]. The noble gases released at the temperature except 1000 °C and 1100 °C are dominated by sub-Q gas in respect of the $(^{36}Ar)_{trap}/^{132}Xe$ ratio. On the other hand, the noble gases released at the temperature of 1000 °C and 1100 °C are dominated by Q gas. The sub-Q gas in KLE98300 EH3 chondrite is released over 900 °C [10]. The release temperature of sub-Q gas of the Moorabie L3 chondrite is consistent with that of the KLE98300 EH3 chondrite except the temperature of 1000 °C and 1100 °C. The exception at 1000 °C and 1100 °C could be caused by dominant release of Q gas at these temperatures. These results suggest that this chondrite would has trapped noble gases mixture of Q gas and sub-Q gas.

Summary:

Noble gases in Moorabie ordinary chondrite were measured. This chondrite has short cosmic ray exposure ages and ^{40}K-^{40}Ar age relative to other L chondrites. Helium and neon in this chondrite is dominated by cosmogenic component in spite of its short exposure ages. Krypton and Xenon isotopic compositions are almost same as those of Q gas. This chondrite could has trapped noble gases mixture of Q gas and low $(^{36}Ar)_{trap}/^{132}Xe$ gases as sub-Q gas in EH3 chondrites.

References:

[1] Patzer A. and Shultz L. (2002) *Geochim. Cosmochim. Acta, 37,* 601-612. [2] Busemann H. et al. (2000) *Meteorit. Planet. Sci., 35,* 949-973. [3] Sears D. W. et al. (1990) *Meteoritics, 25,* 407-408. [4] Wasson J. T., Rubin A. E. and Kallemeyn G. W. (1993) *Geochim. Cosmochim. Acta, 57,* 1867-1878. [5] Park J. et al. (2003) *Geochem. J., 37,* 639-648. [6] Eugster O. (1988) *Geochim. Cosmochim. Acta, 52,* 1649-1662. [7] Marti K. and Graf T. (1992) *Annu. Rev. Earth Planet. Sci., 20,* 221-243. [8]Kirsten T., Krankowsky D. and Zähringer J. (1963) *Geochim. Cosmochim. Acta, 27,* 13-42. [9] Crabb J. and Anders E. (1981) *Geochim. Cosmochim. Acta, 45,* 2443-2464. [10] Nakashima D. et al. (2006) *LPS XXXVII,* Abstract #1119.

Table 1. Concentrations and isotopic compositions of total noble gases in the Moorabie L3 chondrite.

^{4}He	^{3}He/^{4}He	^{20}Ne	^{20}Ne/^{22}Ne	^{21}Ne/^{22}Ne	^{36}Ar	^{38}Ar/^{36}Ar	^{40}Ar/^{36}Ar	^{84}Kr	^{132}Xe
1875	0.0617 ±0.0018	24.6	0.837 ±0.017	0.900 ±0.019	34.4	0.2707 ±0.0040	109.9 ± 1.8	461	853

Concentrations of ^{4}He, ^{20}Ne and ^{36}Ar are given in 10^{-9} cm^{3}STP/g.
^{84}Kr and ^{132}Xe concentrations are given in 10^{-12} cm^{3}STP/g.

Table 2. Concentrations of cosmogenic ^{3}He, ^{21}Ne and ^{38}Ar, production rates, and cosmic ray exposure ages of Moorabie L3 chondrite.

$^{3}He_c$	$^{21}Ne_c$	$^{38}Ar_c$	P_3	P_{21}	P_{38}	T_3	T_{21}	T_{38}
10^{-8} cm^{3}STP/g			10^{-8} cm^{3}STP/g/Ma			Ma		
11.5	2.64	0.32	1.61	0.331	0.0423	7.2	8.0	7.7

PAIRING RELATIONSHIPS AMONG NORTHWEST AFRICAN BASALTIC LUNAR METEORITES BASED ON COMPOSITIONAL AND PETROGRAPHIC CHARACTERISTICS. R.A. Zeigler[1], R. L. Korotev[1], B. L. Jolliff[1], T. E. Bunch[2], and A. J. Irving[3], [1]Dept. Earth & Planetary Sciences, Washington University, Campus Box 1169, St. Louis, MO 63130 zeigler@levee.wustl.edu [2] Dept. of Geology, Northern Arizona University, Flagstaff, AZ 86011. [3]Dept. Earth & Space Sciences, University of Washington, Seattle, WA 98195.

Introduction:

In recent years, several "new" basaltic lunar meteorite stones have been collected in the deserts of Northwest Africa (NWA): NWA 2700, NWA 2727, NWA 2977, and NWA 3160. These stones consist of several different lithologies: a fragmental breccia of very low-Ti (VLT) basaltic material, a cumulate olivine gabbro, a porphyritic olivine basalt, and a coarse-grained ferrogabbro. Petrographic and preliminary geochemical results have been reported for these meteorites [1-2]. Here we discuss the chemical composition of the different lithologies within these aforementioned meteorite stones in more detail. We also examine the pairing relationships among these "new" stones, and compare them with previously studied basaltic lunar meteorites, particularly NWA 773 [3-4].

Methods:

We have obtained chemical compositions for numerous small subsamples (20-40 mg) of the various lithologies present in the different NWA basaltic meteorite stones by instrumental neutron activation analysis [for more detail see 5].

Petrography:

The four prominent lithologies in the "new" NWA meteorites are: (1) fragmental breccia of VLT basaltic material (present in NWA 2700, 2727, and 3160), (2) cumulate olivine gabbro (NWA 2700, 2727, and 2977), (3) porphyritic olivine basalt (NWA 2727 and 3160), and (4) ferrogabbro (NWA 2727). The breccia contains lithic clasts of the other lithologies, as well as abundant olivine and pyroxene clasts, lesser amounts of plagioclase clasts, and trace amounts of Fe,Ti,Cr oxides, silica, and glass clasts. Modally, the cumulate olivine gabbro consists of ~50% olivine, ~30-40% pyroxene, and 10-20% plagioclase. The ferrogabbro has a similar mineral assemblage and compositions as the cumulate, but a coarser grain size. The porphyritic basalt has phenocrysts of olivine and chromite, with a mesostasis of glass and skeletal olivine and pyroxene. The petrography of these meteorites is described in greater detail in [1,2].

Bulk Composition:

Due to the large clast size (relative to the size of our subsamples) of the various lithic components that make up these basaltic meteorites, we made no attempt to determine the bulk composition of each meteorite. Instead, we determined the composition of the individual lithologies that make up each meteorite (the ferrogabbro has not yet been analyzed; Fig. 1). The two igneous lithologies that have been analyzed, the cumulate and the basalt, have compositions typical of previously analyzed lunar basalts/gabbros. The paucity of Ti-bearing oxides indicates that the basalt (and all of the other lithologies as well) have low-Ti, and likely VLT composition. The fragmental breccia of VLT basaltic material has a bulk composition very close to that of the porphyritic olivine basalt, and is composed almost entirely of olivine and pyroxene clasts. A few subsamples of the breccia in NWA 3160 have abnormally high ITE concentrations. The cause of this is unclear at this time, but it is not the result of a heterogeneously mixed KREEP component. The composition that these points trend towards is much more Fe-rich than any known version of KREEP (Fig. 1). The "new" NWA basaltic meteorites are compositionally distinct from most previously studied lunar basalts, in having an enrichment in LREEs, depletion in Na_2O and Eu, and high Th/REE ratios.

Discussion:

Subsamples of all of the lithologies vary in composition, more so in the breccia and cumulate lithologies than in the basalt. The compositional variability among subsamples of a given lithology within a single stone is typically greater than the difference in the average composition of a given lithology between two different stones. The compositional variability we observe among subsamples of a given lithology is due to unrepresentative sampling of the constituent mineral phases, both for major and trace elements. This unrepresentative sampling is intentional and allows us approximate the composition and proportion of a lithology's constituent mineral or lithic components.

On the basis of the compositional similarities of lithologies shared among them, we conclude that the "new" lunar basaltic meteorite stones NWA 2700, 2727, 2977, and 3160 are paired with each other and with NWA 773. (A recently recovered and yet to be officially named NWA stone appears to be another pairing; it contains all four lithologies.)

All of the NWA basaltic meteorite stones in this study share several geochemical characteristics, very low Eu and Na_2O concentrations, LREE enrichment, high Th/REE ratio, that are uncommon in previously analyzed lunar basalts, and this may suggest a common source region for these meteorites, or even a petrogenetic relationship among them.

References:

[1] Zeigler R. A.. et al. (2006) *LPS XXXVII,* Abstract #1804. [2] Bunch T. E. et al. (2006) *LPS*

XXXVII, Abstract #1375. [3] Fagan T. J. et al. (2003) *MAPS* **38**: 529-554. [4] Jolliff B. L. et al. (2003) *GCA* **67**: 4857-4879. [5] Zeigler R. A.. et al. (2006) *MAPS* **40**: 1073-1102.

Acknowledgements:

This work was supported by NASA grant NNG04GG10G.

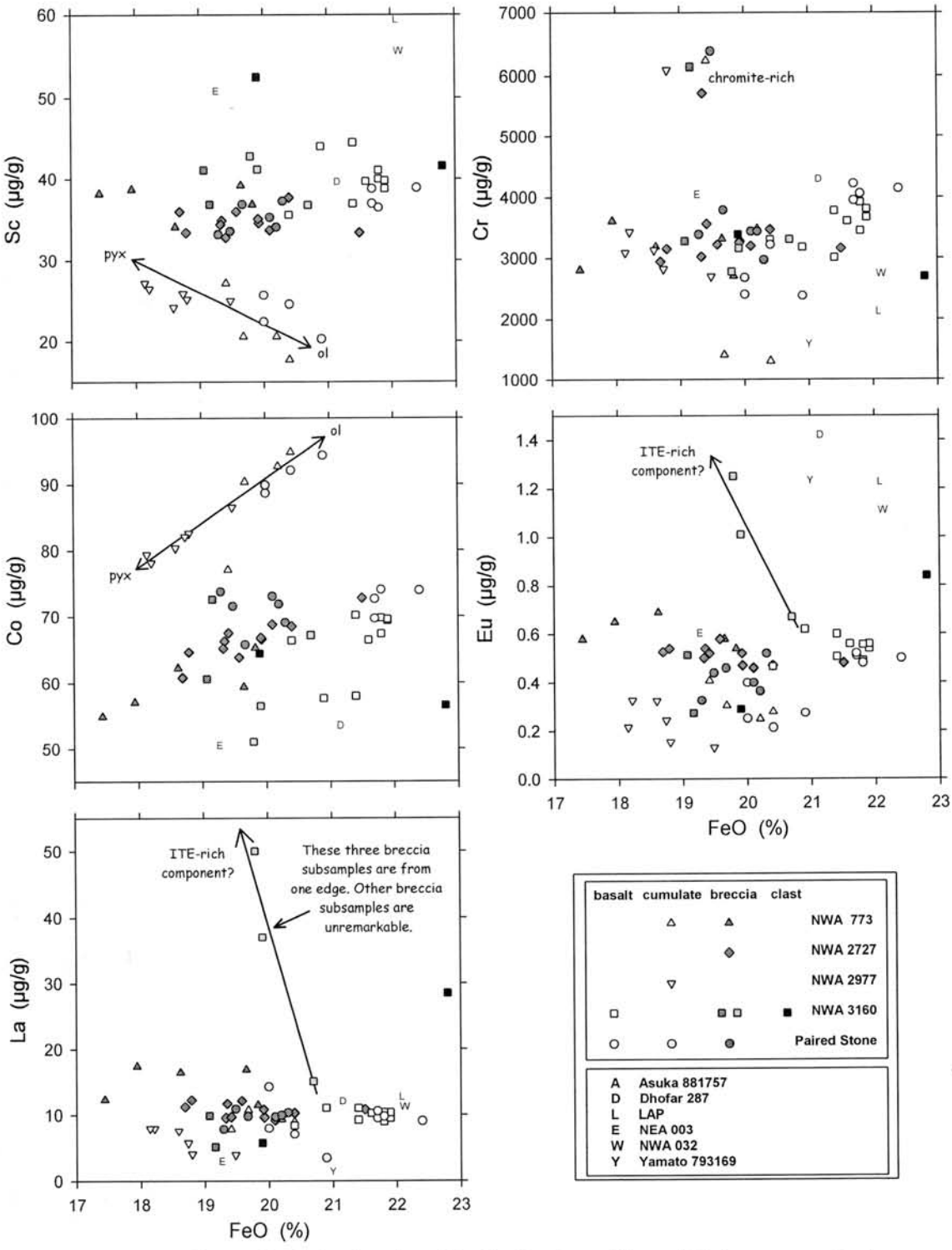

Figure 1: Two-element discrimination plots of Sc, Co, La, Cr, and Eu vs. FeO for many small subsamples of the "new" NWA basaltic meteorites in this work and NWA 773 [3-4]. Symbols are specific to both the NWA meteorite stone and the lithology. Also plotted are the average compositions of other basaltic lunar meteorites (data are unpublished analyses from this lab).

New views on diogenites from meteorites from hot and cold deserts. J. A. Barrat, Université de Bretagne Occidentale, Institut Universitaire Européen de la Mer, C.N.R.S-U.M.R. 6538, Place Nicolas Copernic, 29280 Plouzané Cedex, France.

Introduction

During the last ten years, the number of meteorites recovered from deserts have considerably increased. The vast majority of new samples are of course chondrites, but many achondrites have been identified, and allow a significant improvement of our knowledge of crustal building in small bodies. Howardites, eucrites and diogenites are such meteorites. They are believed to be derived from the same body, possibly the asteroid 4-Vesta [1]. Eucrites are basaltic or gabbroic lithologies and have been extensively studied. In the other hand, diogenites are orthopyroxenic cumulates that display generally a rather dull mineralogical composition. Furthermore they display very low abundances of incompatible trace elements, which are very sensitive to terrestrial weathering (especially in hot deserts). These rocks are difficult to analyze, and obtaining a crystallization age is still an analytical challenge using classical systematics (Rb/Sr, Sm/Nd, U/Pb, Lu/Hf). Consequently, they have generated far less geochemical studies than eucrites despite they comprise a significant portion of the crust of their parent body (e.g. [2]). In this presentation, I will summarize the available data on this type of meteorites, and show new results obtained mainly on recent finds from Sahara and Antarctica.

Do all the diogenites have crystallized at great depth?

Diogenites are generally breccias consisting of a mixture of strongly metamorphosed orthopyroxene debris and rock fragments. The vast majority of orthopyroxene and chromite crystals found in diogenites, have lost their initial zonings and are chemically homogeneous for major elements. Diogenites were typically seen as deep crustal cumulates excavated and exposed by large impacts (e.g. [3]).

Northwest Africa 4215 is a unique unbrecciated diogenite [4]. It consists chiefly of xenomorphic orthopyroxene grains on the order of 500 μm in size, with a few large chromite crystals (<5vol%, up to 3 mm). Orthopyroxenes (En76,2 to En68,6), olivines (Fo76 to Fo 71), chromites (Mg#=14.3-44.0, Cr#=42.2-86.5) are chemically zoned (figs 1 and 2). The minor element behavior in orthopyroxenes and the complex chemical profiles obtained in chromites indicate that the zonings do not mirror the evolution of the parental melt. They resulted more likely from reaction of the crystals with intercumulus melt. In order to preserve the observed zonings, NWA 4215 clearly cooled much faster than other diogenites. Indeed, the cooling rate determined from the diffusion of Cr in olivine abutting chromite is in the order of 10 to 50 °C/a. NWA 4215 formed certainly within a small and shallow intrusion. These observations demonstrate that occasionally, some diogenites have escaped the widespread thermal metamorphism of the 4-Vesta crust. These cumulates are not necessarily always deep crustal lithologies.

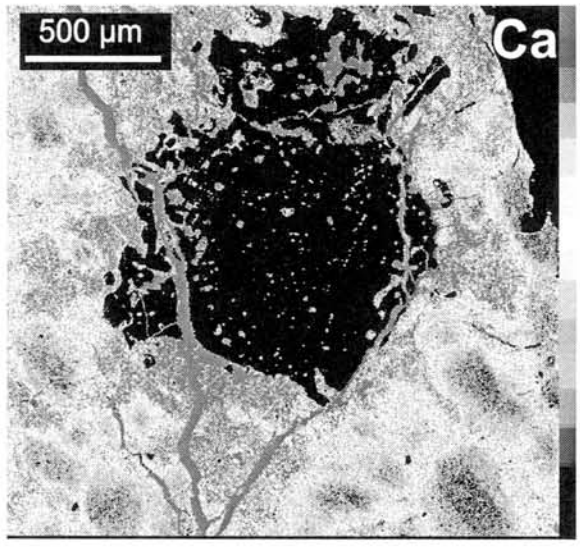

figure 1. Ca distribution map of a selected area of a polished section of NWA 4215. The large black crystal in the center is chromite. Note the zoned orthopyroxenes (blue to red) and the fractures filled with calcite.

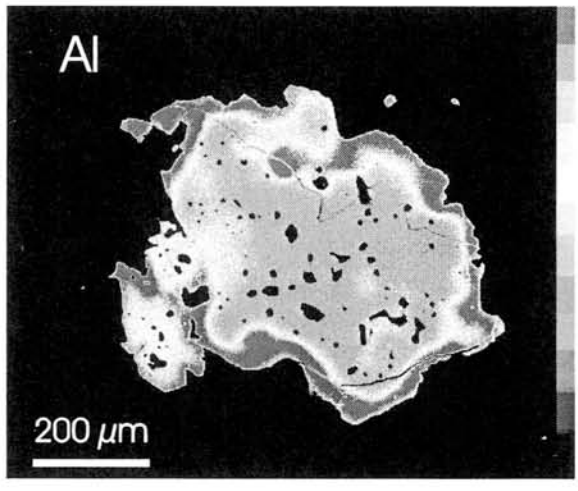

figure 2. Al distribution map of a chromite crystal in NWA 4215.

Geochemistry of diogenites and the compositions of their parental melts.

In contrast to their major element abundances

that mirror the composition of the orthopyroxenes, the minor and trace element abundances in diogenites display an impressive range, especially for the most incompatible elements (e.g. [5,6]). The major and trace elements of a series of diogenites have been analyzed (Bilanga, Johnstown, Tatahouine, NWA 4215, NWA 4272, LAP 02216, LAP 03569, LAP 03630, MET 00422, MET 00424, MET 00425, MET 00436, MIL 03368, EETA 79002, GRO 95555). Among the new diogenites from Antarctica, 5 different types can be distinguished:

-EETA 79002, LAP 02216, LAP 03630, MIL 03368 display the same kind of trace element abundances, and their REE patterns are remarkably similar. It can be inferred that they originated from the same magmatic system, or at least from very similar parental melts.

-LAP 03569 and MET 00422 exhibit incompatible trace element distributions that resemble EETA 79002 but with LREE depletions and Eu anomalies less pronounced.

-MET 00425 and MET 00436 display rather flat REE patterns with pronounced negative Eu anomalies. These diogenites are possibly linked to ALHA 77256 and the Yamato-B meteorites.

-GRO 95555 and MET 00424 are both unique. The analysis of MET 00424 has been extremely difficult. This sample displays extremely low abundances of incompatible trace elements close to the limits of my analytical procedure. It displays the most HREE enrichment measured in diogenites (fig. 3).

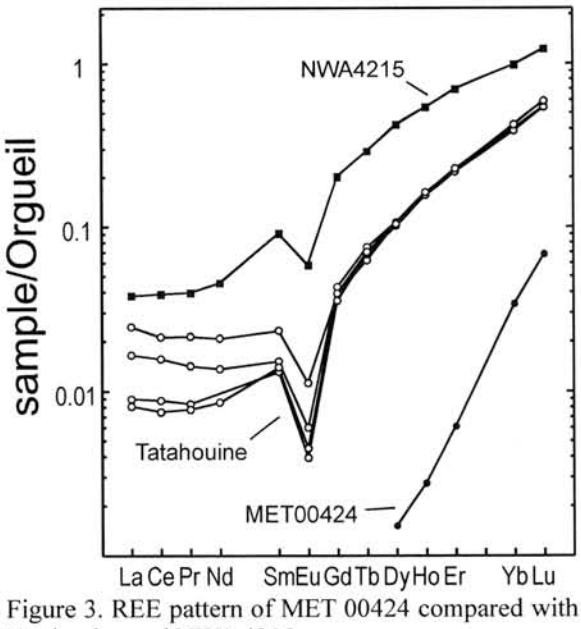

Figure 3. REE pattern of MET 00424 compared with Tatahouine and NWA 4215

It has been already emphasized that the HREE enrichment of diogenitic orthopyroxenes or diogenites is not significantly modified by fractional crystallization, by very low amounts of trapped melts, nor by terrestrial secondary processes. Hence, it is a useful parameter for constraining the genesis of diogenites [7]. The analyses obtained during the course of this study (fig. 4) confirm that diogenites formed from a variety of parental melts [2,6,7]. Some diogenites (e.g. NWA 4215, Tatahouine, MET 00424) crystallized from HREE enriched parental melts which have not yet been identified in the HED samples. More importantly, these samples suggest that the 4-Vesta magmatic activity was certainly far more complex than indicated by the eucrites alone. HREE-enriched melts can be produced by re-melting of a residual source [8] or more likely by melting of mafic cumulates [7]. In both cases, diogenites are possibly younger than eucrites.

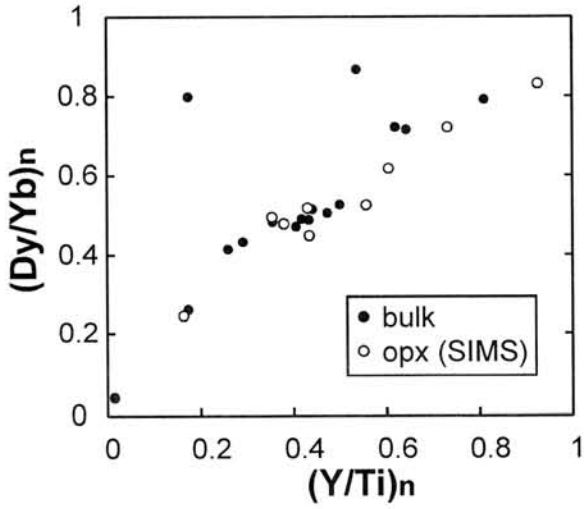

Figure 4. (Dy/Yb)n vs. (Y/Ti)n plot for diogenitic orthopyroxenes [6], and whole rocks (this study). It can be pointed out that Y/Ti ratios mirror the HREE ratios in most cases.

References:

[1] Drake M.J., *MAPS* **36**, 501-513 (2001) [2] Mittlefehldt D.W. et al. *Rev. Miner.* **36**, 4, 1-195 (1998) [3] Takeda H., *Icarus* **40**, 455-470 (1979) [4] Barrat J.A. et al. , *MAPS* in press (2006) [5] Mittlefehldt D.W., *GCA* **58**, 1537-1552 (1994) [6] Fowler G.W. et al., *GCA* **59**, 3071-3084 (1995) [7] Barrat J.A., *MAPS* **39**, 1767-1779 (2004) [8] Stolper E., *GCA* **41**, 587-611 (1977)

AUTHOR INDEX